2007

Granular Contact Lubrication: Theory and Experiment

Karim El Kholy
Louisiana State University and Agricultural and Mechanical College

Recommended Citation

El Kholy, Karim, "Granular Contact Lubrication: Theory and Experiment" (2007). *LSU Doctoral Dissertations*. 1718.
https://digitalcommons.lsu.edu/gradschool_dissertations/1718

GRANULAR CONTACT LUBRICATION: THEORY AND EXPERIMENT

A Dissertation

Submitted to the Graduate Faculty of the
Louisiana State University and
Agricultural and Mechanical College
in partial fulfillment of the
requirements for the degree of
Doctor of Philosophy

in
The Department of Mechanical Engineering

By
Karim El Kholy
B.S., AASTMT, 1994
M.S., AASTMT, 1999
December 2007

This work is entirely dedicated to my beloved father “Nabil El Kholy”

You showed me all my life the true meaning of hard work and devotion. I will be forever thankful for your support and personal sacrifices that you made. I would never be in this stage of life without your guidance, encouragement, and confidence in me. You provided me with everything possible and you taught me the love of learning, the value of hard work, the respect for others, and the concept of setting goals and persistence to complete them. I am who I am today because of you. This dissertation stands as a tribute to you for everything you taught me. I have always wanted to make you proud of me. Dad, no words in the world can express my feelings and gratitude. Thank you from the bottom of my heart for everything.

ACKNOWLEDGMENTS

No word can express my gratitude to Dr. Michael Khonsari, my advisor and major professor, for his kind supervision, continuous help, guidance, valuable instruction and encouragement while working on this fascinating subject. Special thanks to Dr. Peter Wolenski, my minor professor, for his guidance and help throughout my studies in the Department of Mathematics. Also, I am sincerely thankful to Dr. Su-Seng Pang for all his advice, support, and continuous encouragement. Without their support, this journey would not have been completed.

I would like to acknowledge all my committee members, Dr. M. Khonsari, Dr. S. Pang, Dr. Y. Ram, Dr. W. Meng, and Dr. P. Wolenski for their support and spending time in evaluating my dissertation. They provided me the determination and confidence that were needed in order for me to reach this milestone in my life. I would like also to acknowledge and express my appreciation to the valuable help and discussions of Dr. J. Jang and I would like to thank all my other fellow members of the Tribology Group in the Center for Rotating Machinery (CeRoM) for their valuable discussions and remarks during my presentations.

Furthermore, I wish to gratefully acknowledge the partial financial support of the National Science Foundation (under the award no. CMS-0096141) in which Dr. Jorn Larsen - Basse is the Program Director. Also, I express sincere gratitude to Dr. F. Neubrander for choosing me as one of the NSF GK-12 graduate fellow for the last two years of my studies.

Finally, to my parents, my devoted wife and my daughter who have been a constant source of inspiration and encouragement over the years. There is absolutely no way that this achievement could have been possible without their support, confidence, and understanding. Their positive influences have contributed significantly to whatever success I have enjoyed thus far in life. I express sincere gratitude to my wife who stood by my side and helped me in this long but worthy journey.

TABLE OF CONTENTS

LIST OF TABLES

LIST OF FIGURES

NOMENCLATURE

a_c	Average boundary area per granule
$\frac{1}{a_c}$	Number of granules adjacent to the unit area of the surface
$A_{1\to11}$	Dimensionless constant
B	Dimensionless constant
c_{Bott}	Specific heat of the bottom plate
c_p	Specific heat of the granular lubricant
c_{Top}	Specific heat of the top plate
C	Dimensionless constant
d	Granule diameter
D	Dimensionless constant
$\frac{D}{Dt}$	The material derivative
e_p	Coefficient of restitution of granules
e_w	Wall coefficient of restitution
E	Total energy per unit mass of the granular material
E_h	The true thermal energy per unit mass of the granular material
E_{MK}	The kinetic energy per unit mass of the granular material
E_{PB}	Energy loss per granule boundary collision
E_{PT}	The pseudo thermal energy per unit mass of the granular material
$f_{1\to9}(\upsilon)$	A series of non-dimensional functions
$ff_{1\to5}(\upsilon)$	A series of non-dimensional functions
f	Discrete friction coefficient for each x-coordinate
f^*	Overall friction coefficient
F	Friction force
F^*	Non-dimensional frictional force
F_r	Stress constant
F_t	Tangential force per unit area acting on the boundary

g	Gravity acceleration
g_0	The Carnahan-Starling form of radial distribution for granules
g_1	Variable used to eliminate the coupling term $\frac{\partial \upsilon}{\partial y}$
h_1	Gap width of inlet in the slider nearing case $(H = h_1)$
h_2	Gap width at outlet
h_{Bott}	Convection heat transfer at the bottom plate
h_{Top}	Convection heat transfer at the top plate
H	Gap width in the parallel plate case
H^*	Dimensionless gap width
$\boldsymbol{I}$	Identity tensor
k	Heat conductivity of granule lubricant
k_{air}	Thermal conductivity of air
k_{Bott}	Thermal conductivity of the bottom plate
k_{eff}	Effective thermal conductivity of the granular material
k_p	Thermal conductivity of the granular particle
k_{Top}	Thermal conductivity of the top plate
L	Length of the bearing
m	Mass of each spherical granule
$m\phi_w u_{sl}$	Average tangential momentum transferred per collision
$\dot{m}$	Mass flow rate
$\dot{m}^*$	Dimensionless mass flow rate
M_{PW}	Momentum transfer between the granule and the wall
$\boldsymbol{n}$	Unit normal of the boundary pointing into the clearance gap when the granular material flows
n	Integer constant
N	Normal load applied per unit area
N_f	Normal stress contributed by contact force
Pr	Prandtl number
q_h	True energy flux vector

q_{PT}	Flux vector of pseudo thermal energy
q_{slip}	Rate of heat generation due to slip at the boundary
Q	Total energy flux vector
s	Average distance between the boundary and the surface of an adjacent granule
$\boldsymbol{S}$	Deviatoric part of the rate of deformation tensor
t_{Bott}	Thickness of the bottom plate
t_{Top}	Thickness of the top plate
T	Pseudo temperature ($T = \frac{1}{3}V^2$)
T_o	Reference temperature
T_{in}	Inlet temperature $\left(T_{in} = T_o\right)$
T_∞	Ambient temperature
T_{Bott}	True temperature of the bottom plate
T_R	True temperature of granular lubricant
T_{Top}	True temperature of the top plate
T^*	Dimensionless pseudo temperature
T^*_{Bott}	Dimensionless true temperature of the bottom plate
T^*_R	Dimensionless true temperature of granular lubricant
T^*_{Top}	Dimensionless true temperature of the top plate
u	The component of the bulk velocity
u^*	Dimensionless grain flow velocity in x^*- direction
u_{Bottom}	Slip velocity at the bottom plate
u_{sl}	Slip velocity at the boundary
u_{Top}	Slip velocity at the top plate
u_{wall}	Bulk velocity at the boundary
$\frac{u_{sl}}{\lvert u_{sl}\rvert}$	Unit tangential directed in the positive X-direction where shear take place
U_L	Bottom plate velocity
$\boldsymbol{U}$	The bulk velocity tensor
V	Mean fluctuation velocity

V'	Mean fluctuation velocity of the granule after collision with the boundary
W	Load carrying capacity per unit width
W^*	Dimensionless load carrying capacity
x	Coordinate direction along slider length
x^*	Dimensionless coordinate
y	Coordinate direction across slider gap
y_{Top}	Coordinate direction across the top plate
y_{Bott}	Coordinate direction across the bottom plate
y^*	Dimensionless coordinate
y^*_{Top}	Dimensionless coordinate direction across the top plate
y^*_{Bott}	Dimensionless coordinate direction across the bottom plate
α	Flexible number of order unity
α_{Bott}	Thermal diffusivity of the bottom plate
α_{Top}	Thermal diffusivity of the top plate
β	Thermal polarizability
δ	Friction angle between the surface and granule
δ_{ij}	Kronecker Delta
γ	Rate of energy dissipation due to inelastic collisions between granules
ϕ	Internal angle of friction
ϕ_o	Bottom Plate surface roughness
ϕ_H	Top Plate surface roughness
ϕ_w	Roughness of the wall
η	Constant characterizing the inelastic collision between granules
λ	Thermal conductivity for perfectly elastic granules
μ	Shear viscosity for perfectly elastic granules
μ_b	Bulk viscosity for perfectly elastic granules
ρ	Bulk density of the granular material
ρ_{Bott}	Density of the bottom plate
ρ_p	Density of the individual granule

ρ_{Top}	Density of the top plate
σ	Stress tensor
σ_{ck}	Stress tensor caused by collision and kinetic motion
σ_f	Stress tensor caused by enduring contact force
υ	Solid volume fraction
$\upsilon_{\max}$	Value of υ at closest random packing
∇	Symbol for gradient

ABSTRACT

This dissertation is devoted to a theoretical and experimental study of the granular contact lubrication, both. The theory is based on the kinetic of the granular material where the granules interact with each other and with the boundary surfaces through instantaneous, binary collisions, characterized by a constant coefficient of restitution. Specifically this study focuses on granular lubrication in Couette flows. A series of simulations is reported and the results show good agreement with several published papers. Also, a theory that ties the true temperature to the grain mobility is developed. The true temperature of a granular material depends on the balance between the source of energy and the dissipation of energy due to inelastic collisions.

In treating rapid shearing regime the collision is generally considered to be instantaneous. However, in a dense regime and at relatively small sliding speeds, the contact time between the granules is larger than the time between collisions and thus the friction between the granules starts to play an important role. Therefore, the effect of enduring contact becomes dominant over that of the kinetic and collisional stresses. The enduring contact between granules is into consideration by making use of Coulomb friction model. The results reveal that the enduring contact is a strong function of the solid volume fraction and its effect tends to dominate the solution at relatively small sliding speeds.

A series of experimental investigations is presented that demonstrate the lift phenomenon observed in an annular shear cell apparatus. The effects of the friction coefficient and the surface roughness are expressed as a function of the rotational speed and the applied load. The theoretical results and the experimental measurements are compared. The results of experiments provide a unique quantitative evidence for the measure of the phenomenon of the lift. Furthermore, a series of experimental investigation on the nature of stick-slip associated with granular materials sheared at low speeds is demonstrated. The results reveal the occurrence of stick-slip at low speed. The behavior of the stick-slip is similar to the results presented by several researchers interested in physics and geology fields.

CHAPTER 1. INTRODUCTION

1.1 Introduction

Research in granular flow has a rich history of development dating back to more than a century ago. Reynolds [1] was probably the first to lay the foundation of granular flow by describing the dilation property of closely-packed assembly of granular material. Over a half a century later following the Reynolds' study, researchers with expertise in fluid mechanics have studied granular flows beginning with Bagnold [2] who performed a pioneering experimental study of the flow of granular material under shear. In his experiment, dispersed solid spherical granules of uniform size was used and sheared between two concentric drums. Bagnold's experiments shed light on two distinct regimes: granule-inertia regime and macro-viscous regime. A third transition regime was also established and empirical relations for shear stress were formulated.

Over the last two decades there has been significant interest in lubrication characteristics of granular material. Conventional lubricating oils are completely ineffective beyond a certain operating temperature. They tend to break down at operating temperature exceeding 200 ^{o}C, degrading their ability to support load. This is in part due to the fact that viscosities of most motor oils decay exponentially with increasing temperature. Unlike conventional lubricants, which ordinarily become ineffective beyond 200^{o} C, a suitable granular material can effectively lubricate a bearing under extreme temperatures and can resist breaking down as a result of large shear forces. For example, the viscosity of SAE-40 oil at 204 ^{o}C (400 ^{o}F) is approximately 1.3% of its viscosity at 15.5 ^{o}C (60 ^{o}F). This presents a serious problem for the development of the future generation of bearings that need to operate at elevated temperature of 600 ^{o}C and beyond. Thus, alternative lubricants that could withstand extreme temperatures need to be explored. Fine granular lubricants have been introduced as a promising solid material for this specific purpose.

Heshmat [3] reported the first documented experimental investigation of the lubrication characteristics of powders. He injected Titanium Dioxide (TiO_2) into the clearance of a slider bearing to measure the pressure generated across the bearing length (see Figure 1.1). He found that the powder lubricant produce pressure profiles similar to those of oils and he referred to this type of powder flow as "Quasi-Hydrodynamic Lubrication". He pointed out that the peak pressure of the powder lubricant was skewed towards the bearing's trailing edge more than the conventional lubricants. Heshmat [4] determined that there were certain conditions related to the range of granular size relative to the bearing surface features, which should be satisfied in order for the quasi-hydrodynamic lubrication to hold. He reported that very small granules tend to conglomerate and form a kind of solid wedge, while bigger granules behave more like intermediate elastic bodies that cause abrasive wear.

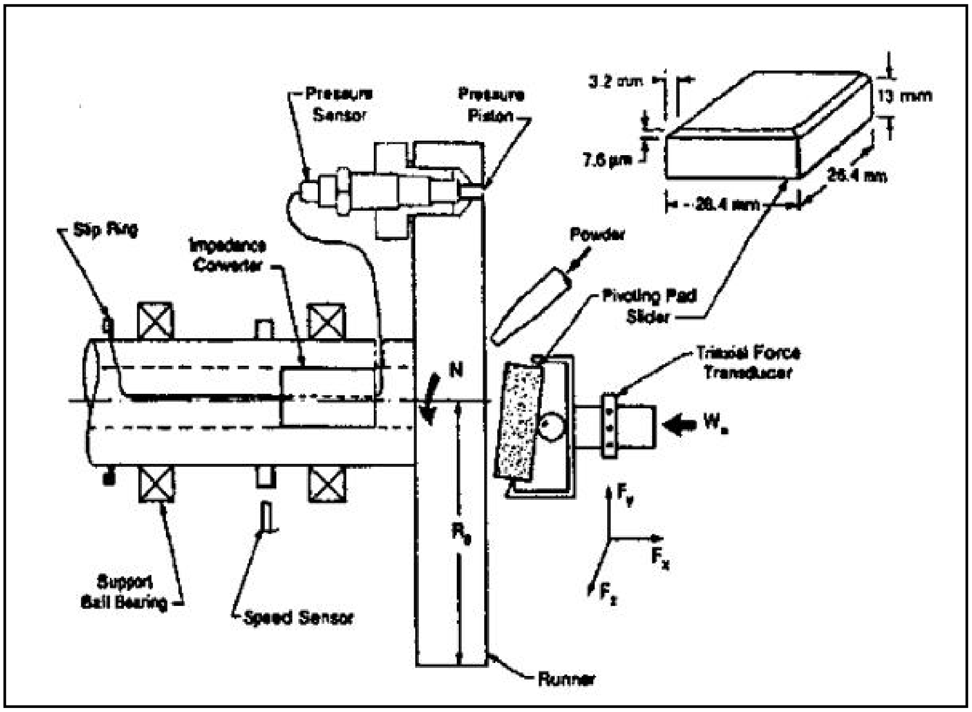

Figure 1.1 : Heshmat's Experimental Test Rig [3]

To gain insight into granular lubrication, one must study the flow behavior of granular materials as they undergo a shearing action within a thin clearance space. Granular flow refers to the motion of an assembly of solid components of granules. In general, prediction of this granular material behavior is very complex. The instantaneous motions of grains, their transitional velocities and spins are different from the mean motion of the bulk. Individual granules may interact with one another in various ways. The stresses are generated through sustained rolling or sliding contacts in rigid clusters of granules, or by instantaneous collisions through which linear and angular momentum are exchanged and the energy is dissipated because of the inelasticity and friction.

To investigate the granular lubrication phenomenon, we concentrate our attention on granular flows in the rapid shearing and transient regimes. In the analysis of the rapid shearing of granular material, the collision between the particles provides the principal mechanism for the transportation of momentum and energy. If the assumption of continuum holds, then the kinetic theory of dense gases can be applied to derive the balance laws and the constitutive relations for idealized granular material. The behavior of granular material in motion is compared with the conventional fluid-mechanical phenomenon. Accordingly, the individual grains are treated as the molecules of a granular fluid. The main difference between molecules and grains is that collisions of the latter are inevitably inelastic; hence, there is energy loss due to grains collisions.

1.2 Literature Review

The study of powder flow has become a fascinating research topic in recent years. One motivation for this is the development of Integrated High Performance Turbine Engine Technology (IHPTET) which calls for engine operation at very high temperatures. Yet, a thorough understanding of the flow characteristics of granular material within the context of lubrication is still lacking.

For a general granular material, the procedure used for the development of governing equations and the constitutive equations (consisting of stresses, energy flux and the collisional rate of energy dissipation) is similar to the approach employed in the kinetic theory of dense gases, where the granular particles are playing the role of molecules. The theory applied is an extension of the original kinetic theory of Maxwell. Therefore, the theory of powder lubrication is developed from the fundamental principles of fluid mechanics with appropriate formalism. This theory is capable of providing a complete description of the behavior of powders as they flow inside the clearance space of a hydrodynamic bearing.

From the microstructure point of view, a number of researchers have dealt with the rapid shear flows. Savage and Jeffrey [5], made the first attempt to apply the ideas contained in the theoretical work dealing with dense gases. They proposed a theory to determine the stress tensor for granular material in a rapid simple shear flow. They assumed that the grains are made of uniform, smooth, and perfectly elastic spheres. The binary collisions between the spheres were assumed to be responsible for most of the momentum transport. The single granular velocity distribution function was taken to be locally Maxwellian. They assumed a modification to the radial distribution function of Carnahan and Starling [6] to account for anisotropy in the spatial distribution of the particles. The components of the stress tensor were expressed as integrals involving a non-dimensional parameter directly related to the dissipation properties of the system.

Extension of Savage and Jeffrey's work to incorporate energy dissipation was performed by Jenkins and Savage [7] and Lun *et al.* [8]. Jenkins and Savage [7] developed a theory applicable to general deformations of a granular material made up of smooth, nearly elastic, spherical particles. Lun *et al.* [8] dealt with simple shear flow with no gradients of the velocity in the y-direction. The collision integrals involving the non-dimensional parameter related to the dissipation properties of the system presented by Savage and Jeffrey [5], were evaluated both numerically and by asymptotic analysis. The predicted theoretical results agreed with those measured.

To gain more insight into the behavior of granular flows, several researchers studied the rotational inertia and the surface friction of grains. The development of these theories came from the study of Jenkins and Richman [9] for systems of smooth, inelastic circular discs; Jenkins and Richman [10] for rough, inelastic circular discs and spheres; and Jenkins and Mancini [11] for both binary mixtures of smooth, inelastic, circular discs and spheres. Moreover, Lun and Savage [12] studied the effect of an impact velocity dependent coefficient of restitution for rough, inelastic, spherical particles, while Walton [13] considered the effect of frictional force for the spheres. These theories consist of the balance equations for certain mean flow fields and the constitutive relations that measure the rate at which momentum and energy are transferred throughout the flow.

Haff [14] put forward a general theory for the flow of granular materials. In Haff's theory, the behavior of granular material in motion was studied and compared with the conventional fluid-mechanical phenomenon. The individual grains were treated as the molecules of the granular fluid. The main difference between molecules and grains was that collisions of the latter were inevitably inelastic. Haff [14] wrote down a set of complete equations, which were modeled based on the usual equations of hydrodynamics. Haff's view of granular flows was motivated by the molecular motion within a dense gas and his theory had the same structure as the corresponding kinetic theories. The appropriate conservation laws were expressed in terms of macroscopic variables and a complete model was formulated by direct appeal to the nature of grain-grain collisions. In Haff's theory, the microscopic properties of the flow were described without carrying out statistical averaging. Nevertheless, several unknown parameters in his model remained unevaluated, which could have helped in more realistic predictions.

Johnson and Jackson [15] introduced a more complicated model which included the effect of enduring contact. They assumed that some particles were sliding while others were colliding (frictional-collisional mechanism). Both normal and tangential friction of sliding particles was related by the Coulomb law of friction. The normal and tangential forces were dominant when the granules were densely packed, and the momentum transfer due to collisions was dominant when the granules were widely spaced. In Johnson and Jackson's model, they considered a case where interparticle contacts are of intermediate duration in the flow region. Further reading on the applicability of this model to tribology is presented by Johnson and Jackson [15], Elrod [16] and Khonsari [17].

The utility of granular lubricants in applications involving auxiliary bearings particularly for use during start-up periods have already been demonstrated by Kaur and Heshmat [18]. The application of the pelletized dry particulate that provides a long life and low power loss backup bearing was investigated by Kaur and Heshmat [18] who developed a prototype of a self-contained solid/powder lubricated auxiliary hydrodynamic bearing. The tests were conducted using several durations, with a bearing operated up to 30,000 RPM, and loads up to 445 N resulting in a validation for the powder lubricated bearings with wider range of operating conditions.

Craig *et al.* [19] studied the rapid shearing flow of dry metal powders in an annular shear cell. Their results showed the dependence of the normal and shear stresses on the shear rate, and a significant dependence on the gap thickness and the solid volume fraction. Heshmat [20] was the first to relate a powder lubrication mechanism to a hydrodynamic fluid film. He found that a sheared layer of the compacted powder generates profiles resembling the fluid film bearing. Heshmat [3] conducted the first documented experiment to investigate the lubrication characteristics of powder lubricant as it flows in the clearance space of a bearing. He showed that the ensuing pressure distribution generated is remarkably similar to that of a liquid lubricant.

Experimental evidence of Savage and Sayed [21], and Hanes and Inman [22] demonstrated that differences in the boundaries that drive identical granular shear flows may be responsible for very significant differences in the stress induced. Yu *et al.* [23] introduced an approximate theory from momentum considerations and performed experiments based on granular material (glass granules) contained in an annular cell formed by flat, parallel plates, and then by a series of convergent wedges. By measuring the normal and shear stresses developed by the cell, they validated the concept of lubrication through granular collisions. Strong boundary effects on the stresses were also realized in the shear cell experiments of Yu and Tichy [24].

To capture some of the powder lubrication features, Dai *et al.* [25] addressed the variable geometry boundary problem by applying Haff's constitutive relations and energy and momentum equations to the powder flow of the slider bearing. They presented theoretical derivations based on the no-slip boundary condition as well as for a situation where a slip distribution function was imposed on the surface. Their theory replicated the trends of the pressure profile measured experimentally by Heshmat [3]. In order to predict the powder flow using a continuum approach, Yu *et al.* [23] proposed the concept of granular collision lubrication by considering the collisional normal stress generated by kinetic energy of the granules and the lubrication normal stress due to converging surfaces. They developed a theory, from momentum considerations, for interpreting the experimental results.

McKeague and Khonsari [26] generalized the boundary interactions for powder lubricated Couette flows following the work of Hui *et al.* [27] and Jenkins and Richman [9]. They provided a set of equations that governs the boundary conditions of the flow velocity and the granular temperature without the need of the slip function. The results of the theory were found to be in good agreement with other authors who have investigated granular Couette flows using direct computer simulations of granular collisions such as those published by Campbell [28] and Elrod and Brewe [29].

On the general modeling of granular flows, Lun *et al.* [8], in a frequently cited paper, developed the complete set of constitutive equations including the viscous dissipation term in the pseudo energy equation. This viscous dissipation was found to be important by Zhou and Khonsari [30] in the simulations of powder lubricants. Following the work of Johnson and Jackson [15], Zhou and Khonsari [30] derived the appropriate governing equations of the granular material sheared between two infinitely long parallel disks to predict the mean velocity, the pseudo temperature (fluctuation velocity), and the solid volume fraction of the granular material across the gap. Sawyer and Tichy [31] performed numerical and particle simulations to generate results that were compared to the granular experiments of Yu and Tichy [24]. They found that trends of both methods were in agreement but the theory over-predicted the experimental results of the normal load and the shear force.

The powder lubrication theory of Dai *et al.* [25] and McKeague and Khonsari [26] is entirely based on the Haff's continuum theory. In that theory, particles do not possess an enduring contact, the friction between particles is neglected, and the viscous dissipation in the energy dissipation is neglected to provide an analytical solution. This means, the stress field is governed entirely by the collision and kinetic stress.

In a classification of dry particulates used as lubricants Wornyoh *et al.* [32] presented a thorough literature review covering the last five decades of published papers. They categorized the works in dry particulate tribology literature expressing the theory, experiments and numerical simulations. Pertinent literature of interest in the present chapter include the work of Yu and Tichy [24] whose experiments revealed that at low speeds, the rotation is accompanied by grinding and some crushing noises due to the high frictional forces between the compressed granules and the surfaces. By increasing the speed, the grinding and crushing noises subsided and the lower cylinder disk began to lift off, hence, surfaces separated from each other.

To gain insight into granular lubrication, one must study the flow behavior of granular materials as they undergo a shearing action within a thin clearance space. Based on Johnson and Jackson [15], the recent powder lubrication theory published by Zhou and Khonsari [30], and Pappur and Khonsari [33] predicted that powders are capable of generating a lifting force even if placed in a configuration of two parallel disks in relative motion. This is intriguing because the hydrodynamic theory of Newtonian fluids predicts that parallel disks are incapable of generating any load-carrying capacity.

For several years, the science and application of third body tribology have been investigated by researchers. A flow transition between two regimes is experienced: the kinetic regime which occurs at low pressure and high speed and the load is essentially transmitted by collisions between the third body granules, and the quasi-fluid regime which occurs when the third body is compressed and the contacts between the granules last for longer periods. To shed light on the transition between kinetic and quasi-fluid regimes, Iordanoff *et al.* [34] proposed an investigation concerning the interactions between microscopic properties of the solid third body and the macroscopic behavior of the contact. Their discrete model uses the distinct element method (DEM) in order to understand phenomena occurring in dry contact. They showed that the particle size has a weak influence when inter-particle forces are repulsive but has a dramatic influence when inter-particle adhesion is considered: solid third body goes from a quasi-fluid to a quasi-solid behavior. Iordanoff and Khonsari [35] reported the development of a quasi-two-dimensional particle dynamic simulation program, which yielded good agreement between the predictions of the particle dynamic simulations and the kinetic model. Furthermore, they demonstrated a link for the flow transition between both regimes.

In order to quantify the normal and shear stress behavior of binary mixtures of dry particulate solids, Hassanpour *et al.* [36], conducted experiments using an annular shear cell and performed a series of numerical simulations using the distinct element method (DEM). They found that the mixtures of different sizes of glass granules indicate a highly non-linear particle displacement distribution across the shear layer. They indicated that the behavior of the mixture is an intermediate regime between quasi-static and rapid shear flows. Higgs and Tichy [37] studied the continuum modeling of shear behavior of various granular flows using a granular kinetic lubrication model (GKL) of simple shearing flow. New parametric curves for the local flow properties of large-particle granules were constructed. Their numerical model showed qualitative agreement but over-predicts quantitatively with past annular shear cell experiments using glass granules.

Based on particle dynamic model, Fillot *et al.* [38] developed a third body source flow model allowing particle detachment of a granular material. They found that there is no correlation between degradation and friction coefficient measured, and concluded that changes in properties of the third body – such as its cohesion and damping – provide equivalent degradations in both kinetic and fluid regimes whereas they affect the friction coefficient dramatically. Their examination of the friction coefficient confirmed the ideas found in the work presented by Wang and Kato [39] concerning the non-correlation between friction and wear.

Based on Johnson and Jackson's granular theory, Jang and Khonsari [40] developed a general theory for characterization of powder flow within the context of the lubrication. Specifically, they derived a 3D generalized Reynolds equation that predicts the pressure profile in a bearing with any specified film profile. The flow velocity, volume fraction, and pseudo temperature (granular fluctuations) were predicted simultaneously. They studied the characteristics and analyzed the behavior of the granular powder, and showed that the pressure profile was, indeed, very similar to the conventional fluid-film hydrodynamic lubrication.

Moreover, comparison with experimental results of Heshmat yielded good agreement both in trend and magnitude. Tsai and Jeng [41] analyzed the performance of hydrodynamic journal bearings using grain flow based on Haff's grain flow theory. They found in their predicted numerical results consistency with the experimental results found by Heshmat and Brewe.

CHAPTER 2. SCOPE OF THE RESEARCH

Granular collision lubrication is a ground-breaking subject in the field of tribology. Recently, several investigations were done to confirm that the use of an appropriate granular material such as Titanium Dioxide (TiO_2) or Molybdenum Disulfide (MoS_2) in a bearing clearance can provide very efficient lubrication. The innovative experiment of Heshmat [3] and related development as reported by Kaur [42] have proven the capability of powders to generate "hydrodynamic type" pressure similar to the conventional lubricants, and thus yield positive load-carrying capacity.

The motivation for this dissertation arises from the need for bearing technology that can accommodate the future generation of engines aiming higher thermodynamic efficiency, less fuel consumption, and increased thrust-to-weight ratio in turbine engines. While the need for oil-free granular lubrication has been identified, the modeling and prediction of granular flows within the context of lubrication still remains poorly understood.

The theory presented in this dissertation closely follows the work of Zhou and Khonsari [30], Johnson and Jackson [15], Lun and Savage [12], Hui and Haff [27], and Jenkins and Savage [7]. A realistic constitutive equation introduced by Lun *et al.* [8] is utilized to study the mechanism of granular lubrication. The effect of viscous dissipation term, neglected by McKeague and Khonsari [26, 43], is included in the pseudo energy equation. This theory is applied to investigate granular lubricant sheared between two parallel plates. The distribution of solid volume fraction together with the mean velocity and granular temperature appear naturally in the governing equations and are directly predicted by the theory presented herein. Therefore, unlike in Haff's theory, there is no need for assuming thickness dilation to determine the solid volume fraction.

This dissertation is devoted to provide a detailed development of the granular contact lubrication theory. The collisional lubrication theory has the same structure as the corresponding kinetic theories. The formulation of the problem starts with the first principles of fluid mechanics, i.e., conservation of mass, momentum and pseudo temperature. The granules possess both a flow velocity and a fluctuation velocity. The granules behavior requires implementing appropriate boundary conditions for the slip velocity and the pseudo temperature. These boundary conditions play a very important role along with the equations of motion and the pseudo energy equation in forming a complete set of equations for predicting the behavior of the granular flows when sheared between parallel disks.

In this theory, an order of magnitude analysis is carried out to simplify the governing granular lubrication equations. The solid volume fraction, together with the mean velocity and the granular temperature, appear naturally in the equations and are directly predicted from a complete set of governing equations and boundary conditions. An accurate and realistic model is introduced to investigate the mechanism of granular lubrication in Couette flows. Because of the complexity and nonlinearity of the governing equations and boundary conditions, an efficient numerical scheme is used to simulate the problem. The effect of the viscous dissipation in the energy equation is considered in the simulations, while other researchers neglect this term. A benchmark is set up based on some published papers to compare the results obtained. Different parameters of interest are investigated, and the results are compared with those by McKeague and Khonsari [26], Zhou and Khonsari [30], Sawyer and Tichy [31], and Pappur and Khonsari [33].

It was found that granular material plays a major role in determining the axial load transmitted (lift) between the surfaces, the sliding friction and the slip velocity, but uncertainties still remain on several issues, which require more investigation. Thus following to the theoretical model, an experimental investigation of the friction and lift characteristics of granular lubrication is presented. Experiments were conducted using 3-mm stainless steel balls, as well as 1.4-mm ceramic balls to demonstrate the lift phenomenon observed in an annular shear cell apparatus. The effects of the friction coefficient and the surface roughness have been expressed as a function of the rotational speed and the applied load. Simulations of the kinetic theory for the granular material are performed and compared with the experimental results for validation purposes.

While the archival literature contains a great deal of research on granular lubrication, a number of important issues remain largely unexplored. Of particular interest is to examine the stick-slip phenomenon associated with granular materials within the context of lubrication. An experimental investigation on the nature of stick-slip associated with granular materials sheared between two parallel disks is demonstrated. In addition to that, a thorough background on the stick-slip phenomenon is also presented and a series of experiments were carried out using ceramic granules to demonstrate its effect on the friction coefficient and the displacement (lift).

Results are presented for the friction coefficient and the displacement as a function of the rotational speed and the applied load.

To further the theory of granular lubrication, a theoretical study on the true temperature of the granular material is presented and analysis is performed. A theory that ties the true temperature to the grain mobility is developed by predicting the true temperature of granular lubricants sheared between two infinitely wide parallel plates. The distribution of the true temperature at both top and bottom interfaces along the x-direction is predicted and the variation of a number of important parameters and their effect on the true temperature is analyzed. For materials packed in a random assembly of microspheres, it is important to estimate correlation for the effective thermal conductivity. An analysis to determine the effective thermal conductivity is presented.

The majority of publications in granular lubrication dealt with the rapid shearing regime of granular material where only kinetic and collision effects are considered whereas the effect of a so-called enduring contact is neglected. However, most of the granular material in the context of lubrication systems operates in a dense regime with a very small gap thickness and high solid volume fraction where friction between granules starts to initiate. Thus, the enduring contact effect needs to be considered. In this dissertation, the Coulomb friction model is introduced to study the effect of the friction force caused by enduring contact between the granules. The characteristics of the flow are investigated in a transient regime where both kinetic-collision effect and enduring contact exists concurrently. The formulation of the governing equations and boundary conditions of the granular flow are formulated along with an efficient numerical simulation.

CHAPTER 3. THEORY OF COLLISIONAL GRANULAR MATERIAL

3.1 Development of Theory

A common feature of collisional granular flow is that grains interact with each other and with the boundary surfaces through collisions. These collisions are responsible for the transfer of momentum and the dissipation of energy in the flow. The granules possess both a flow velocity and a fluctuation velocity. The latter is commonly referred to as pseudo temperature (not a measure of the thermodynamic temperature). According to Johnson and Jackson [15], some of the granules undergo sliding motion while the rest are colliding. Thus, the total stress tensor is the sum of both frictional and collisional-translational stresses. In the theoretical model that follows, granules are assumed to be identical, smooth, frictionless spheres. In chapter 12, the friction between the granules will be considered. Therefore, it is assumed that the work done by the frictional component of stress is translated directly into thermal internal energy; hence the true heat flux (thermodynamic temperature) is not considered in the energy equation, and the collisional-translational component is translated into pseudo thermal energy.

The formulation of the problem starts with the first principles of fluid mechanics, i.e., conservation of mass, momentum and pseudo temperature. For a discussion of the range of applicability of this theory, one can refer to Johnson and Jackson [15] and a review paper by Elrod [16]. The general governing equations for granular flow require consideration of the conservation laws described below.

3.2 General Governing Equations

3.2.1 Conservation of Mass

The governing equation for conservation of mass is:

$$\frac{\partial \rho}{\partial t} + \nabla.(\rho U) = 0 \tag{3-1}$$

where $\rho = \rho_p \upsilon$ is the bulk density of the granular material,

ρ_p is the density of the individual granule,

υ is the solid volume fraction,

U is the bulk velocity defined as $\left(u\hat{i} + v\hat{j} + w\hat{k}\right)$;

u, v, and w are the components of velocity in x, y, and z directions, and

∇ is the symbol for gradient $\left(\nabla = \mathrm{i}\frac{\partial}{\partial x} + \mathrm{j}\frac{\partial}{\partial y} + \mathrm{k}\frac{\partial}{\partial z}\right)$.

3.2.2 Conservation of Momentum

The governing equation for conservation of momentum is:

$$\rho\frac{DU}{Dt} = \rho g - \nabla.\sigma \tag{3-2}$$

where g is the gravity acceleration and σ is the stress tensor (a second order tensor) defined as:

$$\sigma = \begin{bmatrix} \sigma_{xx} & \sigma_{xy} & \sigma_{xz} \\ \sigma_{yx} & \sigma_{yy} & \sigma_{yz} \\ \sigma_{zx} & \sigma_{zy} & \sigma_{zz} \end{bmatrix}$$

$$\sigma = \sigma_{ck} + \sigma_f \tag{3-3}$$

where σ_{ck} is the stress tensor caused by collision and the kinetic motion, and

σ_f represents the stress tensor caused by enduring contact force between granules.

$\frac{D}{Dt}$ is the material derivative and defined as:

$$\frac{D}{Dt} = \underbrace{\frac{\partial}{\partial t}}_{\text{Local derivative}} + \underbrace{u\frac{\partial}{\partial x} + v\frac{\partial}{\partial y} + w\frac{\partial}{\partial z}}_{\text{Convective derivatives}}.$$

3.2.3 Conservation of Energy

The governing equation for conservation of energy is:

$$\frac{D(\rho E)}{Dt} = -\nabla.Q - \sigma : \nabla U \tag{3-4}$$

where $\nabla.Q$ represents the heat conduction term, $\sigma : \nabla U$ is the viscous dissipation term and is defined in a Cartesian coordinate system as follows:

$$\sigma : \nabla U = \sigma_{ij}\frac{\partial u_i}{\partial x_j} = \sigma_{ji}\frac{\partial u_j}{\partial x_i}, \text{ since } \sigma_{ij} \text{ is symmetric}$$

$$\sigma : \nabla U = \sigma_{xx}\frac{\partial u}{\partial x} + \sigma_{xy}\frac{\partial u}{\partial y} + \sigma_{xz}\frac{\partial u}{\partial z} + \sigma_{yx}\frac{\partial v}{\partial x} + \sigma_{yy}\frac{\partial v}{\partial y} + \sigma_{yz}\frac{\partial v}{\partial z} + \sigma_{zx}\frac{\partial w}{\partial x} + \sigma_{zy}\frac{\partial w}{\partial y} + \sigma_{zz}\frac{\partial w}{\partial z} \tag{3-5}$$

Q represents the total energy flux vector:

$$Q = q_{PT} + q_h \tag{3-6}$$

where q_{PT} is the flux of pseudo thermal energy that is related to the fluctuation velocity of granular particles, q_h is the true heat flux and is defined as $q_h = -k\nabla T_R$, and k is the heat conductivity of the granules lubricant.

The parameter E is the total energy per unit mass of the granular material and is composed of:

$$E = E_{MK} + E_{PT} + E_h \tag{3-7}$$

where E_{MK} is the kinetic energy associated with the local average velocity,

E_{PT} is the pseudo thermal energy associated with the fluctuation velocity, and

E_h is the true thermal internal energy of single granule.

Appropriate expression for each term is given below:

$$E_{MK} = \frac{1}{2}\rho|U|^2 \tag{3-8}$$

$$E_{PT} = \frac{1}{2}\rho V^2 = \frac{3}{2}\rho T \tag{3-9}$$

$$E_h = \rho c_p T_R \tag{3-10}$$

where $T = \frac{1}{3}V^2$ is often referred to as the pseudo temperature,

V is the mean fluctuation velocity,

V^2 is the mean square of the velocity fluctuation velocity about the bulk velocity U,

T_R is the parameter of the true temperature, and

c_p is the specific heat of the granular lubricant.

Following the work of Johnson and Jackson [15], it is assumed that the work done by the frictional component of stress contributes only to the true thermal energy. Therefore, the energy equation (3-4) is separated into two equations given below:

$$\frac{D(E_{PT})}{Dt} = -\nabla .q_{PT} - \sigma_{ck} : \nabla U - \gamma \tag{3-11}$$

$$\frac{D(E_h)}{Dt} = -\nabla .q_h - \sigma_f : \nabla U + \gamma \tag{3-12}$$

where $\sigma_{ck} : \nabla U$ is the viscous dissipation done by the component of collision stress,

$\sigma_f : \nabla U$ is the viscous dissipation done by the component of frictional stress, and

γ is the rate of dissipation due to inelastic collisions between granules.

The equation of the conservation of pseudo energy is similar to the pseudo thermal energy equation given by Haff [14] and Jenkins and Savage [7] for the case in which there is no frictional contribution to stress. By separating the pseudo energy and the true thermal energy into two equations (3-11) and (3-12), it is assumed that the granular pseudo temperature is not related to the true temperature. However, the true temperature is affected by the energy dissipation caused by inelastic collision between granules.

CHAPTER 4. CONSTITUTIVE RELATIONS

4.1 Introduction

The governing equations show that constitutive equations are needed for the collisional-translational stress σ_{ck}, the pseudo thermal energy q_{PT}, and the inelastic energy dissipation γ. Lun *et al.* [8] developed two types of constitutive relations based on an accurate evaluation of the collision integral function. The first one was for inelastic granules in the simple shear flow, while the second was for slightly inelastic particles in a general flow. The effects of the enduring contact force between granules were neglected and the granules were treated as smooth, inelastic spheres. According to their work, the stress tensor and the flux of pseudo energy are contributed by two components: kinetic part, and collision part.

4.2 Kinetic and Collision Stress

In this dissertation, the second model is used for the analysis of granular flow. The appropriate constitutive equations for granular material developed by Lun *et al.* [8] based on the original work of Savage and Jeffrey [5] is used assuming that the collisional-translational contribution to stress can be calculated as though it acted in isolation. The description of the model is given below:

4.2.1 The Total Stress Tensor Caused by Kinetic and Collision

$$\begin{aligned}\sigma_{ck} &= \left[\rho T\left(1+4\eta\upsilon g_o\right)-\eta\mu_b\nabla . U\right]I - \\ &\left(\frac{2+\alpha}{3}\right)\left\{\frac{2\mu}{\eta(2-\eta)g_o}\left(1+\frac{8}{5}\eta\upsilon g_o\right)\left[1+\frac{8}{5}\eta(3\eta-2)\upsilon g_o\right]+\frac{6}{5}\mu_b\eta\right\}S \qquad (4\text{-}1)\end{aligned}$$

where *I* is the identity tensor $I=\begin{bmatrix}1&0&0\\0&1&0\\0&0&1\end{bmatrix}$, and

υ is the solid volume fraction and can be defined as:

$$\text{Solid Volume Fraction}=\frac{\text{Volume of spherical granules}}{\text{Channel Volume}}\Rightarrow\upsilon=\frac{m_T\rho_p}{A_sH},$$

m_T is the total mass the spherical granules, *H* is the gap height, A_s is the surface area,

ρ_p is the granular material density, and

S represents the deviatoric part of the rate of deformation tensor, and given by:

$$S = \underbrace{\frac{1}{2}\left(\frac{\partial u_i}{\partial x_j} + \frac{\partial u_j}{\partial x_i}\right)}_{strain\ rate\ tensor} - \frac{1}{3}\frac{\partial u_k}{\partial x_k}\delta_{ij} = \begin{bmatrix} \frac{2}{3}\frac{\partial u}{\partial x} - \frac{1}{3}\frac{\partial V}{\partial y} & \frac{1}{2}\left(\frac{\partial u}{\partial y} + \frac{\partial V}{\partial x}\right) & 0 \\ \frac{1}{2}\left(\frac{\partial u}{\partial y} + \frac{\partial V}{\partial x}\right) & \frac{2}{3}\frac{\partial V}{\partial y} - \frac{1}{3}\frac{\partial u}{\partial x} & 0 \\ 0 & 0 & -\frac{1}{3}\left(\frac{\partial u}{\partial x} + \frac{\partial V}{\partial y}\right) \end{bmatrix} \quad (4\text{-}2)$$

where δ_{ij} is the Kronecker Delta; $\delta_{ij} = \begin{cases} 1 & if\ i = j \\ 0 & if\ i \neq j \end{cases} = \begin{bmatrix} 1 & 0 & 0 \\ 0 & 1 & 0 \\ 0 & 0 & 1 \end{bmatrix}$.

The parameter η is a constant characterizing the inelastic collision between granules, and is defined as:

$$\eta = \frac{1}{2}\left(1 + e_p\right) \quad (4\text{-}3)$$

where e_p denotes the coefficient of restitution of granules. $e_p = 1$ for perfectly elastic granules and $e_p = 0$ for perfectly inelastic granules.

The factor $\left(\frac{2+\alpha}{3}\right)$ was introduced by Johnson and Jackson [15] to provide one adjustable parameter that could increase the shear stress. The parameter α is a constant of order unity (tends to unity when the coefficient of restitution e_p tends to unity and υ tends to zero). In this dissertation, it is assumed that $\alpha = 1$.

The parameter g_o represents the radial distribution function proposed by Carnahan and Starling [6] based on a semi-empirical equation of state from which they obtained the spherically symmetric equilibrium radial distribution function at contact for a single granule. The spatial pair distribution function g_o is expressed in terms of solids fraction as:

$$g_o = \frac{1}{1 - \left(\upsilon / \upsilon_{\max}\right)^{\frac{1}{3}}} \quad (4\text{-}4)$$

where $\upsilon_{\max}$ is the value of υ at closest random packing and is assumed to be 0.65 in this analysis.

According to Johnson and Jackson [15], it ensures that $g_o \rightarrow \infty$, as $\upsilon \rightarrow \upsilon_{\max}$, and hence constrains υ to remain smaller than $\upsilon_{\max}$. Johnson and Jackson [15] point out that when this parameter is inserted into the constitutive equations of Jenkins and Savage [7], they become essentially equivalent to those of Haff [14] . Parameters μ and μ_b represent the shear viscosity for perfectly elastic granules and the bulk viscosity for perfectly elastic granules, respectively. Their definitions are given below:

$$\mu = \frac{5m\left(T/\pi\right)^{\frac{1}{2}}}{16d^2} \tag{4-5}$$

$$\mu_b = \frac{256\,\mu\,\nu^2\,g_o}{5\pi} \tag{4-6}$$

where *m* is the mass of each spherical granule and defined by:

$$m = \rho_p \frac{4}{3}\pi r^3 = \rho_p \frac{4}{3}\pi \frac{d^3}{8} \tag{4-7}$$

4.2.2 The Total Flux of Pseudo Energy

The combined flux of kinetic energy and flux of the collision energy is given by:

$$\begin{aligned} q_{PT} = \frac{-\lambda}{g_o}\left\{\left(1+\frac{12}{5}\eta\upsilon g_o\right)\left[1+\frac{12}{5}\eta^2(4\eta-3)\upsilon g_o\right]+\frac{64}{25\pi}(41-33\eta)(\eta\upsilon g_o)^2\right\}\nabla T \\ -\ \frac{\lambda}{g_o}\left(1+\frac{12}{5}\eta\upsilon g_o\right)\frac{12}{5}\eta(2\eta-1)(\eta-1)\frac{d}{d\upsilon}\left(\upsilon^2 g_o\right)\frac{T}{\nu}\nabla\upsilon \end{aligned} \tag{4-8}$$

where λ represents the thermal conductivity for perfectly elastic granules, and defined by:

$$\lambda = \frac{75m\left(T/\pi\right)^{\frac{1}{2}}}{8\eta(41-33\eta)d^2} \tag{4-9}$$

4.2.3 The Collisional Rate of Energy Dissipation Per Unit Volume

$$\gamma = \frac{48}{\pi^{\frac{1}{2}}}\eta(1-\eta)\frac{\rho_p\,\upsilon^2}{d}g_o\,T^{\frac{3}{2}} \tag{4-10}$$

where ρ_p the density of the grains, and *d* is the granule diameter.

CHAPTER 5. BOUNDARY CONDITIONS

5.1 Introduction

The prediction of the granule behavior requires implementing appropriate boundary conditions to characterize their interaction with the bounding surfaces. Boundary conditions must be developed for both the slip velocity and the pseudo temperature. These boundary conditions will play a very important role together with the equations of motion and the pseudo energy equation to form a complete set of equations that will help in the predictions of the behavior of the granular flows. The flow characteristics and general behavior of granules near a solid surface could differ considerably from what is commonly observed in fluids. It has been shown by Johnson and Jackson [15] that the granular materials tend to slip at the boundary surfaces, hence the need for predicting the slip velocity.

Granular slippage is one of the important characteristics of granular lubrication. During shearing, it provides energy from the boundaries into the granules contained within the gap. Due to the slip, the granules are then loosely packed near the boundaries. Thus, the fluctuation velocity (granular temperature) increases because of the inelastic collisions between the granules and the boundaries, which causes a heat generation.

5.2 Boundary Conditions

In granular flows, the boundaries tend to supply the momentum and the energy to the interior flow by the means of shearing force and the normal force. The supplied energy must be in balance with the stress and the total flux of the energy in the flow. These ideas can be used to obtain the boundary conditions for both, the slip velocity, and the pseudo temperature.

5.2.1 Condition for the Slip Velocity

The boundary condition for the flow velocity is derived by Zhou and Khonsari [30], and Pappur and Khonsari [33] following the work of Johnson and Jackson [15]. The rate of momentum transfer M_{PW} between the granule possessing a mass m and the wall with roughness ϕ_w is given by:

$$M_{PW} = \underbrace{\left(\frac{V}{S}\right)}_{\substack{\text{Collision frequency}\\ \text{of each granule}}} \quad \underbrace{\left(m\phi_w u_{sl}\right)}_{\substack{\text{Average Tangential}\\ \text{momentum transferred}\\ \text{per collision}}} \quad \underbrace{\left(\frac{1}{a_c}\right)}_{\substack{\text{Number of granules}\\ \text{adjacent to unit area}\\ \text{of surface}}} \tag{5-1}$$

where $\frac{1}{a_c}$ represents the number of granules adjacent to the unit area of the surface,

a_c is the average boundary area per granule,

S denotes the average distance between the boundary and the surface of an adjacent granule of diameter *d*.

Both S and a_c are the functions of the solid volume fraction, as given below:

$$S = d\left[\left(\frac{\upsilon_{\max}}{\upsilon}\right)^{\frac{1}{3}} - 1\right] \tag{5-2}$$

$$a_c = d^2\left(\frac{\upsilon_{\max}}{\upsilon}\right)^{\frac{2}{3}} \tag{5-3}$$

Let u represent the bulk velocity of granular flow next to the boundary, and u_{wall} denote the velocity of the plate. Then, the slip velocity u_{sl} is:

$$u_{sl} = u - u_{wall} \tag{5-4}$$

Now considering a unit area at the boundary, the collision frequency for each granule is $\frac{V}{S} = \frac{\sqrt{3T}}{S}$, where V denotes the mean fluctuation velocity of the granule. The average tangential momentum transferred per collision is $m\phi_w u_{sl}$, where ϕ_w is the specularity coefficient. Specularity coefficient is a measure of that fraction of collisions that transfer a significant amount of lateral momentum to the wall. If ϕ_w is close to zero so that most collisions are nearly specular, i.e., a smooth wall, then the amount of slip may be relatively large. For a rough surface, however nearly every grain-wall collision will provide a significant transfer of lateral momentum to the wall; thus in this case ϕ_w is near unity and the amount of slip at the wall is minimized.

The tangential force F_t per unit area acting on the boundary [15] is:

$$F_t = \frac{u_{sl}\ .\ \sigma_{ck}\ .\ n}{\left|u_{sl}\right|} \tag{5-5}$$

where $n = \begin{bmatrix} 0 \\ \pm 1 \\ 0 \end{bmatrix}$ is the unit normal of the boundary pointing into the clearance gap when the granular material flows (bottom plate is positive sign, and top plate is negative sign),

$\sigma_{ck}\,.n$ is the force exerted on the surface with unit normal n, and

$\dfrac{u_{sl}}{|u_{sl}|} = [1 \quad 0 \quad 0]$ represents the unit tangential directed in the positive x-direction where shear take place.

A condition for the slip velocity between the granular material and a bounding surface can be obtained by equating the tangential force per unit area acting on the boundary and the rate of momentum transfer to unit area of the wall by granular collision (Jenkins and Richman [9]). The boundary condition for the slip velocity is

$$\underbrace{\underbrace{\frac{u_{sl}\,.\sigma_{ck}\,.n}{|u_{sl}|}}_{\substack{\text{Corresponding stress within}\\ \text{the particle assembly close}\\ \text{to the boundary}}}}_{\substack{\text{Tangential force per unit area exerted}\\ \text{on the boundary by the particles}}} + \underbrace{\underbrace{\frac{(3T)^{\frac{1}{2}}}{S}}_{\substack{\text{Collision frequency}\\ \text{for each particle}}}\ \underbrace{\frac{\phi_w\,\pi\,\rho_p\,d^3\,u_{sl}}{6}}_{\substack{\text{Average Tangential}\\ \text{momentum transfered}\\ \text{per collision}\\ \phi_w\,m\,u_{sl}}}\ \underbrace{\frac{1}{a_c}}_{\substack{\text{No. of particles}\\ \text{adjacent to unit}\\ \text{area of the surface}}}}_{\substack{\text{Rate of momentum transfer to unit area of the surface}\\ \text{by collisions}}} = 0 \qquad (5\text{-}6)$$

$$\frac{u_{sl}\,.\sigma_{ck}\,.n}{|u_{sl}|} + \frac{(3T)^{\frac{1}{2}}}{d\left[\left(\upsilon_{\max}/\upsilon\right)^{\frac{1}{3}} - 1\right]}\,\frac{\phi_w\,\pi\,\rho_p\,d^3\,u_{sl}}{6}\,\frac{1}{d^2\left(\upsilon_{\max}/\upsilon\right)^{\frac{2}{3}}} = 0 \qquad (5\text{-}7)$$

$$\underbrace{\frac{\phi_w\sqrt{3}\,\pi\,\rho_p\,\upsilon\,T^{\frac{1}{2}}\,|u_{sl}|}{6\upsilon_{\max}\left[1-\left(\dfrac{\upsilon}{\upsilon_{\max}}\right)^{\frac{1}{3}}\right]}}_{\text{Rate of momentum transfer to the wall}} + \underbrace{\frac{u_{sl}\,.\sigma_{ck}\,.n}{|u_{sl}|}}_{\substack{\text{Tangential force}\\ \text{per unit area}\\ \text{acting}\\ \text{on the boundary}}} = 0 \qquad (5\text{-}8)$$

5.2.2 Energy Balance

Following the work of Jenkins and Richman [9], the boundary condition for the pseudo temperature is obtained by equating the rate of heat generation due to slip at the boundary and the rate of dissipation of pseudo thermal energy due to inelastic collisions of granules with unit area of the boundary. Each collision is characterized by a coefficient of restitution e_w that varies from zero to unity. The energy loss per granule boundary collision E_{PB} is given by the difference of kinetic energies before and after collision is given by:

$$E_{PB} = \frac{1}{2} m V^2 - \frac{1}{2} m V'^2 \tag{5-9}$$

where $V'^2 = e_w V^2$.

The rate of heat dissipation of pseudo thermal energy at the boundary is given by [9]:

$$D_{PT} = \underbrace{\left(\frac{V}{S}\right)}_{\text{Collision frequency of each } granule} \underbrace{\left(\frac{\pi \rho_p d^3 T\left(1-e_w^2\right)}{4}\right)}_{\text{Energy loss per } granule\text{-boundary collision}} \underbrace{\left(\frac{1}{a_c}\right)}_{\text{Number of } granules \text{ adjacent to unit area of surface}} \tag{5-10}$$

Substituting with equations (5-2) and (5-3), we have

$$D_{PT} = \underbrace{\left[\frac{(3T)^{\frac{1}{2}}}{d\left[\left(\upsilon_{\max}/\upsilon\right)^{\frac{1}{3}} - 1\right]}\right]}_{\text{Collision frequency per particle}} \underbrace{\left[\frac{1}{4}\pi \rho_p d^3 T\left(1-e_w^2\right)\right]}_{\substack{\text{Energy loss per particle–boundary collision} \\ \frac{1}{2} m \bar{v}^2 \left(1-e_w^2\right)}} \underbrace{\left[\frac{1}{d^3\left(\upsilon_{\max}/\upsilon\right)^{\frac{2}{3}}}\right]}_{\text{Number of particles adjacent to unit area of the boundary}} \tag{5-11}$$

The rate of heat generation due to slip at the boundary is given by the product of the rate of momentum transfer to the wall by the particle impact and the slip velocity,

$$q_{slip} = \left(\frac{\pi\sqrt{3}}{6\upsilon_{\max}}\right) \frac{\phi_w \rho_p \upsilon \sqrt{T} u_{sl}}{1 - \left(\frac{\upsilon}{\upsilon_{\max}}\right)^{1/3}} u_{sl} \tag{5-12}$$

The total flux of the pseudo thermal energy [9] from the wall is the difference between the rate of heat generation due to slip at the boundary (5-12), and the rate of dissipation of pseudo thermal energy at the boundary (5-11), and is given by :

$$n.q_{PT} = \left(\frac{\pi\sqrt{3}}{6\upsilon_{\max}}\right) \frac{\phi_w \rho_p \upsilon \sqrt{T} u_{sl}^2}{1 - \left(\frac{\upsilon}{\upsilon_{\max}}\right)^{1/3}} - \left(\frac{\pi\sqrt{3}}{4\upsilon_{\max}}\right) \frac{\left(1-e_w^2\right)\rho_p \upsilon T^{3/2}}{1 - \left(\frac{\upsilon}{\upsilon_{\max}}\right)^{1/3}} \tag{5-13}$$

$$n.q_{PT} = \left(\frac{\pi\sqrt{3}}{6\upsilon_{\max}}\right) \phi_w \rho_p \upsilon g_o \sqrt{T} u_{sl}^2 - \left(\frac{\pi\sqrt{3}}{4\upsilon_{\max}}\right)\left(1-e_w^2\right)\rho_p \upsilon g_o T^{3/2} \tag{5-14}$$

Equation (5-14) represents the boundary condition for pseudo temperature. In this equation when e_w is close to unity, the first term of the right hand side (RHS) will dominate and hence the wall behaves as heat source. When e_w is small, the second term of RHS will dominate and hence the wall behaves as a sink.

CHAPTER 6. GRANULAR LUBRICATION EQUATIONS

6.1 Introduction

In this chapter, Lun's model is considered to study the mechanism of granular lubricant. The viscous dissipation term was included in the pseudo energy equation and the solid volume fraction, together with the mean velocity and the granular temperature are coupled and is directly predicted from a set of complete governing equations and boundary conditions.

6.2 Analysis

In this section we shall use the constitutive relations to get a general form of the conservation equations and boundary condition equations, which will be simplified in a later step. The constitutive equation for the total stress tensor (4-1) caused by kinetic and collision can be simplified by substituting the set of relations (4-3) to (4-7) as follows:

$$\sigma_{ck} = \lfloor \rho_p\, \upsilon T(1+4\eta\, \upsilon\, g_o) - \eta\mu_b \nabla . \,U \rfloor I -$$

$$\left\{ \frac{2\,\mu}{\eta(2-\eta)g_o}\left(1+\frac{8}{5}\eta\,\upsilon\, g_o\right)\left[1+\frac{8}{5}\eta(3\eta-2)\upsilon\, g_o\right]+\frac{6}{5}\mu_b\,\eta \right\} S$$

$$\sigma_{ck} = \left[\rho_p\, \upsilon T(1+4\eta\,\upsilon\, g_o) - 2\rho_p d\sqrt{T}\,\frac{4}{3}\frac{\eta\upsilon^2 g_o}{\sqrt{\pi}}\nabla . \,U\right] I -$$

$$\left\{ 2\rho_p d\sqrt{T}\,\frac{5\sqrt{\pi}}{96\eta\,(2-\eta)}\left(\frac{1}{g_o}+\frac{8}{5}\eta\,\upsilon\right)\left[1+\frac{8}{5}\eta(3\eta-2)\upsilon\, g_o\right]+2\rho_p d\sqrt{T}\,\frac{8}{5}\frac{\eta\upsilon^2 g_o}{\sqrt{\pi}} \right\} S$$

$$\sigma_{ck} = \left(\rho_p\, T\, f_1(\upsilon) - 2\rho_p d\sqrt{T} f_9(\upsilon)\nabla . \,U\right) I - \left(2\rho_p d\sqrt{T} f_2(\upsilon)\right) S \tag{6-1}$$

where $f_1(\upsilon)$, $f_2(\upsilon)$, and $f_9(\upsilon)$ are non dimensional functions defined as follows:

$$f_1(\upsilon) = \upsilon(1+4\eta\upsilon g_o)$$

$$f_2(\upsilon) = \frac{5\sqrt{\pi}}{96\eta(2-\eta)}\left(\frac{1}{g_o}+\frac{8}{5}\eta\upsilon\right)\left(1+\frac{8}{5}\eta[3\eta-2]\upsilon g_o\right)+\frac{8}{5}\frac{\eta\upsilon^2 g_o}{\sqrt{\pi}}$$

$$f_9(\upsilon) = \frac{4\eta\upsilon^2 g_o}{3\sqrt{\pi}}$$

The equation of the total flux of pseudo energy (4-8) can be simplified by substituting the set of relations (4-3) to (4-7) and relation (4-9) as follows:

$$q_{PT} = -\lambda\left\{\left(\frac{1}{g_o} + \frac{12}{5}\eta\upsilon\right)\left[1 + \frac{12}{5}\eta^2(4\eta - 3)\upsilon g_o\right] + \frac{64}{25\pi}(41 - 33\eta)\eta^2\upsilon^2 g_o\right\}\nabla T$$

$$- \lambda\left\{\left(\frac{1}{g_o\upsilon} + \frac{12}{5}\eta\right)\frac{12}{5}\eta(2\eta - 1)(\eta - 1)\frac{d}{d\upsilon}\left(\upsilon^2 g_o\right)T\right\}\nabla\upsilon$$

$$q_{PT} = -\rho_p\, d\sqrt{T}\,\frac{25\sqrt{\pi}}{16\eta(41 - 33\eta)}$$

$$\left\{\left(\frac{1}{g_o} + \frac{12}{5}\eta\upsilon\right)\left[1 + \frac{12}{5}\eta^2(4\eta - 3)\upsilon g_o\right] + \frac{64}{25\pi}(41 - 33\eta)\eta^2\upsilon^2 g_o\right\}\nabla T$$

$$- \rho_p\, d\sqrt{T}\,\frac{25\sqrt{\pi}}{16\eta(41 - 33\eta)}\left\{\frac{12}{5}\eta(\eta - 1)(2\eta - 1)\left(\frac{1}{g_o\upsilon} + \frac{12}{5}\eta\right)\frac{d}{d\upsilon}\left(\upsilon^2 g_o\right)T\right\}\nabla\upsilon$$

$$q_{PT} = -\rho_p\, d\sqrt{T}\, f_3(\upsilon)\nabla T - \rho_p\, d\, T\sqrt{T}\, f_4(\upsilon)\nabla\upsilon \tag{6-2}$$

where $f_3(\upsilon)$ and $f_4(\upsilon)$ are non dimensional functions defined as follows:

$$f_3(\upsilon) = \frac{25\sqrt{\pi}}{16\eta(41 - 33\eta)}\left\{\left(\frac{1}{g_o} + \frac{12}{5}\eta\upsilon\right)\left(1 + \frac{12}{5}\eta^2[4\eta - 3]\upsilon g_o\right) + \frac{64}{25\pi}(41 - 33\eta)\eta^2\upsilon^2 g_o\right\}$$

$$f_4(\upsilon) = \frac{25\sqrt{\pi}}{16\eta(41 - 33\eta)}\left\{\frac{12}{5}\eta(\eta - 1)(2\eta - 1)\left(\frac{1}{\upsilon g_o} + \frac{12}{5}\eta\right)\frac{d}{d\upsilon}\left(\upsilon^2 g_o\right)\right\}$$

Similarly, the collisional rate of energy dissipation per unit volume (4-10) can be simplified to:

$$\gamma = \frac{48}{\pi^{\frac{1}{2}}}\eta(1 - \eta)\frac{\rho_p\upsilon^2}{d}g_o T^{\frac{3}{2}}$$

$$\gamma = \frac{\rho_p T\sqrt{T}}{d}f_5(\upsilon) \tag{6-3}$$

where $f_5(\upsilon)$ is non dimensional function defined as follows:

$$f_5(\upsilon) = \frac{48}{\sqrt{\pi}}\upsilon^2 g_o\eta(1\text{-}\eta)$$

6.3 General Governing Equations

The general conservation laws, the constitutive equations and the boundary conditions presented are applied to a particular flow field shown in Figure 6.1. Considering the two-dimensional bearing configuration with a film gap *h=h (x)*, the upper plate is stationary while the bottom plate undergoes a constant slider motion U_L. The plates are assumed to be infinitely wide. The flow is considered to be steady, two-dimensional. The Cartesian coordinate system is set up by letting x lie along the plate's length, and y across the thickness of the flow. The flow velocity u, the pseudo temperature T, and the solid volume fraction υ vary across the gap.

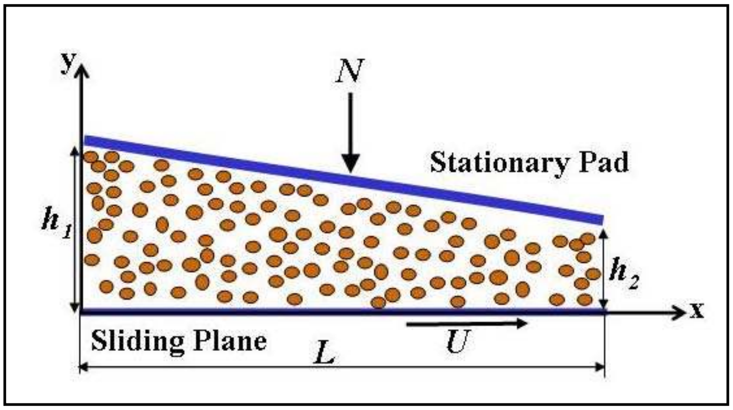

Figure 6.1 : Two-Dimensional Granular Lubricant Flow

6.3.1 Conservation of Mass

Neglecting the time derivative, then the governing equation for conservation of mass (3-1) can be written as:

$$\nabla.(\rho U) = 0$$

$$\frac{\partial(\rho \mathrm{u})}{\partial \mathrm{x}} + \frac{\partial(\rho \mathrm{V})}{\partial \mathrm{y}} = 0$$

Integrating the continuity equation across the film thickness:

$$\int_0^{h(x)} \frac{\partial(\rho \mathrm{u})}{\partial \mathrm{x}} dy + \int_0^{h(x)} \frac{\partial(\rho \mathrm{V})}{\partial \mathrm{y}} dy = 0$$

$$\int_0^{h(x)} \frac{\partial(\rho \mathrm{u})}{\partial \mathrm{x}} dy + (\rho_H V_H - \rho_o V_o) = 0$$

The component of velocity at the bottom plate is zero, then

$$\int_0^{h(x)} \frac{\partial(\rho \mathrm{u})}{\partial \mathrm{x}} dy + \rho_H V_H = 0$$

Furthermore, the squeeze velocity at the top plate can be written as: $V_H = u_H \frac{\partial h}{\partial x}$

$$\int_0^{h(x)} \frac{\partial(\rho \mathrm{u})}{\partial \mathrm{x}} dy + \rho_H u_H \frac{\partial h}{\partial x} = 0$$

Recalling Lebinitz's integration rule, we have

$$\int_0^{h(x)} \frac{\partial(\rho \mathrm{u})}{\partial \mathrm{x}} dy = \frac{\partial}{\partial \mathrm{x}} \int_0^{h(x)} \rho \mathrm{u}\, dy - \rho_H u_H \frac{\partial h}{\partial x}$$

Then by substituting back in the continuity equation we have

$$\frac{\partial}{\partial \mathrm{x}} \int_0^{h(x)} \rho \mathrm{u}\, dy - \rho_H u_H \frac{\partial h}{\partial x} + \rho_H u_H \frac{\partial h}{\partial x} = 0$$

That is,

$$\frac{\partial}{\partial \mathrm{x}} \int_0^{h(x)} \rho \mathrm{u}\, dy = 0 \tag{6-4}$$

6.3.2 Conservation of Momentum

Substituting equation (6-1) in the momentum equation (3-2) yields to the *x* and *y* components of the momentum equation as follow:

$$\nabla.\sigma_{ck} + \rho_p \upsilon \left(u \frac{\partial U}{\partial x} + V \frac{\partial U}{\partial y} \right) = 0 \tag{6-5}$$

Now expanding the total stress tensor caused by kinetic and collision, and substituting with the deviatoric part of the rate of deformation tensor and the identity tensor, we have

$$I = \begin{bmatrix} 1 & 0 & 0 \\ 0 & 1 & 0 \\ 0 & 0 & 1 \end{bmatrix}, \text{ and } S = \begin{bmatrix} \frac{2}{3}\frac{\partial u}{\partial x} - \frac{1}{3}\frac{\partial V}{\partial y} & \frac{1}{2}\left(\frac{\partial u}{\partial y} + \frac{\partial V}{\partial x}\right) & 0 \\ \frac{1}{2}\left(\frac{\partial u}{\partial y} + \frac{\partial V}{\partial x}\right) & \frac{2}{3}\frac{\partial V}{\partial y} - \frac{1}{3}\frac{\partial u}{\partial x} & 0 \\ 0 & 0 & -\frac{1}{3}\left(\frac{\partial u}{\partial x} + \frac{\partial V}{\partial y}\right) \end{bmatrix}$$

That is,

$$\sigma_{ck} = \left(\rho_p T f_1(\upsilon) - 2\rho_p d\sqrt{T} f_9(\upsilon) \nabla . U\right) I - \left(2\rho_p d\sqrt{T} f_2(\upsilon)\right) S$$

$$\sigma_{ck}=\begin{bmatrix}\rho_p T f_1-2\rho_p d\sqrt{T}f_9\left(\frac{\partial u}{\partial x}+\frac{\partial V}{\partial y}\right) & 0 & 0\\ 0 & \rho_p T f_1-2\rho_p d\sqrt{T}f_9\left(\frac{\partial u}{\partial x}+\frac{\partial V}{\partial y}\right) & 0\\ 0 & 0 & \rho_p T f_1-2\rho_p d\sqrt{T}f_9\left(\frac{\partial u}{\partial x}+\frac{\partial V}{\partial y}\right)\end{bmatrix}-$$

$$\begin{bmatrix}\frac{4}{3}\rho_p d\sqrt{T}f_2\frac{\partial u}{\partial x}-\frac{2}{3}\rho_p d\sqrt{T}f_2\frac{\partial V}{\partial y} & \rho_p d\sqrt{T}f_2\left(\frac{\partial u}{\partial y}+\frac{\partial V}{\partial x}\right) & 0\\ \rho_p d\sqrt{T}f_2\left(\frac{\partial u}{\partial y}+\frac{\partial V}{\partial x}\right) & \frac{4}{3}\rho_p d\sqrt{T}f_2\frac{\partial V}{\partial y}-\frac{2}{3}\rho_p d\sqrt{T}f_2\frac{\partial u}{\partial x} & 0\\ 0 & 0 & -\frac{2}{3}\rho_p d\sqrt{T}f_2\left(\frac{\partial u}{\partial x}+\frac{\partial V}{\partial y}\right)\end{bmatrix}$$

$$\sigma_{ck}=\begin{bmatrix}\rho_p T f_1-\rho_p d\sqrt{T}\left(\left[2f_9+\frac{4}{3}f_2\right]\frac{\partial u}{\partial x}+\left[2f_9-\frac{2}{3}f_2\right]\frac{\partial V}{\partial y}\right) & -\rho_p d\sqrt{T}f_2\left(\frac{\partial u}{\partial y}+\frac{\partial V}{\partial x}\right) & 0\\ -\rho_p d\sqrt{T}f_2\left(\frac{\partial u}{\partial y}+\frac{\partial V}{\partial x}\right) & \rho_p T f_1-\rho_p d\sqrt{T}\left(\left[2f_9-\frac{2}{3}f_2\right]\frac{\partial u}{\partial x}+\left[2f_9+\frac{4}{3}f_2\right]\frac{\partial V}{\partial y}\right) & 0\\ 0 & 0 & \rho_p T f_1-\rho_p d\sqrt{T}\left(\left[2f_9-\frac{2}{3}f_2\right]\frac{\partial u}{\partial x}+\left[2f_9-\frac{2}{3}f_2\right]\frac{\partial V}{\partial y}\right)\end{bmatrix} \tag{6-6}$$

Also, we know that collisional-translational stress tensor $\sigma_{ck}=\begin{bmatrix}\sigma_{xx} & \sigma_{xy} & \sigma_{xz}\\ \sigma_{yx} & \sigma_{yy} & \sigma_{yz}\\ \sigma_{zx} & \sigma_{zy} & \sigma_{zz}\end{bmatrix}$.

Again, substituting equation (6-6) in the momentum equation (6-5), we get

$$\nabla.\sigma_{ck}+\rho_p\upsilon\left(u\frac{\partial U}{\partial x}+V\frac{\partial U}{\partial y}\right)=0$$

That is,

$$\nabla\ .\begin{bmatrix}\sigma_{xx} & \sigma_{xy} & \sigma_{xz}\\ \sigma_{yx} & \sigma_{yy} & \sigma_{yz}\\ \sigma_{zx} & \sigma_{zy} & \sigma_{zz}\end{bmatrix}+\rho_p\upsilon u\begin{bmatrix}\frac{\partial u}{\partial x}\\ \frac{\partial V}{\partial x}\\ \frac{\partial w}{\partial x}\end{bmatrix}+\rho_p\upsilon V\begin{bmatrix}\frac{\partial u}{\partial y}\\ \frac{\partial V}{\partial y}\\ \frac{\partial w}{\partial y}\end{bmatrix}=0 \tag{6-7}$$

6.3.2.1 X-Momentum Equation

The x-momentum equation is given by:

$$\frac{\partial}{\partial x}\left(\sigma_{xx}\right)+\frac{\partial}{\partial y}\left(\sigma_{xy}\right)+\rho_p\upsilon\left[u\frac{\partial u}{\partial x}+V\frac{\partial u}{\partial y}\right]=0$$

$$\begin{aligned}&\frac{\partial}{\partial x}\left\{\rho_p Tf_1-\rho_p d\sqrt{T}\left(\left[2f_9+\frac{4}{3}f_2\right]\frac{\partial u}{\partial x}+\left[2f_9-\frac{2}{3}f_2\right]\frac{\partial V}{\partial y}\right)\right\}+\\ &\qquad\frac{\partial}{\partial y}\left\{-\rho_p d\sqrt{T}f_2\left(\frac{\partial u}{\partial y}+\frac{\partial V}{\partial x}\right)\right\}+\rho_p\upsilon\left[u\frac{\partial u}{\partial x}+V\frac{\partial u}{\partial y}\right]=0\end{aligned}$$

$$\begin{aligned}&\frac{\partial}{\partial x}\left\{\rho_p Tf_1-\rho_p d\sqrt{T}\left(ff_1\frac{\partial u}{\partial x}+ff_2\frac{\partial V}{\partial y}\right)\right\}+\\ &\qquad\frac{\partial}{\partial y}\left\{-\rho_p d\sqrt{T}f_2\left(\frac{\partial u}{\partial y}+\frac{\partial V}{\partial x}\right)\right\}+\rho_p\upsilon\left[u\frac{\partial u}{\partial x}+V\frac{\partial u}{\partial y}\right]=0\end{aligned}\tag{6-8}$$

where $ff_1(\upsilon)$ and $ff_2(\upsilon)$ are dimensionless functions defined as follow:

$$\begin{aligned}ff_1(\upsilon)&=2f_9(\upsilon)+\frac{4}{3}f_2(\upsilon)\\ ff_2(\upsilon)&=2f_9(\upsilon)-\frac{2}{3}f_2(\upsilon)\end{aligned}\tag{6-9}$$

6.3.2.2 Y-Momentum Equation

The y-momentum equation is given by:

$$\frac{\partial}{\partial x}\left(\sigma_{yx}\right)+\frac{\partial}{\partial y}\left(\sigma_{yy}\right)+\rho_p\upsilon\left[u\frac{\partial V}{\partial x}+V\frac{\partial V}{\partial y}\right]=0$$

$$\begin{aligned}&\frac{\partial}{\partial x}\left\{-\rho_p d\sqrt{T}f_2\left(\frac{\partial u}{\partial y}+\frac{\partial V}{\partial x}\right)\right\}+\rho_p\upsilon\left[u\frac{\partial V}{\partial x}+V\frac{\partial V}{\partial y}\right]+\\ &\qquad\frac{\partial}{\partial y}\left\{\rho_p Tf_1-\rho_p d\sqrt{T}\left(\left[2f_9-\frac{2}{3}f_2\right]\frac{\partial u}{\partial x}+\left[2f_9+\frac{4}{3}f_2\right]\frac{\partial V}{\partial y}\right)\right\}=0\end{aligned}$$

$$\begin{aligned}&\frac{\partial}{\partial x}\left\{-\rho_p d\sqrt{T}f_2\left(\frac{\partial u}{\partial y}+\frac{\partial V}{\partial x}\right)\right\}+\rho_p\upsilon\left[u\frac{\partial V}{\partial x}+V\frac{\partial V}{\partial y}\right]+\\ &\qquad\frac{\partial}{\partial y}\left\{\rho_p Tf_1-\rho_p d\sqrt{T}\left(ff_2\frac{\partial u}{\partial x}+ff_1\frac{\partial V}{\partial y}\right)\right\}=0\end{aligned}\tag{6-10}$$

6.3.3 Conservation of Energy

Substituting equations (6-1), (6-2), and (6-3) in the energy equation (3-11) yields the following:

$$\frac{3}{2}\rho\frac{DT}{Dt} = -\nabla .\ q_{PT} - \sigma_{ck} : \nabla U - \gamma \tag{6-11}$$

The terms $\nabla .\ q_{PT}$ and $\sigma_{ck} : \nabla U$ are:

$$\nabla . q_{PT} = \nabla . \left\{ -\rho_p d\sqrt{T}\, f_3(\upsilon)\nabla T - \rho_p\, d\, T\sqrt{T}\, f_4(\upsilon)\nabla\upsilon \right\}$$

$$\nabla . q_{PT} = \nabla . \left\{ -\rho_p d\sqrt{T}\, f_3(\upsilon)\begin{bmatrix} \dfrac{\partial T}{\partial x} \\ \dfrac{\partial T}{\partial y} \end{bmatrix} - \rho_p d\, T\sqrt{T}\, f_4(\upsilon)\begin{bmatrix} \dfrac{\partial \upsilon}{\partial x} \\ \dfrac{\partial \upsilon}{\partial y} \end{bmatrix} \right\}$$

$$\begin{aligned} \nabla . q_{PT} = &-\frac{\partial}{\partial x}\left(\rho_p\, d\sqrt{T}\, f_3(\upsilon)\frac{\partial T}{\partial x} + \rho_p\, d\, T\sqrt{T}\, f_4(\upsilon)\frac{\partial \upsilon}{\partial x} \right) - \\ &\frac{\partial}{\partial y}\left(\rho_p\, d\sqrt{T}\, f_3(\upsilon)\frac{\partial T}{\partial y} + \rho_p\, d\, T\sqrt{T}\, f_4(\upsilon)\frac{\partial \upsilon}{\partial y} \right) \end{aligned} \tag{6-12}$$

$\sigma_{ck} : \nabla U = \sigma_{ij}\dfrac{\partial u_i}{\partial x_j} = \sigma_{ji}\dfrac{\partial u_j}{\partial x_i}$ because σ_{ij} is symmetric, then we have

$$\sigma_{ck} : \nabla U = \sigma_{xx}\frac{\partial u}{\partial x} + \sigma_{xy}\frac{\partial u}{\partial y} + \sigma_{yx}\frac{\partial V}{\partial x} + \sigma_{yy}\frac{\partial V}{\partial y}$$

$$\begin{aligned} \sigma_{ck} : \nabla U = &\left\{ \rho_p T f_1 - \rho_p d\sqrt{T}\left(ff_1\frac{\partial u}{\partial x} + ff_2\frac{\partial V}{\partial y} \right) \right\}\frac{\partial u}{\partial x} + \left\{ -\rho_p d\sqrt{T}\, f_2\left(\frac{\partial u}{\partial y} + \frac{\partial V}{\partial x} \right) \right\}\frac{\partial u}{\partial y} + \\ &\left\{ -\rho_p d\sqrt{T}\, f_2\left(\frac{\partial u}{\partial y} + \frac{\partial V}{\partial x} \right) \right\}\frac{\partial V}{\partial x} + \left\{ \rho_p T f_1 - \rho_p d\sqrt{T}\left(ff_2\frac{\partial u}{\partial x} + ff_1\frac{\partial V}{\partial y} \right) \right\}\frac{\partial V}{\partial y} \end{aligned} \tag{6-13}$$

Now substituting equations (6-12) and (6-13) into the energy equation (6-11), we have

$$\frac{3}{2}\rho\frac{DT}{Dt} + \nabla .\ q_{PT} + \sigma_c : \nabla U + \gamma = 0$$

$$\begin{aligned} &\frac{3}{2}\rho_p\upsilon\left(u\frac{\partial T}{\partial x} + V\frac{\partial T}{\partial y} \right) - \frac{\partial}{\partial x}\left(\rho_p d\sqrt{T}\, f_3\frac{\partial T}{\partial x} + \rho_p d\, T\sqrt{T}\, f_4\frac{\partial \upsilon}{\partial x} \right) - \\ &\frac{\partial}{\partial y}\left(\rho_p d\sqrt{T}\, f_3\frac{\partial T}{\partial y} + \rho_p d\, T\sqrt{T}\, f_4\frac{\partial \upsilon}{\partial y} \right) + \left\{ \rho_p T f_1 - \rho_p d\sqrt{T}\left(ff_1\frac{\partial u}{\partial x} + ff_2\frac{\partial V}{\partial y} \right) \right\}\frac{\partial u}{\partial x} \\ &+ \left\{ \rho_p T f_1 - \rho_p d\sqrt{T}\left(ff_2\frac{\partial u}{\partial x} + ff_1\frac{\partial V}{\partial y} \right) \right\}\frac{\partial V}{\partial y} - \rho_p d\sqrt{T}\, f_2\left(\frac{\partial u}{\partial y} + \frac{\partial V}{\partial x} \right)^2 + \frac{\rho_p f_5}{d}T\sqrt{T} = 0 \end{aligned}$$

That is,

$$\begin{gathered}\underbrace{\frac{3}{2}\rho_p\upsilon\left[u\frac{\partial T}{\partial x}+V\frac{\partial T}{\partial y}\right]}_{\text{Convective terms}}-\underbrace{\begin{matrix}\dfrac{\partial}{\partial x}\left[\left(\rho_p df_3\sqrt{T}\right)\dfrac{\partial T}{\partial x}+\left(\rho_p df_4 T\sqrt{T}\right)\dfrac{\partial \upsilon}{\partial x}\right]- \\ \dfrac{\partial}{\partial y}\left[\left(\rho_p df_3\sqrt{T}\right)\dfrac{\partial T}{\partial y}+\left(\rho_p df_4 T\sqrt{T}\right)\dfrac{\partial \upsilon}{\partial y}\right]\end{matrix}}_{\text{Conductive terms}}+\underbrace{\frac{\rho_p f_5}{d}T\sqrt{T}}_{\text{Viscous dissipation}}- \\ \underbrace{\rho_p df_2\sqrt{T}\left(\frac{\partial u}{\partial y}+\frac{\partial V}{\partial x}\right)^2-\rho_p df_2\sqrt{T}\left[\begin{matrix}2f_2\left\{\left(\dfrac{\partial u}{\partial x}\right)^2+\left(\dfrac{\partial V}{\partial y}\right)^2\right\}+ \\ ff_2\left(\dfrac{\partial u}{\partial x}+\dfrac{\partial V}{\partial y}\right)^2\end{matrix}\right]+\rho_p Tf_1\left(\frac{\partial u}{\partial x}+\frac{\partial V}{\partial y}\right)}_{\text{Work done by collisional–translational component of the stress}}=0\end{gathered} \tag{6-14}$$

6.4 Boundary Conditions

6.4.1 Condition on the Slip Velocity

The boundary condition of the slip velocity is obtained by substituting equation (6-1) into equation (5-8):

$$\frac{u_{sl}}{|u_{sl}|}.\sigma_{ck}.n+\frac{\sqrt{3}\,\pi}{6\upsilon_{\max}}\phi_w\,\rho_p\;\upsilon\,g_o\sqrt{T}\,u_{sl}=0$$

$$\begin{bmatrix}1 & 0 & 0\end{bmatrix}.\begin{bmatrix}\sigma_{xx} & \sigma_{xy} & \sigma_{xz} \\ \sigma_{yx} & \sigma_{yy} & \sigma_{yz} \\ \sigma_{zx} & \sigma_{zy} & \sigma_{zz}\end{bmatrix}.\begin{bmatrix}0 \\ \pm 1 \\ 0\end{bmatrix}+\frac{\sqrt{3}\,\pi}{6\upsilon_{\max}}\phi_w\,\rho_p\;\upsilon\,g_o\sqrt{T}\,u_{sl}=0$$

$$\pm\sigma_{xy}+\frac{\sqrt{3}\,\pi}{6\upsilon_{\max}}\phi_w\,\rho_p\;\upsilon\,g_o\sqrt{T}\,u_{sl}=0$$

$$\pm\left[-\rho_p d\sqrt{T}f_2\left(\frac{\partial u}{\partial y}+\frac{\partial V}{\partial x}\right)\right]+\frac{\sqrt{3}\,\pi}{6\upsilon_{\max}}\phi_w\,\rho_p\;\upsilon\,g_o\sqrt{T}\,u_{sl}=0$$

$$\pm\left[-\left(\frac{\partial u}{\partial y}+\frac{\partial V}{\partial x}\right)\right]+\frac{f_8(\upsilon)}{d}\phi_w\,u_{sl}=0 \tag{6-15}$$

where $f_8(\upsilon)$ is a dimensionless function defined as follows:

$$f_8(\upsilon)=\frac{\pi\upsilon g_o}{2\sqrt{3}\upsilon_{\max}f_2(\upsilon)} \tag{6-16}$$

6.4.1.1 At $y = 0$ (Bottom Plate)

$$+\left[-\left(\frac{\partial u}{\partial y}+\frac{\partial V}{\partial x}\right)\right]+\frac{f_8(\upsilon)}{d}\phi_w\left(u-u_{wall}\right)=0$$

$$\frac{\partial u}{\partial y}+\frac{\partial V}{\partial x}=\frac{f_8(\upsilon)}{d}\phi_o\left(u-U\right) \tag{6-17}$$

where $u_{wall}=U \quad \& \quad \phi_w=\phi_o$

6.4.1.2 At $y = H$ (Top Plate)

$$-\left[-\left(\frac{\partial u}{\partial y}+\frac{\partial V}{\partial x}\right)\right]+\frac{f_8(\upsilon)}{d}\phi_w\left(u-u_{wall}\right)=0$$

$$\frac{\partial u}{\partial y}+\frac{\partial V}{\partial x}=-\frac{f_8(\upsilon)}{d}\phi_H\, u \tag{6-18}$$

where $u_{wall}=0 \quad \& \quad \phi_w=\phi_H$

6.4.2 Energy Balance

The boundary condition for the pseudo temperature is obtained by substituting equation (6-2) into equation (5-14):

$$n.q_{PT}=\left(\frac{\pi\sqrt{3}}{6\upsilon_{\max}}\right)\phi_W\rho_p\,\upsilon\,g_o\sqrt{T}\;u_{sl}^2-\left(\frac{\pi\sqrt{3}}{4\upsilon_{\max}}\right)\left(1-e_w^2\right)\rho_p\,\upsilon\,g_oT^{3/2}$$

$$\begin{bmatrix}0\\ \pm1\\ 0\end{bmatrix}.\left\{-\rho_p d\sqrt{T}\,f_3(\upsilon)\begin{bmatrix}\dfrac{\partial T}{\partial x}\\ \dfrac{\partial T}{\partial y}\end{bmatrix}-\rho_p\,d\,T\sqrt{T}\,f_4(\upsilon)\begin{bmatrix}\dfrac{\partial \upsilon}{\partial x}\\ \dfrac{\partial \upsilon}{\partial y}\end{bmatrix}\right\}=$$

$$\left(\frac{\pi\sqrt{3}}{6\upsilon_{\max}}\right)\varphi_W\rho_p\,\upsilon\,g_o\sqrt{T}\;u_{sl}^2-\left(\frac{\pi\sqrt{3}}{4\upsilon_{\max}}\right)\left(1-e_w^2\right)\rho_p\,\upsilon\,g_oT^{3/2}$$

$$\pm\left\{-d\sqrt{T}\,f_3(\upsilon)\frac{\partial T}{\partial y}-d\,T\sqrt{T}\,f_4(\upsilon)\frac{\partial \upsilon}{\partial y}\right\}=$$

$$\left(\frac{\pi\sqrt{3}}{6\upsilon_{\max}}\right)\varphi_w\upsilon\,g_o\sqrt{T}\;u_{sl}^2-\left(\frac{\pi\sqrt{3}}{4\upsilon_{\max}}\right)\upsilon\,g_oT\sqrt{T}\left(1-e_w^2\right)$$

$$\pm\left\{-\frac{\partial T}{\partial y}-T\frac{f_4(\upsilon)}{f_3(\upsilon)}\frac{\partial \upsilon}{\partial y}\right\}=\frac{f_7(\upsilon)\varphi_w}{d}u_{Sl}^2-\frac{f_6(\upsilon)T}{d}\left(1-e_w^2\right) \tag{6-19}$$

where $f_6(\upsilon)$ and $f_7(\upsilon)$ are dimensionless functions defined as follow:

$$f_6(\upsilon) = \frac{\sqrt{3}\pi \upsilon g_o}{4\upsilon_{\max} f_3(\upsilon)}$$

$$f_7(\upsilon) = \frac{\sqrt{3}\pi \upsilon g_o}{6\upsilon_{\max} f_3(\upsilon)} \tag{6-20}$$

6.4.2.1 At *y* = 0 (Bottom Plate)

$$+\left\{-\frac{\partial T}{\partial y} - T\frac{f_4(\upsilon)}{f_3(\upsilon)}\frac{\partial \upsilon}{\partial y}\right\} = \frac{f_7(\upsilon)\varphi_o}{d}u_{sl}^2 - \frac{f_6(\upsilon)T}{d}\left(1-e_w^2\right)$$

$$\frac{\partial T}{\partial y} = -T\frac{f_4(\upsilon)}{f_3(\upsilon)}\frac{\partial \upsilon}{\partial y} - \frac{\varphi_o f_7(\upsilon)}{d}u_{sl}^2 + \frac{T\,f_6(\upsilon)}{d}\left(1-e_w^2\right) \tag{6-21}$$

6.4.2.2 At *y* = *H* (Top Plate)

$$-\left\{-\frac{\partial T}{\partial y} - T\frac{f_4(\upsilon)}{f_3(\upsilon)}\frac{\partial \upsilon}{\partial y}\right\} = \frac{f_7(\upsilon)\varphi_H}{d}u_{sl}^2 - \frac{f_6(\upsilon)T}{d}\left(1-e_w^2\right)$$

$$\frac{\partial T}{\partial y} = -T\frac{f_4(\upsilon)}{f_3(\upsilon)}\frac{\partial \upsilon}{\partial y}\frac{\varphi_H f_7(\upsilon)}{d}u_{sl}^2 - \frac{T\,f_6(\upsilon)}{d}\left(1-e_w^2\right) \tag{6-22}$$

6.5 Functions

All the functions are used for simplifying the equations of motion and the boundary conditions are summarized below in Table 6.1. They are dimensionless functions of the solids volume fraction only.

Table 6.1 : Definition of Functions

$f_1(\upsilon)=\upsilon(1+4\eta\upsilon g_o)$
$f_2(\upsilon)=\frac{5\sqrt{\pi}}{96\eta(2-\eta)}\left(\frac{1}{g_o}+\frac{8}{5}\eta\upsilon\right)\left(1+\frac{8}{5}\eta[3\eta-2]\upsilon g_o\right)+\frac{8}{5}\frac{\eta\upsilon^2 g_o}{\sqrt{\pi}}$
$f_3(\upsilon)=\frac{25\sqrt{\pi}}{16\eta(41-33\eta)}\left\{\left(\frac{1}{g_o}+\frac{12}{5}\eta\upsilon\right)\left(1+\frac{12}{5}\eta^2[4\eta-3]\upsilon g_o\right)+\frac{64}{25\pi}(41-33\eta)\eta^2\upsilon^2 g_o\right\}$
$f_4(\upsilon)=\frac{25\sqrt{\pi}}{16\eta(41-33\eta)}\left\{\frac{12}{5}\eta(\eta-1)(2\eta-1)\left(\frac{1}{\upsilon g_o}+\frac{12}{5}\eta\right)\frac{d}{d\upsilon}\left(\upsilon^2 g_o\right)\right\}$
$\frac{d}{d\upsilon}\left(\upsilon^2 g_o\right)=\frac{d}{d\upsilon}\left[\frac{\upsilon^2}{1-\left(\upsilon/\upsilon_{\max}\right)^{1/3}}\right]=2g_o\upsilon+\frac{1}{3}\upsilon g_o^2\left(\upsilon/\upsilon_{\max}\right)^{1/3}$
$f_5(\upsilon)=\frac{48}{\sqrt{\pi}}\upsilon^2 g_o\eta(1\text{-}\eta)$
$f_6(\upsilon)=\frac{\sqrt{3}\pi\upsilon g_o}{4\upsilon_{\max}f_3(\upsilon)}$
$f_7(\upsilon)=\frac{\sqrt{3}\pi\upsilon g_o}{6\upsilon_{\max}f_3(\upsilon)}$
$f_8(\upsilon)=\frac{\pi\upsilon g_o}{2\sqrt{3}\upsilon_{\max}f_2(\upsilon)}$
$f_9(\upsilon)=\frac{4\eta\upsilon^2 g_o}{3\sqrt{\pi}}$
$ff_1(\upsilon)=2f_9(\upsilon)+\frac{4}{3}f_2(\upsilon)$
$ff_2(\upsilon)=2f_9(\upsilon)-\frac{2}{3}f_2(\upsilon)$

CHAPTER 7. ORDER OF MAGNITUDE ANALYSIS

7.1 Introduction

The following order of magnitude analysis was performed to simplify the momentum equations and the energy equation along with their boundary conditions.

$$x\sim L\ ,\ y\sim H\ ,\ u\sim U\ ,\ V\sim\frac{HU}{L}\ ,\ \text{and}\ \upsilon, f_{1\rightarrow 9}, ff_1, ff_2\sim 1 \tag{7-1}$$

7.2 Governing Equations

7.2.1 X-Momentum Equation

The x-momentum equation (6-8) can be rearranged as follows:

$$\underbrace{\rho_p\upsilon\left[u\frac{\partial u}{\partial x}+V\frac{\partial u}{\partial y}\right]}_{\text{Inertia Forces}}=\underbrace{\frac{\partial}{\partial x}\left[\left(\rho_p d\sqrt{T}\right)\left(ff_1\frac{\partial u}{\partial x}+ff_2\frac{\partial V}{\partial y}\right)\right]+\frac{\partial}{\partial y}\left[\left(\rho_p df_2\sqrt{T}\right)\left(\frac{\partial u}{\partial y}+\frac{\partial V}{\partial x}\right)\right]}_{\text{Viscous Forces}}-\underbrace{\frac{\partial}{\partial x}\left(\rho_p Tf_1\right)}_{\text{Pressure Force}}$$

(7-2)

Now, let us examine the orders of the viscous terms individually:

$$ff_1\frac{\partial^2 u}{\partial x^2}\sim\frac{U}{L^2}\ ,\ ff_2\frac{\partial^2 V}{\partial x\partial y}\sim\frac{HU/L}{LH}=\frac{U}{L^2}\ ,\ f_2\frac{\partial^2 u}{\partial y^2}\sim\frac{U}{H^2}\ ,\ \text{and}\ f_2\frac{\partial^2 V}{\partial x\partial y}\sim\frac{U}{L^2}$$

Generally, in lubrication mechanisms the gap width is much smaller than the bearing length (i.e. $H\langle\langle L$). Thus, $\frac{\partial^2 u}{\partial y^2}\rangle\rangle\frac{\partial^2 u}{\partial x^2},\frac{\partial^2 V}{\partial x\partial y}$ and make much more contribution. Therefore, the other three terms can be neglected.

$$\underbrace{\rho_p\upsilon\left[u\frac{\partial u}{\partial x}+v\frac{\partial u}{\partial y}\right]}_{\text{Inertia Forces}}=\underbrace{\frac{\partial}{\partial y}\left[\left(\rho_p df_2\sqrt{T}\right)\left(\frac{\partial u}{\partial y}\right)\right]}_{\text{Viscous Forces}}-\underbrace{\frac{\partial}{\partial x}\left(\rho_p Tf_1\right)}_{\text{Pressure Force}} \tag{7-3}$$

Examining the inertia terms individually, we have

$\frac{u\,\partial u/\partial x}{V\,\partial u/\partial y}\sim\frac{U^2/L}{\frac{H}{L}U^2/H}=\frac{U^2/L}{U^2/L}=1$, which implies that both terms have the same order.

Based on previous published papers, the ranges of the pseudo temperature always lie between 0.01 and 0.05. Thus, the average pseudo temperature is assumed to be of order of 0.03.

The order of the inertia terms $\left(\sim\frac{U^2}{L}\right)$ is very small comparable to the order of the viscous forces $\left(\sqrt{T}\,f_2\frac{\partial^2 u}{\partial y^2}\sim\frac{U}{H^2}\sqrt{T}\right)$. Therefore, the final form of the x-momentum equation will be:

$$\frac{\partial}{\partial y}\left[\left(\rho_p d f_2\sqrt{T}\right)\left(\frac{\partial u}{\partial y}\right)\right]=\frac{\partial}{\partial x}\left(\rho_p T f_1\right) \tag{7-4}$$

7.2.2 Y-Momentum Equation

The y-momentum equation (6-10) can be rearranged as follows:

$$\underbrace{\rho_p v\left[u\frac{\partial V}{\partial x}+V\frac{\partial V}{\partial y}\right]}_{\text{Inertia Forces}}=\underbrace{\frac{\partial}{\partial x}\left[\left(\rho_p d f_2\sqrt{T}\right)\left(\frac{\partial u}{\partial y}+\frac{\partial V}{\partial x}\right)\right]+\frac{\partial}{\partial y}\left[\left(\rho_p d\sqrt{T}\right)\left(ff_2\frac{\partial u}{\partial x}+ff_1\frac{\partial V}{\partial y}\right)\right]}_{\text{Viscous Forces}}-\underbrace{\frac{\partial}{\partial y}\left(\rho_p T f_1\right)}_{\text{Prressure Force}}$$

(7-5)

Examining the orders of the viscous terms individually, we have

$$ff_1\frac{\partial^2 V}{\partial y^2}\sim\frac{U}{HL},\ ff_2\frac{\partial^2 u}{\partial x\partial y}\sim\frac{U}{HL},\ f_2\frac{\partial^2 V}{\partial x^2}\sim\frac{HU}{L^3},\ \text{and}\ f_2\frac{\partial^2 u}{\partial x\partial y}\sim\frac{U}{HL}$$

$\frac{\partial^2 V}{\partial x^2}\langle\langle\frac{\partial^2 V}{\partial y^2},\frac{\partial^2 u}{\partial x\partial y}$ and can be treated as negligible in comparison to other terms.

Consequently, equation (7-5) simplifies to:

$$\underbrace{\rho_p v\left[u\frac{\partial V}{\partial x}+V\frac{\partial V}{\partial y}\right]}_{\text{Inertia Forces}}=\underbrace{\frac{\partial}{\partial x}\left[\left(\rho_p d f_2\sqrt{T}\right)\left(\frac{\partial u}{\partial y}\right)\right]+\frac{\partial}{\partial y}\left[\left(\rho_p d\sqrt{T}\right)\left(ff_2\frac{\partial u}{\partial x}+ff_1\frac{\partial v}{\partial y}\right)\right]}_{\text{Viscous Forces}}-\underbrace{\frac{\partial}{\partial y}\left(\rho_p T f_1\right)}_{\text{Pressure Force}}$$

(7-6)

Again, by taking the average pseudo temperature to be of the order of 0.03, then the order of the inertia terms $\left(\sim\frac{U^2}{L}\right)$ would be negligibly small comparable to that of the viscous forces $\left(\sim\frac{U\sqrt{T}}{HL}\right)$. Also, the order of the pressure force $\left(\sim\frac{T}{H}\right)$ has much more contribution than the order of the viscous terms $\left(\sim\frac{Ud}{HL}\sqrt{T}\right)$.

Therefore, the final form of the y-momentum equation is:

$$\frac{\partial}{\partial y}\left(\rho_p T f_1\right)=0 \tag{7-7}$$

7.2.3 Energy Equation

The energy equation (6-14) can be rearranged as follows:

$$\underbrace{\frac{3}{2}\rho_p\upsilon\left[u\frac{\partial T}{\partial x}+V\frac{\partial T}{\partial y}\right]}_{\text{Convective terms}}\underbrace{-\frac{\partial}{\partial x}\left[\left(\rho_p df_3\sqrt{T}\right)\frac{\partial T}{\partial x}+\left(\rho_p df_4 T\sqrt{T}\right)\frac{\partial \upsilon}{\partial x}\right]-\frac{\partial}{\partial y}\left[\left(\rho_p df_3\sqrt{T}\right)\frac{\partial T}{\partial y}+\left(\rho_p df_4 T\sqrt{T}\right)\frac{\partial \upsilon}{\partial y}\right]}_{\text{Conductive terms}}+$$

$$\underbrace{\frac{\rho_p f_5}{d}T\sqrt{T}}_{\text{Viscous dissipation}}\underbrace{-\rho_p df_2\sqrt{T}\left(\frac{\partial u}{\partial y}+\frac{\partial V}{\partial x}\right)^2-\rho_p df_2\sqrt{T}\left[2f_2\left\{\left(\frac{\partial u}{\partial x}\right)^2+\left(\frac{\partial V}{\partial y}\right)^2\right\}+ff_2\left(\frac{\partial u}{\partial x}+\frac{\partial V}{\partial y}\right)^2\right]+\rho_p Tf_1\left(\frac{\partial u}{\partial x}+\frac{\partial V}{\partial y}\right)}_{\text{Work done}}=0$$

(7-8)

By examining the order of the convective terms individually, we can see that both terms have the same order $\frac{u\,{\partial T}/{\partial x}}{V\,{\partial T}/{\partial y}}\sim\frac{HT_{ref}/L}{\left(\frac{H}{L}U\right)T_{ref}/H}=1$ and examining the order of the conductive terms, we have $\frac{{\partial}/{\partial x}\left\lfloor\rho_p d\sqrt{T}f_3\,{\partial T}/{\partial x}\right\rfloor}{{\partial}/{\partial y}\left[\rho_p d\sqrt{T}f_3\,{\partial T}/{\partial y}\right]}\sim\frac{T_{ref}/L^2}{T_{ref}/H^2}=\left(\frac{H}{L}\right)^2\langle\langle 1$, which means that $\frac{\partial^2 T}{\partial x^2}\langle\langle\frac{\partial^2 T}{\partial y^2}$ and similarly $\frac{\partial^2 \upsilon}{\partial x^2}\langle\langle\frac{\partial^2 \upsilon}{\partial y^2}$. Therefore, the terms containing x gradient are negligible.

Similarly by examining the work done terms individually, it results that $\frac{\partial u}{\partial y}\rangle\rangle\frac{\partial V}{\partial x}$ since $\frac{{\partial u}/{\partial y}}{{\partial V}/{\partial x}}\sim\frac{U/H}{\left(\frac{H}{L}U\right)/L}=\left(\frac{L}{H}\right)^2\rangle\rangle 1$. Moreover, $\frac{{\partial u}/{\partial x}}{{\partial V}/{\partial y}}\sim\frac{U/L}{\left(\frac{H}{L}U\right)/H}=1$, showing that both terms have the same order $\left(\frac{\partial u}{\partial x}\sim\frac{\partial V}{\partial y}\right)$. Furthermore, it is clear that the term $\left(\frac{\partial u}{\partial y}\right)^2\rangle\rangle\left(\frac{\partial u}{\partial x}\right)^2,\frac{\partial u}{\partial x}$

Thus the energy equation (7-8) is simplified to:

$$\underbrace{\frac{3}{2}\rho_p \upsilon\left[u\frac{\partial T}{\partial x}+V\frac{\partial T}{\partial y}\right]}_{\text{Convective terms}}-\underbrace{\frac{\partial}{\partial y}\left[\left(\rho_p d f_3\sqrt{T}\right)\frac{\partial T}{\partial y}+\left(\rho_p d f_4 T\sqrt{T}\right)\frac{\partial \upsilon}{\partial y}\right]}_{\text{Conductive terms}}+\underbrace{\frac{\rho_p f_5}{d}T\sqrt{T}}_{\text{Viscous dissipation}}\underbrace{-\rho_p d f_2\sqrt{T}\left(\frac{\partial u}{\partial y}\right)^2}_{\text{Work done}}=0$$

(7-9)

Finally, we will compare the order of the convective terms $\left(\sim\frac{UT}{L}\right)$ with the order of the viscous dissipation term $\left(\sim\frac{T^{3/2}}{d}\right)$, the work done term $\left(\sim\frac{dTU^2}{H^2}\right)$, and the conductive terms $\left(\sim\frac{dT^{3/2}}{H^2}\right)$.

It is clear that convective term can be neglected.

Therefore, the final form of the energy equation is:

$$\frac{\partial}{\partial y}\left[\left(\rho_p d f_3\sqrt{T}\right)\frac{\partial T}{\partial y}+\left(\rho_p d f_4 T\sqrt{T}\right)\frac{\partial \upsilon}{\partial y}\right]+\rho_p d f_2\sqrt{T}\left(\frac{\partial u}{\partial y}\right)^2-\frac{\rho_p f_5}{d}T\sqrt{T}=0 \qquad (7\text{-}10)$$

7.2.4 Elimination of the Volume Fraction

The coupling term involving the volume fraction can be eliminated from the energy equation and the pseudo temperature boundary condition to further simplify the governing equations. Using equation (7-7) and substituting with the dimensionless functions given in Table 6.1, we have:

$$\frac{\partial}{\partial \mathrm{y}}\left(T\upsilon\left(1+4\eta\upsilon \mathrm{g_o}\right)\right)=0$$

$$\frac{\partial T}{\partial \mathrm{y}}\left(\upsilon\left(1+4\eta\upsilon \mathrm{g_o}\right)\right)+T\frac{\partial \upsilon}{\partial \mathrm{y}}\left(1+4\eta\upsilon \mathrm{g_o}\right)+T\upsilon\left(4\eta\frac{\partial \upsilon}{\partial \mathrm{y}}g_o+4\eta\upsilon\frac{\partial \mathrm{g_o}}{\partial \mathrm{y}}\right)=0 \qquad (7\text{-}11)$$

where $g_o=\dfrac{1}{1-\left(\upsilon/\upsilon_{\max}\right)^{1/3}}=\dfrac{\upsilon_{\max}^{1/3}}{\upsilon_{\max}^{1/3}-\upsilon^{1/3}}$, and $\dfrac{\partial g_o}{\partial y}=\dfrac{g_o^2}{3\upsilon_{\max}}\left(\dfrac{\upsilon_{\max}}{\upsilon}\right)^{2/3}\dfrac{\partial \upsilon}{\partial y}$

Therefore,

$$\frac{\partial T}{\partial y}f_1+\frac{\partial \upsilon}{\partial y}\frac{Tf_1}{\upsilon}+\frac{\partial \upsilon}{\partial y}4\eta\, g_o T\upsilon+4\eta\upsilon^2 T\frac{g_o^2}{3\upsilon_{\max}}\left(\frac{\upsilon_{\max}}{\upsilon}\right)^{2/3}\frac{\partial \upsilon}{\partial y}=0$$

$$\frac{\partial T}{\partial y}f_1+\frac{\partial \upsilon}{\partial y}\left[\frac{Tf_1}{\upsilon}+4\eta\, g_o T\upsilon+\frac{4}{3}\eta\upsilon^2 T\, g_o^2\,\frac{1}{\upsilon^{2/3}\upsilon_{\max}^{1/3}}\right]=0$$

$$\frac{\partial \upsilon}{\partial y} = -\frac{f_1}{T\left[\frac{f_1}{\upsilon} + 4\eta\, g_o \upsilon + \frac{4}{3}\eta \upsilon^2\, g_o^2\, \frac{1}{\upsilon^{2/3}\upsilon_{\max}^{1/3}}\right]}\frac{\partial T}{\partial y} \tag{7-12}$$

Substituting back in the denominator of (7-12) with the values of g_o and f_1 (Table 6.1), we have

$$\frac{\partial \upsilon}{\partial y} = -\frac{g_1(\upsilon)}{T}\frac{\partial T}{\partial y} \tag{7-13}$$

where $g_1(\upsilon) = \dfrac{f_1}{1 + \dfrac{8\eta\, \upsilon\upsilon_{\max}^{1/3}}{\upsilon_{\max}^{1/3} - \upsilon^{1/3}} + \dfrac{\frac{4}{3}\eta \upsilon^{4/3}\, \upsilon_{\max}^{1/3}}{\left(\upsilon_{\max}^{1/3} - \upsilon^{1/3}\right)^2}}$

Substituting (7-13) in the energy equation (7-10) results the following equation:

$$\frac{\partial}{\partial y}\left[\left(f_3 - f_4 g_1\right)\sqrt{T}\,\frac{\partial T}{\partial y}\right] + f_2\sqrt{T}\left(\frac{\partial u}{\partial y}\right)^2 - \frac{f_5 T^{3/2}}{d^2} = 0 \tag{7-14}$$

7.3 Boundary Conditions

7.3.1 Condition on the Slip Velocity

Comparing the order of magnitude of the gradient of the velocity $\frac{\partial u}{\partial y} \rangle\rangle \frac{\partial V}{\partial x}$ in equations (6-17) and (6-18), the condition on the slip velocity is simplified to:

7.3.1.1 At $y = 0$ (Bottom Plate)

$$\frac{\partial u}{\partial y} = \frac{f_8 \varphi_o}{d}\left(u - U\right) \tag{7-15}$$

7.3.1.2 At $y = H$ (Top Plate)

$$\frac{\partial u}{\partial y} = -\frac{f_8 \varphi_H}{d} u \tag{7-16}$$

7.3.2 Energy Balance

Substituting the coupling equation (7-13) in equations (6-21) and (6-22) for the pseudo temperature boundary conditions to eliminate the volume fraction term, results the following simplified equations:

7.3.2.1 At $y = 0$ (Bottom Plate)

$$\frac{\partial T}{\partial y} = -T\frac{f_4}{f_3}\frac{\partial \upsilon}{\partial y} - \frac{\varphi_o f_7}{d}\left(u_{sl}\right)^2 + T\frac{f_6\left(1-e_w^2\right)}{d}$$

$$\frac{\partial T}{\partial y} = T\frac{f_4}{f_3}\frac{g_1}{T}\frac{\partial T}{\partial \mathrm{y}} - \frac{\varphi_o f_7}{d}\left(u_{sl}\right)^2 + T\frac{f_6\left(1-e_w^2\right)}{d}$$

$$\left(\frac{f_4 g_1}{f_3} - 1\right)\frac{\partial T}{\partial y} + T\frac{f_6\left(1-e_w^2\right)}{d} = \frac{\varphi_o f_7}{d}\left(u-U\right)^2$$

$$\frac{\partial T}{\partial y} = T\frac{\left(1-e_w^2\right)}{d}\left(\frac{f_3 f_6}{f_3 - f_4 g_1}\right) - \frac{\varphi_o}{d}\left(\frac{f_3 f_7}{f_3 - f_4 g_1}\right)\left(u-U\right)^2$$

$$\frac{\partial T}{\partial y} = T\frac{ff_3\left(1-e_w^2\right)}{d} - \frac{ff_4\varphi_o}{d}\left(u-U\right)^2 \tag{7-17}$$

where $ff_3 = \dfrac{f_3 f_6}{f_3 - f_4 g_1}$, and $ff_4 = \dfrac{f_3 f_7}{f_3 - f_4 g_1}$

7.3.2.2 At $y = H$ (Top Plate)

$$\frac{\partial T}{\partial y} = -T\frac{f_4}{f_3}\frac{\partial \upsilon}{\partial y} + \frac{\varphi_H f_7}{d}\left(u_{sl}\right)^2 - T\frac{f_6\left(1-e_w^2\right)}{d}$$

$$\frac{\partial T}{\partial y} = T\frac{f_4}{f_3}\frac{g_1}{T}\frac{\partial T}{\partial \mathrm{y}} + \frac{\varphi_H f_7}{d}\left(u_{sl}\right)^2 - T\frac{f_6\left(1-e_w^2\right)}{d}$$

$$\left(1 - \frac{f_4 g_1}{f_3}\right)\frac{\partial T}{\partial y} + T\frac{f_6\left(1-e_w^2\right)}{d} = \frac{\varphi_H f_7}{d}u^2$$

$$\frac{\partial T}{\partial y} = -T\left(\frac{f_3 f_6}{f_3 - f_4 g_1}\right)\frac{\left(1-e_w^2\right)}{d} + \frac{\varphi_H}{d}\left(\frac{f_3 f_7}{f_3 - f_4 g_1}\right)u^2$$

$$\frac{\partial T}{\partial y} = -T\frac{ff_3\left(1-e_w^2\right)}{d} + \frac{ff_4\varphi_H}{d}u^2 \tag{7-18}$$

CHAPTER 8. APPLICATION TO TWO PARALLEL PLATES FLOW

8.1 Introduction

In this chapter, Lun's model is considered to study the mechanism of granular lubricant passing through two parallel plates. The results are compared with those obtained by McKeague and Khonsari [26], Zhou and Khonsari [30], Sawyer and Tichy [31], and Pappur and Khonsari [33].

8.2 Lubrication Equations

The general conservation laws, the constitutive equations and the boundary conditions presented in the previous sections are applied to a particular flow field where a granular lubricant passes through two parallel plates (Figure 8.1).

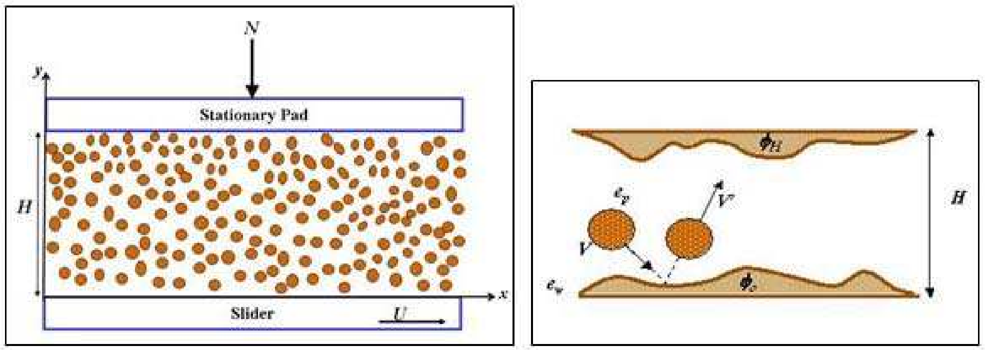

Figure 8.1: Two-Dimensional Granular Lubricant in a Couette Flow

The upper plate is stationary while the bottom plate undergoes a constant sliding motion *U*. Because of the thickness of the gap is very small, the spin effect of the granules and the gravity force are neglected. The grains are treated as smooth frictionless spheres of identical size, and the plates are assumed to be infinitely wide. The flow is considered to be steady, two-dimensional, and fully developed. The Cartesian coordinate system is set up by letting x lie along the plate's length, and y across the thickness of the flow. Since the flow is considered to be fully developed, all the gradients in x direction are zero $\left(\frac{\partial}{\partial x}=0\right)$. Therefore, the mean velocity, granular temperature, and solid volume fraction only have gradient along the y direction. The x-momentum in equation (7-4) for the application of two parallel plates flow can be rewritten in the form below:

$$\frac{d}{dy}\left[\left(\rho_p d f_2 \sqrt{T}\right)\left(\frac{du}{dy}\right)\right] = 0 \tag{8-1}$$

The y-momentum (7-7) becomes,

$$\frac{d}{dy}\left(\rho_p T f_1\right) = 0$$

$$\rho_p T f_1 = \text{constant} = N \tag{8-2}$$

where N is the normal load applied per unit area. The energy equation (7-14) along with the boundary conditions (7-15) to (7-18), remains the same since they contain only gradients along the y direction.

8.3 Dimensionless Forms

In what follows, we shall make use of the following dimensionless parameters:

$$u = Uu^*,\ T = \frac{N}{\rho_p}T^*,\ y = Hy^* \tag{8-3}$$

where U is the bottom plate velocity and H is the thickness of the gap. Substituting with the above parameters (8-3) in equations (7-14), (8-1) and (8-2) yields to the following dimensionless governing equations:

8.3.1 Dimensionless X-Momentum

$$AC\frac{d}{dy^*}\left[f_2\sqrt{T^*}\left(\frac{du^*}{dy^*}\right)\right] = 0 \tag{8-4}$$

8.3.2 Dimensionless Y-Momentum

$$T^* f_1(\upsilon) = 1 \tag{8-5}$$

8.3.3 Dimensionless Pseudo Energy

$$\frac{d}{dy^*}\left[\left(f_3 - f_4 g_1\right)\sqrt{T^*}\frac{dT^*}{dy^*}\right] + A^2 f_2 \sqrt{T^*}\left(\frac{du^*}{dy^*}\right)^2 - \frac{f_5 T^{*3/2}}{C^2} = 0 \tag{8-6}$$

where $A = \frac{U\sqrt{\rho_p}}{\sqrt{N}}, C = \frac{d}{H}$

8.3.4 Dimensionless Mass Flow Rate

For a Couette type flow, the distribution of bulk velocity is independent of the flowing direction. Hence, the mass flow rate in the gap of a Couette flow is constant. Rewriting equation (6-4) accounting for a fixed gap and the fact that $\rho = \rho_p \upsilon$, we have:

$$\frac{d}{d\mathrm{x}}\int_0^H \rho_p \upsilon \,\mathrm{u}\, dy = 0$$

and in dimensionless form,

$$\overset{\bullet}{m}{}^* = \frac{\overset{\bullet}{m}}{\rho_p U H} = \frac{d}{d\mathrm{x}^*}\int_0^1 \upsilon \,\mathrm{u}^*\, dy^* \tag{8-7}$$

8.3.5 Dimensionless Boundary Conditions

Substituting (8-3) in equations (7-15) to (7-18) yields to the following dimensionless boundary condition equations:

8.3.5.1 At y^* = 0 (Bottom Plate)

$$\frac{du^*}{dy^*} = \frac{f_8 \varphi_o}{C}\left(u^* - 1\right) \tag{8-8}$$

$$\frac{dT^*}{dy^*} = \frac{T^* f f_3}{C}\left(1 - e_w^2\right) - \frac{A^2 f f_4 \phi_o}{C}\left(u^* - 1\right)^2 \tag{8-9}$$

8.3.5.2 At y^* = 1 (Top Plate):

$$\frac{du^*}{dy^*} = -\frac{f_8 \varphi_H u^*}{C} \tag{8-10}$$

$$\frac{dT^*}{dy^*} = -\frac{T^* ff_3}{C}\left(1 - e_w^2\right) + \frac{A^2 ff_4 \phi_H}{C} u^{*2} \tag{8-11}$$

8.4 Numerical Scheme

The momentum and the energy equation are coupled, ordinary differential equations. Because of the complexity of these equations, numerical schemes are utilized. In the simulations presented, the thickness of the gap is fixed and the normal load is specified. Finite difference method is employed to discretize the dimensionless governing equations and boundary equations, which forms a set of algebraic equations. Newton's iteration method is used to solve the resulting set of equations for velocity and temperature. Bisection method is used to solve the volume fraction equation. There are three loops in the computations, the inner loop solves the velocity, the second loop solves the temperature, and the outer loop solves the volume fraction. The iteration is repeated until the results converge, and then the mass flow rate is computed by integrating the volume fraction and the velocity along the gap thickness. The tolerance level used is 10^{-6} per iteration.

8.5 Results and Discussion

The following focuses on applying the theory to predict the performance of the granular flow between two parallel plates. A benchmark is set up based on the papers presented by McKeague and Khonsari [26] and Zhou and Khonsari [30]. The input parameters for the benchmark are presented in Table 8.1. The top plate is stationary, the velocity of the bottom plate is $U = 4.6\,\mathrm{m/sec}$, and the thickness of the gap is equivalent to 14 particle diameters. The granular material used in the lubrication is made of Titanium Dioxide (TiO_2) as reported by Heshmat [3]. The particle has a diameter of $5\,\mu\mathrm{m}$ and a density $\rho_p = 4260\,\mathrm{kg/m^3}$. The coefficients of restitution for both particle and wall are assumed to be $e_p = e_w = 0.8$, and the roughness of both moving and stationary plate is $\phi_o = \phi_H = 0.5$.

In the simulation presented, several mesh points and error tolerances refinement were performed. It was found that 21 grid points given along the fixed gap thickness is the optimum number of grid points. The error tolerance is set to be 10^{-6}, and the CPU time for each simulation is about 4 seconds. Increasing the grid points more than 21 did not improve the results. The mass flow rate in the gap must be specified and adjusted by changing the applied load.

Table 8.1 : Input List for Benchmark Case Used in the Computer Simulations

Parameter	Value	Parameter	Value
e_p	0.8	L	0.0264 m
e_w	0.8	U	4.6 m/s
$\upsilon_{\max}$	0.65	H	$70\,\mu\text{m}$
ρ_p	$4260\,\text{kg/m}^3$	ϕ_o	0.5
d	$5\,\mu\text{m}$	ϕ_H	0.5

8.5.1 Benchmark Simulations

Figure 8.2 demonstrates the distribution of the flow velocity, the pseudo temperature, and the solid volume fraction. It is clear that there is a slip velocity at the boundaries, and the energy supplied from the boundary caused by the slip velocity is transferred to the interior gap. For a liquid lubricated system, there would have been no slip velocity at the boundaries. Instead, when powder is used, the theory predicted a slip velocity at both boundaries.

Granular slippage is one of the important characteristics of granular lubrication. During shearing, it provides energy from the boundaries into the granules contained within the gap. In addition to this energy transferred due to the slip, energy is developed within the flow field due to viscous dissipation. Since the top and bottom plates assumed to have the same roughness, then the velocity profile exhibit equal slip at the boundaries.

The fluctuation velocity of the granular material (pseudo temperature) decreases gradually from the boundaries to the center of the gap. At the boundaries, the pseudo temperature is large due to the granular slip responsible in generating energy that is transferred to the middle of the gap. On the other hand, the inelastic collision between the granules in the middle of the gap causes a decrease in the energy dissipation. Hence, there is less fluctuation in the middle of the gap compared to those at the boundaries and the pseudo temperature is small. The viscous dissipation term that appears in the pseudo energy equation (8-6) is ruled mainly by the coefficient of restitution. The coefficient of restitution is a constant parameter that describes

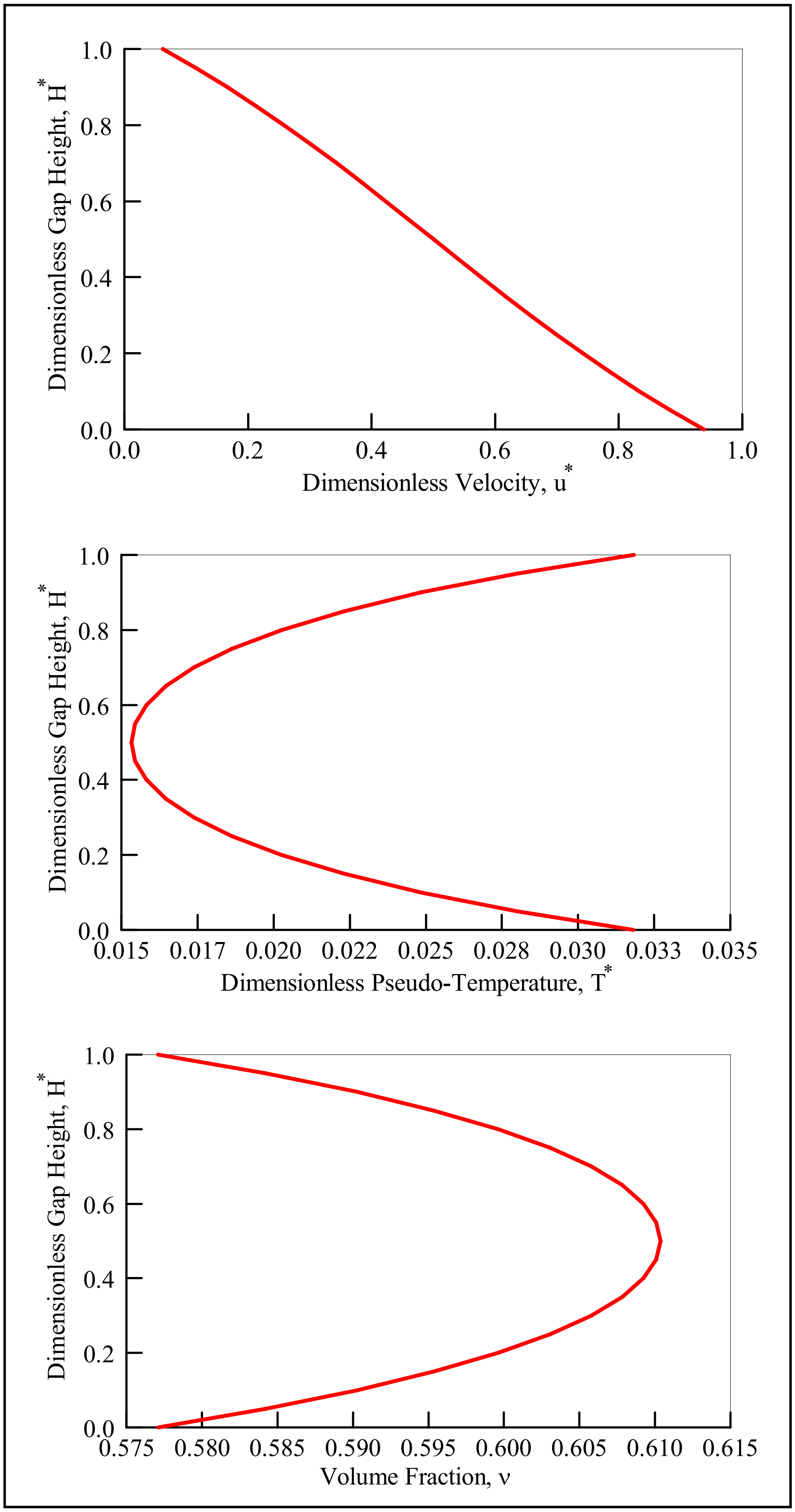

Figure 8.2 : Benchmark Simulations of the Flow Velocity, Granular Temperature, and Solid Volume Fraction

the inelastic collision between the granules. Therefore, the pseudo temperature profile is determined by both, the viscous dissipation and the slip velocity.

This behavior of the fluctuation velocity can be explained by examining the volume fraction profile. The volume fraction increases in the middle of the gap, meaning that the grains are densely packed. Thus, less fluctuation velocity and a decrease in the energy dissipation will took place. Closer to the boundaries, the granules are less dense and there will be more fluctuation velocity which results in an increase in the pseudo temperature. Therefore, the distribution of the solid volume fraction takes a parabolic shape with the maximum value in the middle of the gap.

These predicted results have similar trends to those obtained by other researchers. For a specified dimensionless mass flow rate of 0.3, the normal load was found to be 7241 N/m^2. The values of the fluctuation velocity and the solid volume fraction on the boundaries are predicted to be 0.0315 (0.053 m^2/sec^2) and 0.576, corresponding to 0.12 (0.1 m^2/sec^2) and 0.6 reported by McKeague and Khonsari [26], 0.081 (0.046 m^2/sec^2) and 0.57 by Zhou and Khonsari [30], and 0.03 (0.049 m^2/sec^2) and 0.45 by Pappur and Khonsari [33]. The friction coefficient is predicted to be 0.407, which is very close to 0.41 by Zhou and Khonsari [30], and 0.42 Pappur and Khonsari [33]. In the experimental work of Savage and Sayed [21], the friction factor of granular material is given around 0.3 to 0.4.

The predicted result of the fluctuation velocity in this dissertation differed slightly from the one predicted by Zhou and Khonsari [30] since there was a difference in the normal load. The difference in the prediction of the fluctuation velocity between this dissertation and McKeague and Khonsari [26], can be attributed to the use of difficult constitutive equations as presented by Haff [14]. McKeague and Khonsari [26] show that Haff's approach is very simple to apply and has a very clear physical meaning. But Lun's model used in the simulations reported here is more realistic because some of the parameters are function of the local solid volume fraction, instead of some constants in the Haff's model.

8.5.2 Effect of the Granular Coefficient of Restitution, e_p

Figure 8.3 shows the sensitivity of the flow velocity, granular temperature, and the solid volume fraction to the granules coefficient of restitution. The slip velocity decreases at the boundaries as e_p increases. The larger the e_p, the more elastic the granules become. Hence, there

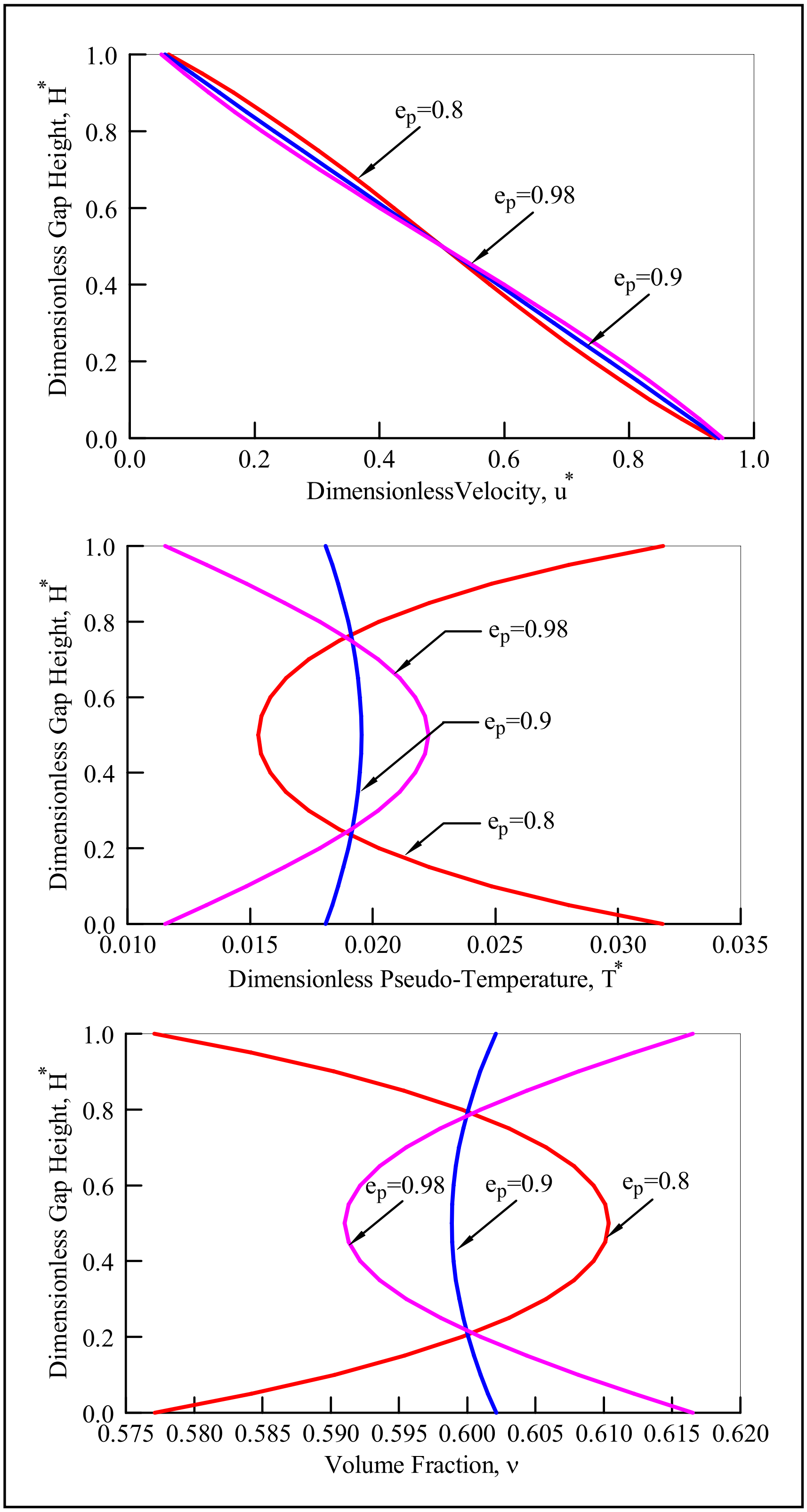

Figure 8.3 : Variation of the Flow Velocity, Granular Temperature, and Solid Volume Fraction with the Granular Coefficient of Restitution, e_p

is less energy loss by inelastic collision between granules. The trend of the granular temperature and the solid volume fraction changes drastically at the higher values of e_p (0.9 and 0.98) compared to the benchmark case where $e_p = 0.8$. There are two energy sources which arise in the formulation of the granular temperature. One comes from the slip velocity at the boundary and the other is the viscous dissipation in the interior of the flow. When e_p is large, the slip velocity at the boundary decreases and the viscous dissipation in the interior flow increases. Therefore, there is more energy generated in the interior flow than the one generated at the boundaries by the granular slip. Hence, the energy is transferred from the middle of the gap to the boundaries.

The solid fraction trend is directly related to the pseudo temperature. When there is more pseudo energy generated in the interior of the flow, implies that the surrounded granules will experience much larger fluctuation than the ones near the boundaries. Therefore, less concentration of the granular material will occur in the middle of the gap and more accumulation of the granules at the boundaries.

At higher e_p, the load is increased by almost 10 times compared to the benchmark data. When e_p is 0.8, the normal load is $N = 7241$ Pa, and the friction factor $f = 0.4$ and when e_p is 0.98, the normal load is $N = 6293$ Pa, and the friction factor $f = 0.3$. According to the above analysis, as e_p goes to 1, the solid volume fraction near the boundaries is larger than that at the center of the channel. Under this condition of low shear stress and high normal stress, it is clear that powders are likely to conglomerate at the boundaries. The results are in good agreement to those obtained by Zhou and Khonsari [30], and McKeague and Khonsari [26].

8.5.3 Effect of the Wall Coefficient of Restitution, e_w

Figure 8.4 shows the variation of the flow velocity, granular temperature, and the solid volume fraction to the coefficient of restitution of both, top and bottom plates. The slip velocity increases as e_w increases. An increase in e_w means that the wall is more elastic. Hence, there is less energy loss during collision between the wall and the granules which implies that more energy is supplied from the boundaries to the flow. The granular temperature increases at the boundaries and decreases in the middle of the gap.

As e_w increases, the curvature profile of the granular temperature and the solid volume fraction becomes greater because of the change in the normal load to match the specified mass

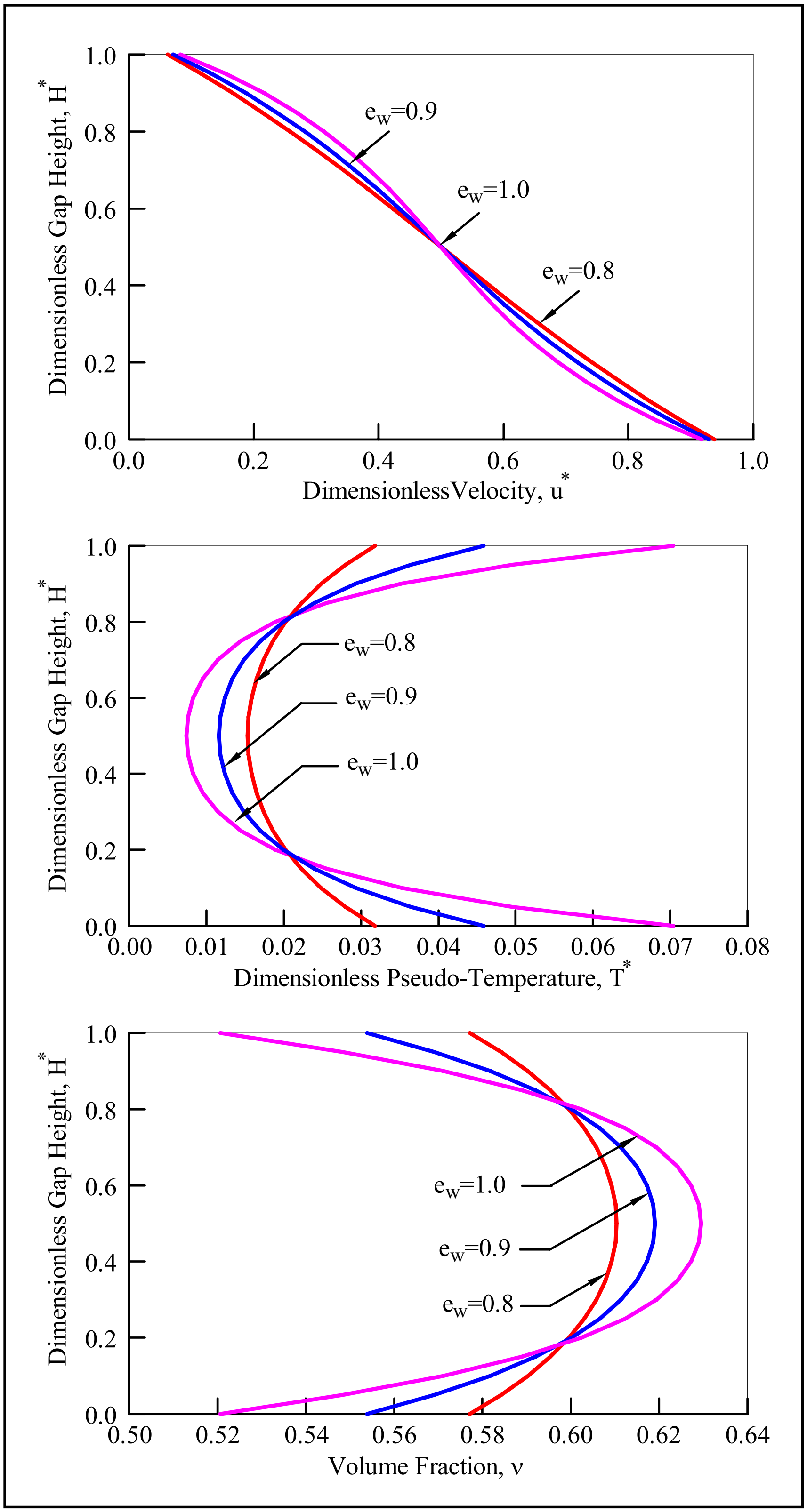

Figure 8.4 : Variation of the Flow Velocity, Granular Temperature, and Solid Volume Fraction with the Wall Coefficient of Restitution, e_w

flow rate. As e_w increases, the normal stress increases but there is no change in the trends of the granular temperature and the solid volume fraction. The parameter e_w affects only the slip velocity, not the interior of the flow.

At higher e_w the normal load is not largely affected as compared to the benchmark data. When e_w is 0.8, the normal load is N = 7241 Pa, and the friction factor f = 0.41 and when e_w is 1.0, the normal load is N = 8035 Pa, and the friction factor f = 0.37. Hence, the effect on the normal load caused by changing e_w is much less than that of e_p which implies that the coefficient of restitution of the granules play a much more substantial role than the coefficient of restitution of the wall. The results are in good agreement to those obtained by Zhou and Khonsari [30].

8.5.4 Effect of the Surface Roughness at the Top and Bottom Plates, ϕ_o and ϕ_H

Figure 8.5 and Figure 8.6 present the variation of the flow velocity, granular temperature, and the solid volume fraction by varying the roughness of the top stationary wall and the bottom moving wall respectively. The roughness ϕ_H of the stationary top boundary surface ranges from 0 when it is completely smooth, to 1 when it is completely rough.

When ϕ_H is large, the slip velocity at the top boundary becomes smaller. Hence, the particles around this boundary become almost stationary which means the slip effect becomes nil. Thus, as the roughness of the top plate becomes larger, there is more energy being transferred from the bottom plate than from the top plate. Since the bottom plate is supplying much more momentum to the adjacent grains through the slip velocity than that at the top plate, the granular temperature at the bottom plate is relatively larger than the top plate. These effects are also reflected in the solid volume fraction profile, where the larger the slip velocity at the bottom plate tends to loosen the grains there whereas the top plate experiences the exact opposite effect. The value of the maximum solid volume fraction appears near the top stationary plate, and this phenomenon happens because of the viscous dissipation term. The results are in good agreement to those obtained by Zhou and Khonsari [30].

Similarly, the roughness ϕ_o of the moving bottom boundary surface ranges from 0 when it is completely smooth, to 1 when it is completely rough. When ϕ_o is large, the slip velocity at the bottom boundary becomes smaller and the energy transferred from this boundary decreases.

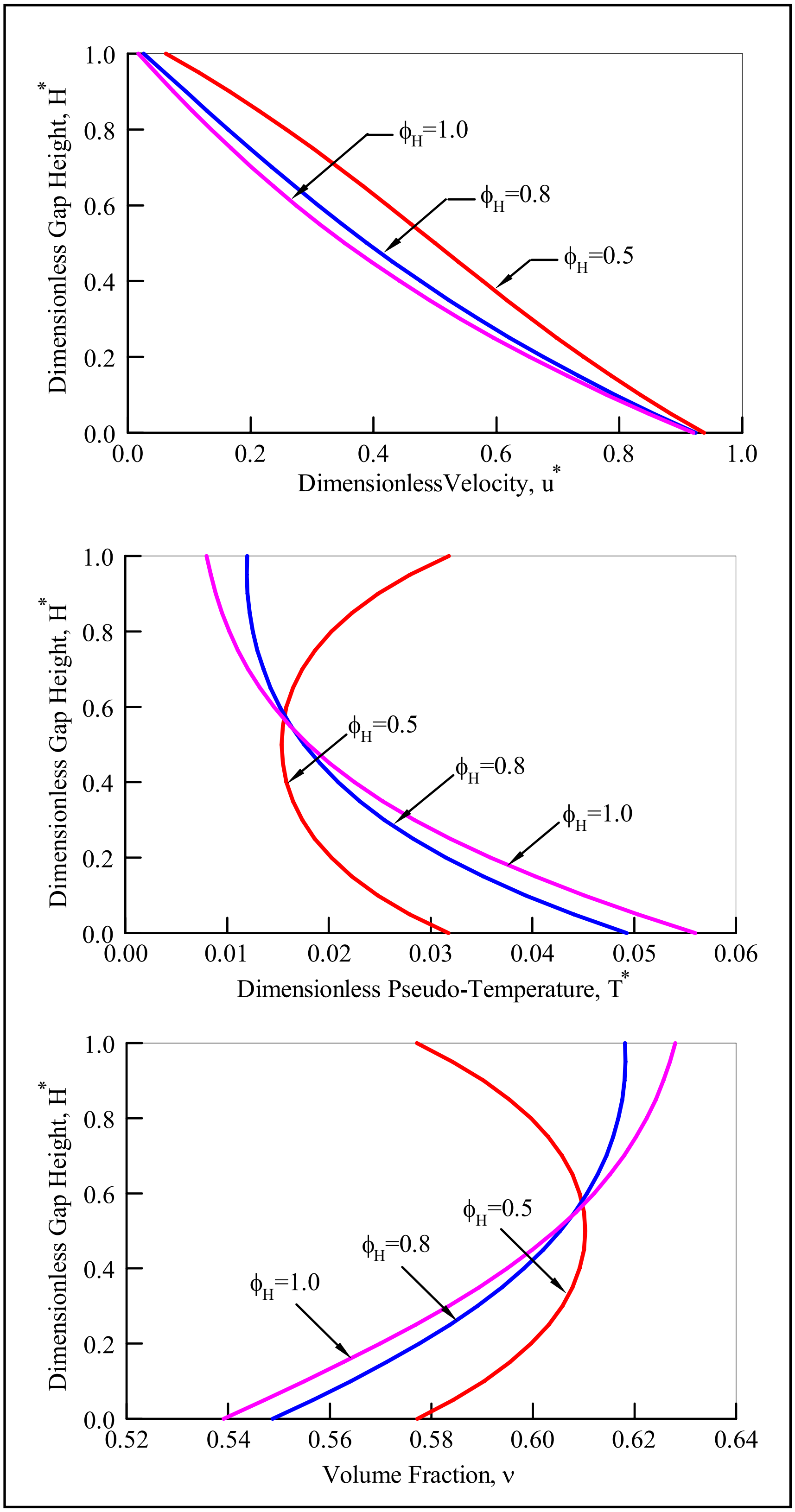

Figure 8.5 : Variation of the Flow Velocity, Granular Temperature, and Solid Volume Fraction with the Roughness of the Top Plate ϕ_H

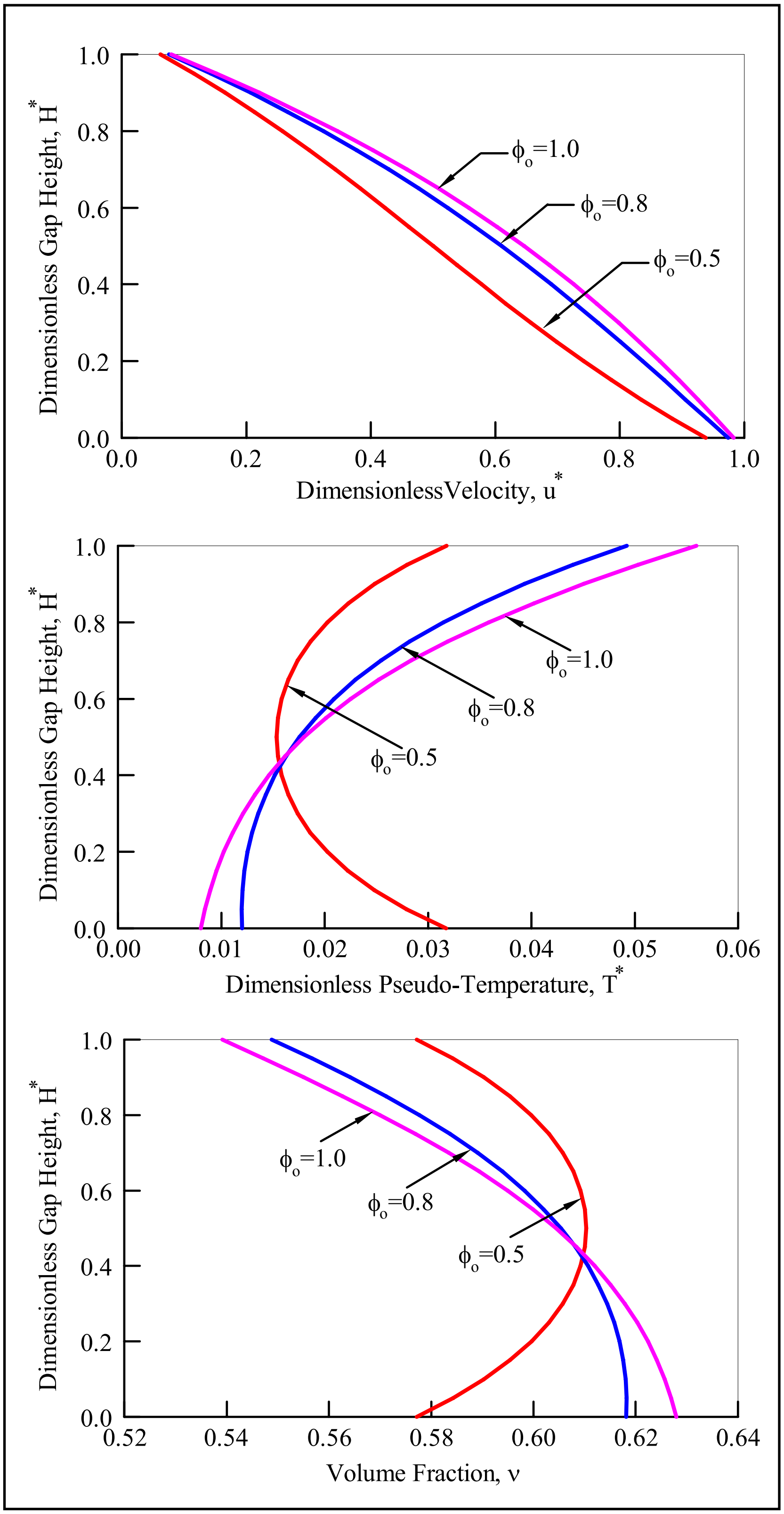

Figure 8.6 : Variation of the Flow Velocity, Granular Temperature, and Solid Volume Fraction with the Roughness of the Bottom Plate ϕ_o

Therefore, more energy is being transferred from the top plate than from the bottom plate to the middle of the gap. The reduction in the amount of energy transferred from the bottom plate, results in a decrease in the pseudo temperature in that boundary accompanied by an increase in the solid volume fraction. In the middle of the gap, increasing the bottom plate surface roughness tends to increase the pseudo temperature due to the slip velocity.

8.5.5 Effect of the Gap Thickness, *H*

Figure 8.7 demonstrates the variation of the flow velocity, granular temperature, and the solid volume fraction by varying the thickness of the gap. The mass flow rate decreases as the gap thickness H is changed from $20d$ to $7d$. As H decreases, fewer granules flow inside the channel and the chance of collision between granules decreases. The granular material becomes more concentrated and result a decrease in the fluctuation velocity which in turn decreases the energy loss by inelastic collision. Therefore, there is less energy loss through the gap and more energy will be supplied to the middle of the gap by the granular slip at the boundaries. The granules in the middle of the channel are more influenced by the boundaries. Thus, the distribution of the granular temperature and the solid volume fraction across the gap becomes more flat in shape. The flow velocity becomes almost linear. As H increases, the effect of the boundaries on the distribution of the particles in the middle of the gap becomes less distinct and this result a "solid plug" phenomenon as mentioned in McKeague and Khonsari [26]. Simulations were performed with H=$20d$ to illustrate this phenomenon. For a fixed mass flow rate, the normal stress increases as H decreases. Varying the particle diameter and fixing the gap width would results same trends.

8.5.6 Effect of the Mass Flow Rate

Figure 8.8 presents the variation of the flow velocity, granular temperature, and the solid volume fraction by varying the mass flow rate. Increasing the mass flow rate increases the average solid volume fraction across the gap. As the average volume fraction across the gap is large, the granular temperature in the flow becomes smaller. Therefore, the slip velocity at the boundaries decreases and less energy is supplied from the boundaries.

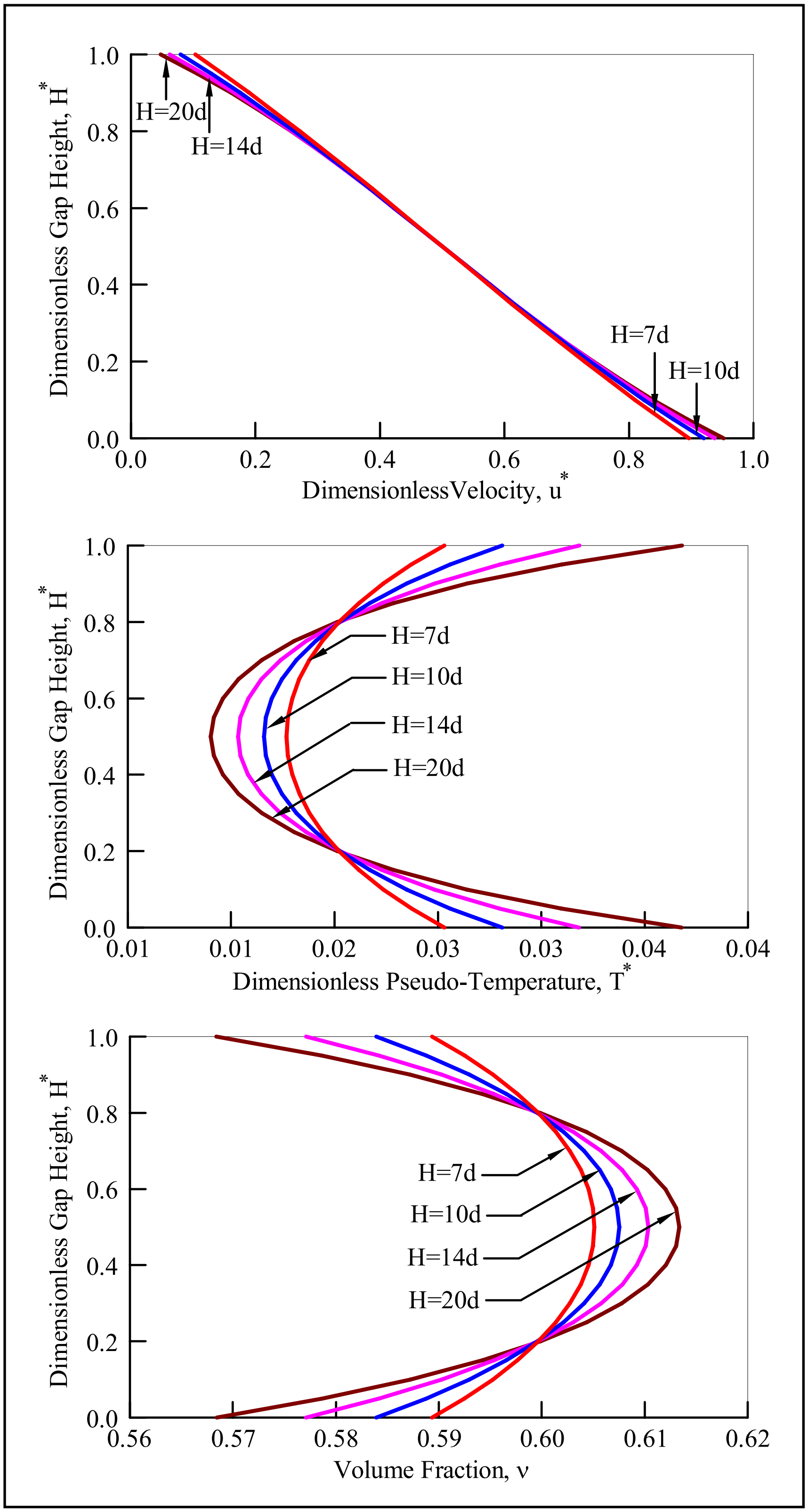

Figure 8.7 : Variation of the Flow Velocity, Granular Temperature, and Solid Volume Fraction with the Gap Thickness, *H*

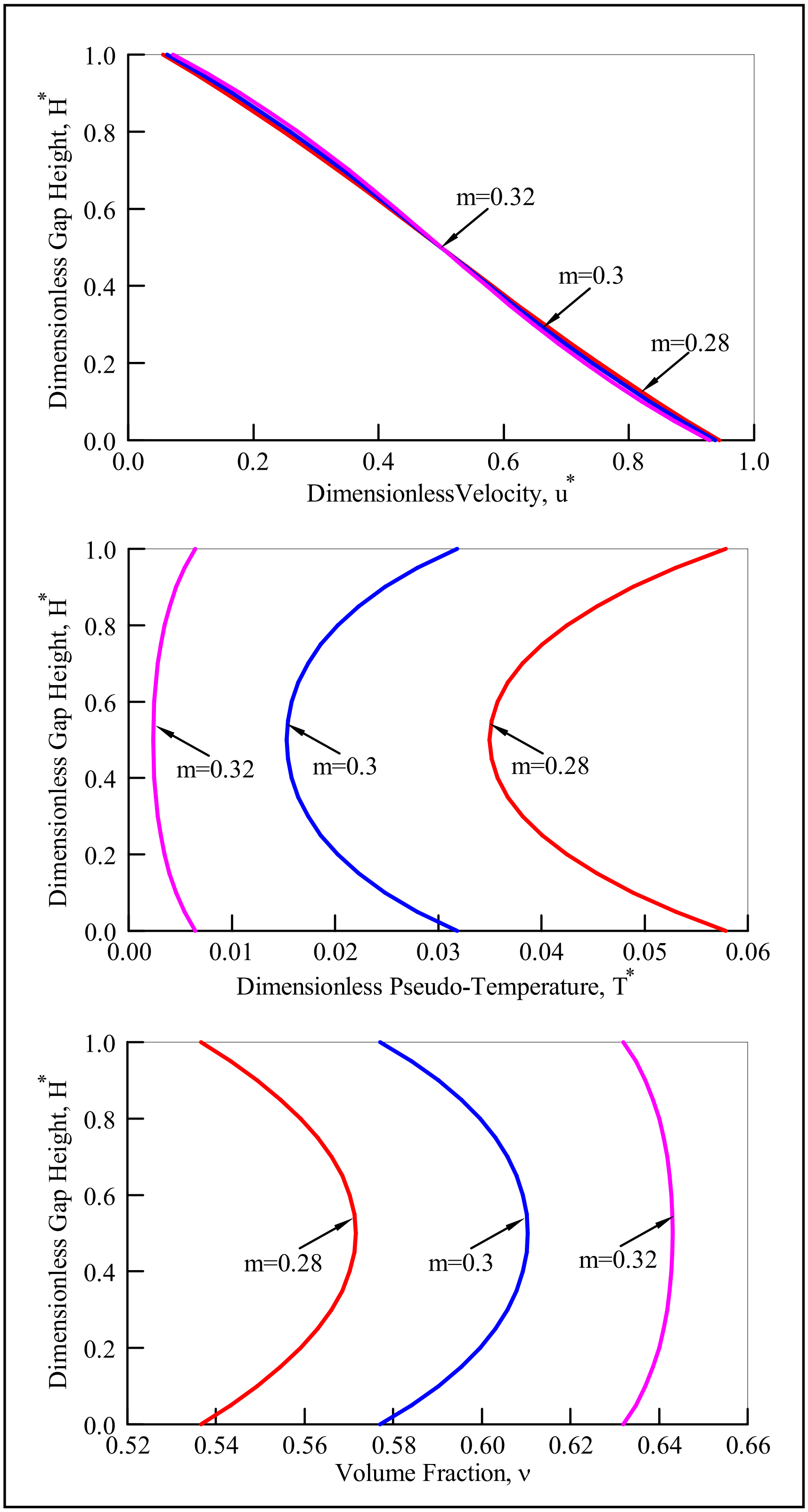

Figure 8.8 : Variation of the Flow Velocity, Granular Temperature, and Solid Volume Fraction with the Mass Flow Rate

8.5.7 Effect of the Coefficient of Restitution on the Friction Coefficient

Figure 8.9 demonstrates the effect of both coefficient of restitution of the granules and the wall on the friction coefficient. With fixed e_w, the larger the e_p, the more elastic the granules become causing more uniform distribution to the granules across the gap. Hence, there is less energy loss by inelastic collision between granules and a decrease in the energy generated by slip at the boundaries. Therefore, there is more energy generated in the interior flow than the one generated at the boundaries. Thus, the friction coefficient decreases significantly. With e_p fixed, the variation of the friction coefficient with the coefficient of restitution of the wall is not significant. An increase in e_w means that the wall is more elastic. Hence, there is less energy loss during collision between the wall and the granules which implies that more energy is supplied from the boundaries to the flow.

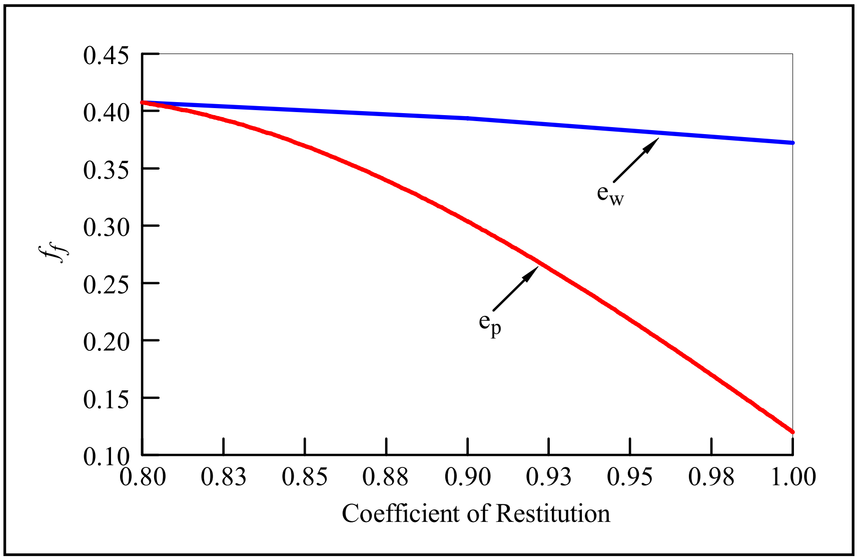

Figure 8.9 : Effect of the Coefficient of Restitution on the Friction Coefficient

8.5.8 Effect of the Coefficient of Restitution on the Mass Flow Rate

Figure 8.10 presents the effect of both coefficient of restitution of the particles and the wall on the mass flow rate. With fixed e_w, the larger e_p, the more elastic the granules become causing the average volume fraction to decrease. Decreasing the mass flow rate decreases the average solid volume fraction across the gap or vice versa. Thus, when e_p increases, the mass flow rate decreases. With fixed e_p, as e_w increases, it shows negligible effect on the mass flow rate.

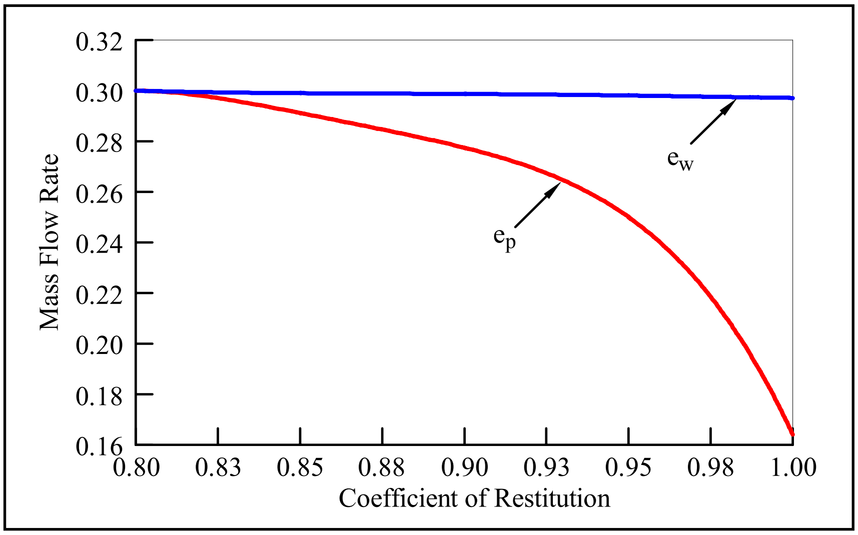

Figure 8.10 : Effect of the Coefficient of Restitution on the Mass Flow Rate

8.6 Conclusions

This chapter deals with simulation of granular flow between two parallel plates with infinite width. The formulation of the governing equations and boundary conditions are formulated along with an efficient numerical simulation. The effect of the viscous dissipation in the energy equation is considered in the simulations, similar to Zhou and Khonsari [30]. The solid volume fraction appears naturally in the equations. The constitutive equations in this chapter are based on the model of Lun et al [8]. The results are explained and compared with those of McKeague and Khonsari [26] , Zhou and Khonsari [30], and Pappur and Khonsari [33].

The energy supply to the granular flow is from two sources: one from the slip velocity at the boundaries, and the other from the viscous dissipation. For a liquid lubricated system, there would have been no slip velocity at the boundaries. Instead, when granules are used, the theory predicted a slip velocity at both boundaries. Granular slippage is one of the important characteristics of granular lubrication. During shearing, it provides energy from the boundaries into the granules contained within the gap. The slip at the boundaries increases the pseudo temperature and hence more energy is being supplied to the interior flow.

The results with Lun's model have similar trends to those of Zhou and Khonsari [30], and McKeague and Khonsari [26]. The friction factor is around 0.4 that is the same as the experimental measurement presented by Savage and Sayed [21]. The coefficient of restitution of the granules plays a major role in the pseudo temperature and the solid volume fraction. When granules become nearly elastic, the simulations predict a different distribution for the granular temperature and the solid volume fraction. There is much more energy generated in the interior flow which is transferred to the boundaries. Hence, the distribution of the granules at the boundaries is dense, while sparse in the interior flow. This trend was predicted because of the viscous dissipation term included in the formulation of the equations, and could not be predicted if we neglect this term.

CHAPTER 9. GRANULAR COLLISION LUBRICATION: EXPERIMENTAL INVESTIGATION AND COMPARISON WITH THEORY

9.1 Introduction

The tribology of dry particulate lubricants is a subject of considerable interest to researchers working on powder lubrication. Two distinct types are used: cohesive lubricants (powder) and cohesionless lubricants (granular). Cohesive lubricants are soft particles that accommodate slip velocity mostly by adhering to surfaces and shearing in the bulk medium, i.e. behave similar to hydrodynamic fluids. Cohesionless lubricants are hard particles that transfer momentum and accommodate slip velocity through shearing and rolling at low shear rates, and through collisions at high shear rates. Granular materials can resist breaking down as a result of large shear forces and provide a useful alternative for lubrication under extreme conditions such as those encountered in high performance turbine engines, where the operating temperatures are very high (~800 ^{o}C). Other applications using granular materials can vary from auxiliary bearings particularly during start-up periods, to the use in micro-nano-scale systems such as MEMS devices [44].

The motivation for the present chapter arises from the need for bearing technology that can accommodate the future generation of engines aiming for higher thermodynamic efficiency, less fuel consumption and increased thrust-to-weight ratio in turbine engines. Despite the fact that there is a general agreement on the needs for such a new oil-free granular lubrication mechanisms, modeling and prediction of granular flows is very complex and still distant from being well understood. It was established that granular material plays a major role in determining the axial load transmitted (lift) between the surfaces, the sliding friction and the slip velocity, but uncertainties still remain on several issues which require more investigation. In the present chapter, experiments were prepared to demonstrate the vertical displacement (lift) observed in an annular shear cell apparatus and to study the effect of the rotational speed, the normal load, and the surface roughness on the friction coefficient and the lift. Results of theoretical prediction are also presented that substantiate the validity of the findings.

9.2 Experiment

9.2.1 The Apparatus

The test rig used is an automated tribometer controlled and monitored by a computer as illustrated in Figure 9.1. The tribometer has a DC servomotor, which provides at a low gear ratio, a torque of 11.3 N-m (100 lbf-in) and rotational speeds up to 1,000 rpm. It is equipped with a computerized data acquisition system capable of recording real-time values of friction coefficient, wear/displacement, and speed. The load on the testing component is applied from the loading mechanism located in the bottom section of the apparatus. It can provide and maintain a normal load up to 2224 N (500 lbs) using a 4:1 lever arm. The tribometer measures friction and displacement to 0.635 μm (25 μin) giving an accurate assessment of displacement and friction as a function of time. The vertical displacement and the friction coefficient values are recorded automatically every 20 seconds.

Displacement is measured by means of the linear variable differential transformer (LVDT). When the bottom disk moves upward or downward, the LVDT senses this rectilinear motion. If the sensor records an upward displacement, it presents an indication of wear and if it records a downward displacement, it gives an indication of a positive displacement due to the fact that the granules are pushing the bottom disk away from the top disk which provides an indication of lift. To measure the friction coefficient, the top vertical shaft is rotating but restricted from the motion in the vertical direction while the bottom holder is restrained from rotation by a torque arm. This torque arm is connected to a force transducer and senses the frictional torque applied by the granular medium which measures the friction and in turn determines the friction coefficient. Since the normal stress is originally specified, thus the shear stress can be calculated simply by having the friction coefficient measurements.

The shear cell as shown in Figure 9.2 consists of two concentric steel disks. The upper disk is mounted on a rotating vertical shaft but restricted from the motion in the vertical direction. The bottom disk is restricted from rotation, but can move in the vertical direction. The shear cell has an annular channel of 31.4 mm wide and a mean radius of 34.7 mm. The channel is 45.8 mm deep and contains the granular material to be used. The top disk has an annular protrusion that fits into the channel of the bottom disk. This annular protrusion does not contact the side walls of the bottom disk channel. The side walls of the granular cell are made of clear acrylic to visualize the granular flow and a wall thickness of 6.35 mm (0.25 inches).

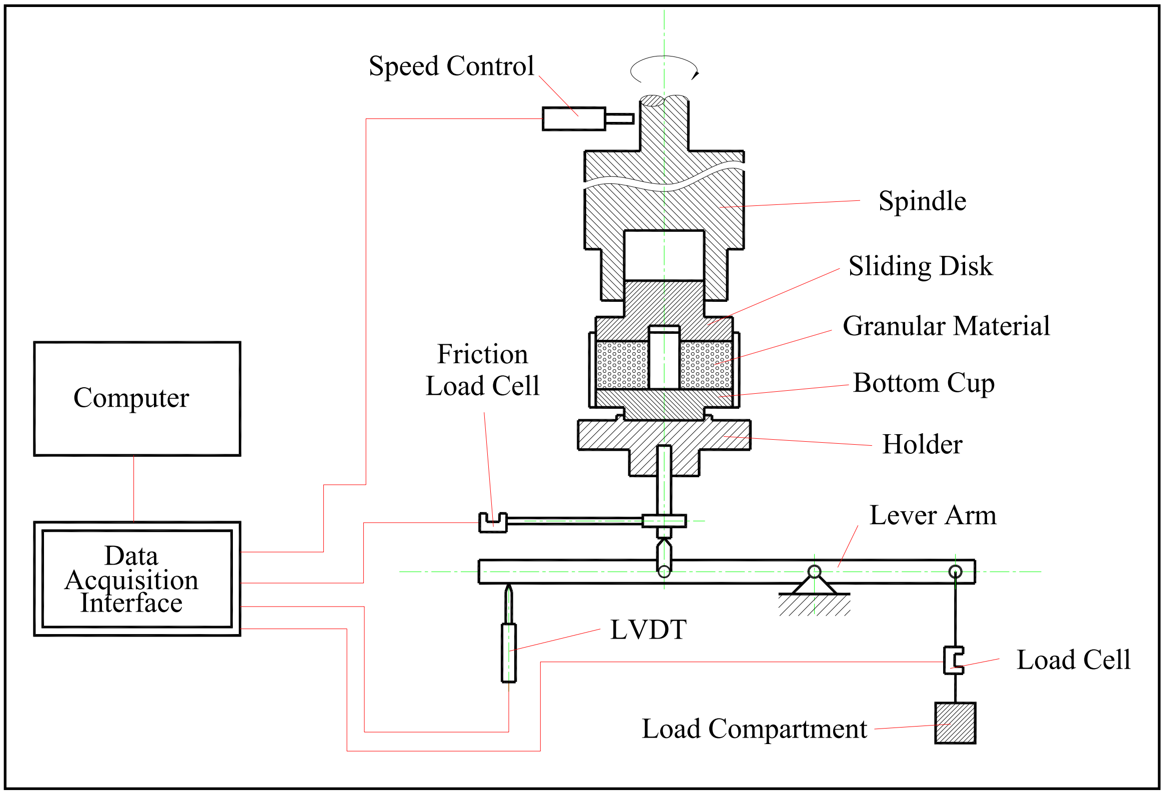

Figure 9.1 : Schematic of the Experimental Apparatus

The operating temperature for the acrylic material is 0^o to 66^oC (0^o to 150^oF), and its tensile strength is 62 MPa (9000 Psi). A high-temperature high-strength epoxy and a set of screws were used to attach the acrylic wall to the bottom disk. The bottom disk is free to move vertically, so as to allow for the expansion of the sheared granular material. The bottom disk is attached to a vertical shaft with a sensor on its other end to measure the vertical displacement and friction coefficient as a function of time and rotational speed of the top disk. The shear cell dimensions and the steel granules properties are summarized in Table 9.1.

9.2.2 Experimental Procedures

The gap in the annular shear cell is divided into three regions. The first region is the layer of granules adjacent to the upper moving disk; the second region is the layer of "locked granules" adjacent to the stationary lower disk, and an intermediate layer between those two regions (interior flow). A total of 18 experiments were conducted to illustrate the lift phenomenon in a parallel plate configuration using granular material with six different applied loads. In addition, three configurations for roughness, for it are established that surface roughness plays an important role in granular simulations and experiments.

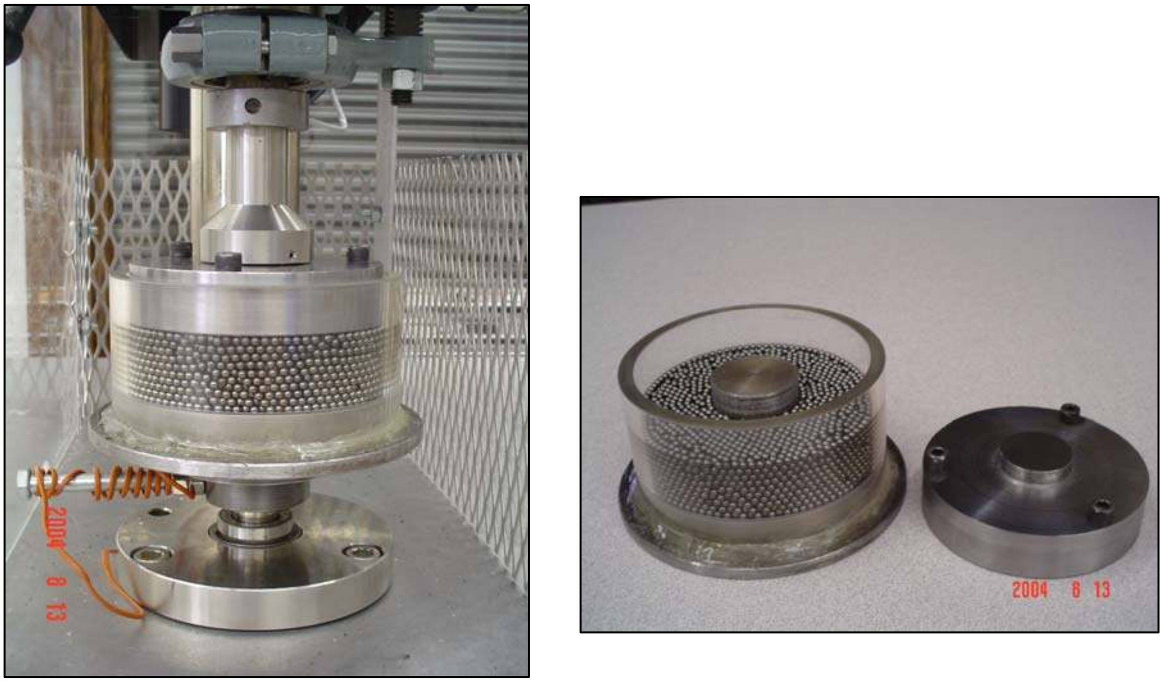

Figure 9.2 : **Shear Cell Assembly**

In the kinetic theory presented in this dissertation (Chapter 8), a wall roughness parameter is used. This parameter is a measure of the fraction of collisions that transfer a lateral momentum to the wall and so-called specularity coefficient. Its value varies from 0 to 1 representing a very smooth to a very rough surface, respectively. When the surface of the wall is smooth, the granule-wall collisions are very small and in turn result a large quantity of granule slip at the wall. In the case of rough surface, the granule-wall collisions will provide a major transport of lateral momentum to the wall and the slip at the wall becomes much less. As described below, in the experiments, roughness was applied to the surfaces by attaching a series of adjacent granules along the length of each surface to help drive the granules of the interior flow. In one series of tests, the upper disk—the driver—was roughened while keeping the lower disk smooth. In another set of tests, the configuration was reversed by making the lower disk rough and the upper disk smooth. Finally, a series of tests was performed where both disks were rough.

Table 9.1 : Shear Cell Dimensions and Steel Granules Properties

Channel Width	31.4 mm
Channel Depth	45.8 mm
Mean Radius (R_{mean})	34.7 mm
Shearing Area $\left(A_{Shear} = \pi\left(r_o^2 - r_i^2\right)\right)$	6846 mm^2
Mean Length $\left(L_{mean} = 2\pi R_{mean}\right)$	218.24 mm
Gap Height (H)	21 – 27 mm
Particle Diameter (D)	3 mm
H/D	7 – 9
Particle Density	7850 kg/m^3
Rotational Speed	50 – 800 rpm
Linear Speed $\left(U = 2\pi R_{mean} N / 60\right)$	0.18 – 3.0 m/sec

The following procedure was used in creating the desired surface roughness. Stainless steel wire mesh was used for the rest of the experiments with the proper mesh size as shown in Figure 9.3. The wire mesh was first glued to the surface, and then some stainless steel balls enough to cover this surface was glued to it using high-impact high-strength epoxy. The wire mesh along with the high-strength epoxy provided a very high shear strength and very high torque resistance to the balls glued to it.

A typical experiment starts by placing a specified mass of granules in the lower channel of the shear cell. The upper disk is then lowered until it just touches the granules, thereby packing them in place. A specified normal load is applied to the granules through the bottom surface causing them to be compressed. Corresponding counter weight need to be considered when normal load is specified to compensate the weight of the bottom disk and the specified mass of granules. The top disk is then given the rotational motion causing the granules to move and exchange places at low speeds. Then, at higher speeds they start to collide and tend to push the bottom disk downward.

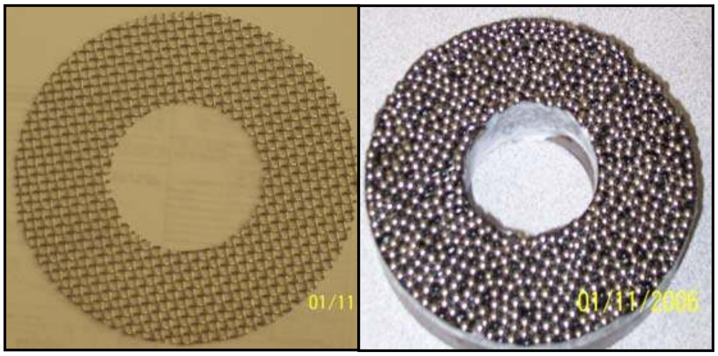

Figure 9.3 : Surface Roughness

a) Wire Mesh **b) Steel Balls Glued to the Surface Using the Wire Mesh**

With a specified normal load, the drive motor is set to rotate the upper disk slowly for a few seconds first to make sure that the granules are well distributed and initially compacted in the channel. The motor is then stopped to adjust the positioning of the upper disk if needed after the granules being well distributed and compacted to ensure that it just touches the granules. The driving motor starts to rotate the upper disk again and increases the rotational speed in a step fashion every 5 minutes ranging from 50 to 800 rpm by an increment of 50 rpm. By increasing the rotational rate of the upper disk, the granules start to push the bottom disk downward.

Real time data for the vertical displacement and the friction coefficient are recorded to study the lift phenomenon and the effect of the speed on the friction coefficient. To investigate the effect of the load on the friction coefficient and the displacement, the applied load was varied from 5.8 to 9.2 kPa. Also, the effect of the surface roughness was investigated by changing the upper or lower disk configuration from rough to smooth and vice versa.

9.3 Experimental Results

9.3.1 Series A: Both the Sliding and Stationary Disks Are Rough

Physically, shear stress is the applied force per unit area parallel to the plane required to produce deformation in a fluid. When applied to granular material, shear stress causes adjacent planes of granules to slip on one another. Normal stress is the stress acting perpendicular to the adjacent plane. The coefficient of friction is defined as shear stress divided by normal stress. In each set of experiments, the normal load is maintained at a specified value and shear is introduced by means of rotation of one of the disks.

The values of the friction coefficient for two different loads (6.5 kPa and 8.5 kPa) are shown in Figure 9.4. The experimental results were recorded every 20 seconds in each stage (i.e. speed range), and then data were saved and averaged for each speed. Also shown are curves fitted to the experimental data with 98% accuracy.

9.3.1.1 Effect of the Rotational Speed

The effect of the rotational speed on the friction coefficient is shown in Figure 9.4. The contact between the granules is governed by Coulomb law of friction, which imposes a limit on the ratio of the tangential force to the normal force at area of contact. When this limit is reached, a relative slip motion at the contact area is possible. When the shear stress is applied and the rotational speed is small (50 rpm and below), sliding starts gradually at a frictional force smaller than that generated during steady sliding (steady state friction). While the shear stress gradually increases, more and more contacts will reach the Coulomb threshold and slip occurs. Slip motion between the granules in contacts causes dynamical rearrangement~~s~~ and changes in the friction forces. With increasing shear, frictional strength increases and sliding stabilizes. The motion of the spherical granules becomes more stable when the slip at contacts accumulates over the time.

The effect of rotational speed on the vertical displacement is shown in Figure 9.5 along with the curve-fitted results. By increasing the speed of the top disk, the collision rate of the granules is enhanced and more momentum is passed on to the lower disk pushing it gradually downward, resulting in an increase in the displacement. The higher the speed, the greater the collision rate until it reaches a value where the agitation of the granules overcome completely the applied normal load and the lift between the top and bottom disks occurs.

The friction coefficient and displacement trends can be explained as follows: rolling is to some extent restrained in larger size granules, and thus translation of such granules must be contained by sliding and dilation. The friction level of spherical granules increases as granules follow an increase in their spatial arrangement by increasing the speed. The increase in the momentum transfer due to the spatial arrangement translates to an increase in displacement

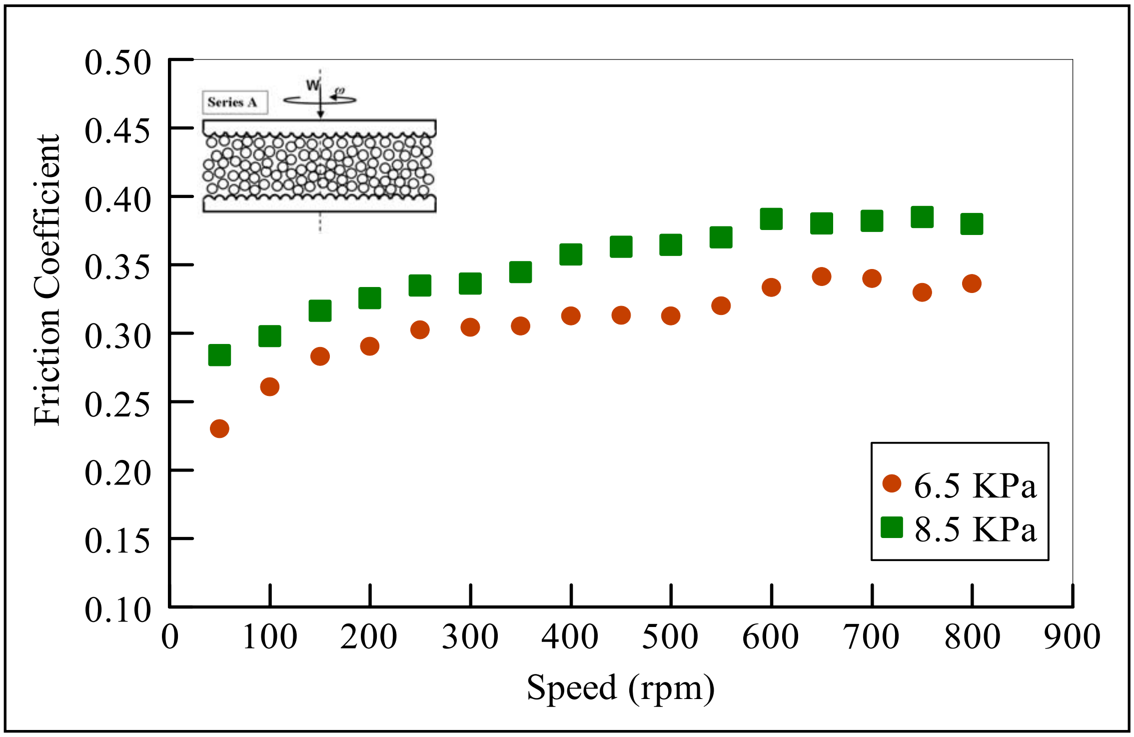

Figure 9.4 : Effect of the Rotational Speed on the Friction Coefficient (Series A: Both the Sliding and Stationary Disks are Rough)

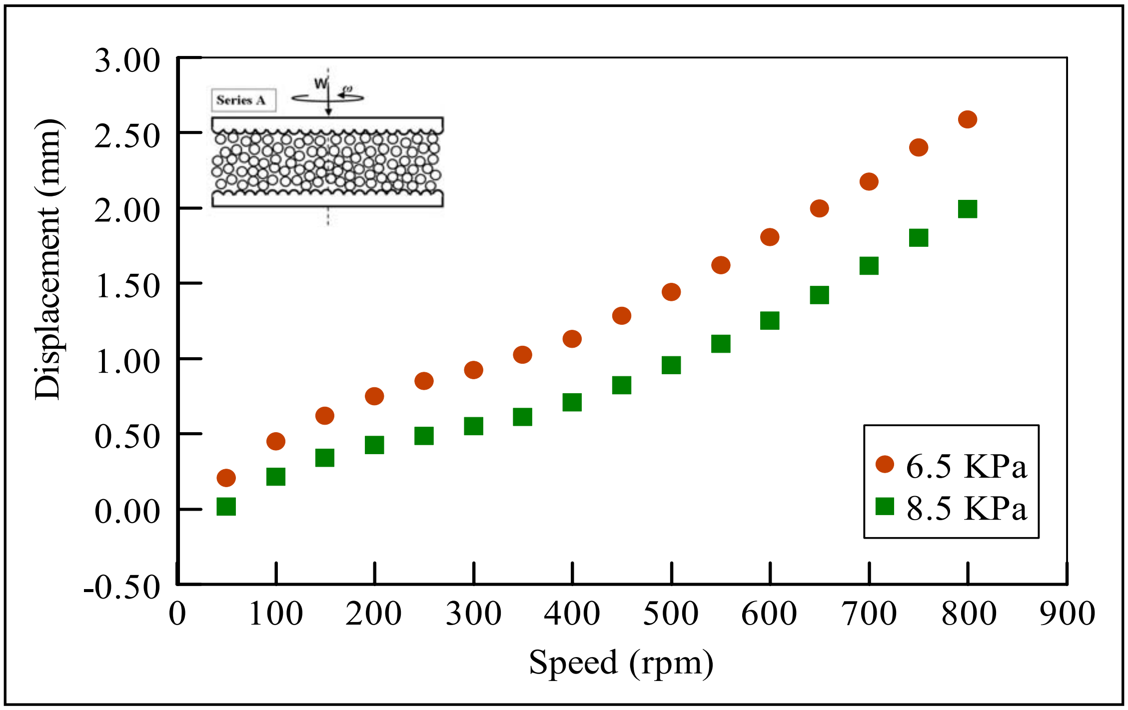

Figure 9.5 : Effect of the Rotational Speed on the Vertical Displacement (Series A: Both the Sliding and Stationary Disks are Rough)

between the granules. In other words, at low speed the layers of the spherical steel granules must dilate against the applied normal load to accommodate the shearing force. By increasing the speed, the proportion of rolling to sliding decreases leading to higher friction and larger displacement.

9.3.1.2 Effect of the Load

Sliding friction increases with increasing the applied load as shown in Figure 9.6. The friction levels that we report for spherical material approach the levels often observed in experiments and numerical simulations where idealized circular granules are modeled. These results agree qualitatively with several published papers (Yu et al. [23], Yu and Tichy [24], Hayakawa [45], Sawyer and Tichy [23], Frye and Marone [46], Mair *et al.* [47], Iordanoff *et al.* [34], Fillot et al. [38]).

Figure 9.7 presents the result of the displacement (lift) plotted as a function of load. At a given speed, the larger the applied load the lesser the displacement (lift) produced by the granules to push the lower disk downward due to the increase in the packing of the granules within the gap. The results of experiments provide the first quantifiable measure of the lift, providing clear evidence that granular material is capable of producing lift force when sheared between two parallel disks.

9.3.2 Series B: Rough Sliding Surface and Smooth Stationary Disk

In order to study the behavior of the granular material and the effect of the surface roughness on the friction coefficient and the displacement, several patterns of roughness need to be investigated. Previous results of “Series A” as shown in Figure 9.4 to Figure 9.7 presented the case when both disks were rough. Figure 9.8 and Figure 9.9 represent the case were the sliding surface is rough while the stationary disk is smooth and Figure 9.10 and Figure 9.11 represent the case where the sliding surface is smooth while the stationary disk is rough.

In Figure 9.8, when the moving disk is rough and the stationary disk is smooth, a slight decrease in the friction coefficient was noticed compared to the case when both disks were rough due to the fact that some of the layers in contact with the smooth surface do not experience similar shear forces like the other layers. This reduces the sliding and results in a slight reduction in the friction coefficient. Similarly when the stationary disk is smooth, the collision rate of the

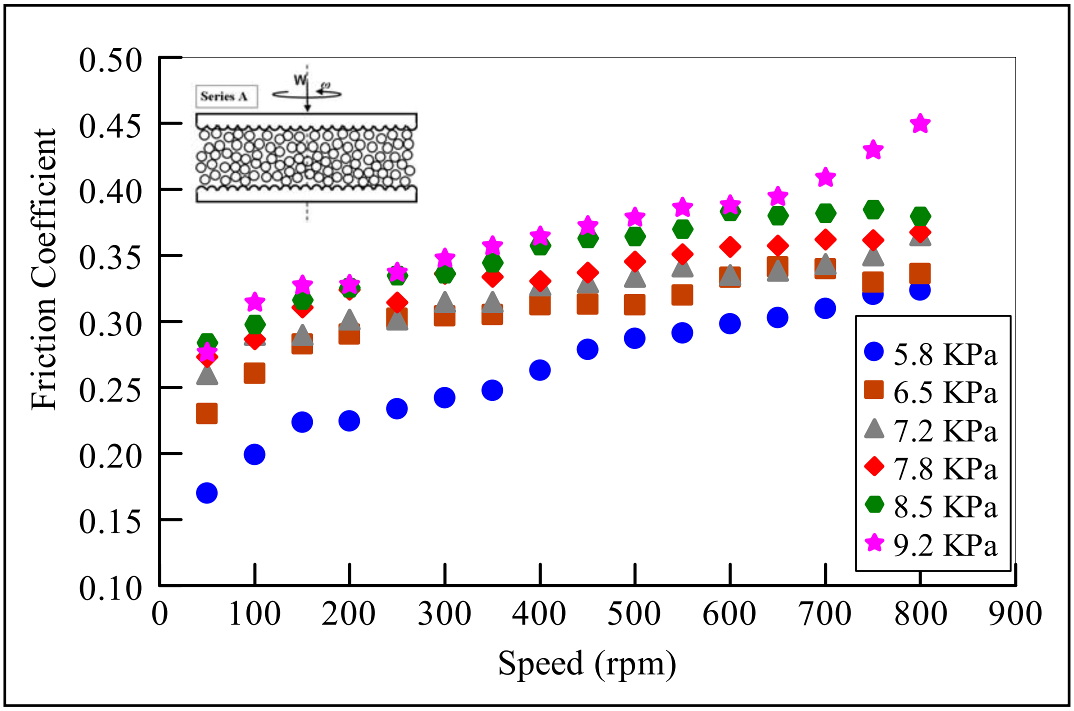

Figure 9.6 : Effect of the Normal Load on the Friction Coefficient (Series A: Both the Sliding and Stationary Disks are Rough)

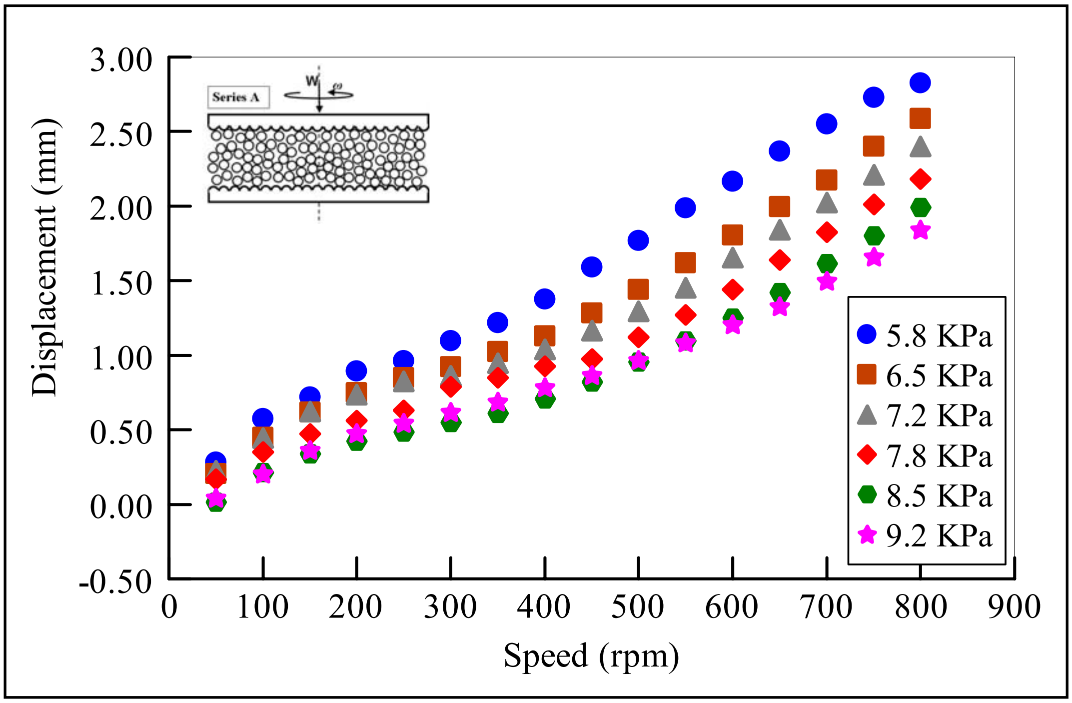

Figure 9.7 : Effect of the Normal Load on the Vertical Displacement (Series A: Both the Sliding and Stationary Disks are Rough)

granules is enhanced and the momentum is passed on to the lower disk gradually pushing it apart from the upper disk to create the lift as shown in Figure 9.9. Such a trend is similar to the case where both disks are rough (Series A), except that some variations in the displacement measurements are experienced especially for the two smallest loads (5.8 and 6.5 kPa). The smooth surface causes disrupted collisional rate where granules do not experience similar shear forces at low loads.

9.3.3 Series C: Smooth Sliding Surface and Rough Stationary Disk

Slip motion between the granules in contacts is the key factor that causes dynamical rearrangements and changes in the friction forces. When the granular coefficient of friction is large, the slip velocity at the boundary decreases and the viscous dissipation in the interior of the gap increases as reported by Zhou and Khonsari [30]. This increase in the viscous dissipation causes an increase in the slip motion between the granules in contacts. Therefore, there is more energy generated in the interior of the flow than there is at the boundaries which causes the granular dynamical rearrangements. When the roughness factor is large, the slip velocity at the boundaries is smaller and thus more energy is transferred to the flow which also causes the granular dynamical rearrangements.

Figure 9.10 shows the effect of the rotational speed and applied load on the friction coefficient. When the sliding disk is smooth, slip occurs between the sliding disk and the adjacent layer of granules which results in a decrease in the shear force and in turn a decrease in the frictional strength. At low speed, the smooth sliding disk starts to drag gradually some of the adjacent granules causing a slight increase in the friction coefficient. By increasing the speed, the smooth sliding disk loses its ability to drag the granules which leads to weakening the shear force, and in turn, reducing the friction. On the other hand, Figure 9.11 demonstrates the effect of the rotational speed and applied load on the displacement. At low speed, small collision rate is produced and some momentum is passed on to the lower disk, resulting in a very small displacement. But once the speed increases and the slip between the sliding surface and the adjacent layer increases, the shear force will decay and the momentum is no longer capable to separate the disks.

Figure 9.6 to Figure 9.11 illustrate the effect of the surface roughness on the friction coefficient and the displacement. Three different roughness series were used: In series “A”, both

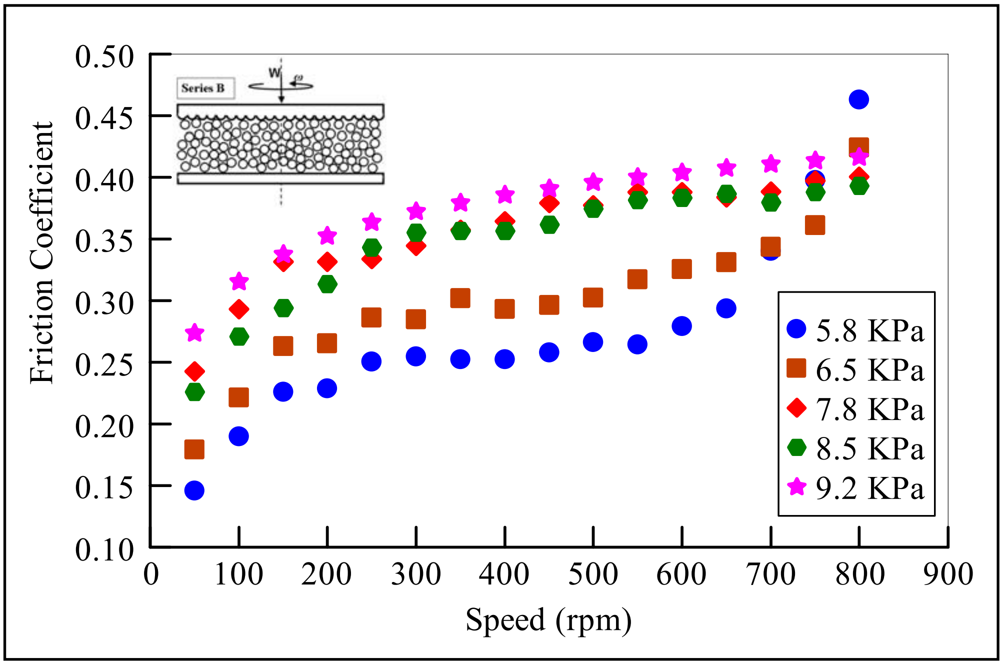

Figure 9.8 : Effect of the Normal Load on the Friction Coefficient (Series B: Rough Sliding Surface and Smooth Stationary Disk)

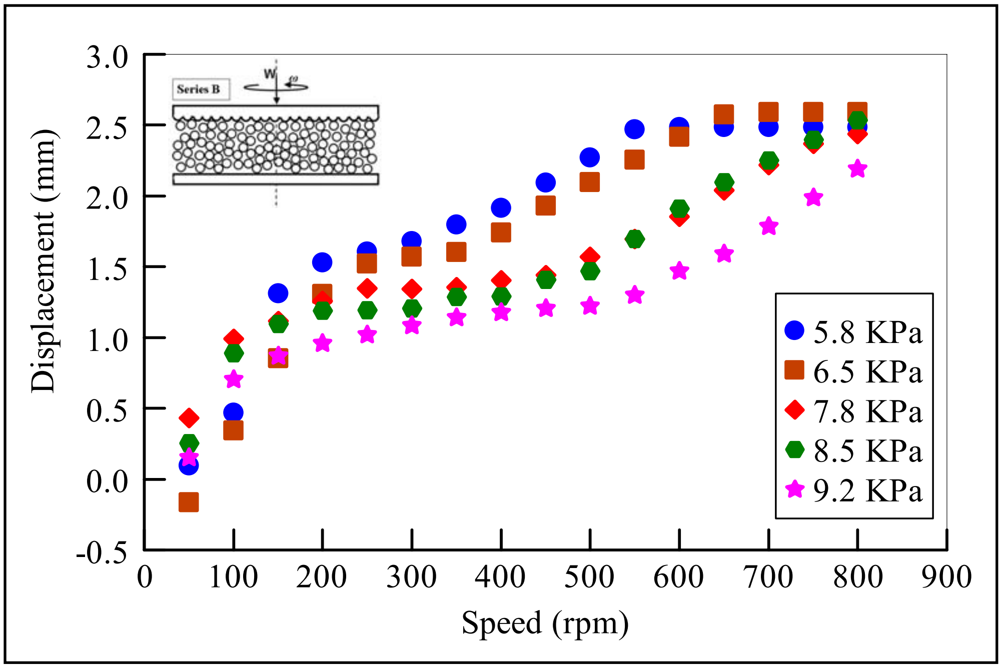

Figure 9.9 : Effect of the Normal Load on the Displacement (Series B: Rough Sliding Surface and Smooth Stationary Disk)

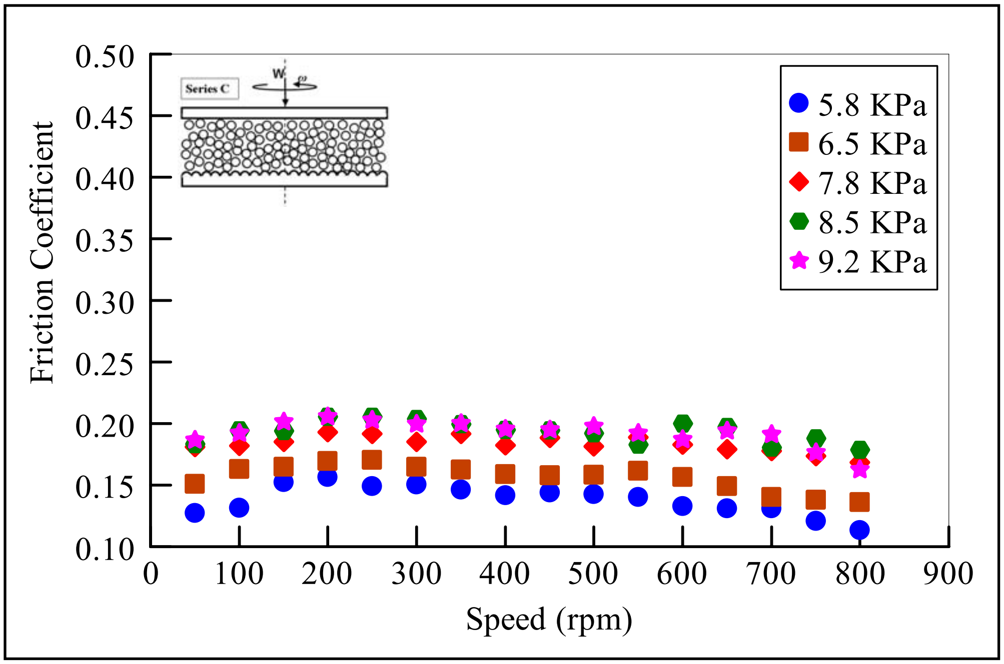

Figure 9.10 : Effect of the Normal Load on the Friction Coefficient (Series C: Smooth Sliding Surface and Rough Stationary Disk)

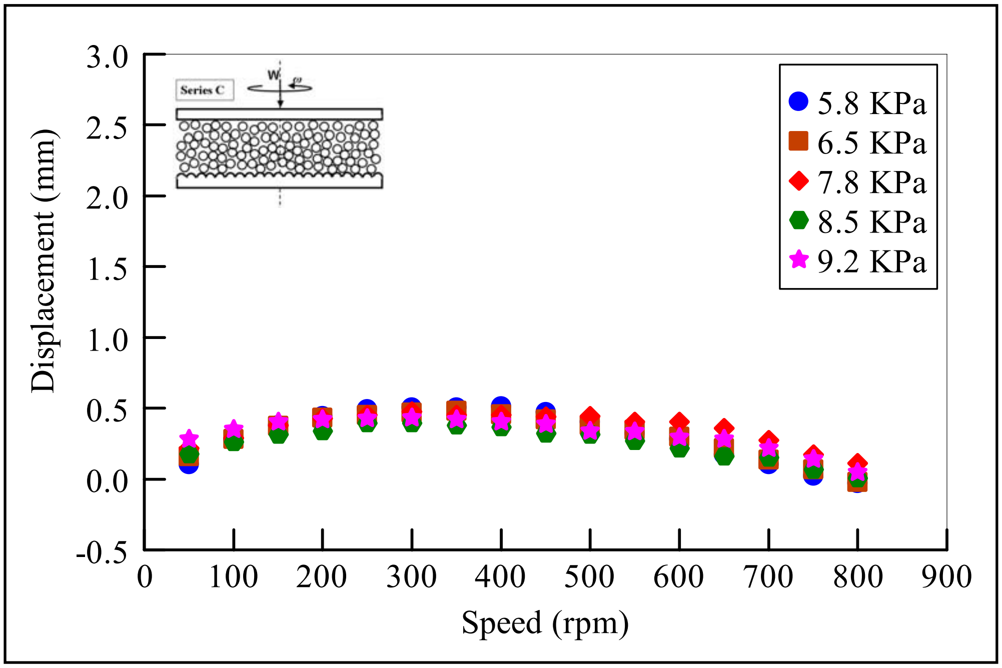

Figure 9.11 : Effect of the Normal Load on the Displacement (Series C: Smooth Sliding Surface and Rough Stationary Disk)

sliding and stationary disks were rough, in series “B”, the sliding disk was rough and the stationary was smooth, and in series “C”, the sliding disk was smooth whereas the stationary disk was rough. By looking to all three series, one can easily conclude the importance of having the sliding disk rough since series “C” failed to produce lift. The roughness effect on the friction coefficient and displacement in series “A” and “B” is very similar except some disturbed collisions in the later case. It is expected that series “A” were both surfaces are rough will create more lift than series “B” due to the continuous shearing effect while increasing the speed.

9.3.4 Series D: Rough Indents Sliding Surface and Smooth Stationary Disk

In the previous series “A, B, and C”, the surface roughnesses were manufactured by protrusions of the steel granules to the disk surfaces, whereas in this series “D”, the roughness was manufactured by indentations on the surface. A computer numerical control “CNC” machine was used to provide the indentations (surface roughness) for the sliding disk by drilling a 1.6 mm (sixteenth of an inch) holes on the surface of the disk as shown in Figure 9.12. This method is not typical since all surfaces are usually roughened by gluing granules on top of the surface. Experiments were conducted using the same granular material (stainless steel balls) to monitor the effect of the roughness method on the granular behavior.

Figure 9.12 : Upper Disk Roughness Using CNC Machine

The layer of granules facing the upper disk was protruded partially from the holes of the disk providing the roughness for the rest of the layers. The results shown in Figure 9.13 and Figure 9.14 provide evidence that the behavior of the granular material did not change. Four different loads were exploited and similar trends were obtained for the friction coefficient and the displacement comparing to “Series B” in Figure 9.8 and Figure 9.9 (similar configuration).

One can conclude that the order of magnitude was reduced by half using this method which proves it was not effective to produce greater displacement (lift).

9.4 Theoretical Analysis

The theory presented in this chapter is based on the hypothesis of binary collision (kinetic theory). Following the work of Johnson and Jackson [15] and utilizing the constitutive equations developed by Lun *et al.* [8], the dimensionless governing equations where the conservation of momentum is directly coupled with the pseudo energy equation along with the boundary conditions [equations (8-4) to (8-11)] are presented in this chapter as derived and summarized in the Chapter 8 (Johnson and Jackson [15], Lun *et al.* [8], McKeague and Khonsari [26], Zhou and Khonsari [30], Jang and Khonsari [40]). The schematic model of the granular lubricated system is shown in Figure 8.1.

9.5 Theoretical Results

Figure 9.15 shows the velocity, pseudo temperature, and solid fraction distribution for stainless steel granular material. The granule has a diameter of 3 mm and a density of $\rho_p = 7850\,kg/m^3$. The bottom disk is stationary, the velocity of the top disk is $U = 3\,m/\sec$, and the thickness of the gap is equivalent to 7 – 9 granular diameters. The normal load used is 8.5 kPa, and the surface roughness of both moving and stationary disks is chosen to be $\phi_o = \phi_H = 0.95$ (very rough). The coefficient of restitution between the granules is $e_p = 0.9$, and between the wall and the granules is $e_w = 0.8$.

For a liquid lubricated system, the assumption of no slip velocity at the boundaries generally holds. However, when granular material is used, the theory deemed a slip velocity at both boundaries. There are two energy sources which arise in the formulation of the granular temperature. One comes from the slip velocity at the boundary and the other is the viscous dissipation in the interior of the flow. Granular slippage is one of the important characteristics of granular lubrication. During shearing, it provides energy from the boundaries into the granules contained within the gap. When e_p is large, the slip velocity at the boundary decreases and the viscous dissipation in the interior flow increases. Therefore, there is more energy generated in the interior flow than at the boundaries by the slip velocity mechanism. Hence, the boundaries receive more heat from the interior flow. For more details, see Zhou and Khonsari [30].

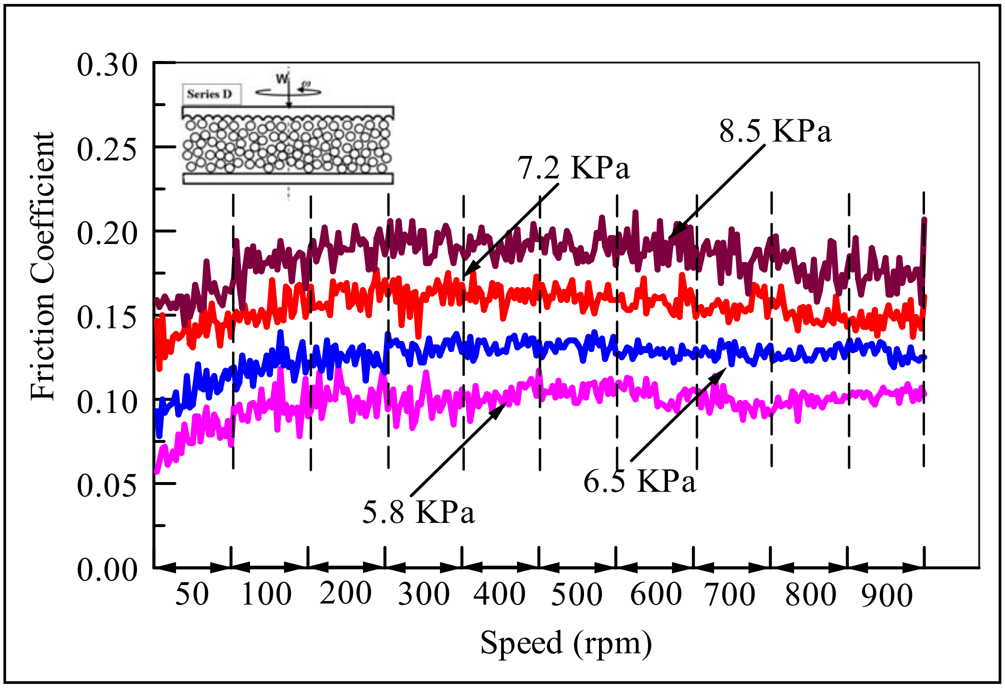

Figure 9.13 : Effect of the Normal Load and Rotational Speed on the Friction Coefficient (Series D: Rough Indents Sliding Surface and Smooth Stationary Disk)

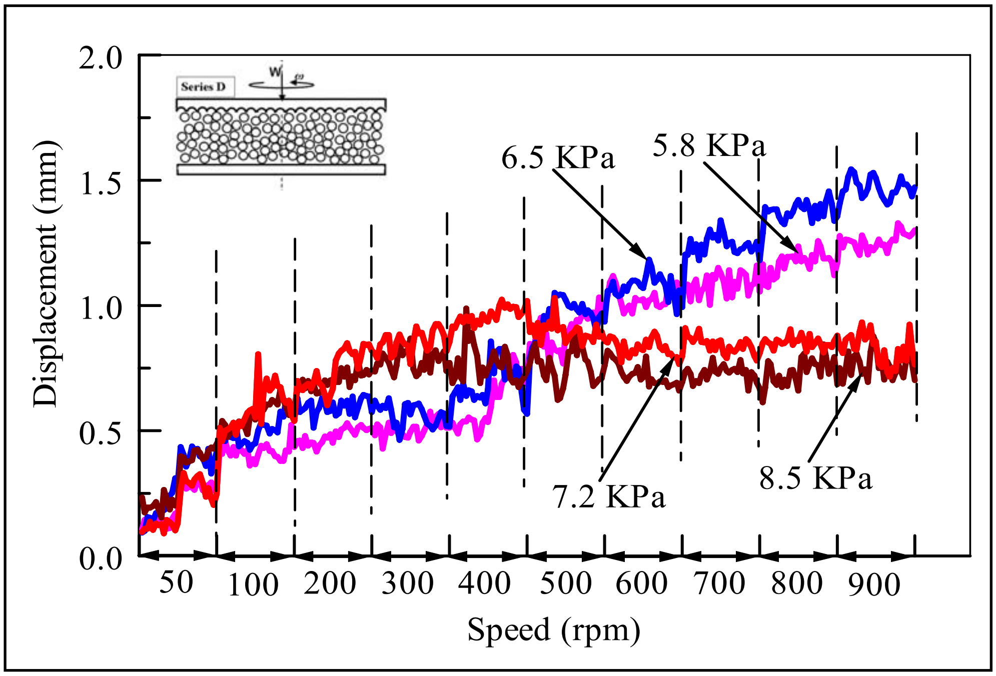

Figure 9.14 : Effect of the Normal Load and Rotational Speed on the Displacement (Series D: Rough Indents Sliding Surface and Smooth Stationary Disk)

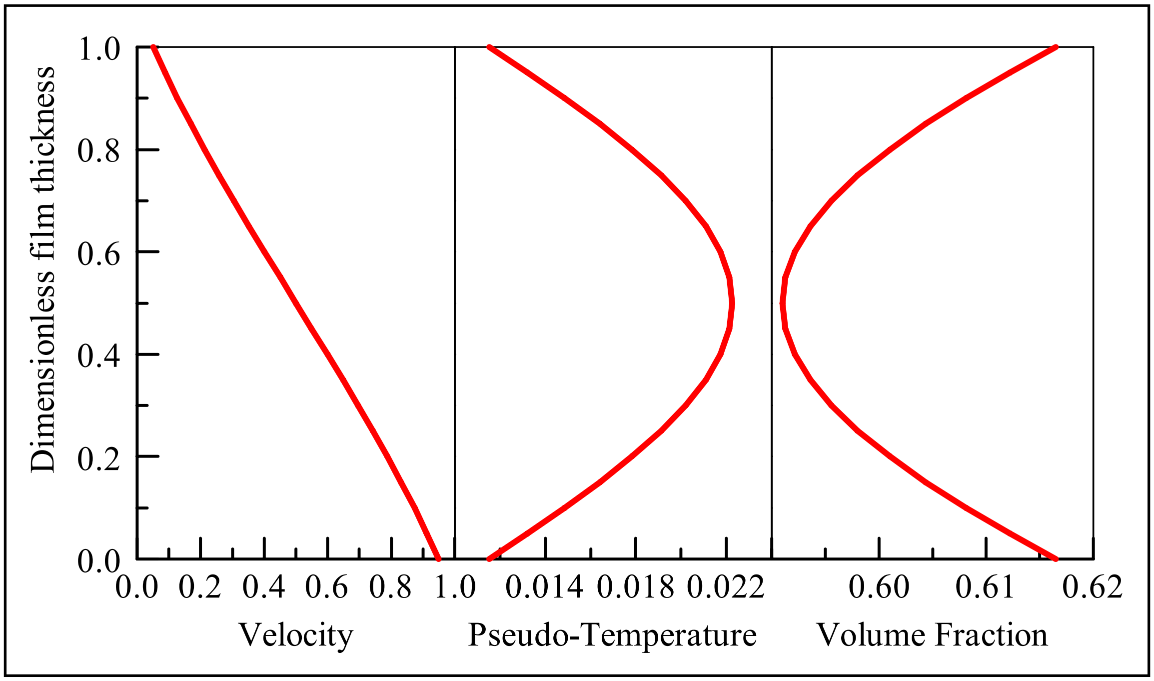

Figure 9.15 : Velocity, Temperature, and Solid Fraction Distribution for Granular Material Sheared Between Two Parallel Plates (In Dimensionless Form)

The solid fraction trend is directly related to the granular temperature. When there is more pseudo energy generated in the interior of the flow, granules surrounding the interior of the flow have much greater fluctuation velocity than those near the boundaries. Hence, the granular distribution becomes less dense in the interior of the flow and much more granules accumulate at the boundaries. According to the above analysis with large e_p, the solid volume fraction near the boundaries is larger than that at the center of the channel. Under this condition of low shear stress and high normal stress, it is clear that granular materials are likely to conglomerate at the boundaries. The results are in good agreement to those obtained by Zhou and Khonsari [30] which is based on Johnson and Jackson's formulation, and McKeague and Khonsari [26] based on Haff's theory.

9.6 Comparison of Theory and Experiment

The analysis presented in this section is used for comparison purposes with experimental results. The overall comparison is shown in Figure 9.16 to Figure 9.20. Shear stresses are compared as a function of the normal stress and the nominal shear rate as well as normal stress as a function with the shear rate. The maximum volume fraction was approximated to be 0.6 knowing the weight of the granules, the particle density, the shearing area and the gap height. The coefficient of restitution between the granules was chosen to be 0.9 based on several researchers (Kudrolli *et al.* [48]) where they conducted experiments to calculate the coefficient of restitution. They used 3.2 mm diameter stainless steel granules rolling on a Delrin surface that was machined and polished to a uniformity of 0.001 cm, and found the coefficient of restitution for the steel granules to be 0.93 with 2% variation. Since the best experimental results for the purpose of comparison with the theory were obtained from the case when both disks were rough, the roughness factor used in the simulations was set to be 0.95 for both disks (i.e. very rough surfaces).The mass flow rate was calculated from the experiments shear cell dimensions using the equation below as a function of speed and specified in the simulations putting into consideration the width factor considering the infinitely wide approximation.

$$\dot{m} = \int_0^H \int_{r_i}^{r_o} \rho u.dr.dy = \int_0^H \int_{r_i}^{r_o} \rho_p \upsilon u.dr.dy$$

Figure 9.16 plots the friction coefficient as a function of the rotational speed of the moving disk. The simulation data show uniform values for the friction coefficient, while the experimental data showed a slight increase by increasing the speed until it levels off over a period of time. The reason for this trend is likely due to change of the granule rolling and sliding proportions as explained in Figure 9.4. Slip motion is another reason where the spherical granules reach stability when the slip at contacts gets accumulated over the time. In simulations there are no gradual changes but the values of the friction coefficient were within the same range. The trends of the theoretical simulation results are in quantitative agreement with the experimental results. From the series of experiments conducted, investigations showed successfully the lift phenomenon for two parallel plate's configuration.

Additionally, Figure 9.17 illustrates the increase in the gap height by increasing the speed at any load measured. The trends showed similarities at low speed. By increasing the speed, a slight deviation was observed between theoretical simulation results and experimental results. The main reason for this trend is due to the slip velocity. At low speed, the effect of the slip velocity is small. At higher speeds, granules loose more energy through the experimental setup more than the simulation due to the infinitely wide approximation of the latter. The energy lost directly affects the granules collision which in turn reduces slightly the increase in gap height.

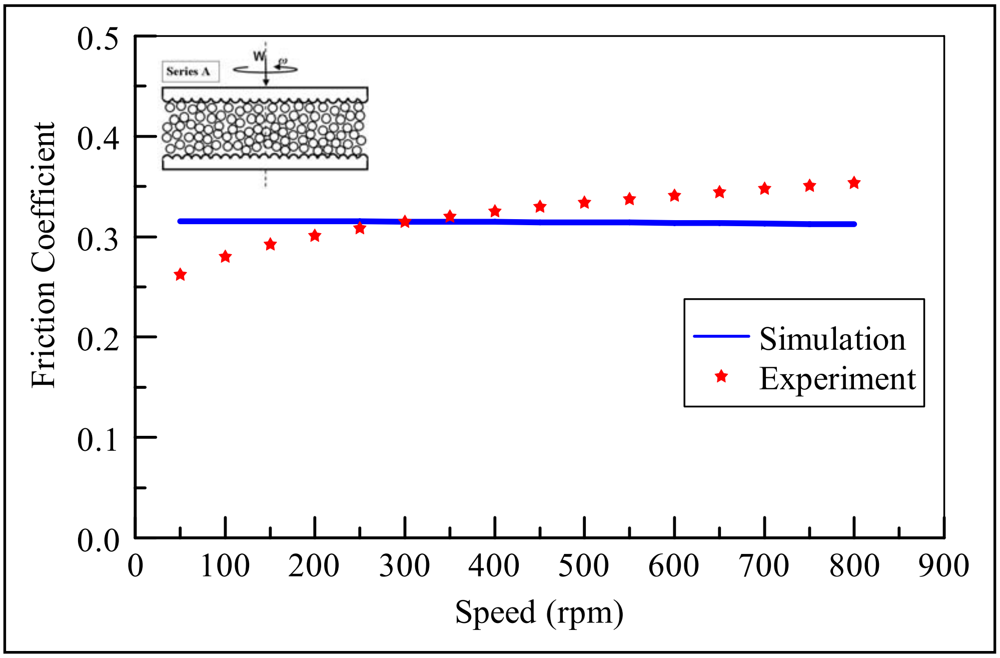

Figure 9.16 : Variation of the Friction Coefficient with Speed at 7.8 kPa (Series A: Rough Sliding Surface and Rough Stationary Disk)

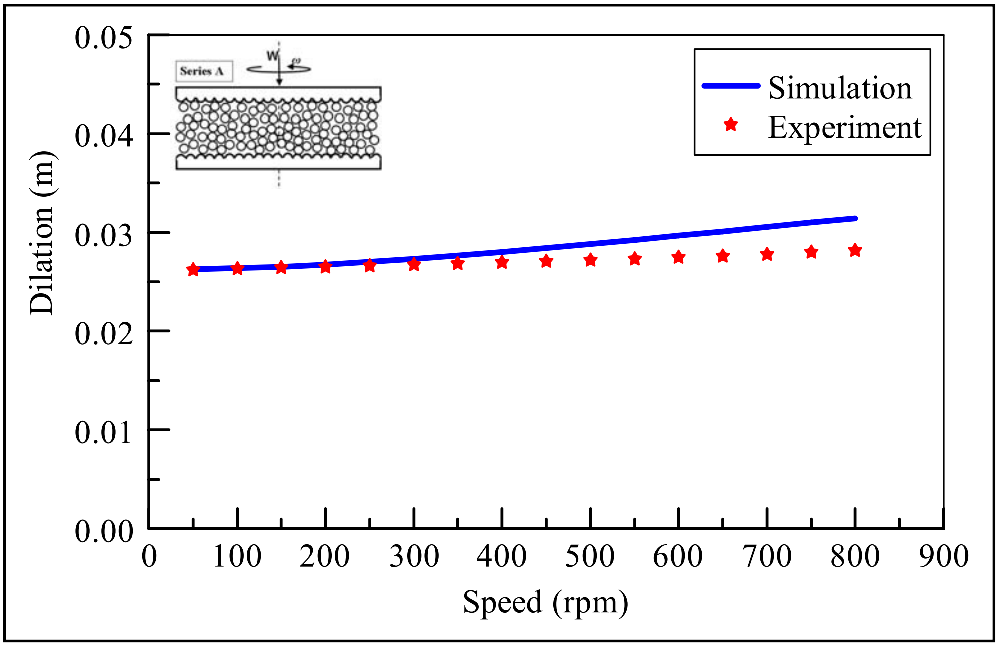

Figure 9.17 : Variation in the Gap Dilation with Speed at 7.8 kPa (Series A: Rough Sliding Surface and Rough Stationary Disk)

The effect of the load on the gap height increase (dilation) was investigated and demonstrated in Figure 9.18 relating the theory to the experiments. Load varied from 6.5 to 9.2 kPa and the speed ranged from 50 to 800 rpm. It was shown that increasing the load applied decreases the ability of granules to expand which results a decrease in their dilation. These results showed that the trends between theory and experiment are similar and the increase in height was within the same order of magnitude.

Figure 9.19 shows the variations of the shear stress and the normal stress with the shear rate. The shear stress increases linearly by increasing the shear rate. Similarly, the normal stress shows direct dependence on the shear rate as well. It is clear that both the shear stress and normal stress depend linearly on the shear rate. Same trend prevails with Figure 9.20 where the shear stress shows the dependence on the normal stress. Shear stress also depends on the granules size and the surface roughness. These trends are similar to those presented by Craig *et al.* [19, 49] and Yu and Tichy [24].

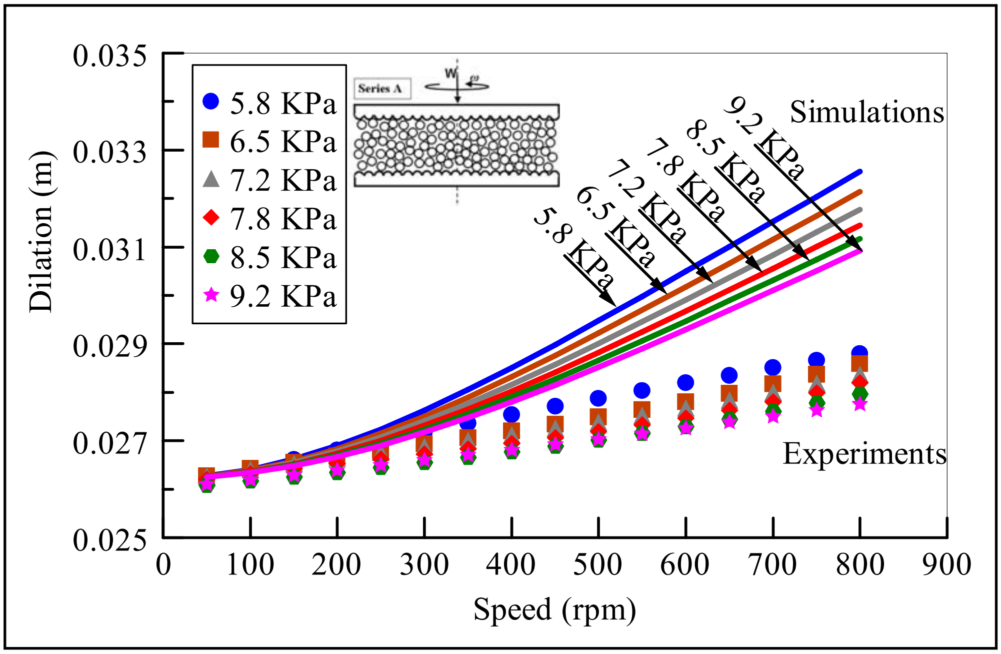

Figure 9.18 : Effect of the Normal Load on the Variation in the Gap Dilation (Series A: Rough Sliding Surface and Rough Stationary Disk)

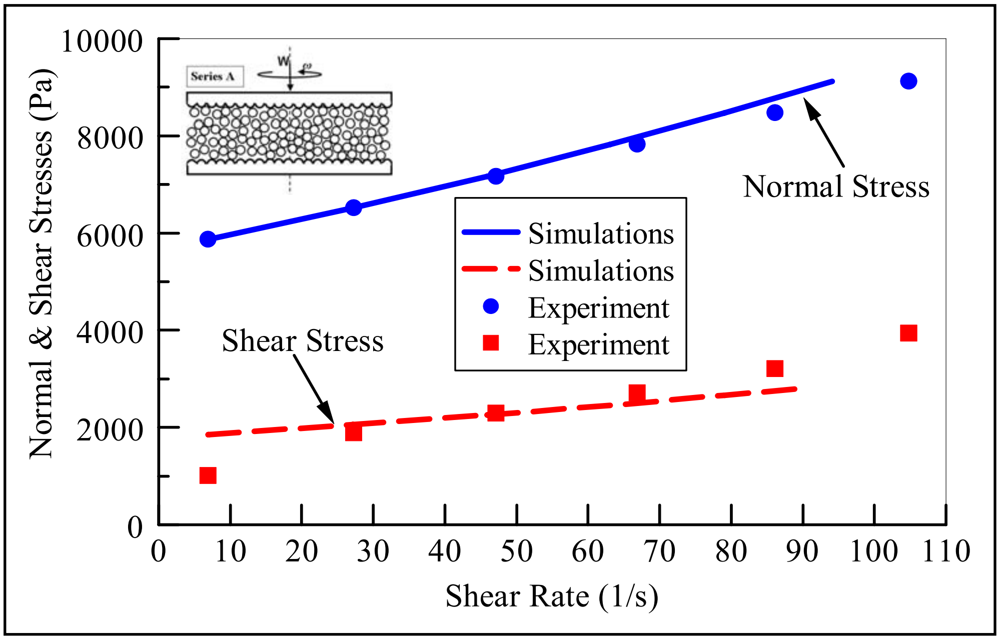

Figure 9.19 : Variation of the Shear Stress and Normal Stress with the Shear Rate (Series A: Rough Sliding Surface and Rough Stationary Disk)

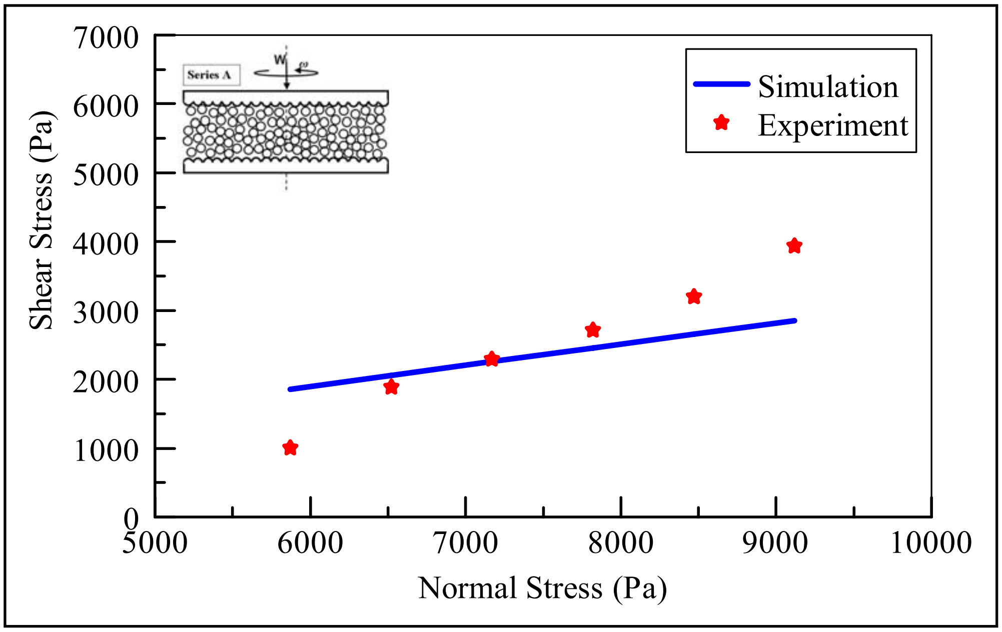

Figure 9.20 : Variation of the Shear Stress with the Normal Stress (Series A: Rough Sliding Surface and Rough Stationary Disk)

9.7 Conclusions

Experiments were conducted using 3-mm stainless steel balls to demonstrate the lift phenomenon observed in an annular shear cell apparatus. The effects of the friction coefficient and the surface roughness have been expressed as a function of the rotational speed and the applied load. Simulations of the kinetic theory for the granular material were performed and compared with the experimental results. The agreement between the theory and the experiment is illustrated. Furthermore, no adjustments for the friction coefficients or displacements were made to obtain a better fit.

The following conclusions can be drawn from the experimental and theoretical results:

- The frictional force that can be generated within a sheared granular material is critical to understanding its strength but has significant applications in geophysics and technology.
- When shear stress is applied, sliding starts gradually at a frictional force smaller than the frictional force generated during steady sliding, but by increasing the shear, the frictional strength increases and sliding stabilizes.
- At low speed spherical granules accommodate strain preferentially by rolling, then by increasing the speed, the proportion of rolling to sliding decreases leading to higher friction.
- By increasing the speed of the rotating disk, the collision rate of the granules is enhanced and more momentum is passed on to the lower disk to ensure complete lift between the top and bottom surfaces and then reach a steady state.
- In the kinetic regime, sliding friction increases with increasing the applied load.
- The presented set of experiments provides an evidence of the phenomenon of the lift force between two parallel plates lubricated with granular material.
- The larger the applied load the lesser the lift produced due to the increase of compactness of the granules within the gap.
- Importance of the surface roughness is demonstrated especially the moving surface to help drag the granules and initiate shear force.
- When the moving surface was rough and the stationary disk is smooth, similar trends were obtained from the case when both surfaces were rough. A slight decrease in the

friction coefficient is noticed. It is due to the fact that the layer in contact with the smooth surface does not experience similar shear forces.

- When the moving disk is smooth, it resulted a failure of producing enough shear force and no longer were the granules capable of creating adequate lift to separate the disks.

CHAPTER 10. EXPERIMENTAL INVESTIGATION ON THE STICK-SLIP PHENOMENON IN GRANULAR COLLISION LUBRICATION

10.1 Introduction

While the archival literature contains a great deal of research on granular lubrication, a number of important issues remain largely unexplored. Of particular interest in this chapter is to examine the stick-slip phenomenon associated with granular materials within the context of lubrication. In what follows, we begin by providing a pertinent background for the stick-slip research.

Stick-slip behavior in granular materials is of vital importance in understanding the dynamics of solid on solid friction [50, 51], avalanches [52], and earthquake dynamics [53]. The mechanism of the stick-slip behavior of the granular layer was also addressed by Hayakawa [45] who introduced a global order parameter (OP) which characterized the phase state of the layer. Similar stick-slip oscillations have been observed by Albert *et al.* [54] in cases when an object is moving through granular medium.

The applied external stress results in the development of an internal structure resisting the stress called jammed state. In a jammed state, forces do not propagate uniformly through the granular sample but are localized along directional force chains. They found that successive formation and collapse of jammed states resulted in fluctuations that are typically observed in systems that exhibit stick-slip. These fluctuations were periodic when grain size was small, but became steeped (i.e., non-periodic) when larger grains were used.

Granular flows exhibit a variety of phenomena that have both fluid and solid aspects [55, 56] and have captured the attention of scientists from different disciplines. Given the recent interest in the tribology of powders, it is surprising that there have been limited studies relevant to investigation of the stick-slip phenomenon in granular lubrication. In this chapter, we focus our attention on the influence of the stick-slip of the granular material sheared between two parallel disks. A series of experiments were carried out using ceramic granules to investigate the influence of the rotational speed on the displacement (lift) and the friction coefficient.

10.2 Background

In the mid 1950's, Rabinowicz's research on the origin of wear led him to lay the foundation of stick-slip in materials [57]. Burridge & Knopoff [58] established one of the first models linking stick-slip with faulting. Byerlee & Brace [59] and Byerlee [60] were the first to perform laboratory experiments that showed occurrence of stick-slip in geological materials like granite materials. They proposed that stick-slip instabilities in laboratory friction experiments might be similar to earthquakes. Additionally, they found that stick-slip was periodic in time but their experiment demonstrated a speed weakening, which could not be explained by a simple variation of the friction coefficient.

Following these findings, Dieterich [61] and Ruina [62] proposed a new theory which uses an internal state parameter, called contact ageing, and a velocity-dependent friction law. These state parameter laws have been reviewed by Persson [63] in a review of friction that includes consideration of microscopic physics, and have been also reviewed and confirmed in a book by Scholz [64]. According to Persson [63] and Meyer *et al.* [65], understanding the nature of sliding friction is essential for nearly all practical problems with engineering applications. For example, low friction without disturbance (stick-slip) is a necessary feature for the successful operation in applications like information storage and micro-electro mechanical systems.

In the late 1980's and early 1990's, it became necessary to develop a better understanding of the friction acting between the slipping surfaces in order to design reliable machinery. The experimental results presented by several researchers [66-68] have provided insight into the nature of friction and lubrication involving slip. Using a surface force apparatus (SFA), they observed that the granular films could support a finite shear stress and exhibit either stick-slip dynamics or steady sliding depending on a variety of experimental parameters including the spring stiffness (k) and the pulling speed (V).

By mid 1990's, the physicists tried to explain the stick-slip phenomenon from a different angle. Heslot *et al.* [69] and Nasuno *et al.* [70] exposed granular media to shearing and observed jerks during the movement. They introduced dilation as a new variable that played a major role on the friction strengthening, where the static friction coefficient increases with the time of static contact but only in the presence of an imposed shear stress. The stick-slip observed in these experiments was periodic similar to what was observed by Byerlee [60]. They found that the stick-slip mechanism was correlated with Hopf bifurcation [71, 72], and is now well accepted by geo-physicists. Recent studies of Gayvallet & Geminard [73] showed that stick-slip is associated with the dilation effect and attributed the ageing effect (stick-slip state) to corrosion and to surface chemical reaction.

To explore the nature of the transitions between stick-slip and steady sliding, Batista & Carlson [71] investigated the bifurcations from steady sliding to stick-slip in models of boundary lubrication type. The models used are based on the rate and state approach that characterizes the behavior of dry interfaces [62]. They found that for large values of (*k*) and (*V*), both models exhibited only steady sliding solutions, characterized by constant spring force. Conversely, when (*k*) and (*V*) are decreased adequately, there is a transition to a series of stick-slip pulses. Batista & Carlson [71] concluded that the transition from steady sliding to stick-slip is typically irregular and sometimes hysteretic. When hysteresis is observed, it is associated with a sub-critical Hopf-bifurcation. In either case, they observed a sudden and discontinuous start in the amplitude of oscillations at the bifurcation point.

Radjai *et al.* [74] found that axial compression of granular matter exhibit smooth mechanical responses, independent of the deformation rate. However, Nasuno *et al.* [70] showed that there are situations where the response was not smooth but exhibited stick-slip behavior. They found that stick-slip was not periodic and did not depend on the strain rate history. Furthermore, Nasuno *et al.* [75] studied the motion of a heavy plate pushed above a thin granular layer with a soft spring with a constant velocity of the pulling point. A general trend is that the samples with stick-slip exhibited both smoothening and weakening when the rate of deformation is increased. They concluded that at large pulling speed, the plate moves with a constant velocity, whereas at smaller speeds the motion of the plate is irregular: long periods of sticks are followed by short slip events. Research by Howell *et al.* [76] revealed that for a given rate of deformation, the larger the sample, the less scattered the instabilities. For dry granular material, it was concluded that stick-slip behavior can be either periodic or non-periodic.

Adjémian & Evesque [77] conducted experiments to study the stick-slip behavior with glass beads and Hostun sand. They found that the mechanics of the deformation was stable and concluded that the strain rate plays a vital role in the amplitudes of the stick-slip. When the strain rate is very fast, the stick-slip does not have enough time to develop completely. Furthermore, they concluded that stick-slip disappears in relatively large specimens (i.e., large H/D, where H is the gap height and D is the granular diameter). Alshibli & Roussel [78] pointed out the importance of understanding the behavior of the stick-slip phenomenon for geological processes. They performed a series of axisymmetric triaxial experiments on glass beads to investigate the factors influencing stick-slip behavior. They observed continuous volume increase (dilation) even at relatively high strains resulting from the uniform shape of the spherical particles used. They found also that the load oscillations that appeared in small size beads are due to the stick-slip phenomenon.

10.3 Experiment

10.3.1 The Apparatus

The test rig used is an automated tribometer controlled and monitored by a computer as illustrated in Figure 10.1. The experimental apparatus presented in this chapter has been described in details in Chapter 9 and by Elkholy & Khonsari [79] where 3-mm stainless steel balls were used. A brief description of the test rig is as follows. The apparatus is equipped with a computerized data acquisition system, which records real-time values of friction coefficient, wear/displacement, and speed. The load on the testing component is applied from the loading mechanism located in the bottom section of the apparatus. This tribometer measures friction and displacement to 0.635 μm (25 μin) giving an accurate assessment of displacement and friction as a function of time. To measure the coefficient of friction, the top vertical shaft is rotating but restricted from the motion in the vertical direction while the bottom holder is restrained from rotation also senses the frictional torque applied by the granular medium, using a force load cell. The vertical displacement and the friction coefficient values are recorded every 20 seconds.

The shear cell as shown in Figure 10.2 consists of two concentric steel disks. The upper disk is mounted on a rotating vertical shaft but restricted from the motion in the vertical direction. The bottom disk is restricted from rotation, but can move in the vertical direction. The top disk has an annular protrusion that fits into the channel of the bottom disk. This annular protrusion does not contact the side walls of the bottom disk channel. The clearance between these two surfaces is ~100 microns, to prevent granular material jamming or overflow. The bottom disk is free to move vertically, so as to allow for the expansion of the sheared granular material. The bottom disk is attached to a vertical shaft with a sensor on its other end to measure the vertical displacement and friction coefficient as a function of time and rotational speed of the top disk.

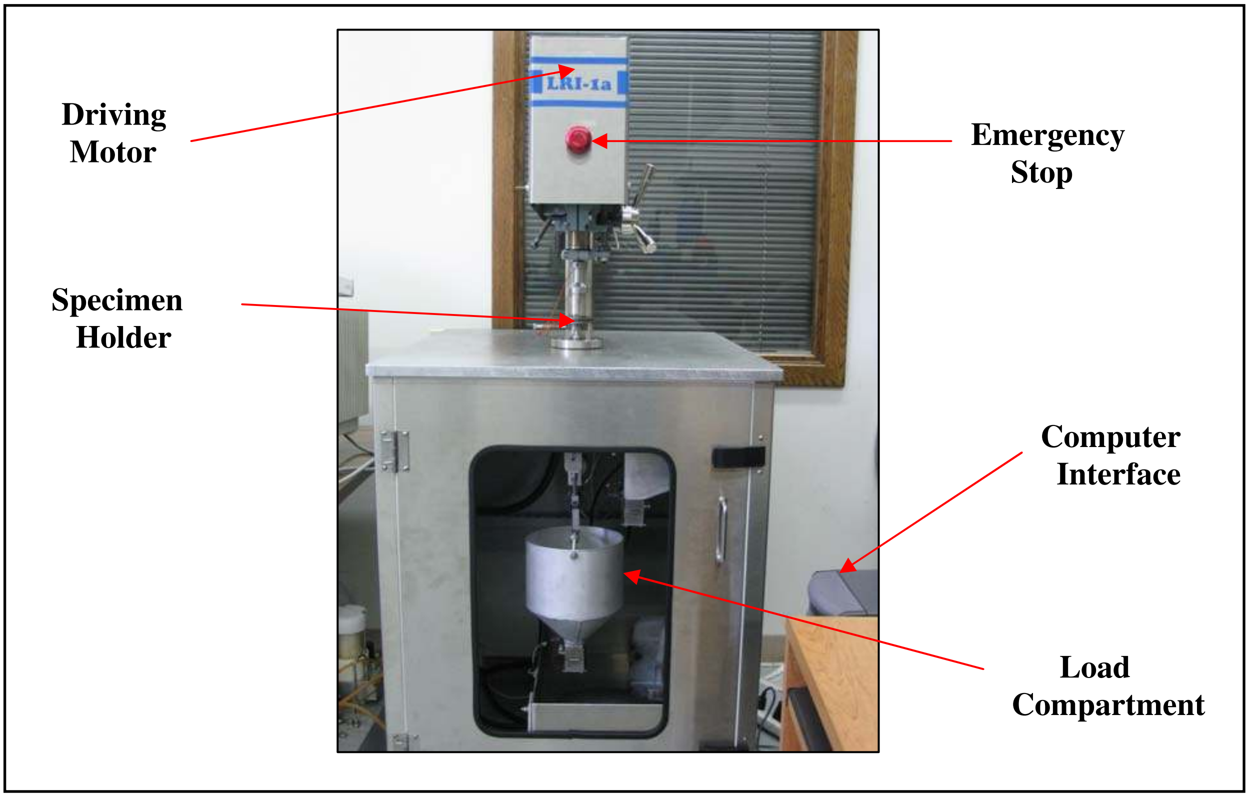

Figure 10.1 : Experimental Apparatus

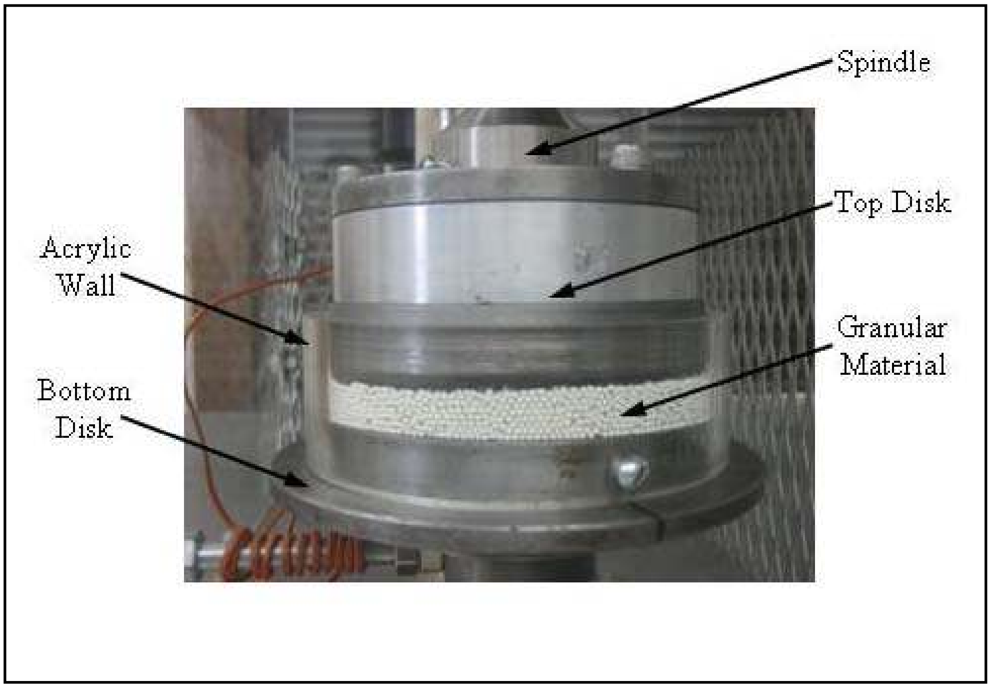

Figure 10.2 : Shear Cell Assembly

10.3.2 Experimental Procedures

The gap in the annular shear cell is divided into three regions. The first region is the layer of granules adjacent to the upper moving disk; the second region is the layer of locked granules adjacent to the stationary lower disk, and an intermediate layer between those two regions (interior flow). A total of 12 experiments were conducted to investigate the stick-slip phenomenon in a parallel plate configuration using ceramic granular material with six different applied loads. A summary of the cell dimensions and the granular material properties is shown in Table 10.1.

Surface roughness plays an important role on the performance of granular materials. Upon coming into contact with a smooth surface, the granule-wall collisions are very small and granule slip at the wall is relatively large. In the contrast, when interacting with rough surfaces, the granules slippage at the wall is small and granule-wall collisions will provide a major transport of lateral momentum to the wall. To provide this roughness in the experiments, the disk surfaces are constructed by attaching a series of adjacent granules along the length of each surface to help drive the granules of the interior flow.

Experiments are conducted where both the stationary and sliding disks are rough. The following procedure is used in creating the desired surface roughness. Stainless steel wire mesh is used with the proper mesh size. The wire mesh is first glued to the surface, and then some ceramic granules enough to cover this surface are glued to it as shown in Figure 10.3 using high-impact high-strength epoxy. The wire mesh along with the high-strength epoxy provided a very high shear strength and very high torque resistance to the granules glued to it**.**

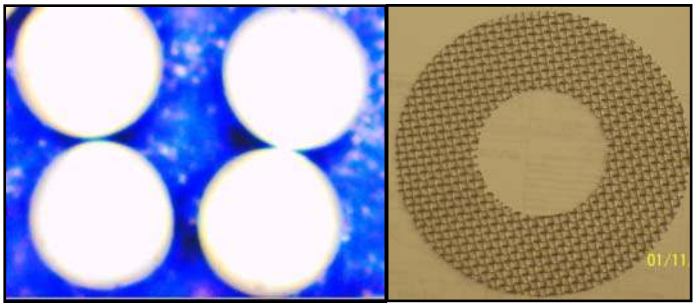

Figure 10.3 : Granular Material & Surface Roughness

Table 10.1 : Shear Cell Dimensions and Granular Material Properties

Channel Width	31.4 mm
Channel Depth	45.8 mm
Mean Radius (R_{mean})	34.7 mm
Shearing Area $\left(A_{Shear} = \pi\left(r_o^2 - r_i^2\right)\right)$	6846 mm^2
Mean Length $(L_{mean} = 2\pi R_{mean})$	218.24 mm
Gap Height (H)	9.8 – 12.6 mm
Granular Material Name	Zirconium Silicate (QBZ-58A)
Composition	ZrO2 – 58 % + SiO2 – 37 %
Hardness	800 Vickers
Sphere Count	95 %
Average Crush Strength	> 133,000 PSI
Granule Diameter (d)	1.4 mm
H/d	7 – 9
Particle Density	4000 kg/m^3
Rotational Speed	5 – 950 rpm
Linear Speed $(U = 2\pi R_{mean} N / 60)$	0.02 – 3.5 m/sec

Experiments are divided into two series in order to detect the region where stick-slip took place. They are: relatively high speed tests where the speed ranged from 150 to 950 rpm at an increment of 50 rpm, and low speed tests from 5 to 100 rpm with a 5 rpm increment. It is necessary to have a small increment in the low-speed tests since stick-slip typically occurs at low speed. The testing procedure is as follows. First, a specified mass of granules is placed in the lower channel of the shear cell. The upper disk is then lowered until it just touches the granules, thereby packing them in place. A specified normal load is then applied to the granules through the bottom surface causing them to be compressed. Corresponding counter weight is specified to compensate the weight of the bottom disk and the specified mass of granules. The top disk is then given the rotational motion causing the granules to move and exchange places at low speeds. At higher speeds the granules start to collide and tend to push the bottom disk downward, creating a lift.

With a specified normal load, the drive motor is set to rotate the upper disk slowly for a few seconds first to make sure that the granules are well distributed and initially compacted in the channel. The motor is then stopped to adjust the positioning of the upper disk if needed. To start each experiment, the driving motor is set to rotate the upper disk again by increasing the rotational speed from 5 to 100 rpm in a step-wise fashion every 2 minutes ranging an increment of 5 rpm for the slow-speed tests and an increment of 50 rpm for the relatively high-speed range of 150 to 950 rpm. Data for the vertical displacement and the friction coefficient are recorded to analyze the fluctuations for every load during each speed range. To investigate the effect of the load on the stick-slip phenomenon, the applied load is varied from 5.8 to 9.2 kPa.

10.4 Experimental Results

Generally the stick-slip phenomenon occurs in the granular material when the granules begin to exhibit both rolling and sliding, and its behavior is usually detected during shearing. The shear resistance between two granules is the force that must be applied to cause a relative sliding and rotation between the granules. The experimental work discussed was performed by shearing uniform spherical ceramic granules with known size (1.4 mm). Different sources contribute to the frictional resistance which is represented by the coefficient of friction and in turn contribute to the friction force, such as rolling and sliding of the granular material, granule interlocking/resistance to dilatancy. Dense granular materials have exhibit an increase in volume (dilatancy) when they are sheared.

10.4.1 Friction Pattern

In the experiments, the normal load applied is not necessarily uniform on each granule because of the scattered arrangements of granules. Granular material form chains of granules to support the applied load. When the chain becomes unstable, some granules will slide out of the column causing the load to drop. This drop causes a sudden reduction in the stresses during compression. The load then builds up again as new chains of columns form followed by a collapse and so on. Each granule may be carrying a low-to-moderate stress, or it may be possible that sets of highly localized granule chains (stress chains of aligned granules) where fewer granules are involved but each experience much higher local contact stresses [76, 78]. Breaking these stress chains results in redistributions of the granular packing.

Upon applying a shearing force, the stress chains tend to break and reform continuously, thereby creating small fluctuations in the global stress of the granular material [74, 80]. This phenomenon is also thought to be responsible for the granular material to dilate [81]. Sudden releases (slip events) are observed during the deformation of the granular material, whereas during sticking the granules are closely packed and have high shear resistance [78].

In order to investigate the effect of stick-slip phenomenon closely, it is important to focus our attention the pertinent range of speed. Figure 10.4 demonstrates the effect of the rotational speed and the normal load on the friction coefficient for the two ranges of speed (5 to 100 and 150 to 950 rpm). Cases A through F in all figures presented thereafter correspond to the variation of normal load from 5.8 to 9.2 kPa. To effectively capture the behavior of the granular material, six data point were recorded for each speed. The distinction between the stick-slip region and the sliding region are shown.]

The results show that at the low speed range (5 to 100 rpm) there exist large fluctuations in the friction coefficient due to the continuous stick-slip events. At the higher range, a much smoother behavior was experienced where sliding starts gradually at a frictional force smaller than that generated during steady sliding (steady state friction). In this later case, slight fluctuations were recorded at some locations of the speed, but they were followed by a smoother trend. Such behavior is due to the low strength of the granular jammed state at this higher speed range [54].

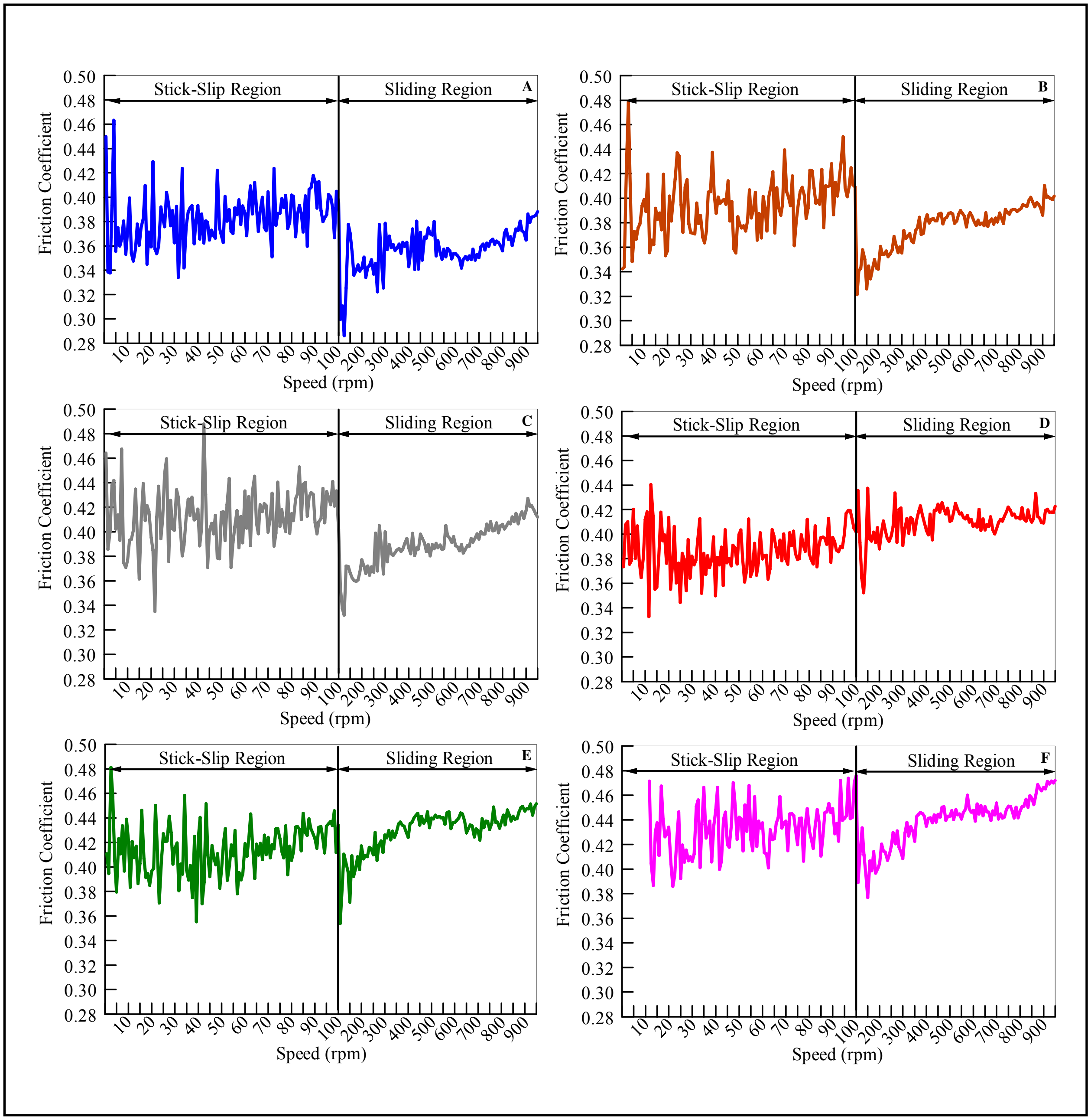

Figure 10.4 : Distinction between the Stick-Slip Region and the Sliding Region.
Case "A" – 5.8 kPa, "B" – 6.5 kPa, "C" – 7.2 kPa, "D" – 7.8 kPa, "E" – 8.5 kPa, and "F" – 9.2 kPa

10.4.2 Identification of Stick-Slip

Let us now turn our attention to the low speed range (5 to 100 rpm) where the stick-slip events took place. Figure 10.5 presents the effect of the rotational speed and the normal load on the friction coefficient for this low speed range. Translation of the granular material must be achieved by both sliding and dilation. Slip motion between the granules in contacts causes dynamical rearrangements and fluctuation in the friction forces occurs. As the speed is increased, the shearing resistance (friction level) of the spherical granules initially increases as granules rearrange spatially. When shear strain is applied sliding starts gradually and while the stress increases gradually, more and more contacts causes slip events.

With increasing shear strain, the frictional strength stabilizes and the magnitude of the stick-slip spikes decreases. The motion of the spherical granules becomes more stable when the slip at contacts accumulates over time and less stick-slip occurs. Noticeably small random pattern of stick-slip was due to the relatively large grain size used in the experiments [77]. Also shown in Figure 10.5 are a series of magnified snapshots where we have zoomed into several speed values in order to investigate the stick-slip events more closely. All cases with six different applied loads clearly revealed stick-slip events. Four different speed locations were chosen for each load case. Each zoomed frame represents the variation of the friction coefficient at a particular speed for two minutes of recorded data showing a stick-slip event.

The results presented in this chapter illustrating the occurrence stick-slip phenomenon in granular lubrication are qualitatively in agreement with the results published by several researchers. For example, Batista & Carlson [71] explored the nature of the transitions between stick-slip and steady sliding in boundary lubrication. They observed a sudden and discontinuous onset in the amplitude of oscillations at the bifurcation point as they increase the speed. Their observations agreed with the results presented in Figure 10.4 where we show that the bifurcation point from stick-slip to continuous sliding occurs by increasing the speed. Nasuno *et al.* [70] showed that the dynamics of spherical granules is always irregular. Microscopic events for the non-periodic (irregular) stick-slip motion at high stiffness and low driving velocity were also demonstrated.

Their results showing the behavior of the granular material before and after a major slip event agreed with our magnified snapshots presented in Figure 10.5. Johansen *et al.* [50] showed that the stick-slip exists at small speed, whereas a damped harmonic motion (continuous sliding) at higher speed in a spring-block system as a function of the pulling velocity. The spring force can be somewhat comparable to the friction coefficient in the case presented in this chapter.

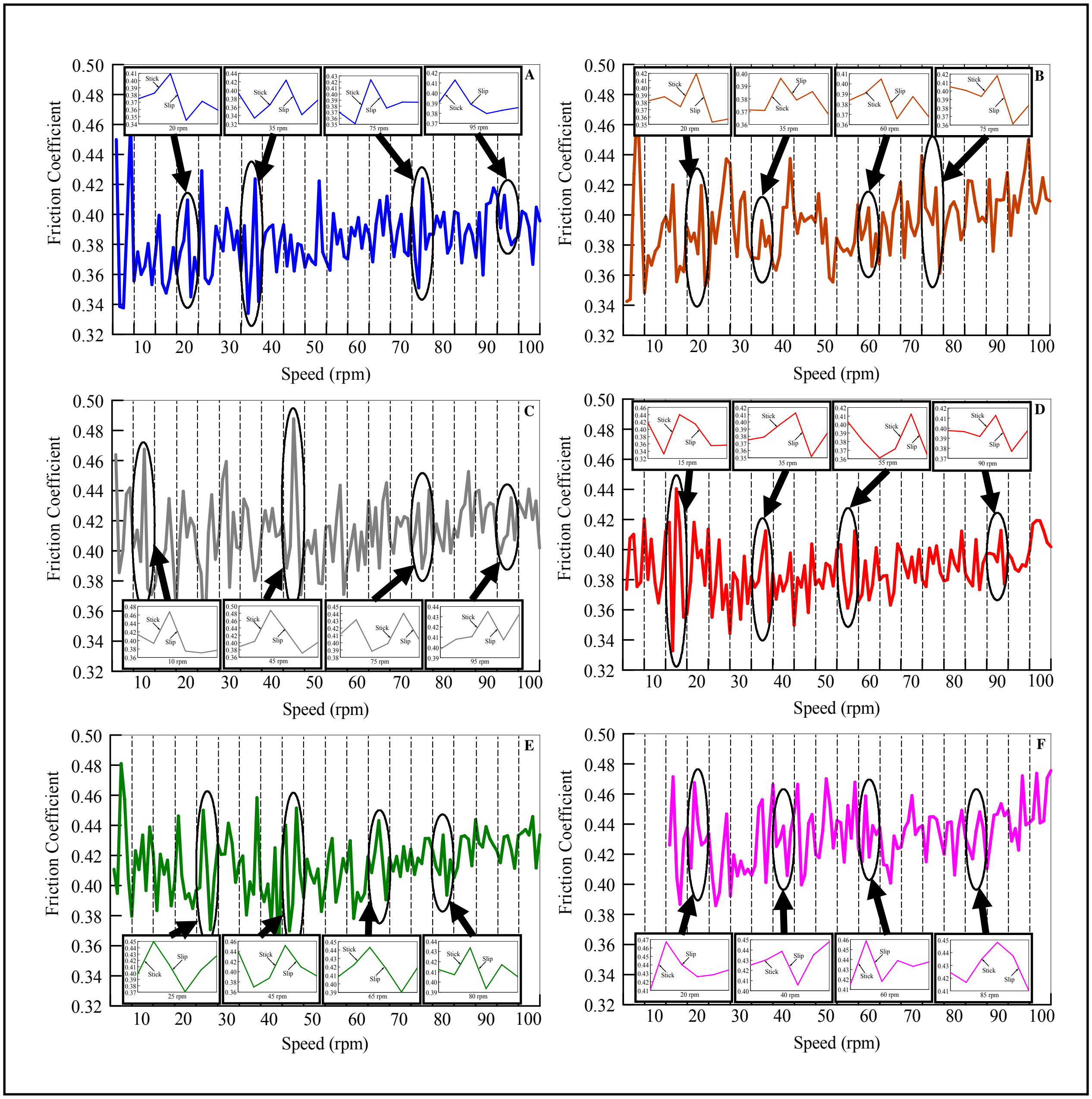

Figure 10.5 : Effect of the Rotational Speed and the Normal Load on the Friction Coefficient.
Case "A" – 5.8 kPa, "B" – 6.5 kPa, "C" – 7.2 kPa, "D" – 7.8 kPa, "E" – 8.5 kPa, and "F" 9.2 kPa

The behavior of the stick-slip is similar to the results presented in Figure 10.4 and Figure 10.5. Adjémian & Evesque [77] demonstrated the mechanical behavior of a macroscopic ensemble of glass beads where they presented the evolution of the vertical overload as a function of the sample strain. The strain behavior resemble to the friction behavior presented in Figure 10.4. Also they showed the effect of the velocity on the stick-slip which is similar to the results found in Figure 10.4.

10.4.3 Displacement/Lift Behavior

The effect of the rotational speed and the normal load on vertical displacement is depicted in Figure 10.6. The shear forces move the granules, causing an increase in the volume (dilation) which in turn causes an increase in the displacement. Displacement was measured using the linear variable differential transducer (LVDT) where it senses the relative displacement of the bottom cup from the upper disk. When this relative displacement is positive, it means that there is a separation that took place between the cup and the disk which in turn indicates a lift.

At low speed, layers of the spherical ceramic granules must dilate against the applied normal load to accommodate the shearing force. By increasing the speed slightly, the proportion of rolling to sliding decreases leading to larger displacement. At this low speed range, the increase in the momentum transfer due to the granules spatial arrangement translates to an increase in displacement between them but the stick-slip ceases to have any significant effect on the displacement due to its small magnitudes.

Figure 10.7 presents the result of the displacement (lift) plotted as a function of the wide range of speed for a better understanding for the effect of the normal load. The results indicated that under the conditions tested at low speed range (5 – 100 rpm) the applied normal load had a minimal influence on the displacement. On the other hand, at the higher speed range, the larger the applied load the lesser the displacement (lift). In other words, when the applied load is greater, the displacement —produced by the granules that push the lower disk downward— due to the increase in the packing of the granules within the gap is reduced.

By increasing the normal load, the lift produced by the granules decreases since higher normal load suppress dilatancy of the material. Also when the sliding speed is much higher (100 – 1000 rpm), the collision rate of the granules is enhanced and more momentum is passed on from the rotating disk (top) to the stationary disk (bottom) pushing it gradually downward, thus increasing the separation between the two disks. The results of the experiments provide a quantifiable measure and evidence that granular material can produce lift between two parallel disks.

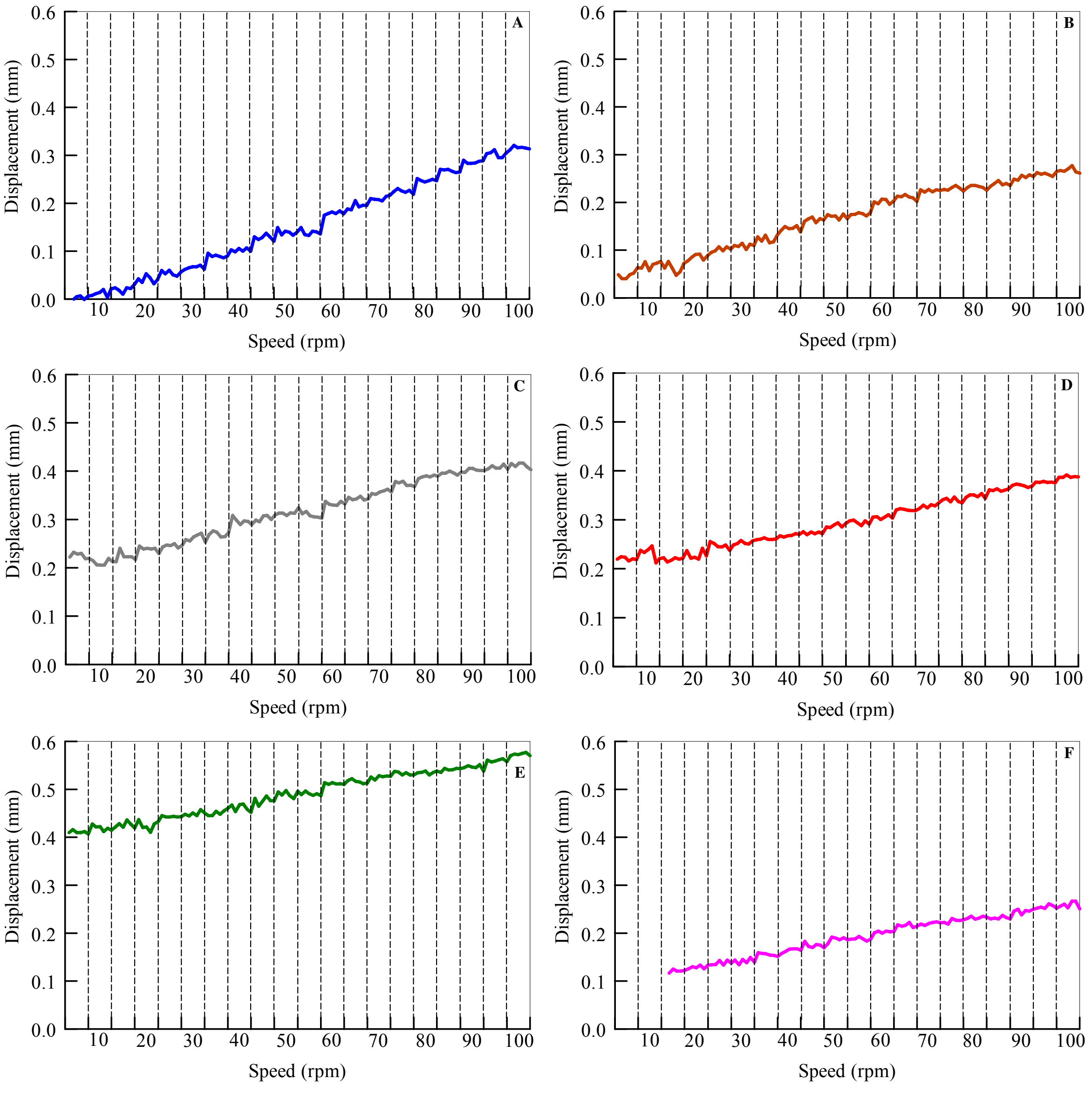

Figure 10.6 : Effect of the Rotational Speed and the Normal Load on the Vertical Displacement.
Case "A" – 5.8 kPa, "B" – 6.5 kPa, "C" – 7.2 kPa, "D" – 7.8 kPa, "E" – 8.5 kPa, and "F" – 9.2 kPa

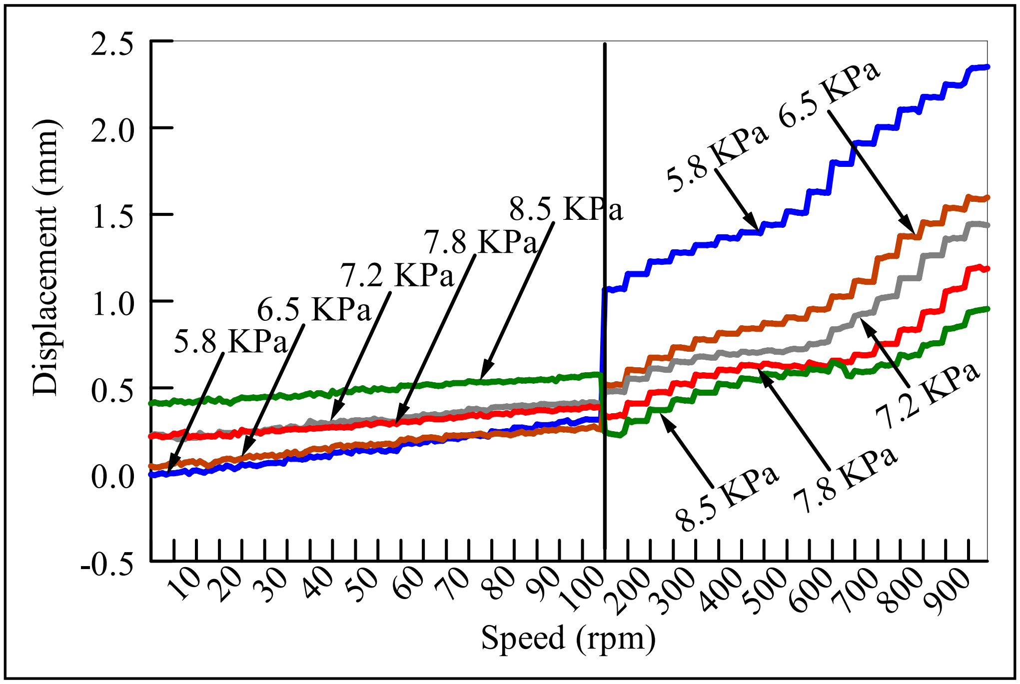

Figure 10.7 : Effect of the Normal Load on the Vertical Displacement

10.5 Conclusions

Stick-slip is a complex phenomenon that depends on many parameters. Experiments were conducted using 1.4-mm ceramic balls to study the stick-slip phenomenon in an annular shear cell apparatus. The results reveal the occurrence of stick-slip within the context of granular lubrication. Specifically, the effect of stick-slip on the friction and the change in the spatial arrangement of granules in a granular shear cell are demonstrated.

The following conclusions of this experimental study can be summarized as follow:

- The experiments provide an evidence of the existence of the stick-slip phenomenon at low speed and provide an evidence of formation of granular lift force between two parallel disks.
- The higher the speed of the rotating disk, the greater the collision rate of the granules and the higher the momentum which is passed on to the lower disk to bring about a lift.
- The larger the applied load, the lesser the lift produced due to suppressing dilatancy tendency.

- Stick-slip fluctuations are strongly influenced by the long range nature of the force propagation in granular materials at low speed, and at higher speed the jamming originates from a localized applied stress.
- The velocity of the sliding surface influences the stick-slip spikes. At slow speed, the surrounding grains are displaced causing dynamical rearrangements which result in large fluctuations. By increasing the speed, the granular material no longer sticks to the moving surface and instead we observe continuous sliding.

CHAPTER 11. THE TRUE TEMPERATURE BETWEEN TWO PARALLEL PLATES

11.1 Introduction

Heat transport through complex and often dynamic porous materials such as granular materials is an essential requirement for modern technology such as high performance cryogenic insulation, heterogeneous catalysts and catalytic reactors. The true temperature of a granular material depends on its entropy, and is difficult to measure in the laboratory. It is important to develop a theory that ties the true temperature to the grain mobility. Under certain conditions, the behavior of individual granules is qualitatively similar to the motion of a gas molecule. However, there is a significant difference between a fluidized granular material and a gas molecule. The temperature of the gas, gives the magnitude of the velocity fluctuations (the so-called pseudo temperature in granular material), while the true temperature of a granular material depends on the balance between the source of energy, and the dissipation of energy due to inelastic collisions.

The purpose of this chapter is to focus our attention on evaluating the granular material's true temperature considering the case where the flow of a granular material lubricant is sheared between two infinitely wide parallel plates as shown in Figure 8.1.

11.2 Theory

The grains are treated as smooth frictionless spheres of identical size, and the plates are assumed to be infinitely wide. The governing equations are derived, normalized and solved numerically. A series of results are presented to show the distribution of the true temperature across the gap, and to investigate the effect of the true temperature on the top and bottom interfaces. The upper plate is stationary while the bottom plate undergoes a constant sliding motion, *U*. It is assumed that the spin effect of the granules and the gravity force are neglected due to the smallness of the thickness of the gap. The flow is considered to be steady, two-dimensional, and fully developed. As shown in Figure 11.1, a Cartesian coordinate is set up by letting *x* lie along the plate's length, and *y* across the thickness of the flow.

The analysis of this problem requires consideration of the heat transfer within the gap, heat conduction into the bounding plates, and heat convection into the surroundings. Therefore, the problem is divided into the granular domain as well as the heat transfer in the upper and lower plates. In what follows the governing equations and the related boundary conditions are presented.

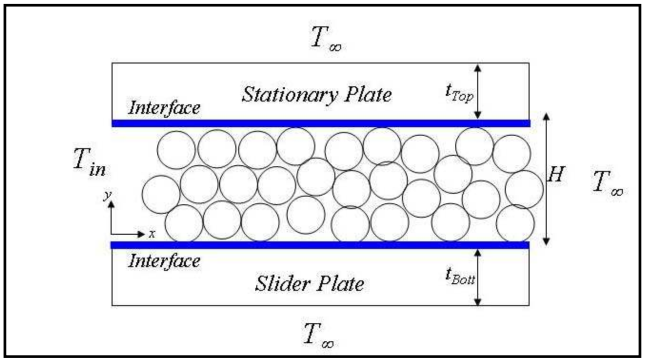

Figure 11.1 : True Temperature Regions

11.3 Governing Equations

11.3.1 Granular Flow

The governing equation for the conservation of energy (3-4) of the granular material is given by:

$$\frac{D(\rho E)}{Dt} = -\nabla.Q - \sigma : \nabla U$$

Following the work of Johnson and Jackson [15], it is assumed that the work done by the frictional component of stress contributes only to the true thermal energy. Therefore, the energy equation is separated into two equations (3-11), (3-12) given below. The energy equation of the pseudo temperature is,

$$\frac{D(E_{PT})}{Dt} = -\nabla.q_{PT} - \sigma_{ck} : \nabla U - \gamma \tag{11-1}$$

and the energy equation of the true temperature is,

$$\frac{D(E_h)}{Dt} = -\nabla.q_h - \sigma_f : \nabla U + \gamma \tag{11-2}$$

where $\frac{D}{Dt}$ is the material derivative; E_h is the true thermal internal energy of single granule defined as $E_h = c_p T_R$; c_p is the specific heat of the granular material; q_h represents the true heat flux defined as $q_h = -k_p \nabla T_R$; k_p denotes the heat conductivity of the granular material; T_R

represents the true temperature of the granular material; σ_f represents the stress tensor caused by enduring contact force between granules; $\sigma_f : \nabla U$ is the viscous dissipation done by the component of frictional stress; and γ is the rate of dissipation due to inelastic collisions between granules defined from equation (6-3) as $\gamma = \frac{\rho_p f_5(\upsilon) T^{3/2}}{d}$.

It is assumed that the flow is two-dimensional, fully developed, and steady state. Thus, the energy equation of the true temperature is simplified as follows:

$$\frac{D}{Dt}(\rho c_p T_R) = -\nabla.(-k_p \nabla T_R) + \gamma \tag{11-3}$$

Now, let us examine the orders of the conduction terms individually:

$$\nabla.(k_p \nabla T_R) = \frac{\partial}{\partial x}\left(k_p \frac{\partial T_R}{\partial x}\right) + \frac{\partial}{\partial y}\left(k_p \frac{\partial T_R}{\partial y}\right)$$

The following order of magnitude analysis was performed to simplify the energy equation as follow, $\frac{\frac{\partial}{\partial x}\left(k_p \frac{\partial T_R}{\partial x}\right)}{\frac{\partial}{\partial y}\left(k_p \frac{\partial T_R}{\partial y}\right)} \sim \frac{T_{ref}/L^2}{T_{ref}/H^2} = \left(\frac{H}{L}\right)^2 \langle\langle 1$ which means that the term $\frac{\partial^2 T}{\partial y^2}$ has a greater contribution to the granular material governing equation than $\frac{\partial^2 T}{\partial x^2}$.

Practically, the thermal conductivity of the granular flow is a function of the solid volume fraction. It is, therefore, necessary to obtain an effective thermal conductivity for treating the true temperature in granular flow. For this purpose, the granular material is treated like a solid with continuous pores of air.

There are mainly two phases present in the porous material: air which is a continuous medium of conductivity k_{air} and granules (spheres, dispersed phase) with conductivity k_p and a solid volume fraction υ. For materials packed in a random assembly of microspheres, the effective thermal conductivity is essentially affected by the relation between the thermal conductivities of the two phases (air and Titanium Dioxide, for example), the solid volume fraction of the dispersed phase, and the thermal polarizability which is defined by Gonzo [82] as:

$$\beta = \frac{k_p - k_{air}}{k_p + 2k_{air}} \tag{11-4}$$

To estimate correlations for the effective thermal conductivity of granular materials, Gonzo [82] classified three main groups of materials. Type (A): low-dense porous materials (volume fraction of spheres up to 10%); Type (B): medium-dense materials with volume fraction in the range 0.15–0.85; and Type (C): high-dense materials (volume fraction higher than 90%). The Type (B) porous materials address the class of granular material used in this work. Gonzo [82] demonstrated an improved form of Maxwell's model [83] proposed by Chiew and Glandt [84] in the early 1980's for this type of granules and given by the following expression:

$$k_{eff}(\upsilon) = k_{air}\frac{1+2\beta\upsilon+\left(k_p-3\beta^2\right)\upsilon^3}{1-\beta\upsilon} \tag{11-5}$$

The energy equation for evaluating the true temperature $T_R = T_R(\upsilon)$ can be then rewritten as:

$$\frac{D}{Dt}(\rho c_p T_R) = \nabla.(k_{eff}\nabla T_R) + \gamma$$

$$\underbrace{\rho_p\,\upsilon c_p u\frac{\partial T_R(\upsilon)}{\partial x}}_{Convection} = \underbrace{k_{eff}(\upsilon)\frac{\partial^2 T_R(\upsilon)}{\partial y^2} + \frac{\partial k_{eff}(\upsilon)}{\partial y}\frac{\partial T_R(\upsilon)}{\partial y}}_{Conduction} + \underbrace{\frac{\rho_p f_5(\upsilon)T^{3/2}}{d}}_{Dissipation} \tag{11-6}$$

where u represents the component of the bulk velocity, ρ_p is the density of the individual granule, υ represents the solid volume fraction, and $k_{eff}(\upsilon)$ is the effective thermal conductivity. In order to solve the above heat equation, the granular flow governing equations for the velocity, pseudo temperature, and solid volume fraction must be solved.

11.3.2 Bottom Plate

The general form of the heat equation with a moving surface is:

$$\rho_{Bott}c_{Bott}\vec{V}.(\nabla T_{Bott}) = k_{Bott}\nabla^2 T_{Bott} \tag{11-7}$$

where ρ_{Bott} is the density of the bottom plate material; c_{Bott} is the specific heat of the bottom plate; $\vec{V}$ represents the velocity vector and since the plate move only with a constant velocity U in x-direction, then we can rewrite:

$$\rho_{Bott}c_{Bott}U\frac{\partial T_{Bott}}{\partial x} = k_{Bott}\left(\frac{\partial^2 T_{Bott}}{\partial x^2} + \frac{\partial^2 T_{Bott}}{\partial y_{Bott}^2}\right) \tag{11-8}$$

The final form of the governing equation for the true temperature of the bottom plate is:

$$U\frac{\partial T_{Bott}}{\partial x} = \alpha_{Bott}\left(\frac{\partial^2 T_{Bott}}{\partial x^2} + \frac{\partial^2 T_{Bott}}{\partial y_{Bott}^2}\right) \tag{11-9}$$

where (x, y_{Bott}) represents the Cartesian coordinate for the bottom plate, and α_{Bott} represents the thermal diffusivity of the bottom plate defined as:

$$\alpha_{Bott} = \frac{k_{Bott}}{\rho_{Bott}\, c_{Bott}}$$

11.3.3 Top Plate

The general form of the heat equation with constant thermal conductivity is:

$$\frac{1}{\alpha_{Top}}\frac{\partial T_{Top}}{\partial t} = \frac{\partial^2 T_{Top}}{\partial x^2} + \frac{\partial^2 T_{Top}}{\partial y_{Top}^2} \tag{11-10}$$

where (x, y_{Top}) represents the Cartesian coordinate for the top stationary plate, ρ_{Top} the density of the top plate material, c_{Top} represents the specific heat of the top plate, and α_{Top} represents the thermal diffusivity of the top plate defined as:

$$\alpha_{Top} = \frac{k_{Top}}{\rho_{Top}\, c_{Top}}$$

For steady state condition and no heat generation, the Laplacian equation will be simplified as follows,

$$\frac{\partial^2 T_{Top}}{\partial x^2} + \frac{\partial^2 T_{Top}}{\partial y_{Top}^2} = 0 \tag{11-11}$$

11.4 Boundary Conditions

Figure 11.2 illustrates the boundary conditions for the granular flow, the bottom plate, and the top plate respectively.

11.4.1 Granular Flow

In the x-direction the inlet temperature of the granular material may be taken to as the granular supply temperature. In the *y*-direction, the heat generated transfers into the boundary surfaces only by conduction. At the interface between the granules and the upper and lower plates (disks), the heat flux is continuous and the temperatures are equal.

At $x = 0$ (Inlet):

$$T_R(0, y) = T_{in} \tag{11-12}$$

At $y = 0$ (Matching boundary condition at the bottom Interface):

$$k_{eff}\left(\frac{\partial T_R}{\partial y}\right)_{y=0} = k_{Bott}\left(\frac{\partial T_{Bott}}{\partial y_{Bott}}\right)_{y_{Bott}=t_{Bott}} \quad \text{and} \quad T_R\big|_{y=0} = T_{Bott}\big|_{y_{Bott}=t_{Bott}} \tag{11-13}$$

At $y = H$ (Matching boundary condition at the top interface):

$$k_{eff}\left(\frac{\partial T_R}{\partial y}\right)_{y=H} = k_{Top}\left(\frac{\partial T_{Top}}{\partial y_{Top}}\right)_{y_{Top}=0} \quad \text{and} \quad T_R\big|_{y=H} = T_{Top}\big|_{y_{Top}=0} \tag{11-14}$$

where H represents the film thickness, T_{in} is the inlet temperature, k_{Bott} is the heat conductivity of the bottom plate, T_{Bott} is the true temperature of the bottom plate, t_{Bott} is the thickness of the bottom plate, k_{Top} is the heat conductivity of the top plate, and T_{Top} is the true temperature of the top plate.

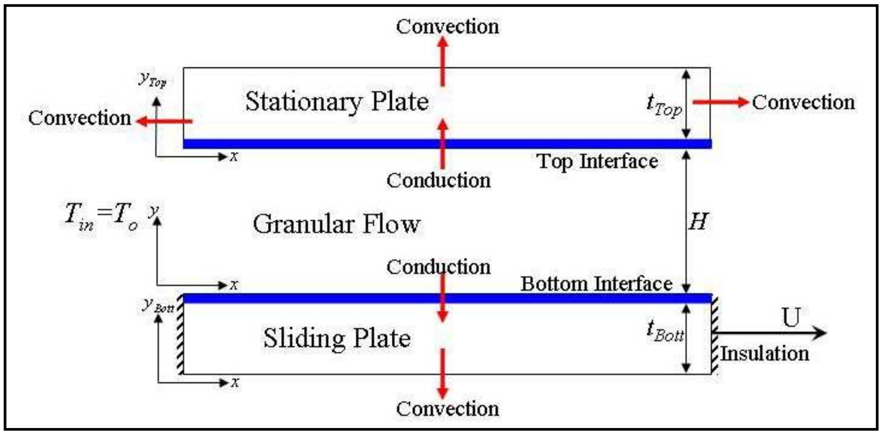

Figure 11.2 : Boundary Conditions

11.4.2 Bottom Plate

This plate is the sliding plate and due the symmetric condition at the inlet and outlet, the temperature at the inlet and outlet is assumed to be adiabatic.

At x = 0 (Inlet):

$$\left(\frac{\partial T_{Bott}}{\partial x}\right)_{x=0} = 0 \tag{11-15}$$

At x = L (Outlet):

$$\left(\frac{\partial T_{Bott}}{\partial x}\right)_{x=L} = 0 \tag{11-16}$$

At $y_{Bott} = t_{Bott}$ (Matching boundary condition at the bottom Interface):

$$k_{Bott}\left(\frac{\partial T_{Bott}}{\partial y_{Bott}}\right)_{y_{Bott}=t_{Bott}} = k_{eff}\left(\frac{\partial T_R}{\partial y}\right)_{y=0} \text{ and } T_{Bott}\Big|_{y_{Bott}=t_{Bott}} = T_R\Big|_{y=0} \tag{11-17}$$

At y_{Bott} = 0 (Convection boundary condition):

$$k_{Bott}\left(\frac{\partial T_{Bott}}{\partial y_{Bott}}\right)_{y_{Bott}=0} = h_{Bott}\left(T_{Bott}(x,0) - T_\infty\right) \tag{11-18}$$

where h_{Bott} represents the convection heat transfer coefficient at the interface between the bottom plate and the ambient.

11.4.3 Top Plate

The boundary conditions for the top plate are specified considering the continuity of the heat flux at the granular-solid interface (y_{Top}= 0) and at the solid-ambient boundaries (x = 0, x = L, and $y_{Top}= t_{Top}$).

In x-direction at both inlet and outlet, the plate is subjected to convection boundary condition

At x = 0 (Inlet):

$$k_{Top}\left(\frac{\partial T_{Top}}{\partial x}\right)_{x=0} = h_{Top}\left(T_{Top}(0, y_{Top}) - T_\infty\right) \tag{11-19}$$

where h_{Top} is the convection heat transfer coefficient at the interface between the top plate and the ambient.

At x = L (Outlet):

$$-k_{Top}\left(\frac{\partial T_{Top}}{\partial x}\right)_{x=L} = h_{Top}\left(T_{Top}(L, y_{Top}) - T_\infty\right) \tag{11-20}$$

At $y_{Top}= 0$ (Matching boundary condition at the top interface):

$$k_{Top}\left(\frac{\partial T_{Top}}{\partial y_{Top}}\right)_{y_{Top}=0} = k_{eff}\left(\frac{\partial T_R}{\partial y}\right)_{y=H} \quad \text{and} \quad T_{Top}\Big|_{y_{Top}=0} = T_R\Big|_{y=H} \tag{11-21}$$

At $y_{Top} = t_{Top}$ (Convection boundary condition):

$$-k_{Top}\left(\frac{\partial T_{Top}}{\partial y_{Top}}\right)_{y_{Top}=t_{Top}} = h_{Top}\left(T_{Top}(x,t_{Top}) - T_\infty\right) \tag{11-22}$$

where t_{Top} is thickness of the top plate

11.5 Dimensionless Form

In what follows, we shall make use of the following dimensionless parameters:

$$x^* = \frac{x}{L},\ y^* = \frac{y}{H},\ y^*_{Top} = \frac{y_{Top}}{t_{Top}},\ y^*_{Bott} = \frac{y_{Bott}}{t_{Bott}},\ u^* = \frac{u}{U},\ A^* = \sqrt{\frac{\rho_p U^2}{N}},\ T^*_R = \frac{T_R}{T_{in}},\ T^*_\infty = \frac{T_\infty}{T_{in}},$$

$$T^*_{Bott} = \frac{T_{Bott}}{T_{in}},\ T^*_{Top} = \frac{T_{Top}}{T_{in}},\ T^* = \frac{\rho_p T}{N},\ k^*_{eff} = \frac{k_{eff}}{k_p} \tag{11-23}$$

Substituting in the governing equations and boundary conditions with the above parameters yields to the non-dimensional equations below:

11.5.1 Granular Flow

11.5.1.1 Dimensionless Governing Equation

$$\frac{\rho_p\ c_p U T_{in}}{L}\upsilon u^*\frac{\partial T^*_R}{\partial x^*} = \frac{T_{in}k_{eff}}{H^2}\frac{\partial^2 T^*_R}{\partial y^{*2}} + \frac{T_{in}}{H^2}\frac{\partial k_{eff}}{\partial y^*}\frac{\partial T^*_R}{\partial y^*} + \frac{\rho_p N^{3/2}}{\rho_p^{3/2} d}T^{*3/2} f_5$$

$$\upsilon u^*\frac{\partial T^*_R}{\partial x^*} = \frac{k_p\ \ L}{\rho_p\ c_p U H^2}k^*_{eff}\frac{\partial^2 T^*_R}{\partial y^{*2}} + \frac{k_p\ \ L}{\rho_p\ c_p U H^2}\frac{\partial k^*_{eff}}{\partial y^*}\frac{\partial T^*_R}{\partial y^*} + \frac{NL}{\rho_p\ c_p T_{in} d}\frac{N^{1/2}}{U\rho_p^{1/2}}T^{*3/2} f_5$$

$$\upsilon u^*\frac{\partial T^*_R}{\partial x^*} = \left(A^*_2\right)k^*_{eff}\frac{\partial^2 T^*_R}{\partial y^{*2}} + \left(A^*_2\right)\frac{\partial k^*_{eff}}{\partial y^*}\frac{\partial T^*_R}{\partial y^*} + \left(\frac{A^*_3}{A^*_1}\right)T^{*3/2} f_5 \tag{11-24}$$

where A^*_1, A^*_2, A^*_3 are constants defined as $A^*_1 = \dfrac{\rho_p^{1/2} U}{N^{1/2}}$, $A^*_2 = \dfrac{\alpha_p L}{UH^2}$, $\alpha_p = \dfrac{k_p}{\rho_p c_p}$, $A^*_3 = \dfrac{NL}{\rho_p c_p T_{in} d}$

11.5.1.2 Dimensionless Boundary Conditions

At $x^* = 0$ (Inlet):

$$T_R^*(0, y^*) = 1 \tag{11-25}$$

At $y^* = 0$ (Bottom interface):

$$\left(\frac{\partial T_R^*}{\partial y^*}\right)_{y^*=0} = \left(\frac{A_4^*}{k_{eff}^*}\right)\left(\frac{\partial T_{Bott}^*}{\partial y_{Bott}^*}\right)_{y_{Bott}^*=1} \text{ and } T_R^*\Big|_{y^*=0} = T_{Bott}^*\Big|_{y_{Bott}^*=1} \tag{11-26}$$

where $A_4^* = \dfrac{k_{Bott} H}{k_p t_{Bott}}$

At $y^* = 1$ (Top interface):

$$\left(\frac{\partial T_R^*}{\partial y^*}\right)_{y^*=1} = \left(\frac{A_5^*}{k_{eff}^*}\right)\left(\frac{\partial T_{Top}^*}{\partial y_{Top}^*}\right)_{y_{Top}^*=0} \text{ and } T_R^*\Big|_{y^*=1} = T_{Top}^*\Big|_{y_{Top}^*=0} \tag{11-27}$$

where $A_5^* = \dfrac{k_{Top} H}{k_p t_{Top}}$

11.5.2 Bottom Plate

11.5.2.1 Dimensionless Governing Equation

$$\frac{\partial T_{Bott}^*}{\partial x^*} = \left(A_9^*\right)\frac{\partial^2 T_{Bott}^*}{\partial x^{*2}} + \left(A_{10}^*\right)\frac{\partial^2 T_{Bott}^*}{\partial y_{Bott}^{*2}} \tag{11-28}$$

where $A_9^* = \dfrac{\alpha_{Bott}}{LU}$, $\quad A_{10}^* = \dfrac{L\alpha_{Bott}}{t_{Bott}^2 U}$

11.5.2.2 Dimensionless Boundary Conditions

At $x^* = 0$ (Inlet):

$$\left(\frac{\partial T_{Bott}^*}{\partial x^*}\right)_{x^*=0} = 0 \tag{11-29}$$

At $x^* = 1$ (Outlet):

$$\left(\frac{\partial T_{Bott}^*}{\partial x^*}\right)_{x^*=1} = 0 \tag{11-30}$$

At $y^*_{Bott} = 1$ (Bottom Interface):

$$\left(\frac{\partial T^*_{Bott}}{\partial y^*_{Bott}}\right)_{y^*_{Bott}=1} = \left(\frac{k^*_{eff}}{A^*_4}\right)\left(\frac{\partial T^*_R}{\partial y^*}\right)_{y^*=0} \quad \text{and} \quad T^*_{Bott}\Big|_{y^*_{Bott}=1} = T^*_R\Big|_{y^*=0} \tag{11-31}$$

At $y^*_{Bott} = 0$:

$$\left(\frac{\partial T^*_{Bott}}{\partial y^*_{Bott}}\right)_{y^*_{Bott}=0} = \left(A^*_{11}\right)\left(T^*_{Bott}(x^*,0) - T^*_\infty\right) \tag{11-32}$$

where $A^*_{11} = \dfrac{h_{Bott} t_{Bott}}{k_{Bott}}$

11.5.3 Top Plate

11.5.3.1 Dimensionless Governing Equation

$$\frac{\partial^2 T^*_{Top}}{\partial x^{*2}} + \left(A^*_6\right)\frac{\partial^2 T^*_{Top}}{\partial y^{*2}_{Top}} = 0 \tag{11-33}$$

where $A^*_6 = \dfrac{L^2}{t^2_{Top}}$

11.5.3.2 Dimensionless Boundary Conditions

At $x^* = 0$ (Inlet):

$$\left(\frac{\partial T^*_{Top}}{\partial x^*}\right)_{x^*=0} = \left(A^*_7\right)\left(T^*_{Top}(0, y^*_{Top}) - T^*_\infty\right) \tag{11-34}$$

where $A^*_7 = \dfrac{h_{Top} L}{k_{Top}}$

At $x^* = 1$ (Outlet):

$$\left(\frac{\partial T^*_{Top}}{\partial x^*}\right)_{x^*=1} = \left(-A^*_7\right)\left(T^*_{Top}(1, y^*_{Top}) - T^*_\infty\right) \tag{11-35}$$

At $y^*_{Top} = 0$ (Top Interface):

$$\left(\frac{\partial T^*_{Top}}{\partial y^*_{Top}}\right)_{y^*_{Top}=0} = \left(\frac{k^*_{eff}}{A^*_5}\right)\left(\frac{\partial T^*_R}{\partial y^*}\right)_{y^*=1} \quad \text{and} \quad T^*_{Top}\Big|_{y^*_{Top}=0} = T^*_R\Big|_{y^*=1} \tag{11-36}$$

At $y^*_{Top} = 1$:

$$\left(\frac{\partial T^*_{Top}}{\partial y^*_{Top}}\right)_{y^*_{Top}=1} = \left(-A^*_8\right)\left(T^*_{Top}(x^*,1) - T^*_\infty\right) \qquad (11\text{-}37)$$

where $A^*_8 = \dfrac{h_{Top} t_{Top}}{k_{Top}}$

11.6 Numerical Scheme

The energy equation for the granular flow (11-24), the heat conduction equations for both the bottom and the top plates (11-28), (11-33) are coupled through their respective boundary conditions. These equations must be solved numerically in an iterative fashion. A finite difference method is employed to discretize the dimensionless governing equations and boundary conditions, which forms a set of algebraic equations. Newton's iteration method and the marching technique are used to solve the resulting set of equations for the true temperature of the granular material and the top and bottom plates. In order to solve the governing equation of the true temperature, the characteristics of the granular flow (i.e. velocity, pseudo temperature, and solid volume fraction) need to be first obtained. The true temperature of the granular material and the plates' temperature were solved using the main iteration loop. The procedure is repeated until the results of all temperatures converge. The error tolerance used is 10^{-8}. There are 21 mesh points across each plate and across the gap and 51 along the length of the pad.

11.7 Discretization

The appropriate finite difference equations and the detailed discretization are as follow. Parameter i represents the index for the x-direction. j_{Flow}, j_{Bott} and j_{Top} represent the indexes for the y-direction of the granular flow, the bottom plate, and the top plate respectively. Since the inlet temperature is specified, the temperature is solved at every fixed i-section by using the marching technique. Newton's iteration method is also applied in the simulations. In the granular flow governing equation (11-24), first order forward differentiation formula was used for the convection term since the flow is moving in the x-direction with a specified inlet temperature, while a second order central differencing formula was used for the conduction and dissipation terms. Second order forward and backward approximations were used to discretize the interface equations (11-26) and (11-27) respectively.

Given below are the set of discretized equations along with their boundary conditions used in the Newton's iteration method:

11.7.1 Granular Flow

$$\frac{(\upsilon u)_{i,j_{Flow}}}{\Delta x}\left[T_{Ri,j_{Flow}} - T_{Ri-1,j_{Flow}}\right] = \left(\frac{A_2^*}{\Delta y^2}\right)\left(k_{eff}^*\right)_{i,j_{Flow}}\left[T_{Ri,j_{Flow}-1} - 2T_{Ri,j_{Flow}} + T_{Ri,j_{Flow}+1}\right] +$$

$$\left(\frac{A_2^*}{\Delta y}\right) DKDY_{i,j}\left(T_{Ri,j_{Flow}+1} - T_{Ri,j_{Flow}-1}\right) + \left(\frac{A_3^*}{A_1^*}\right)\left(T^{*3/2} f_5\right)_{i,j_{Flow}}$$

where $DKDY_{i,j} = \left(\frac{k_{eff\,i,j_{Flow}+1}^* - k_{eff\,i,j_{Flow}-1}^*}{\Delta y}\right)$

$$\left\{\frac{(\upsilon u)_{i,j_{Flow}}}{\Delta x} + \left(\frac{2A_2^*}{\Delta y^2}\right)\left(k_{eff}^*\right)_{i,j_{Flow}}\right\}T_{Ri,j_{Flow}} = \frac{(\upsilon u)_{i,j_{Flow}}}{\Delta x}T_{Ri-1,j_{Flow}} + \left\{\left(\frac{A_2^*}{\Delta y^2}\right)\left(k_{eff}^*\right)_{i,j_{Flow}} - \left(\frac{A_2^*}{\Delta y}\right)DKDY_{i,j}\right\}T_{Ri,j_{Flow}-1}$$

$$+\left\{\left(\frac{A_2^*}{\Delta y^2}\right)\left(k_{eff}^*\right)_{i,j_{Flow}} + \left(\frac{A_2^*}{\Delta y}\right)DKDY_{i,j}\right\}T_{Ri,j_{Flow}+1} + \left(\frac{A_3^*}{A_1^*}\right)\left(T^{*3/2} f_5\right)_{i,j_{Flow}}$$

That is,

$$T_{Ri,j_{Flow}} = \frac{\dfrac{(\upsilon u)_{i,j_{Flow}}}{\Delta x}}{\left\{\dfrac{(\upsilon u)_{i,j_{Flow}}}{\Delta x} + \left(\dfrac{2A_2^*}{\Delta y^2}\right)\left(k_{eff}^*\right)_{i,j_{Flow}}\right\}}T_{Ri-1,j_{Flow}} + \frac{\left\{\left(\dfrac{A_2^*}{\Delta y^2}\right)\left(k_{eff}^*\right)_{i,j_{Flow}} - \left(\dfrac{A_2^*}{\Delta y}\right)DKDY_{i,j}\right\}}{\left\{\dfrac{(\upsilon u)_{i,j_{Flow}}}{\Delta x} + \left(\dfrac{2A_2^*}{\Delta y^2}\right)\left(k_{eff}^*\right)_{i,j_{Flow}}\right\}}T_{Ri,j_{Flow}-1}$$

$$+\frac{\left\{\left(\dfrac{A_2^*}{\Delta y^2}\right)\left(k_{eff}^*\right)_{i,j_{Flow}} + \left(\dfrac{A_2^*}{\Delta y}\right)DKDY_{i,j}\right\}}{\left\{\dfrac{(\upsilon u)_{i,j_{Flow}}}{\Delta x} + \left(\dfrac{2A_2^*}{\Delta y^2}\right)\left(k_{eff}^*\right)_{i,j_{Flow}}\right\}}T_{Ri,j_{Flow}+1} + \frac{\left(\dfrac{A_3^*}{A_1^*}\right)\left(T^{*3/2} f_5\right)_{i,j_{Flow}}}{\left\{\dfrac{(\upsilon u)_{i,j_{Flow}}}{\Delta x} + \left(\dfrac{2A_2^*}{\Delta y^2}\right)\left(k_{eff}^*\right)_{i,j_{Flow}}\right\}} \tag{11-38}$$

$$T_{R_{1,j_{Flow}}} = 1$$

$$T_{R_{i,1}} = \left(\frac{4}{3}\right)T_{R_{i,2}} - \left(\frac{1}{3}\right)T_{R_{i,3}} + \left[-\left(\frac{A_4^*}{k_{eff\,i,1}^*}\right)T_{Bott_{i,m_{Bott}}} + \left(\frac{4A_4^*}{3k_{eff\,i,1}^*}\right)T_{Bott_{i,m_{Bott}-1}} - \left(\frac{A_4^*}{3k_{eff\,i,1}^*}\right)T_{Bott_{i,m_{Bott}-2}}\right]$$

$$T_{R_{i,m_{Flow}}}=\left(\frac{4}{3}\right)T_{R_{i,m_{Flow}-1}}-\left(\frac{1}{3}\right)T_{R_{i,m_{Flow}-2}}+\left[-\left(\frac{A_5^*}{k_{eff\,i,m}^*}\right)T_{Top_{i,1}}+\left(\frac{4A_5^*}{3k_{eff\,i,m}^*}\right)T_{Top_{i,2}}-\left(\frac{A_5^*}{3k_{eff\,i,m}^*}\right)T_{Top_{i,3}}\right]$$

11.7.2 Bottom Plate

$$\begin{aligned}T_{Bott_{i,j_{Bott}}}=&\frac{\left(\frac{A_9^*}{\Delta x}+1\right)}{\left(\frac{2\Delta xA_{10}^*}{\Delta y^2}+\frac{2A_9^*}{\Delta x}+1\right)}T_{Bott_{i-1,j_{Bott}}}+\frac{\left(\frac{A_9^*}{\Delta x}\right)}{\left(\frac{2\Delta xA_{10}^*}{\Delta y^2}+\frac{2A_9^*}{\Delta x}+1\right)}T_{Bott_{i+1,j_{Bott}}}+\\&\frac{\left(\frac{\Delta xA_{10}^*}{\Delta y^2}\right)}{\left(\frac{2\Delta xA_{10}^*}{\Delta y^2}+\frac{2A_9^*}{\Delta x}+1\right)}T_{Bott_{i,j_{Bott}-1}}+\frac{\left(\frac{\Delta xA_{10}^*}{\Delta y^2}\right)}{\left(\frac{2\Delta xA_{10}^*}{\Delta y^2}+\frac{2A_9^*}{\Delta x}+1\right)}T_{Bott_{i,j_{Bott}+1}}\end{aligned}\tag{11-39}$$

$$T_{Bott_{1,j_{Bott}}}=\left(\frac{4}{3}\right)T_{Bott_{2,j_{Bott}}}-\left(\frac{1}{3}\right)T_{Bott_{3,j_{Bott}}}$$

$$T_{Bott_{n,j_{Bott}}}=\left(\frac{4}{3}\right)T_{Bott_{n-1,j_{Bott}}}-\left(\frac{1}{3}\right)T_{Bott_{n-2,j_{Bott}}}$$

$$T_{Bott_{i,1}}=\left(\frac{4}{2\Delta yA_{11}^*+3}\right)T_{Bott_{i,2}}-\left(\frac{1}{2\Delta yA_{11}^*+3}\right)T_{Bott_{i,3}}+\left[\left(\frac{2\Delta yA_{11}^*}{2\Delta yA_{11}^*+3}\right)T_\infty^*\right]$$

11.7.3 Top Plate

$$\begin{aligned}T_{Top_{i,j_{Top}}}=&\frac{\left(\frac{1}{\Delta x^2}\right)}{\left(\frac{2}{\Delta x^2}+\frac{2A_6^*}{\Delta y^2}\right)}T_{Top_{i-1,j_{Top}}}+\frac{\left(\frac{1}{\Delta x^2}\right)}{\left(\frac{2}{\Delta x^2}+\frac{2A_6^*}{\Delta y^2}\right)}T_{Top_{i+1,j_{Top}}}+\\&\frac{\left(\frac{A_6^*}{\Delta y^2}\right)}{\left(\frac{2}{\Delta x^2}+\frac{2A_6^*}{\Delta y^2}\right)}T_{Top_{i,j_{Top}-1}}+\frac{\left(\frac{A_6^*}{\Delta y^2}\right)}{\left(\frac{2}{\Delta x^2}+\frac{2A_6^*}{\Delta y^2}\right)}T_{Top_{i,j_{Top}+1}}\end{aligned}\tag{11-40}$$

$$T_{Top_{1,j_{Top}}}=\left(\frac{4}{2\Delta xA_7^*+3}\right)T_{Top_{2,j_{Top}}}-\left(\frac{1}{2\Delta xA_7^*+3}\right)T_{Top_{3,j_{Top}}}+\left[\left(\frac{2\Delta xA_7^*}{2\Delta xA_7^*+3}\right)T_\infty\right]$$

$$T_{Top_{n,jTop}} = \left(\frac{4}{2\Delta x A_7^* + 3}\right) T_{Top_{n-1,jTop}} - \left(\frac{1}{2\Delta x A_7^* + 3}\right) T_{Top_{n-2,jTop}} + \left[\left(\frac{2\Delta x A_7^*}{2\Delta x A_7^* + 3}\right) T_\infty\right]$$

$$T_{Top_{i,mTop}} = \left(\frac{4}{2\Delta y A_8^* + 3}\right) T_{Top_{i,mTop-1}} - \left(\frac{1}{2\Delta y A_8^* + 3}\right) T_{Top_{i,mTop-2}} + \left[\left(\frac{2\Delta y A_8^*}{2\Delta y A_8^* + 3}\right) T_\infty\right]$$

11.8 Results and Discussion

The results presented in this section focus on applying the theory to determine the true temperature of the granular flow between two parallel plates and also predict how hot the interfaces of the top and bottom plates can become. These predictions are based on the solution of the flow velocity, pseudo temperature, and solid volume fraction presented in Chapter 8. The input parameters used in the simulations are summarized in Table 11.1. The thermal properties presented were evaluated at room temperature and assumed to remain constant.

Both the top and the bottom plates are made of Stainless Steel. They both have a length of 26 mm and thickness of 13 mm. The top plate is stationary, while the velocity of the bottom plate is $U = 4.6\,\text{m/sec}$. The properties of the Stainless Steel are chosen from the CRC Materials Science and Engineering handbook [85]. The thermal conductivity is selected as $k_{Top} = k_{Bott} = 16.3\,\text{W/mK}$, the specific heat is $c_{Top} = c_{Bott} = 500\ \text{J/kgK}$, and the density is $\rho_{Top} = \rho_{Bott} = 8000\,\text{kg/m}^3$. The effective thermal conductivity is computed based on the prediction of the solid volume fraction. The Value of the convection heat transfer coefficient *(h)* for the moving plate is unknown, but was estimated based on Holman [86] and Incropera & DeWitt [87]. Assuming that the conditions for convective heat transfer were the same as for laminar air flow over isolated flat plates of the same dimensions one can determine Reynolds number from: $\text{Re} = u_{air}x / \nu_{air}$, where *x* is the length of the section of the body in the direction of air flow (length of the moving plate), $\text{U} = 4.6\ \text{m/sec}$ is the plate velocity, and ν_{air} is the kinematic viscosity of air ($\nu_{air} = 15.69\text{x}10^{-6}\ \text{m}^2/\text{s}$ at 300K). The Reynolds number can be rewritten as: $\text{Re} = UL/\nu_{air} = 7.74\text{x}10^3 \le 10^5$ and the mean Nusselt number (*Nu*) was determined from $Nu = 0.664\,\text{Re}^{0.5}\,\text{Pr}^{0.333} = 52.07$, where Pr is the dimensionless Prandtl number ($\text{Pr} = 0.708$ for air at 300K). The mean value of *h* was calculated from $h = Nu\,k_{air}/L = 51.3\ \text{W/m}^2\text{K}$, where

k_{air} is the air thermal conductivity ($k_{air} = 0.026\,\text{W/mK}$). The convection heat transfer coefficient for the moving plate is assumed then to be $h_{Bott} = 50\ \text{W/m}^2\text{K}$, while for the stationary plate the convection heat transfer coefficient is much smaller and is assumed to be $h_{Top} = 15\ \text{W/m}^2\text{K}$.

Table 11.1 : Input List for Benchmark Case Used in the Computer Simulations

Parameter	Value	Parameter	Value
U	$4.6\,\text{m/sec}$	L	$0.0264\,\text{m}$
$\upsilon_{\max}$	0.65	H	$70\,\mu\text{m}$
e_w	0.8	ϕ_o	0.5
e_p	0.8	ϕ_H	0.5
ρ_p	$4260\,\text{kg/m}^3$	d	$5\,\mu\text{m}$
c_p	711 J/kgK	T_{in}	30°C
k_p	8.79 W/mK	T_∞	30°C
ρ_{Bott}	$8000\,\text{kg/m}^3$	ρ_{Top}	$8000\,\text{kg/m}^3$
c_{Bott}	500 J/kgK	c_{Top}	500 J/kgK
k_{Bott}	16.3 W/mK	k_{Top}	16.3 W/mK
h_{Bott}	$50\ \text{W/m}^2\text{K}$	h_{Top}	$15\ \text{W/m}^2\text{K}$
t_{Bott}	0.013 m	t_{Top}	0.013 m

Based on the benchmark simulations in Chapter 8, the particle of granular lubrication used is made of Titanium Dioxide (TiO_2) and the thickness of the gap is equivalent to 14 particle diameters. The particle has a diameter of $5\,\mu\text{m}$ and a density $\rho_p = 4260\,\text{kg/m}^3$. The coefficients of restitution for both particle and wall are assumed to be $e_p = e_w = 0.8$, and the roughness of both moving and stationary plate is $\phi_o = \phi_H = 0.5$. The properties of the Titanium Dioxide are chosen from the literature [88]. The density, thermal conductivity, and the specific heat are selected as $\rho_p = 4260\,\text{kg/m}^3$, $k_p = 8.79\ \text{W/mK}$, and $c_p = 711\ \text{J/kgK}$ respectively. The effective thermal conductivity is computed based on the prediction of the solid volume fraction using equation (8-5).

11.8.1 Benchmark Simulations

Figure 11.3 presents the predicted distribution of the true temperature at the bottom and top interfaces along the moving direction (x-direction). The true temperature at both interfaces increases from inlet to outlet. The temperature rise predicted over the stationary disk is greater than the one predicted over the moving disk. This phenomenon can be explained by examining the energy equation of the granular flow. Three terms governed this equation: the convection term, the conduction (diffusion) term, and the dissipation (source) term.

The convection term represents the rate of temperature transported through the movement of the flow from inlet to outlet by convection relative to the interfaces. The dissipation term supplies the energy to the flow as a result of inelastic collision between the granules. As a result of the convection and dissipation terms, heat is produced due to the inelastic collision between the granules and thus the true temperature is predicted to increase from the inlet to the outlet. Since the effective thermal conductivity for the granular flow used is very small, it results in a prediction of small rise in the temperatures at the interfaces and heat is retained within the granular flow.

Figure 11.4 demonstrates how the true temperature is distributed within the granular flow and in the fields of both bottom and top plates. The energy is transferred to the top and bottom plates via the thin layer of the plates' thickness that is in contact with the temperature produced within the flow of the granular material. It is noted that the temperature at the top plate interface is slightly larger than the bottom plate interface due to the high heat convection coefficient of the moving plate. The true temperature distribution within the granular flow demonstrates the effect of the viscous dissipation term. The temperature builds up from the inlet to the outlet due to the heat source. The energy dissipated due to the inelastic collision between the granules is the major factor affecting the increase of the true temperature in the granular flow. This energy dissipated is related to the viscous dissipation term that appears in the pseudo energy equation, which is a function of the fluctuation velocity (pseudo temperature) and the solid volume fraction. The larger the fluctuation velocity becomes, the greater the chance of the collision between the granules and associated energy dissipation.

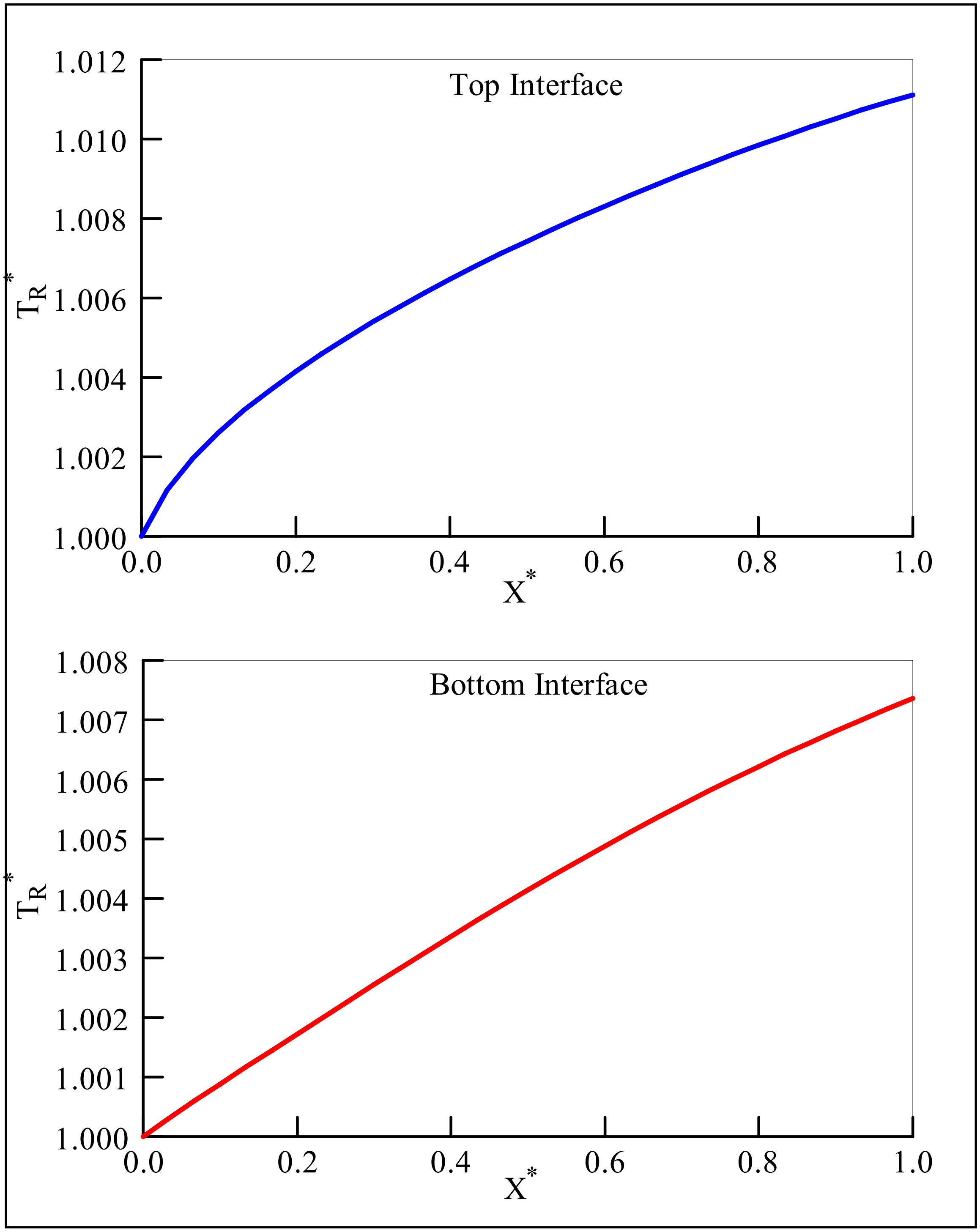

Figure 11.3 : The Film Temperature at Both Interfaces (Benchmark Simulations)

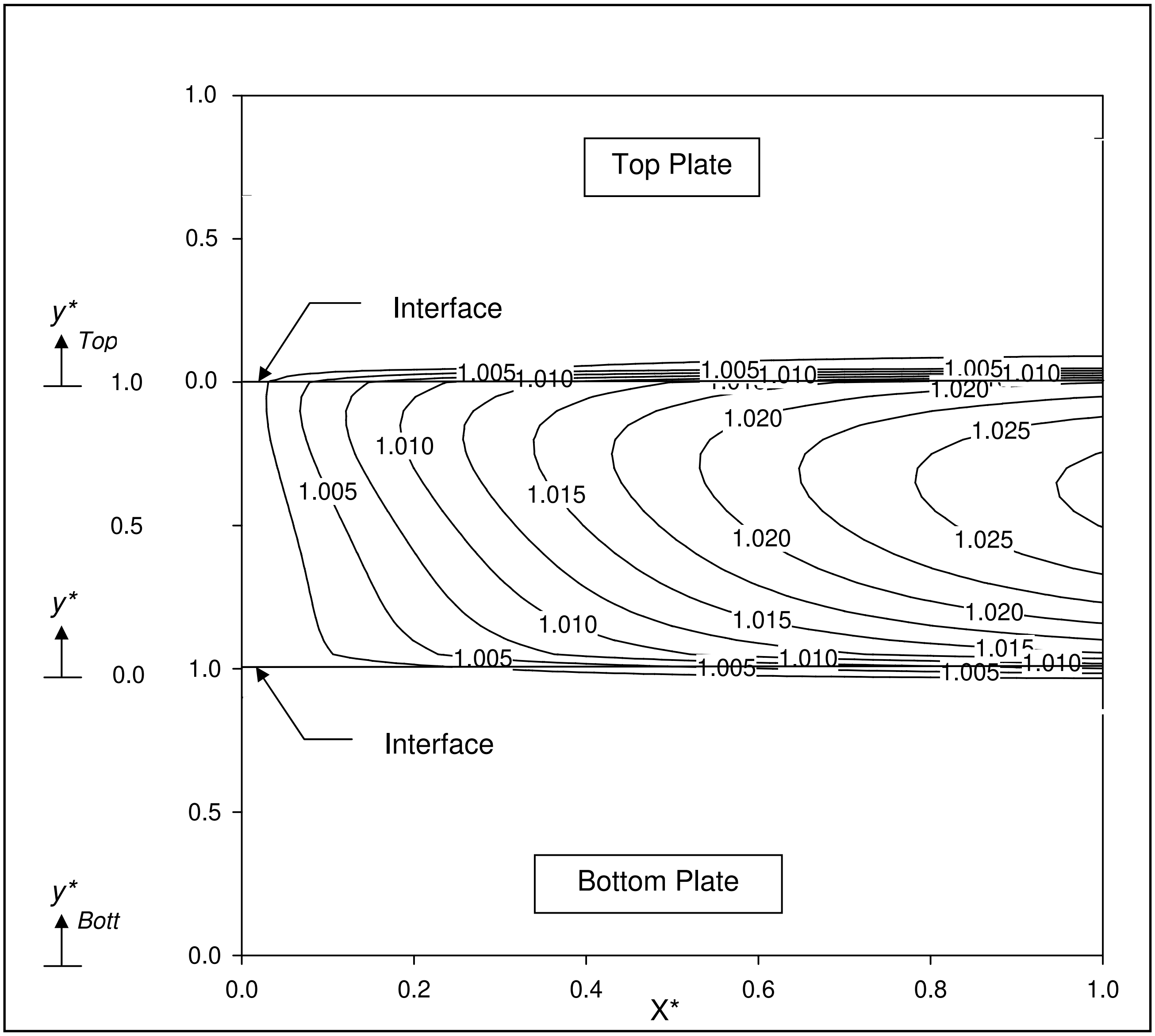

Figure 11.4 : The Distribution of the True Temperature in the Granular Flow and the Fields of the Top and Bottom Plates (Benchmark Simulations)

11.8.2 Variation of the True Temperature with the Granular Coefficient of Restitution, e_p

The change in the true temperature profiles along the moving direction at the top and bottom interfaces is shown in Figure 11.5 by varying the granular coefficient of restitution while restraining the wall coefficient of restitution to 0.8. As e_p increases, the true temperature decreases at both top and bottom interfaces. The reason for that can be explained from the true temperature energy equation (11-6) along with the constitutive relations of the energy dissipation (6-3). The true temperature is related to the rate of energy dissipation due to inelastic collisions between granules, which is related to the granular coefficient of restitution. At low granular coefficient of restitution, more energy is dissipated due to the inelastic collision leading to an increase in the true temperature from the interior of the flow to the interfaces. The larger the e_p, the more elastic the granules become. As a result, there is less energy loss by inelastic collision between granules (less heat dissipation) and the true temperature drops. The distribution of the true temperature within the granular flow and in the top and bottom fields for the case when $e_p = 0.98$ is also demonstrated in Figure 11.6. Similar trends were obtained for the true temperature of the flow and both plate fields along the x-direction with a decrease in the heat dissipated compared to the benchmark case in Figure 11.4.

11.8.3 Variation of the True Temperature with the Roughness for Both Top Plate (ϕ_H) and Bottom Plate (ϕ_o)

The change in the true temperature profiles at the top and bottom interfaces by varying the roughness of the top and the bottom plates is shown in Figure 11.7. When the roughness factor of the top plate is varied, the bottom plate roughness is kept constant and when the roughness factor of the bottom plate is varied, the top plate roughness is kept constant. Generally, the roughness factor ϕ of the boundary surface ranges from 0 when it is completely smooth, to 1 when it is completely rough. As ϕ_H increases, it causes a decrease in the slip velocity at the top boundary. Hence, the granules around this boundary become almost stationary which means the slip effect becomes nil and less fluctuation velocity occurs. Thus, as the roughness of the top plate becomes larger, there is less energy being transferred from the top plate to the adjacent layer of granules which decreases in turn the true temperature at this interface. Likewise, when ϕ_o is large, the slip velocity at the bottom boundary becomes smaller and less energy being transferred and similar explanation to the trend happens but for the bottom plate roughness.

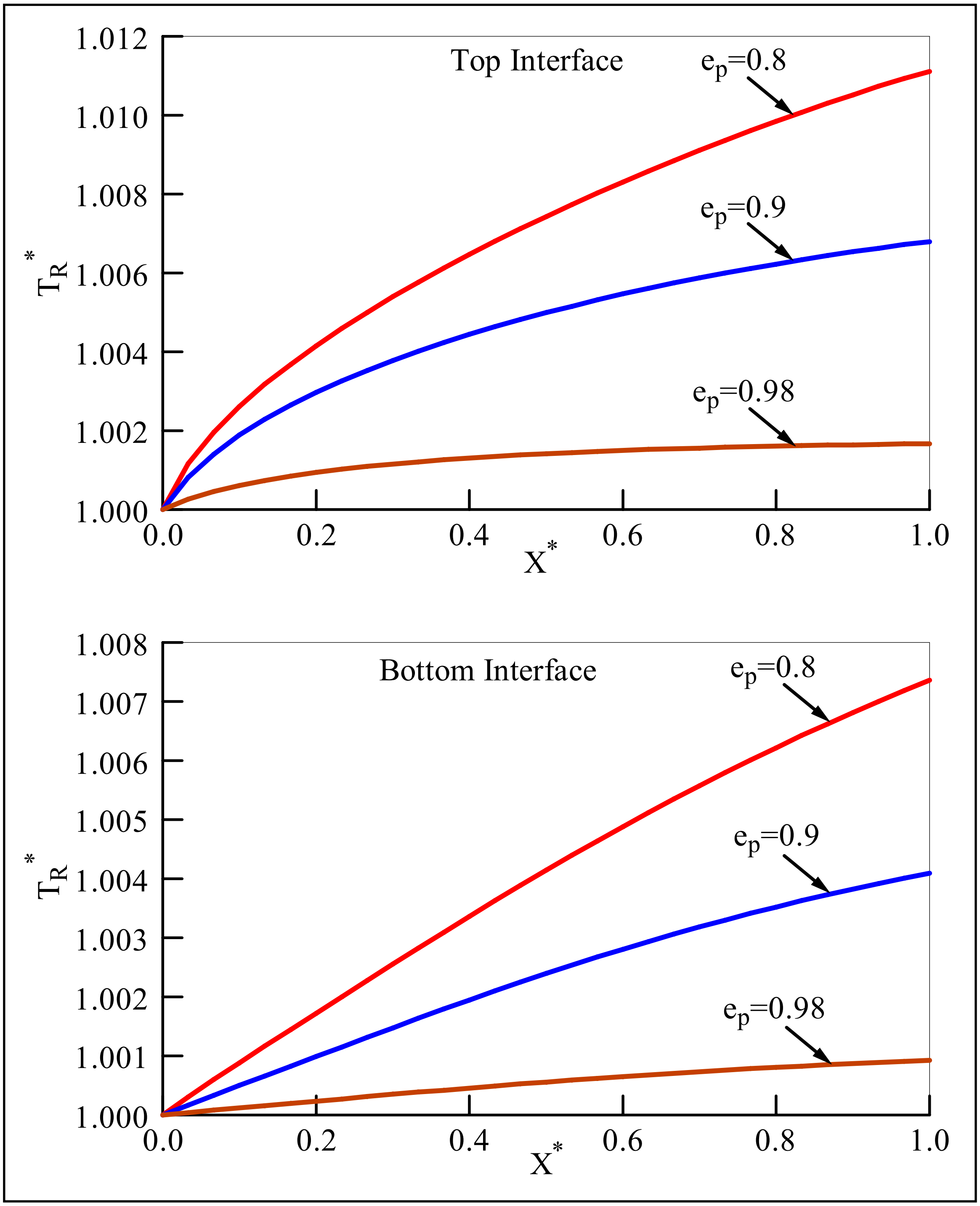

Figure 11.5 : The Film Temperature Change with the Granular Coefficient of Restitution at Both Interfaces

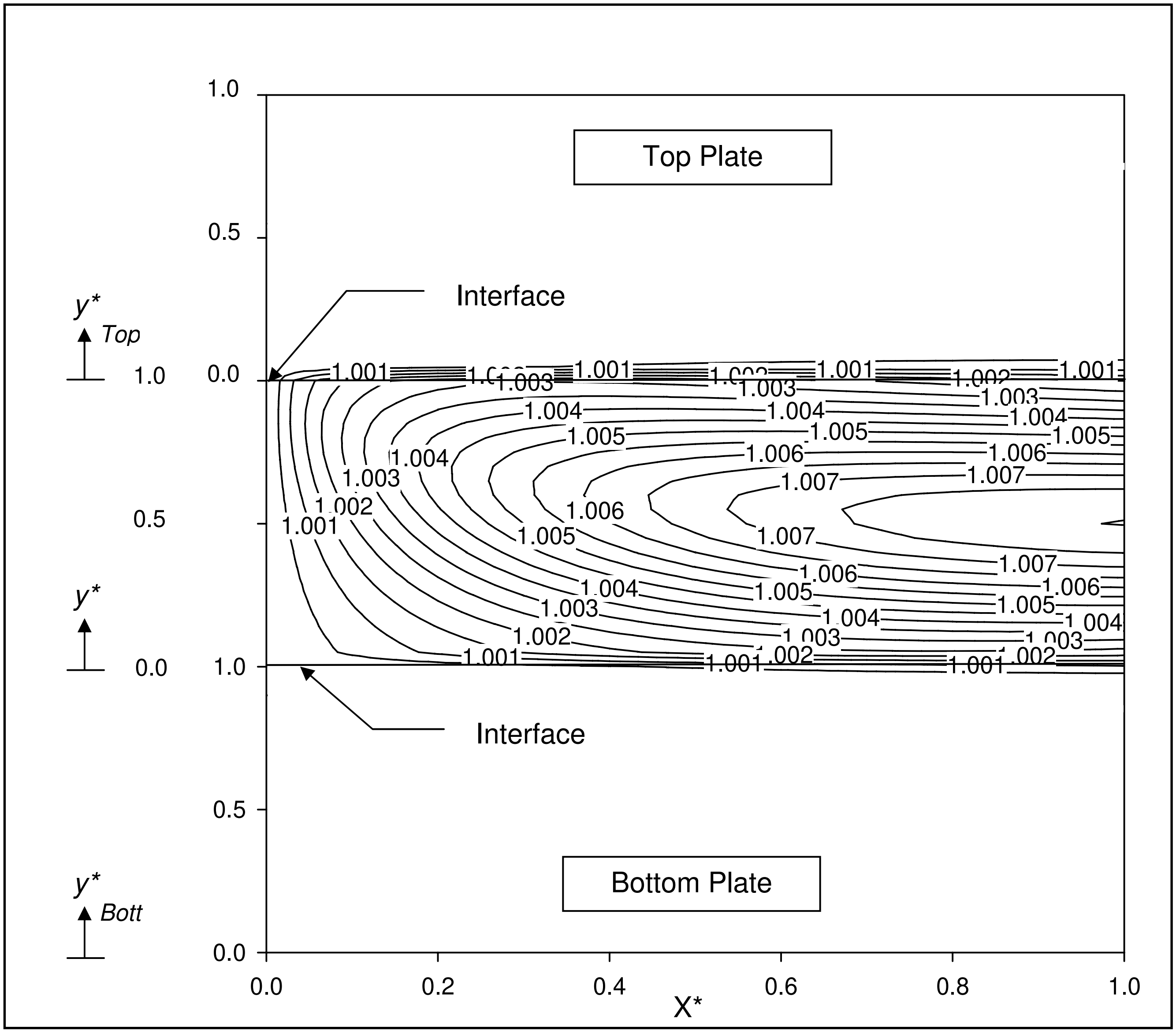

Figure 11.6 : The Distribution of the True Temperature in the Granular Flow and the Fields of the Top and Bottom Plates for $e_p = 0.98$

11.8.4 Variation of the True Temperature with Velocity of the Moving Plate

Figure 11.8 presents the change in the true temperature profiles on the top and bottom interfaces by varying the sliding velocity of the bottom plate. The temperature tends to increase by increasing the sliding velocity for both interfaces. To explain this trend, one must consider the energy equations for the granular flow (11-6) and the governing equation of the bottom plate (11-8). The effect of the convection terms in those two equations have a clear influence and become more pronounced on the true temperature of the granular flow and the moving plate as the speed of the moving plate increases. As shown in Figure 11.4 the distribution of the true temperature on both the stationary and the moving plates indicate that only a thin layer of both plates that are close to the granular material and are affected by the heat generated in the granular flow. Therefore, there is less energy out through the bottom and top plates which make them behave as if they were insulated. Thus the true temperature in the channel is increased with increasing the sliding velocity.

11.9 Conclusions

The true temperature of the granular material flowing between two parallel plates is studied. The distribution of the true temperature at both top and bottom interfaces along the x-direction is predicted and the variation of a number of important parameters and their effect on the true temperature is analyzed. The results show that the temperature increases from the inlet to the outlet for both top and bottom interfaces. The viscous dissipation term is found to play a role on predicting the true temperature. It supplies the energy to the flow as a result of inelastic collision between the granules. In addition, the specific heat and the effective thermal conductivity have their effect on predicting the true temperature. The viscous dissipation appears in the pseudo energy equation and is a function of the fluctuation velocity (pseudo temperature) and the solid volume fraction. The larger the fluctuation velocity, the greater becomes the chance of collision between granules. Therefore, the energy dissipation caused by the inelastic collision increases which cause the true temperature to increase. Increasing the granular material coefficient of restitution results a lower temperature at the interfaces due to the fact that the more elastic the material, the less energy loss by inelastic collision between granules (less heat dissipation). As the roughness factor increases, it causes a decrease in the slip velocity at the top boundary and the granules around this boundary become almost stationary which means the slip effect becomes nil. Thus, as the roughness becomes larger, less fluctuation velocity occurs and there is less energy being transferred to the adjacent layer of granules which in turn decreases the true temperature at this interface. On the other hand, the temperature tends to increase by increasing the sliding velocity of the bottom plate for both interfaces due to the pronounced effect of the convection terms in the granular flow and the bottom plate equations.

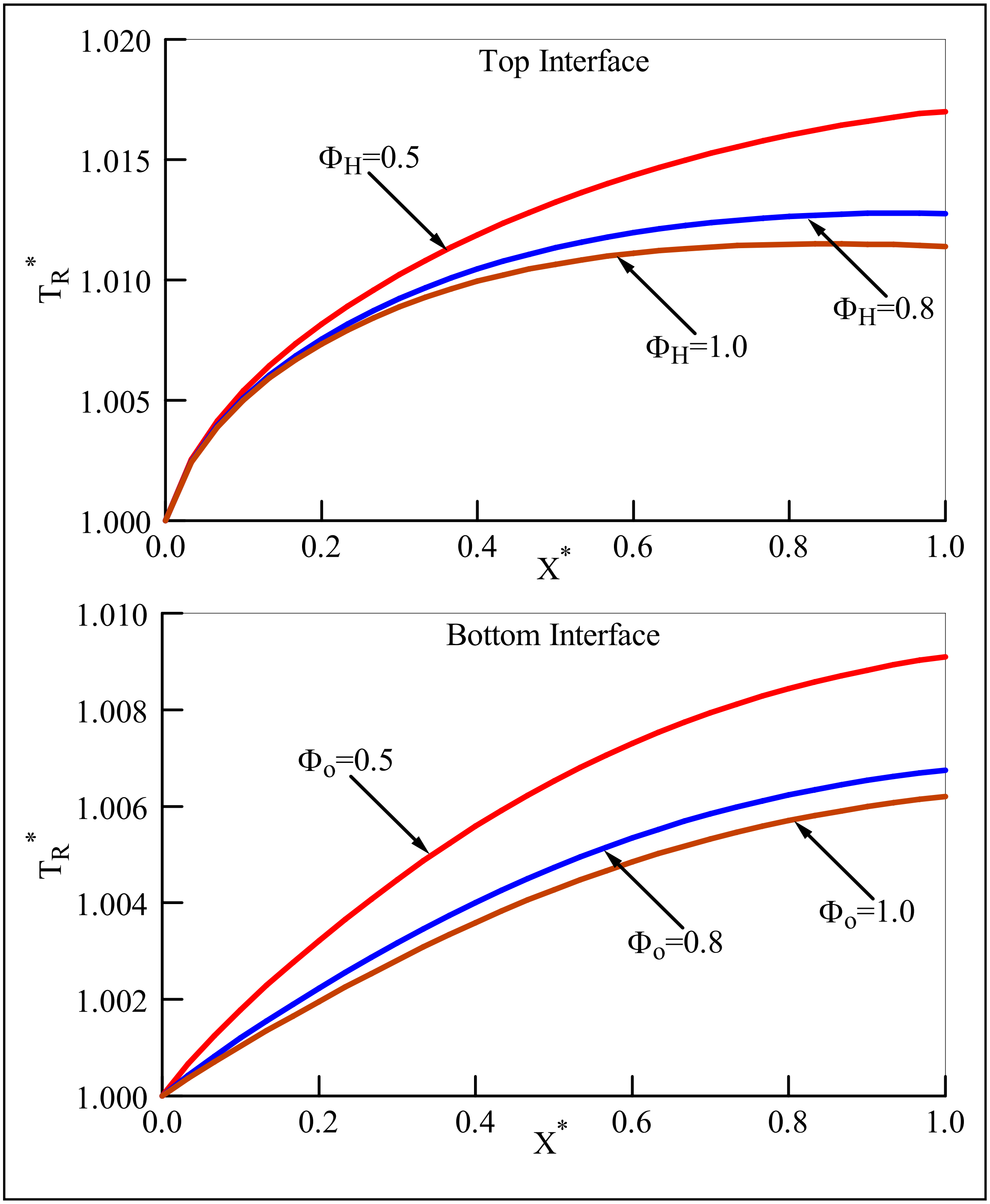

Figure 11.7 : The Film Temperature Change with the Roughness Factor for the Top Plate (ϕ_H) and the Roughness Factor for the Bottom Plate (ϕ_o)

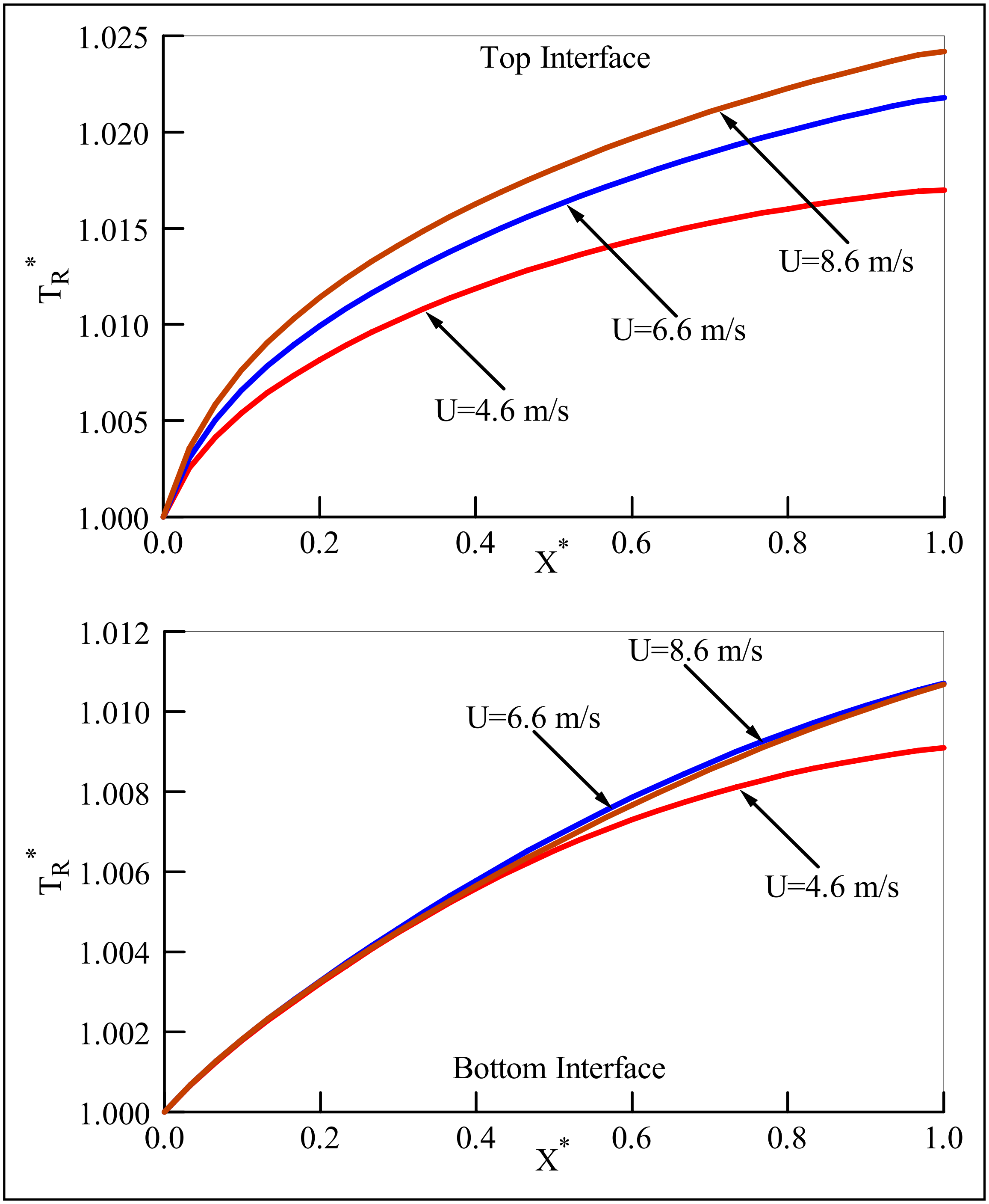

Figure 11.8 : The Film Temperature Change with the Velocity of the Moving Plate at Both Interfaces

It is concluded that for a flow between two parallel plates, a very small rise of the true temperature is experienced in the direction of motion from inlet to outlet. Whereas, Heshmat and Brewe [89] described experimentally the thermal phenomena and the heat characteristics of a slider-type powder lubricated bearings. At 30,000 rpm, the rise of the true temperature was approximately 60^oC. They also showed that the thermal stability was achieved at different load and speed combinations. This is an interesting phenomenon since it indicates that in thrust-type bearings, the wedge effect has a pronounced effect on the true temperature.

CHAPTER 12. ENDURING CONTACT IN GRANULAR LUBRICATION

12.1 Introduction

In most of the published literature in granular material, the formulation is restricted to rapid shearing where the kinetics and collision effect and granular stresses are generated by the instantaneous binary inelastic collisions between the granules. As such, the effect of the so-called “enduring contact” is neglected. However, in a dense regime the granules are sliding and the contact may not be necessarily instantaneous. The enduring contact can play an important role on the friction behavior. Hence, the effect of enduring contact must be carefully examined, particularly in the view of relatively small clearance gaps and high solid volume fraction in applications involving granular lubrication.

Pioneering experiments of Bagnold [2] dating back to 1954 have revealed the development of the so-called transient regime where both collision and enduring contact between the granules exist simultaneously. Johnson and Jackson [15] developed a model that takes into account the effect of the enduring contact between the granules using the Coulomb law of friction to relate the tangential and normal forces of the sliding granules. Jang and Khonsari [89] applied the theory to study the enduring contact between granules of powder lubricant in a bearing. They found that the enduring contact tends to dominate the kinetic regime of a powder lubricant at low speed. Another important effect that is often neglected is the true temperature of a granular material during the shearing process and its influence on the grain mobility. In contrast, the influence of the so-called pseudo temperature in granular material which represents the velocity fluctuation has been studied in many papers [25, 26, 33, 40, and 43].

In this paper, the effect of the enduring contact and the true temperature are investigated for a granular lubricant sheared between two parallel plates. The appropriate equations are derived including both the enduring contact as well as the inelastic collision between the granules.

12.2 Theory

In this section, The theory presented in this paper closely follows the work of Johnson and Jackson [15], Lun and Savage [12], Hui and Haff [27], and Jenkins and Savage [7] and Zhou and Khonsari [30]. A realistic constitutive equation introduced by Lun *et al.* [8] is utilized to study the mechanism of powder lubrication. The effect of viscous dissipation term is included in the pseudo energy equation and the distribution of solid volume fraction together with the mean velocity and the pseudo temperature appear naturally in the governing equations and are directly predicted by the theory presented herein. The general conservation laws, the constitutive equations and the boundary conditions are applied to a particular flow field where a granular lubricant sheared between two parallel plates taking into consideration the enduring contact effect between the granules. As shown in Figure 8.1, the upper plate is stationary while the bottom plate undergoes a constant slider motion *U*. For parallel plates, the conservation of mass is satisfied automatically.

This kinetic theory is based on the binary collision hypothesis in which enduring contact is to be considered, the stress tensor is composed of the collision and kinetic motion as well as the enduring contact. The characteristics of the flow are investigated in a transient regime where both kinetic-collision effect and enduring contact exists concurrently. The Coulomb friction model is introduced to study the effect of the friction force caused by enduring contact between the granules. The formulation of the enduring contact developed by Johnson and Jackson [15] is used in this paper.

12.3 Governing Equations

The general governing equation (3-1), (3-2), (3-4), along with the constitutive relations (4-1), (4-8) and (4-10) are reduced to the following set of equations:

12.3.1 Conservation of Mass

The governing equation for conservation of mass is:

$$\frac{d(\rho u)}{dx} = 0 \tag{12-1}$$

12.3.2 Conservation of Momentum

The governing equation for conservation of momentum is:

$$\rho \frac{DU}{Dt} = \rho g - \nabla . \sigma \tag{12-2}$$

where $\sigma = \sigma_{ck} + \sigma_f$, σ_{ck} is the stress tensor caused by collision and the kinetic motion, and σ_f represents the stress tensor caused by enduring contact force between granules.

Based on Coulomb failure criterion, the shear stress is proportional to the normal stress in a fully developed plane shear and the granules are assumed to be cohesionless (Figure 12.1). The contribution of the enduring contact to shear stress is:

$$S_f = N_f Sin\phi \tag{12-3}$$

where ϕ is the internal angle of friction and N_f represents the frictional normal stress (enduring contact contribution to normal stress) and defined by:

$$N_f = \frac{F_r}{(\upsilon_{\max} - \upsilon)^n} \tag{12-4}$$

where F_r is a dimensional stress constant carrying units of $\mathrm{kg/ms^2}$ and n is an integer constant. At the boundaries, the magnitude of the tangential component of enduring contact is $N_f \tan\delta$, where δ is the angle of friction between the surface and the granule.

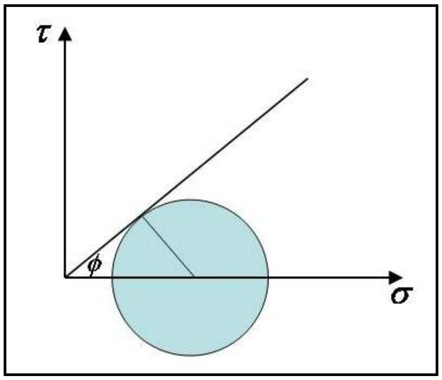

Figure 12.1 : Mohr Stress Diagram

The stress tensor by enduring contact presented by Johnson and Jackson [15] is given by,

$$\sigma_f = \begin{bmatrix} N_f & -\Gamma N_f Sin\phi & 0 \\ -\Gamma N_f Sin\phi & N_f & 0 \\ 0 & 0 & N_f \end{bmatrix} \tag{12-5}$$

where, $\Gamma = \begin{cases} 1 & \text{for } \partial u / \partial y > 0 \\ -1 & \text{for } \partial u / \partial y < 0 \end{cases}$

12.3.2.1 X-Momentum Equation

$$\frac{d}{dy}\left(\sigma_{xy}\right)=0$$

That is,

$$\frac{d}{dy}\left[\left(\rho_p df_2\sqrt{T}\right)\left(\frac{du}{dy}\right)-N_f Sin\phi\right]=0 \tag{12-6}$$

12.3.2.2 Y-Momentum Equation

$$\frac{d}{dy}\left(\sigma_{yy}\right)=0 \Rightarrow \frac{d}{dy}(\rho_p Tf_1+N_f)=0 \tag{12-7}$$

$$\rho_p Tf_1+N_f=N \tag{12-8}$$

12.3.3 Conservation of Energy

The general conservation of energy given by equation (3-4) is divided into two parts, conservation of pseudo energy and conservation of true thermal energy as shown below:

12.3.3.1 Pseudo Energy Equation

$$\frac{D\left(E_{PT}\right)}{Dt}=-\nabla.q_{PT}-\sigma_{ck}:\nabla U-\gamma \tag{12-9}$$

12.3.3.2 True Thermal Energy Equation

$$\frac{D\left(E_h\right)}{Dt}=-\nabla.q_h-\sigma_f:\nabla U+\gamma \tag{12-10}$$

where $\sigma_{ck}:\nabla U$ is the viscous dissipation done by the component of collision stress, $\sigma_f:\nabla U$ represents the viscous dissipation done by the component of frictional stress, and γ is the rate of dissipation due to inelastic collisions between granules.

Using equations (6-12) and (6-13) for $\nabla.\, q_{PT}$ and $\sigma_{ck}:\nabla U$, the conservation of pseudo energy equation can be rewritten as follow:

$$\frac{d}{dy}\left[\left(\rho_p df_3\sqrt{T}\right)\frac{dT}{dy}+\left(\rho_p df_4 T^{3/2}\right)\frac{d\upsilon}{dy}\right]+\rho_p df_2\sqrt{T}\left(\frac{du}{dy}\right)^2-\frac{\rho_p f_5 T^{3/2}}{d}=0 \tag{12-11}$$

12.4 Boundary Conditions

The boundary conditions shown in Figure 12.2 are obtained by substituting the Lun’s constitutive equations into the boundary condition equations (5-8) and (5-14) including the effect of enduring contact.

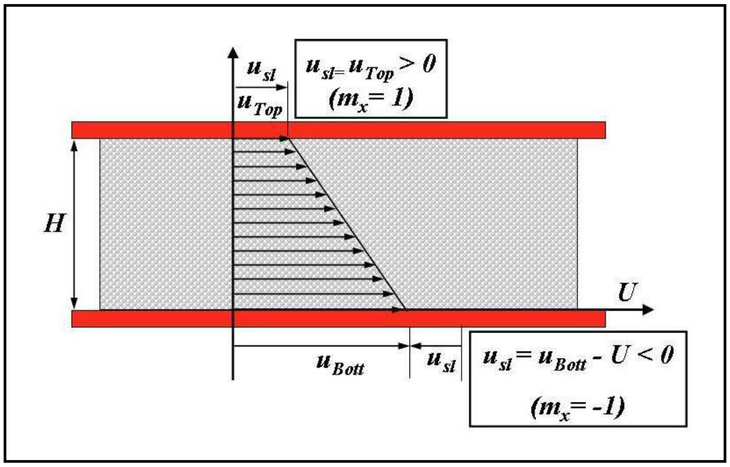

Figure 12.2 : Slip Velocity Boundary Conditions

12.4.1 Slip Velocity Boundary Condition

The condition for the slip velocity (5-1) to (5-8) between the boundary and the granules is derived following the work of Johnson and Jackson [15]. In granular flows, the boundaries tend to supply the momentum and the energy to the interior flow by the means of shearing force and normal force. The supplied energy must be in balance with the stress and the total flux of the energy in the flow. The condition for the slip velocity is obtained by equating the total tangential force acting on the boundary and the rate of momentum transfer to unit area of the surface by collision. The tangential component of the enduring contact is also added to (5-6) and the general form of the slip boundary condition is given by:

$$\underbrace{\frac{\phi_w \sqrt{3}\,\pi\,\rho_p\,\upsilon T^{\frac{1}{2}}|u_{sl}|}{6\upsilon_{\max}\left[1-\left(\dfrac{\upsilon}{\upsilon_{\max}}\right)^{\frac{1}{3}}\right]}}_{\text{Rate of momentum transfer to the wall}} + \underbrace{\frac{u_{sl}.(\sigma_{ck}+\sigma_f).n}{|u_{sl}|} + N_f \tan}_{\text{Tangential force per unit area acting on the boundary}}\delta = 0 \qquad (12\text{-}12)$$

Again we can rewrite the slip velocity equation as follow:

$$\frac{u_{sl}}{|u_{sl}|}.\left(\sigma_{ck}+\sigma_f\right).n+\frac{\sqrt{3}\,\pi}{6\upsilon_{\max}}\phi_w\,\rho_p\;\upsilon\,g_o\sqrt{T}\,|u_{sl}|+N_f\tan\delta=0$$

That is,

$$\frac{u_{sl}}{|u_{sl}|}.\begin{bmatrix}\sigma_{xx} & \sigma_{xy} & \sigma_{xz}\\ \sigma_{yx} & \sigma_{yy} & \sigma_{yz}\\ \sigma_{zx} & \sigma_{zy} & \sigma_{zz}\end{bmatrix}.\begin{bmatrix}0\\ \pm 1\\ 0\end{bmatrix}+\frac{\sqrt{3}\,\pi}{6\upsilon_{\max}}\phi_w\;\rho_p\;\upsilon\,g_o\sqrt{T}\,|u_{sl}|+N_f\tan\delta=0 \qquad (12\text{-}13)$$

Using equations (6-1) and (12-5), the total stress tensor is defined by:

$$\sigma=\sigma_{ck}+\sigma_f=\begin{bmatrix}\sigma_{xx} & \sigma_{xy} & \sigma_{xz}\\ \sigma_{yx} & \sigma_{yy} & \sigma_{yz}\\ \sigma_{zx} & \sigma_{zy} & \sigma_{zz}\end{bmatrix}=\begin{bmatrix}\rho_p Tf_1+N_f & -\rho_p d\sqrt{T}f_2\left(\frac{\partial u}{\partial y}\right)+N_f Sin\phi & 0\\ -\rho_p d\sqrt{T}f_2\left(\frac{\partial u}{\partial y}\right)+N_f Sin\phi & \rho_p Tf_1+N_f & 0\\ 0 & 0 & \rho_p Tf_1+N_f\end{bmatrix}$$

(12-14)

where σ_{ck} is the stress tensor caused by collision and the kinetic motion, and σ_f represents the stress tensor caused by enduring contact force between granules.

12.4.1.1 Top Plate

$$\frac{u_{sl}}{|u_{sl}|}.\left(-\sigma_{xy}\right)+\frac{\sqrt{3}\,\pi}{6\upsilon_{\max}}\phi_w\,\rho_p\;\upsilon\,g_o\sqrt{T}\,|u_{sl}|+N_f\tan\delta=0$$

$$\frac{u_{sl}}{|u_{sl}|}.\left(\rho_p df_2\sqrt{T}\left(\frac{du}{dy}\right)+\Gamma N_f Sin\phi\right)+\frac{\sqrt{3}\,\pi}{6\upsilon_{\max}}\phi_w\,\rho_p\;\upsilon\,g_o\sqrt{T}\,|u_{sl}|+N_f\tan\delta=0$$

$$\left[\rho_p df_2\sqrt{T}\left(\frac{du}{dy}\right)+\Gamma N_f Sin\phi+\frac{\sqrt{3}\,\pi}{6\upsilon_{\max}}\phi_w\,\rho_p\;\upsilon\,g_o\sqrt{T}\,u_{sl}\right]m_x+N_f\tan\delta=0$$

and since u_{sl} is positive and Γ is negative at the top plate, we can rewrite the top boundary condition as follow:

$$\left[\rho_p df_2\sqrt{T}\left(\frac{du}{dy}\right)+\Gamma N_f Sin\phi+\frac{\sqrt{3}\,\pi}{6\upsilon_{\max}}\phi_H\,\rho_p\;\upsilon\,g_o\sqrt{T}u\right]+N_f\tan\delta=0$$

$$\rho_p d f_2 \sqrt{T}\left(\frac{du}{dy}\right)+\frac{\sqrt{3}\,\pi}{6\upsilon_{\max}}\phi_H\,\rho_p\,\upsilon\, g_o\sqrt{T}u+N_f\left(\tan\delta-Sin\phi\right)=0$$

$$\frac{du}{dy}+\frac{\sqrt{3}\,\pi\,\upsilon\, g_o\phi_H}{6\upsilon_{\max}f_2\, d}u+\frac{N_f}{\rho_p d f_2\sqrt{T}}\left(\tan\delta-Sin\phi\right)=0$$

The slip boundary conditions for the top plate can be reduced to the following form:

$$\frac{du}{dy}+\frac{f_8\,\phi_H}{d}u+\frac{N_f}{\rho_p d f_2\sqrt{T}}\left(\tan\delta-Sin\phi\right)=0 \tag{12-15}$$

12.4.1.2 Bottom Plate

$$\frac{u_{sl}}{\left|u_{sl}\right|}.\sigma_{xy}+\frac{\sqrt{3}\,\pi}{6\upsilon_{\max}}\phi_w\,\rho_p\,\upsilon\, g_o\sqrt{T}\left|u_{sl}\right|+N_f\tan\delta=0$$

$$\frac{u_{sl}}{\left|u_{sl}\right|}.\left(\rho_p d f_2\sqrt{T}\left(\frac{du}{dy}\right)+\Gamma N_f Sin\phi\right)-\frac{\sqrt{3}\,\pi}{6\upsilon_{\max}}\phi_w\,\rho_p\,\upsilon\, g_o\sqrt{T}\left|u_{sl}\right|-N_f\tan\delta=0$$

$$\left[\rho_p d f_2\sqrt{T}\left(\frac{du}{dy}\right)+\Gamma N_f Sin\phi-\frac{\sqrt{3}\,\pi}{6\upsilon_{\max}}\phi_w\,\rho_p\,\upsilon\, g_o\sqrt{T}\,u_{sl}\right]m_x-N_f\tan\delta=0$$

and because u_{sl} and Γ are negative at the bottom plate, we can rewrite the bottom boundary condition as follow:

$$\left[-\rho_p d f_2\sqrt{T}\left(\frac{du}{dy}\right)-\Gamma N_f Sin\phi+\frac{\sqrt{3}\,\pi}{6\upsilon_{\max}}\phi_o\,\rho_p\,\upsilon\, g_o\sqrt{T}\left(u-U\right)\right]-N_f\tan\delta=0$$

$$\rho_p d f_2\sqrt{T}\left(\frac{du}{dy}\right)-\frac{\sqrt{3}\,\pi}{6\upsilon_{\max}}\phi_o\,\rho_p\,\upsilon\, g_o\sqrt{T}\left(u-U\right)+N_f\left(\tan\delta-Sin\phi\right)=0$$

$$\frac{du}{dy}-\frac{\sqrt{3}\,\pi\,\upsilon\, g_o\phi_o}{6\upsilon_{\max}f_2\, d}\left(u-U\right)+\frac{N_f}{\rho_p d f_2\sqrt{T}}\left(\tan\delta-Sin\phi\right)=0$$

The slip boundary conditions for the bottom plate can be reduced to the following form:

$$\frac{du}{dy}-\frac{f_8\,\phi_o}{d}\left(u-U\right)+\frac{N_f}{\rho_p d f_2\sqrt{T}}\left(\tan\delta-Sin\phi\right)=0 \tag{12-16}$$

12.4.2 Pseudo Temperature Boundary Condition

The boundary condition for the pseudo temperature is obtained by equating the rate of heat generation due to slip at the boundary to the rate of heat dissipated due to the granules inelastic-collision. The general form of the pseudo temperature boundary condition is given by:

$$n.q_{PT} = \left(\frac{\pi\sqrt{3}}{6\upsilon_{\max}}\right)\phi_w \rho_p \,\upsilon\, g_o \sqrt{T}\; u_{sl}^2 - \left(\frac{\pi\sqrt{3}}{4\upsilon_{\max}}\right)\left(1-e_w^2\right)\rho_p\,\upsilon\, g_o T^{3/2} \tag{12-17}$$

The boundary conditions for the pseudo temperature at both top and bottom plates are obtained from equations (6-21) and (6-22) as follow:

12.4.2.1 Top Plate

$$\frac{dT}{dy} = -T\frac{f_4}{f_3}\frac{d\upsilon}{dy} + \frac{\varphi_H f_7}{d}\left(u_{sl}\right)^2 - T\frac{f_6\left(1-e_w^2\right)}{d} \tag{12-18}$$

12.4.2.2 Bottom Plate

$$\frac{dT}{dy} = -T\frac{f_4}{f_3}\frac{d\upsilon}{dy} - \frac{\varphi_o f_7}{d}\left(u_{sl}\right)^2 + T\frac{f_6\left(1-e_w^2\right)}{d} \tag{12-19}$$

The above equations are in agreement with Jang and Khonsari [89].

12.5 Elimination of the Volume Fraction

The equations can be simplified by eliminating the coupling term of the volume fraction from the pseudo energy equation (12-11), and the pseudo temperature boundary conditions (12-18) and (12-19) as follow:

By using the y-momentum equation (12-7), and substituting with the functions given in Table 6.1 we have:

$$\rho_p\frac{d}{dy}T\upsilon\left(1+4\eta\upsilon g_o\right) + \frac{d}{dy}N_f = 0$$

$$\rho_p\left[\frac{dT}{dy}\left(\upsilon\left(1+4\eta\upsilon g_o\right)\right) + T\frac{d\upsilon}{dy}\left(1+4\eta\upsilon g_o\right) + T\upsilon\left(4\eta\frac{d\upsilon}{dy}g_o + 4\eta\upsilon\frac{dg_o}{dy}\right)\right] + \frac{d}{dy}N_f = 0$$

where $f_1(\upsilon) = \upsilon\left(1+4\eta\upsilon g_o\right)$

Also since $g_o = \frac{1}{1-\left(\upsilon/\upsilon_{\max}\right)^{1/3}} = \frac{\upsilon_{\max}^{1/3}}{\upsilon_{\max}^{1/3} - \upsilon^{1/3}}$, and $\frac{dg_o}{dy} = \frac{g_o^2}{3\upsilon_{\max}}\left(\frac{\upsilon_{\max}}{\upsilon}\right)^{2/3}\frac{d\upsilon}{dy}$ then we have,

$$\rho_p\left[\frac{dT}{dy}\left(\upsilon(1+4\eta\upsilon g_o)\right) + T\frac{d\upsilon}{dy}(1+4\eta\upsilon g_o) + T\upsilon\left(4\eta\frac{d\upsilon}{dy}g_o + 4\eta\upsilon\frac{dg_o}{dy}\right)\right] + \frac{d}{dy}N_f = 0$$

$$\rho_p\left[\frac{dT}{dy}f_1 + \frac{d\upsilon}{dy}\frac{Tf_1}{\upsilon} + \frac{d\upsilon}{dy}4\eta g_o T\upsilon + 4\eta\upsilon^2 T\frac{g_o^2}{3\upsilon_{\max}}\left(\frac{\upsilon_{\max}}{\upsilon}\right)^{2/3}\frac{d\upsilon}{dy}\right] + \frac{d}{dy}N_f = 0$$

$$\frac{dT}{dy}f_1 + \frac{d\upsilon}{dy}\left[\frac{Tf_1}{\upsilon} + 4\eta g_o T\upsilon + \frac{4}{3}\eta\upsilon^2 T g_o^2\frac{1}{\upsilon^{2/3}\upsilon_{\max}^{1/3}}\right] + \frac{1}{\rho_p}\frac{d}{dy}N_f = 0$$

$$\frac{d\upsilon}{dy} = -\frac{dT}{dy}\frac{f_1}{\left[\frac{Tf_1}{\upsilon} + 4\eta g_o T\upsilon + \frac{4}{3}\eta\upsilon^2 T g_o^2\frac{1}{\upsilon^{2/3}\upsilon_{\max}^{1/3}}\right]} - \frac{dN_f}{dy}\frac{1}{\rho_p\left[\frac{Tf_1}{\upsilon} + 4\eta g_o T\upsilon + \frac{4}{3}\eta\upsilon^2 T g_o^2\frac{1}{\upsilon^{2/3}\upsilon_{\max}^{1/3}}\right]}$$

$$\frac{d\upsilon}{dy} = -\frac{f_1}{T\left[\frac{f_1}{\upsilon} + 4\eta g_o\upsilon + \frac{4}{3}\eta\upsilon^2\ g_o^2\ \frac{1}{\upsilon^{2/3}\upsilon_{\max}^{1/3}}\right]}\frac{dT}{dy} - \frac{1}{\rho_p T\left[\frac{f_1}{\upsilon} + 4\eta g_o\upsilon + \frac{4}{3}\eta\upsilon^2\ g_o^2\ \frac{1}{\upsilon^{2/3}\upsilon_{\max}^{1/3}}\right]}\frac{dN_f}{dy}$$

Substituting with the values of g_o and f_1 in the denominator, we have

$$\frac{d\upsilon}{dy} = -\frac{g_1(\upsilon)}{T}\left(\frac{dT}{dy} + \frac{1}{\rho_p}\frac{dN_f}{dy}\right) \tag{12-20}$$

where $g_1(\upsilon) = \dfrac{f_1}{1 + \dfrac{8\eta\upsilon\upsilon_{\max}^{1/3}}{\upsilon_{\max}^{1/3} - \upsilon^{1/3}} + \dfrac{\frac{4}{3}\eta\upsilon^{4/3}\upsilon_{\max}^{1/3}}{\left(\upsilon_{\max}^{1/3} - \upsilon^{1/3}\right)^2}}$

12.5.1 Pseudo Energy Equation

Using equation (12-20) back in the energy equation (12-11) we have the final form of the pseudo temperature energy equation as follows:

$$\frac{d}{dy}\left\{f_3\sqrt{T}\frac{dT}{dy} - f_4 g_1\sqrt{T}\frac{dT}{dy} - \frac{f_4 g_1}{\rho_p}\sqrt{T}\frac{dN_f}{dy}\right\} + f_2\sqrt{T}\left(\frac{du}{dy}\right)^2 - \frac{f_5 T^{3/2}}{d^2} = 0$$

$$\frac{d}{dy}\left[(f_3 - f_4 g_1)\sqrt{T}\frac{dT}{dy}\right] - \frac{d}{dy}\left[\left(\frac{f_4 g_1}{\rho_p}\right)\sqrt{T}\frac{dN_f}{dy}\right] + f_2\sqrt{T}\left(\frac{du}{dy}\right)^2 - \frac{f_5 T^{3/2}}{d^2} = 0 \tag{12-21}$$

12.5.2 Pseudo Temperature Boundary Condition

Similarly, substitute equation (12-20) in the pseudo temperature boundary condition equations (12-18) and (12-19) yield the following equations:

12.5.2.1 Top Plate

$$\frac{dT}{dy} = -T\frac{f_4}{f_3}\left[-\frac{g_1}{T}\left(\frac{dT}{dy}+\frac{1}{\rho_p}\frac{dN_f}{dy}\right)\right]+\frac{\varphi_H f_7}{d}\left(u_{sl}\right)^2 - T\frac{f_6\left(1-e_w^2\right)}{d}$$

$$\frac{dT}{dy} = \frac{f_4 g_1}{(f_3 - f_4 g_1)}\frac{1}{\rho_p}\frac{dN_f}{dy} - T\frac{f_3 f_6}{(f_3 - f_4 g_1)}\frac{\left(1-e_w^2\right)}{d} + \frac{f_3 f_7}{(f_3 - f_4 g_1)}\frac{\varphi_H}{d}u^2$$

$$\frac{dT}{dy} = \frac{ff_5}{\rho_p}\frac{dN_f}{dy} - T\frac{ff_3\left(1-e_w^2\right)}{d} + \frac{ff_4 \varphi_H}{d}u^2 \tag{12-22}$$

12.5.2.2 Bottom Plate

$$\frac{dT}{dy} = -T\frac{f_4}{f_3}\left[-\frac{g_1}{T}\left(\frac{dT}{dy}+\frac{1}{\rho_p}\frac{dN_f}{dy}\right)\right]-\frac{\varphi_o f_7}{d}\left(u_{sl}\right)^2 + T\frac{f_6\left(1-e_w^2\right)}{d}$$

$$\frac{dT}{dy} = \frac{f_4 g_1}{\left(f_3 - f_4 g_1\right)}\frac{1}{\rho_p}\frac{dN_f}{dy} + T\frac{f_3 f_6}{\left(f_3 - f_4 g_1\right)}\frac{\left(1-e_w^2\right)}{d} - \frac{f_3 f_7}{\left(f_3 - f_4 g_1\right)}\frac{\varphi_o}{d}\left(u-U\right)^2$$

$$\frac{dT}{dy} = \frac{ff_5}{\rho_p}\frac{dN_f}{dy} + T\frac{ff_3\left(1-e_w^2\right)}{d} - \frac{ff_4 \varphi_o}{d}\left(u-U\right)^2 \tag{12-23}$$

where $ff_3 = \dfrac{f_3 f_6}{f_3 - f_4 g_1}$, $ff_4 = \dfrac{f_3 f_7}{f_3 - f_4 g_1}$, and $ff_5 = \dfrac{f_4 g_1}{(f_3 - f_4 g_1)}$

12.6 True Temperature Energy Equation

Let us now consider the equation of the conservation of the true thermal energy (12-10). By substituting with the values of the true heat flux and the true thermal internal energy of single granule (3-10) along with the correlation of the effective thermal conductivity (11-5) discussed in Chapter 11, the true thermal energy equation can be rewritten as follow:

$$\frac{D}{Dt}(\rho c_p T_R) = -\nabla.(-k_{eff}\nabla T_R) - \sigma_f : \nabla U + \gamma$$

By dropping the low order terms and substituting with the stress tensor by enduring contact (12-5), we have

$$\underbrace{\rho_p \upsilon c_p u \frac{\partial T_R}{\partial x}}_{\text{Convection}} = \underbrace{k_{eff} \frac{\partial^2 T_R}{\partial y^2} + \frac{\partial k_{eff}}{\partial y} \frac{\partial T_R}{\partial y}}_{\text{Conduction}} \underbrace{- N_f Sin\phi \frac{\partial u}{\partial y} + \frac{\rho_p f_5 T^{3/2}}{d}}_{\text{Dissipation}} \tag{12-24}$$

where $k_{eff}(\upsilon) = k_{air} \dfrac{1 + 2\beta\upsilon + \left(k_p - 3\beta^2\right)\upsilon^3}{1 - \beta\upsilon}$

12.7 Normalization

In what follows, we shall make use of the following dimensionless parameters:

$$u^* = \frac{u}{U},\ T^* = \frac{\rho_p T}{N},\ y^* = \frac{y}{H}\ ,\ N_f^* = \frac{N_f}{N} \tag{12-25}$$

where N is the normal load per unit area, and H is the gap thickness.

12.7.1 Dimensionless Governing Equations

Using the dimensionless parameters (12-25) yields to the following dimensionless governing equations and boundary conditions:

12.7.1.1 X-Momentum Equation

$$\frac{d}{dy^*}\left[ACf_2\sqrt{T^*}\left(\frac{du^*}{dy^*}\right) - N_f^* Sin\phi \right] = 0 \tag{12-26}$$

12.7.1.2 Y-Momentum Equation

$$T^* f_1 + N_f^* = 1 \tag{12-27}$$

12.7.1.3 Pseudo Energy Equation

$$\frac{d}{dy^*}\left[(f_3 - f_4 g_1)\sqrt{T^*}\frac{dT^*}{dy^*} \right] - \frac{d}{dy^*}\left[(f_4 g_1)\sqrt{T^*}\frac{dN_f^*}{dy^*} \right] + A^2 f_2 \sqrt{T^*}\left(\frac{du^*}{dy^*}\right)^2 - \frac{f_5 T^{*3/2}}{C^2} = 0 \tag{12-28}$$

where $A = \dfrac{U\sqrt{\rho_p}}{\sqrt{N}}, C = \dfrac{d}{H}$

12.7.1.4 True Temperature Energy Equation

Using of the dimensionless parameters (11-23) in addition to the dimensionless parameters (12-25) yields to the true thermal energy equation in dimensionless form as follow:

$$\upsilon u^* \frac{\partial T_R^*}{\partial x^*} = \frac{k_p L}{\rho_p c_p U H^2} k_{eff}^* \frac{\partial^2 T_R^*}{\partial y^{*2}} + \frac{k_p L}{\rho_p c_p U H^2} \frac{\partial k_{eff}^*}{\partial y^*} \frac{\partial T_R^*}{\partial y^*} - \frac{NL}{\rho_p c_p T_{in} H} N_f^* Sin\phi \frac{\partial u^*}{\partial y^*} + \frac{N^{3/2} L}{c_p T_{in} U \rho_p^{3/2} d} T^{*3/2} f_5$$

That is,

$$\upsilon u^* \frac{\partial T_R^*}{\partial x^*} = \left(A_2^*\right) k_{eff}^* \frac{\partial^2 T_R^*}{\partial y^{*2}} + \left(A_2^*\right) \frac{\partial k_{eff}^*}{\partial y^*} \frac{\partial T_R^*}{\partial y^*} - \left(\frac{A_3^*}{C}\right) N_f^* Sin\phi \frac{\partial u^*}{\partial y^*} + \left(\frac{A_3^*}{A_1^*}\right) T^{*3/2} f_5 \qquad (12\text{-}29)$$

where A_1^*, A_2^*, A_3^*, and C are constants defined as $A_1^* = \frac{\rho_p^{1/2} U}{N^{1/2}}$, $A_2^* = \frac{\alpha_p L}{U H^2}$, $A_3^* = \frac{NL}{\rho_p c_p T_{in} d}$,

$\alpha_p = \frac{k_p}{\rho_p c_p}$, and $C = \frac{d}{H}$

12.7.1.5 Continuity Equation

For a Couette flow, the distribution of bulk velocity is independent of the flowing direction. Hence, the mass flow rate in the gap of a Couette flow is constant, and the conservation of mass is automatically satisfied. Rewriting equation (12-1) accounting for a fixed gap and the fact that $\rho = \rho_p \upsilon$, we have

$$\frac{d}{dx} \int_0^H \rho_p \upsilon \, \mathrm{u} \, dy = 0$$

and in dimensionless form, we can write:

$$\dot{m}^* = \frac{\dot{m}}{\rho_p U H} = \frac{d}{dx^*} \int_0^1 \upsilon \, \mathrm{u}^* \, dy^* \qquad (12\text{-}30)$$

12.7.2 Dimensionless Boundary Conditions

The results of the dimensionless boundary conditions are summarized below:

12.7.2.1 At y^*= 1 (Top Plate)

$$\frac{du^*}{dy^*} = -\frac{f_8 \phi_H u^*}{C} - \frac{N_f^*}{A C f_2 \sqrt{T^*}} \left(\tan\delta - Sin\phi\right) \qquad (12\text{-}31)$$

$$\frac{dT^*}{dy^*} = ff_5 \frac{dN_f^*}{dy^*} - \frac{T^* ff_3\left(1-e_w^2\right)}{C} + \frac{A^2 ff_4 \varphi_H u^{*2}}{C} \tag{12-32}$$

12.7.2.2 At $y^*= 0$ (Bottom Plate)

$$\frac{du^*}{dy^*} = \frac{f_8\, \phi_o\left(u^*-1\right)}{C} - \frac{N_f^*}{ACf_2\sqrt{T^*}}\left(\tan\delta - Sin\phi\right) \tag{12-33}$$

$$\frac{dT^*}{dy^*} = ff_5 \frac{dN_f^*}{dy^*} + \frac{T^* ff_3\left(1-e_w^2\right)}{C} - \frac{A^2 ff_4 \varphi_o\left(u^*-1\right)^2}{C} \tag{12-34}$$

12.8 Discretization

The following focuses on presenting the appropriate finite difference equations and the detailed discretization for equations (12-26) to (12-34). Parameter i represents the index for the x-direction and parameter j represents the index for the y-direction. Parameters j_{Flow}, j_{Bott} and j_{Top} are used in the true temperature equation (12-29) and represent the indexes for the y-direction of the granular flow, the bottom plate, and the top plate respectively.

A second order central differencing formula was used for the x-momentum and pseudo energy equation, while a second order forward and backward schemes were used for the bottom and top boundaries respectively. Since the inlet temperature for the true temperature equation is specified, the temperature is solved at every fixed i-section by using the marching technique. Newton's iteration method is also applied in the simulations. In the granular flow governing equation (12-29), first order differentiation formula was used for the convection term since the flow is moving in the x-direction with a specified inlet temperature, while a second order central differencing formula was used for the conduction and dissipation terms.

12.8.1 X-Momentum

$$AC\frac{d}{dy^*}\left[f_2\sqrt{T^*}\left(\frac{du^*}{dy^*}\right)\right] - \frac{d}{dy^*}\left(N_f^* Sin\phi\right) = 0$$

$$\left[\sqrt{T^*}\left(\frac{df_2}{dy^*}\right) + f_2\left(\frac{d\sqrt{T^*}}{dy^*}\right)\right]\left(\frac{du^*}{dy^*}\right) + f_2\sqrt{T^*}\left(\frac{d^2u^*}{dy^{*2}}\right) - \frac{Sin\phi}{AC}\left(\frac{dN_f^*}{dy^*}\right) = 0$$

$$\left[\sqrt{T^*_{i,j}}\left(\frac{f_{2i,j+1}-f_{2i,j-1}}{2\Delta y}\right)+\frac{f_2}{2\sqrt{T^*_{i,j}}}\left(\frac{T^*_{i,j+1}-T^*_{i,j-1}}{2\Delta y}\right)\right]\left(\frac{u^*_{i,j+1}-u^*_{i,j-1}}{2\Delta y}\right)+$$

$$f_2\sqrt{T^*_{i,j}}\left(\frac{u^*_{i,j-1}-2u^*_{i,j}+u^*_{i,j+1}}{\Delta y^2}\right)-\frac{Sin\phi}{AC}\left(\frac{N^*_{f_{i,j+1}}-N^*_{f_{i,j-1}}}{2\Delta y}\right)=0$$

$$\frac{2f_{2i,j}\sqrt{T^*_{i,j}}}{\Delta y^2}u^*_{i,j}=\left[\frac{f_{2i,j}\sqrt{T^*_{i,j}}}{\Delta y^2}+\frac{\sqrt{T^*_{i,j}}}{4\Delta y^2}\left(f_{2i,j+1}-f_{2i,j-1}\right)+\frac{f_{2i,j}}{8\Delta y^2\sqrt{T^*_{i,j}}}\left(T^*_{i,j+1}-T^*_{i,j-1}\right)\right]u^*_{i,j+1}+$$

$$\left[\frac{f_{2i,j}\sqrt{T^*_{i,j}}}{\Delta y^2}-\frac{\sqrt{T^*_{i,j}}}{4\Delta y^2}\left(f_{2i,j+1}-f_{2i,j-1}\right)-\frac{f_{2i,j}}{8\Delta y^2\sqrt{T^*_{i,j}}}\left(T^*_{i,j+1}-T^*_{i,j-1}\right)\right]u^*_{i,j-1}+$$

$$\left[-\frac{Sin\phi}{2\Delta yAC}\left(N^*_{f_{i,j+1}}-N^*_{f_{i,j-1}}\right)\right]$$

$$\left[8f_{2i,j}\right]u^*_{i,j}=\left[4f_{2i,j}+f_{2i,j+1}-f_{2i,j-1}+\frac{f_{2i,j}}{2T^*_{i,j}}\left(T^*_{i,j+1}-T^*_{i,j-1}\right)\right]u^*_{i,j+1}+$$

$$\left[4f_{2i,j}-f_{2i,j+1}+f_{2i,j-1}-\frac{f_{2i,j}}{2T^*_{i,j}}\left(T^*_{i,j+1}-T^*_{i,j-1}\right)\right]u^*_{i,j-1}+\left[\frac{2\Delta ySin\phi}{AC\sqrt{T^*_{i,j}}}\left(N^*_{f_{i,j-1}}-N^*_{f_{i,j+1}}\right)\right] \qquad (12\text{-}35)$$

12.8.2 Pseudo Energy Equation

$$\left(\frac{d\left(f_3-f_4g_1\right)}{dy^*}\right)\sqrt{T^*}\left(\frac{dT^*}{dy^*}\right)+\left(f_3-f_4g_1\right)\left(\frac{d\sqrt{T^*}}{dy^*}\right)\left(\frac{dT^*}{dy^*}\right)+\left(f_3-f_4g_1\right)\sqrt{T^*}\left(\frac{d^2T^*}{dy^{*2}}\right)+A^2f_2\sqrt{T^*}\left(\frac{du^*}{dy^*}\right)^2$$

$$-\frac{f_5T^{*3/2}}{C^2}-\left(\frac{d\left(f_4g_1\right)}{dy^*}\right)\sqrt{T^*}\left(\frac{dN^*_f}{dy^*}\right)-\left(f_4g_1\right)\left(\frac{d\sqrt{T^*}}{dy^*}\right)\left(\frac{dN^*{}_f}{dy^*}\right)-\left(f_3-f_4g_1\right)\sqrt{T^*}\left(\frac{d^2N^*_f}{dy^{*2}}\right)=0$$

$$\left(\frac{\left(f_3-f_4g_1\right)_{i,j+1}-\left(f_3-f_4g_1\right)_{i,j-1}}{2\Delta y}\right)\sqrt{T^*_{i,j}}\left(\frac{T^*_{i,j+1}-T^*_{i,j-1}}{2\Delta y}\right)+\frac{\left(f_3-f_4g_1\right)_{i,j}}{2\sqrt{T^*_{i,j}}}\left(\frac{T^*_{i,j+1}-T^*_{i,j-1}}{2\Delta y}\right)^2+$$

$$\left(f_3-f_4g_1\right)_{i,j}\sqrt{T^*_{i,j}}\left(\frac{T_{i,j-1}-2T_{i,j}+T_{i,j+1}}{\Delta y^2}\right)+A^2f_{2i,j}\sqrt{T^*_{i,j}}\left(\frac{u^*_{i,j+1}-u^*_{i,j-1}}{2\Delta y}\right)^2-\frac{f_{5i,j}T^{*3/2}_{i,j}}{C^2}-$$

$$\left(\frac{\left(f_4g_1\right)_{i,j+1}-\left(f_4g_1\right)_{i,j-1}}{2\Delta y}\right)\sqrt{T^*_{i,j}}\left(\frac{N^*_{f_{i,j+1}}-N^*_{f_{i,j-1}}}{2\Delta y}\right)-\frac{\left(f_4g_1\right)_{i,j}}{2\sqrt{T^*_{i,j}}}\left(\frac{T^*_{i,j+1}-T^*_{i,j-1}}{2\Delta y}\right)\left(\frac{N^*_{f_{i,j+1}}-N^*_{f_{i,j-1}}}{2\Delta y}\right)-$$

$$\left(f_3-f_4g_1\right)_{i,j}\sqrt{T^*_{i,j}}\left(\frac{N^*_{f_{i,j-1}}-2N^*_{f_{i,j}}+N^*_{f_{i,j+1}}}{\Delta y^2}\right)=0$$

$$\left(8f_3-8f_4g_1+\frac{4\Delta y^2 f_5}{C^2}\right)_{i,j}T^*_{i,j}=$$

$$\left[f_{3_{i,j+1}}-\left(f_4g_1\right)_{i,j+1}-f_{3_{i,j-1}}+\left(f_4g_1\right)_{i,j-1}+\left(4f_3-4f_4g_1\right)_{i,j}-\left(\frac{f_4g_1}{2T^*_{i,j}}\right)_{i,j}\left(N^*_{f_{i,j+1}}-N^*_{f_{i,j-1}}\right)\right]T^*_{i,j+1}+$$

$$\left[f_{3_{i,j-1}}-\left(f_4g_1\right)_{i,j-1}-f_{3_{i,j+1}}+\left(f_4g_1\right)_{i,j+1}+\left(4f_3-4f_4g_1\right)_{i,j}+\left(\frac{f_4g_1}{2T^*}\right)_{i,j}\left(N^*_{f_{i,j+1}}-N^*_{f_{i,j-1}}\right)\right]T^*_{i,j-1}+ \tag{12-36}$$

$$\left(\frac{f_3-f_4g_1}{2T^*}\right)_{i,j}\left(T^*_{i,j+1}-T^*_{i,j-1}\right)^2+A^2f_{2_{i,j}}\left(u^*_{i,j+1}-u^*_{i,j-1}\right)^2+\left(8f_3-8f_4g_1\right)_{i,j}N^*_{f_{i,j}}+$$

$$\left[\left(f_4g_1\right)_{i,j-1}-\left(f_4g_1\right)_{i,j+1}+\left(4f_4g_1-4f_3\right)_{i,j}\right]N^*_{f_{i,j+1}}+\left[\left(f_4g_1\right)_{i,j+1}-\left(f_4g_1\right)_{i,j-1}+\left(4f_4g_1-4f_3\right)_{i,j}\right]N^*_{f_{i,j-1}}$$

12.8.3 Boundary Conditions

12.8.3.1 At $y^*=1$ (Top Plate)

$$\frac{u^*_{i,m-2}-4u^*_{i,m-1}+3u^*_{i,m}}{2\Delta y}=-\frac{\phi_H f_{8i,m}}{C}u^*_{i,m}-\frac{N^*_{f_{i,m}}\left(\tan\delta-Sin\phi\right)}{ACf_{2i,m}\sqrt{T^*_{i,m}}}$$

$$\left(\frac{2\Delta y\phi_H f_{8i,m}}{C}+3\right)u^*_{i,m}=4u^*_{i,m-1}-u^*_{i,m-2}-\frac{2\Delta yN^*_{f_{i,m}}\left(\tan\delta-Sin\phi\right)}{ACf_{2i,m}\sqrt{T^*_{i,m}}}$$

$$u^*_{i,m}=\frac{4u^*_{i,m-1}-u^*_{i,m-2}}{\left(\dfrac{2\Delta y\phi_H f_{8i,m}}{C}+3\right)}-\frac{2\Delta yN^*_{f_{i,m}}\left(\tan\delta-Sin\phi\right)}{ACf_{2i,m}\sqrt{T^*_{i,m}}\left(\dfrac{2\Delta y\phi_H f_{8i,m}}{C}+3\right)} \tag{12-37}$$

$$\frac{T^*_{i,m-2}-4T^*_{i,m-1}+3T^*_{i,m}}{2\Delta y}=\frac{ff_{5i,m}}{2\Delta y}\left(N^*_{f_{i,m-2}}-4N^*_{f_{i,m-1}}+3N^*_{f_{i,m}}\right)-\frac{\left(1-e_w^2\right)ff_{3i,m}}{C}T^*_{i,m}+\frac{A^2\varphi_H ff_{4i,m}u^{*2}_{i,m}}{C}$$

$$\left(\frac{2\Delta y\left(1-e_w^2\right)ff_{3i,m}}{C}+3\right)T^*_{i,m}=4T^*_{i,m-1}-T^*_{i,m-2}+\frac{2\Delta yA^2\varphi_H ff_{4i,m}u^{*2}_{i,m}}{C}+ff_{5i,m}\left(N^*_{f_{i,m-2}}-4N^*_{f_{i,m-1}}+3N^*_{f_{i,m}}\right)$$

$$T^*_{i,m}=\frac{4T^*_{i,m-1}-T^*_{i,m-2}+\dfrac{2\Delta yA^2\varphi_H ff_{4i,m}u^{*2}_{i,m}}{C}}{\left(\dfrac{2\Delta y\left(1-e_w^2\right)ff_{3i,m}}{C}+3\right)}+\frac{ff_{5i,m}\left(N^*_{f_{i,m-2}}-4N^*_{f_{i,m-1}}+3N^*_{f_{i,m}}\right)}{\left(\dfrac{2\Delta y\left(1-e_w^2\right)ff_{3i,m}}{C}+3\right)} \tag{12-38}$$

12.8.3.2 At $y^*= 0$ (Bottom Plate)

$$\frac{-3u_{i,1}^* + 4u_{i,2}^* - u_{i,3}^*}{2\Delta y} = \frac{\phi_o f_{8i,1}}{C} u_{i,1}^* - \frac{\phi_o f_{8i,1}}{C} - \frac{N_{f_{i,1}}^* \left(\tan\delta - Sin\phi\right)}{ACf_{2i,1}\sqrt{T_{i,1}^*}}$$

$$\left(\frac{2\Delta y\,\phi_o f_{8i,1}}{C} + 3\right) u_{i,1}^* = 4u_{i,2}^* - u_{i,3}^* + \frac{2\Delta y\,\phi_o f_{8i,1}}{C} + \frac{2\Delta y N_{f_{i,1}}^* \left(\tan\delta - Sin\phi\right)}{ACf_{2i,1}\sqrt{T_{i,1}^*}}$$

$$u_{i,1}^* = \frac{4u_{i,2}^* - u_{i,3}^* + \dfrac{2\Delta y\,\phi_o f_{8i,1}}{C}}{\left(\dfrac{2\Delta y\,\phi_o f_{8i,1}}{C} + 3\right)} + \frac{2\Delta y N_{f_{i,1}}^* \left(\tan\delta - Sin\phi\right)}{ACf_{2i,1}\sqrt{T_{i,1}^*}\left(\dfrac{2\Delta y\,\phi_o f_{8i,1}}{C} + 3\right)} \qquad (12\text{-}39)$$

$$\frac{-3T_{i,1}^* + 4T_{i,2}^* - T_{i,3}^*}{2\Delta y} = ff_{5i,1}\frac{-3N_{f_{i,1}}^* + 4N_{f_{i,2}}^* - N_{f_{i,3}}^*}{2\Delta y} + \frac{\left(1 - e_w^2\right)ff_{3i,1}}{C} T_{i,1}^* - \frac{A^2\varphi_o ff_{4i,1}\left(u_{i,1}^* - 1\right)^2}{C}$$

$$\left(\frac{2\Delta y\left(1 - e_w^2\right)ff_{3i,1}}{C} + 3\right) T_{i,1}^* = 4T_{i,2}^* - T_{i,3}^* + \frac{2\Delta y A^2\varphi_o ff_{4i,1}\left(u_{i,1}^* - 1\right)^2}{C} - ff_{5i,1}\left(-3N_{f_{i,1}}^* + 4N_{f_{i,2}}^* - N_{f_{i,3}}^*\right)$$

$$T_{i,1}^* = \frac{4T_{i,2}^* - T_{i,3}^* + \dfrac{2\Delta y A^2\varphi_o ff_{4i,1}\left(u_{i,1}^* - 1\right)^2}{C}}{\left(\dfrac{2\Delta y\left(1 - e_w^2\right)ff_{3i,1}}{C} + 3\right)} - \frac{ff_{5i,1}\left(-3N_{f_{i,1}}^* + 4N_{f_{i,2}}^* - N_{f_{i,3}}^*\right)}{\left(\dfrac{2\Delta y\left(1 - e_w^2\right)ff_{3i,1}}{C} + 3\right)} \qquad (12\text{-}40)$$

12.8.4 True Temperature Equation

$$\frac{\left(\upsilon u^*\right)_{i,j_{Flow}}}{\Delta x}\left[T_{R_{i,jFlow}}^* - T_{R_{i-1,jFlow}}^*\right] = \left(\frac{A_2^*}{\Delta y^2}\right)\left(k_{eff}^*\right)_{i,j_{Flow}}\left[T_{R_{i,jFlow-1}}^* - 2T_{R_{i,jFlow}}^* + T_{R_{i,jFlow+1}}^*\right] +$$

$$\left(\frac{A_2^*}{\Delta y}\right) DKDY_{i,j_{Flow}}\left(T_{R_{i,jFlow+1}}^* - T_{R_{i,jFlow-1}}^*\right) - \left(\frac{A_3^* Sin\phi}{C}\right)\left(N_f^*\right)_{i,j_{Flow}} DUDY_{i,j_{Flow}} + \left(\frac{A_3^*}{A_1^*}\right)\left(T^{*3/2} f_5\right)_{i,j_{Flow}}$$

where $DKDY_{i,j_{Flow}} = \left(\dfrac{k_{eff\,i,j_{Flow}+1}^* - k_{eff\,i,j_{Flow}-1}^*}{\Delta y}\right)$, and $DUDY_{i,j_{Flow}} = \left(\dfrac{u_{i,j_{Flow}+1}^* - u_{i,j_{Flow}-1}^*}{\Delta y}\right)$

$$\left\{\frac{\left(\upsilon u^*\right)_{i,j_{Flow}}}{\Delta x} + \left(\frac{2A_2^*}{\Delta y^2}\right)\left(k_{eff}^*\right)_{i,j_{Flow}}\right\} T_{R_{i,jFlow}}^* = \frac{\left(\upsilon u^*\right)_{i,j_{Flow}}}{\Delta x} T_{R_{i-1,jFlow}}^* + \left\{\left(\frac{A_2^*}{\Delta y^2}\right)\left(k_{eff}^*\right)_{i,j_{Flow}} - \left(\frac{A_2^*}{\Delta y}\right) DKDY_{i,j_{Flow}}\right\} T_{R_{i,jFlow-1}}^*$$

$$+ \left\{\left(\frac{A_2^*}{\Delta y^2}\right)\left(k_{eff}^*\right)_{i,j_{Flow}} + \left(\frac{A_2^*}{\Delta y}\right) DKDY_{i,j_{Flow}}\right\} T_{R_{i,jFlow+1}}^* - \left(\frac{A_3^* Sin\phi}{C}\right)\left(N_f^*\right)_{i,j_{Flow}} DUDY_{i,j_{Flow}} + \left(\frac{A_3^*}{A_1^*}\right)\left(T^{*3/2} f_5\right)_{i,j_{Flow}}$$

$$T^*_{R_{i,jFlow}} = \frac{\dfrac{\left(\upsilon u^*\right)_{i,j_{Flow}}}{\Delta x}}{\left\{\dfrac{\left(\upsilon u^*\right)_{i,j_{Flow}}}{\Delta x} + \left(\dfrac{2A_2^*}{\Delta y^2}\right)\left(k^*_{eff}\right)_{i,j_{Flow}}\right\}} T^*_{R_{i-1,jFlow}} + \frac{\left\{\left(\dfrac{A_2^*}{\Delta y^2}\right)\left(k^*_{eff}\right)_{i,j_{Flow}} - \left(\dfrac{A_2^*}{\Delta y}\right) DKDY_{i,j_{Flow}}\right\}}{\left\{\dfrac{\left(\upsilon u^*\right)_{i,j_{Flow}}}{\Delta x} + \left(\dfrac{2A_2^*}{\Delta y^2}\right)\left(k^*_{eff}\right)_{i,j_{Flow}}\right\}} T^*_{R_{i,jFlow-1}} +$$

$$\frac{\left\{\left(\dfrac{A_2^*}{\Delta y^2}\right)\left(k^*_{eff}\right)_{i,j_{Flow}} + \left(\dfrac{A_2^*}{\Delta y}\right) DKDY_{i,j_{Flow}}\right\}}{\left\{\dfrac{\left(\upsilon u^*\right)_{i,j_{Flow}}}{\Delta x} + \left(\dfrac{2A_2^*}{\Delta y^2}\right)\left(k^*_{eff}\right)_{i,j_{Flow}}\right\}} T^*_{R_{i,jFlow+1}} - \frac{\left(\dfrac{A_3^* Sin\phi}{C}\right)\left(N_f^*\right)_{i,j_{Flow}} DUDY_{i,j_{Flow}}}{\left\{\dfrac{\left(\upsilon u^*\right)_{i,j_{Flow}}}{\Delta x} + \left(\dfrac{2A_2^*}{\Delta y^2}\right)\left(k^*_{eff}\right)_{i,j_{Flow}}\right\}} + \frac{\left(\dfrac{A_3^*}{A_1^*}\right)\left(T^{*3/2} f_5\right)_{i,j_{Flow}}}{\left\{\dfrac{\left(\upsilon u^*\right)_{i,j_{Flow}}}{\Delta x} + \left(\dfrac{2A_2^*}{\Delta y^2}\right)\left(k^*_{eff}\right)_{i,j_{Flow}}\right\}} \tag{12-41}$$

12.9 Numerical Scheme

The momentum and the energy equation are ordinary differential equations coupled through their boundary conditions. Because of the complexity of these equations, they were solved numerically. A benchmark input parameters are chosen based on the theory of granular lubrication. In the simulations presented, the thickness of the gap is fixed and the normal load is specified. Finite difference method is employed to discretize the dimensionless governing equations and boundary equations, which forms a set of nonlinear algebraic equations. There are three loops in the computations, the inner loop solves the velocity, the second loop solves the pseudo temperature, and the outer loop solves the volume fraction.

The Newton iteration method is used to solve the resulting set of equations for the velocity (12-35) and pseudo temperature (12-36) along with their boundary conditions (12-37) to (12-40). Bisection method is then used to solve the volume fraction from equation (12-27) since it cannot be computed analytically. The iterations are repeated until the results converge when the difference in the computed velocity, pseudo temperature and volume fraction between two successive iterations are below the specified tolerance. Then the mass flow rate is computed by integrating the volume fraction and the velocity along the gap thickness. The tolerance level used is 10^{-7} per all iterations in each loop. The mesh points are 21 in the lateral direction for the film thickness. The numerical simulations indicate that a finer mesh does not influence the results but necessitates more computational time. After convergence of the velocity, pseudo temperature and volume fraction, the granular flow true temperature equation (12-41) is then solved numerically using the Newton iteration method along with the equations for the top and bottom plates and necessary boundary conditions presented in Chapter 11.

12.10 Results

The input parameters used in the simulations are given in Table 12.1. The operating conditions and properties are chosen to mimic the simulations of McKeague & Khonsari [26] and Zhou & Khonsari [30]. The lower plate undergoes a sliding velocity while the top plate is stationary. The thickness of the gap is assumed to be 14 particle diameters and the granular material used is Titanium Dioxide (TiO$_2$) with a $5\,\mu\text{m}$ diameter and density $4260\,\text{kg/m}^3$.

Table 12.1: Data for Benchmark Simulations

Parameter	Value	Parameter	Value
U	4.6 m/s	L	0.0264 m
$\upsilon_{\max}$	0.65	H	70μm
e_w	0.8	ϕ_o	0.5
e_p	0.8	ϕ_H	0.5
ρ_p	$4260\,\text{kg/m}^3$	d	$5\,\mu\text{m}$
F_r	$4.0\text{x}10^{-32}\,\text{kg/m.s}^2$	ϕ	25^o
n	23	δ	22.9^o

To characterize enduring contact, two additional constant parameters are introduced in the simulations: F_r and n that appear in the coulomb friction model equation (12-3) as described by Johnson and Jackson [15]. Based on experimental measurements for two different types of beads, they proposed the following values for the stress constant F_r and the integer constant n: $F_r = 3.65\text{x}10^{-32}\,\text{kg/m.s}^2$ for glass beads and $F_r = 4.0\text{x}10^{-32}\,\text{kg/m.s}^2$ for polystyrene beads with n = 40 for both cases. However, there are no experimental data available for the Titanium Dioxide (TiO$_2$). To carry on the analysis, it is assumed that F_r is fixed at $F_r = 4.0\text{x}10^{-32}\,\text{kg/m.s}^2$. To estimate values for n for the type of granular material used in the simulations, the following analysis is used based on the work of Zhou [90] and Jang & Khonsari [40]: The normal stress contributed by the enduring contact N_f must be less than or equal to the specified normal load N applied on the plate. Thus, the parameter n can be determined by the following equation,

$$n \leq \frac{\log(F_r / N)}{\log(\upsilon_{\max} - \upsilon)} \tag{12-42}$$

Appropriate range of the parameter *n* can be evaluated for different values of $(\upsilon_{\max} - \upsilon)$. The results are summarized in Table 12.2. It is clear that the difference of volume fraction plays an important role on *n*, while the normal load does not have much significance on *n*. At $N = 7.25$ kPa (benchmark), the value of $(\upsilon_{\max} - \upsilon)$ is roughly 0.05 and Table 12.2 shows that the parameter *n* should be less or equals to 27. Then $n = 23$ is selected as the benchmark input in the simulations presented.

Table 12.2 : The Range of Parameter *n*

$(\upsilon_{\max} - \upsilon)$		0.014	0.017	0.021	0.025	0.029	0.034	0.039	0.044	0.05
N =7.25 kPa	*n*	19	20	21	22	23	24	25	26	27
N =10 kPa	*n*	19.09	20.01	21.10	22.09	23.02	24.1	25.12	26.09	27.2
N =30 kPa	*n*	19.35	20.27	21.38	22.39	23.33	24.43	25.46	26.44	27.6

12.10.1 Benchmark Simulations

In this section, the results of a series of simulations are presented that predict the performance of the granular material as they are sheared between two parallel plates. Figure 12.3 shows the variations of the flow velocity, pseudo temperature, and volume fraction for the Couette-type flow across the gap. The results with and without the consideration of the enduring contact are shown for comparison purposes.

The parameter *n* controls the influence of the enduring contact. At $n = 20$, the results show that the effect of enduring contact is negligibly small and yield nearly identical trends and magnitudes to the results without enduring contact. As *n* increases, the effect on enduring contact becomes more significant. The profiles of the volume fraction and the pseudo temperature across the gap become more flattened when the enduring contact force between the granules begins to play a role in supporting the applied load. The velocity profile is roughly linear across the gap.

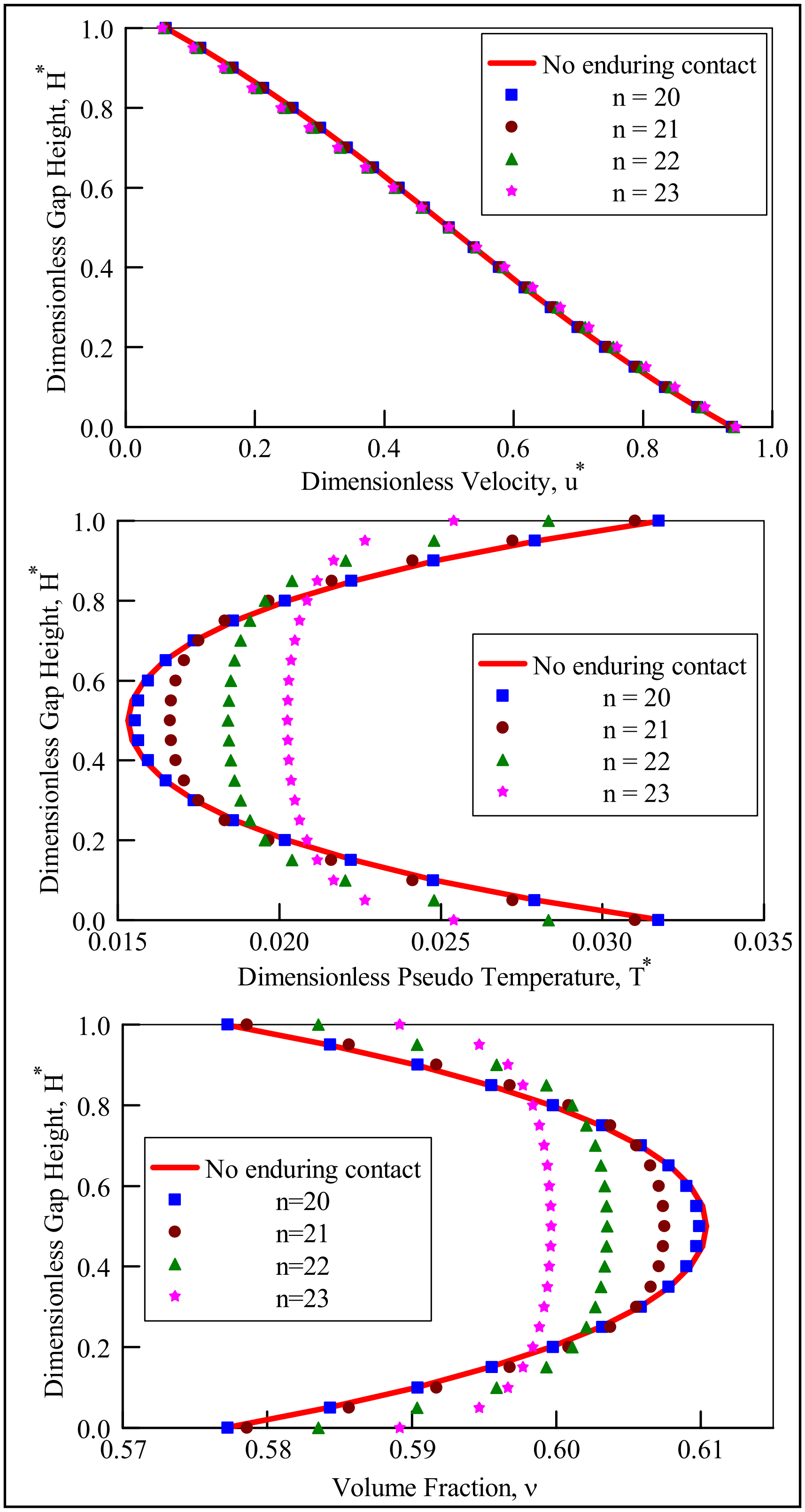

Figure 12.3 : Benchmark Simulations of the Flow Velocity, Granular Temperature and Solid Volume Fraction

The enduring force between the granules tends to limit the relative motion between the granules and causes the pseudo temperature (fluctuation velocity) to decrease around the boundaries and increases in the middle of the gap compared to the case without the enduring contact effect. As the friction force between the granules increases, the rate of collisions decreases. Therefore, the granules in the middle of the gap become more packed causing a decrease in the pseudo temperature. Since the solid volume fraction is directly related to the pseudo temperature, it becomes greater around the boundaries and smaller in the middle of the gap, thus tending to flattened across the gap thickness to support the applied load.

12.10.2 Effect of the Sliding Velocity, *U*

Research by Jang and Khonsari [89] shows that if the operating speed is below 4 m/s, the effect of the enduring contact becomes large and cannot be neglected. Figure 12.4 shows the velocity, pseudo temperature, volume fraction, and the shear stress distributions with the consideration of the enduring contact as a function of the sliding speed. The simulations presented here are under the same operating conditions as Jang and Khonsari [89], where the speed ranges from 2.6 to 10.6 m/s. At a moderately high speed, the effect of enduring contact is very small and, the trends are analogous to the cases without the consideration of the enduring contact. On the other hand, as the sliding speed decreases, the enduring contact force between the granules begins to play a role in supporting the applied load. The results of Fig. 5 demonstrate that at a sliding speed $U = 4.6$ m/s and below, the effect of the enduring contact is significant. When the sliding speed is very small, the shear stress due to the enduring contact becomes noticeable over the kinetic and collisional stresses. In this case, the load is solely carried by the dense granules across the gap.

Under the conditions simulated, at very low sliding speeds (less than 4.6 m/s), the volume fraction is predicted to be around 0.6 and its distribution across the gap becomes nearly flat to support the load. At the boundaries, the effect of the enduring contact is relatively small since the pseudo temperature is higher due to the energy added to the system through the slip velocity and by the boundary through the disks surface roughness. The lower the speed, the greater the enduring contact and the smaller the kinetic-collisional stress becomes due to the small number of collision between granules. As the speed increases, the enduring contact effect becomes less and kinetic energy due to collision between granules increases and the total shear

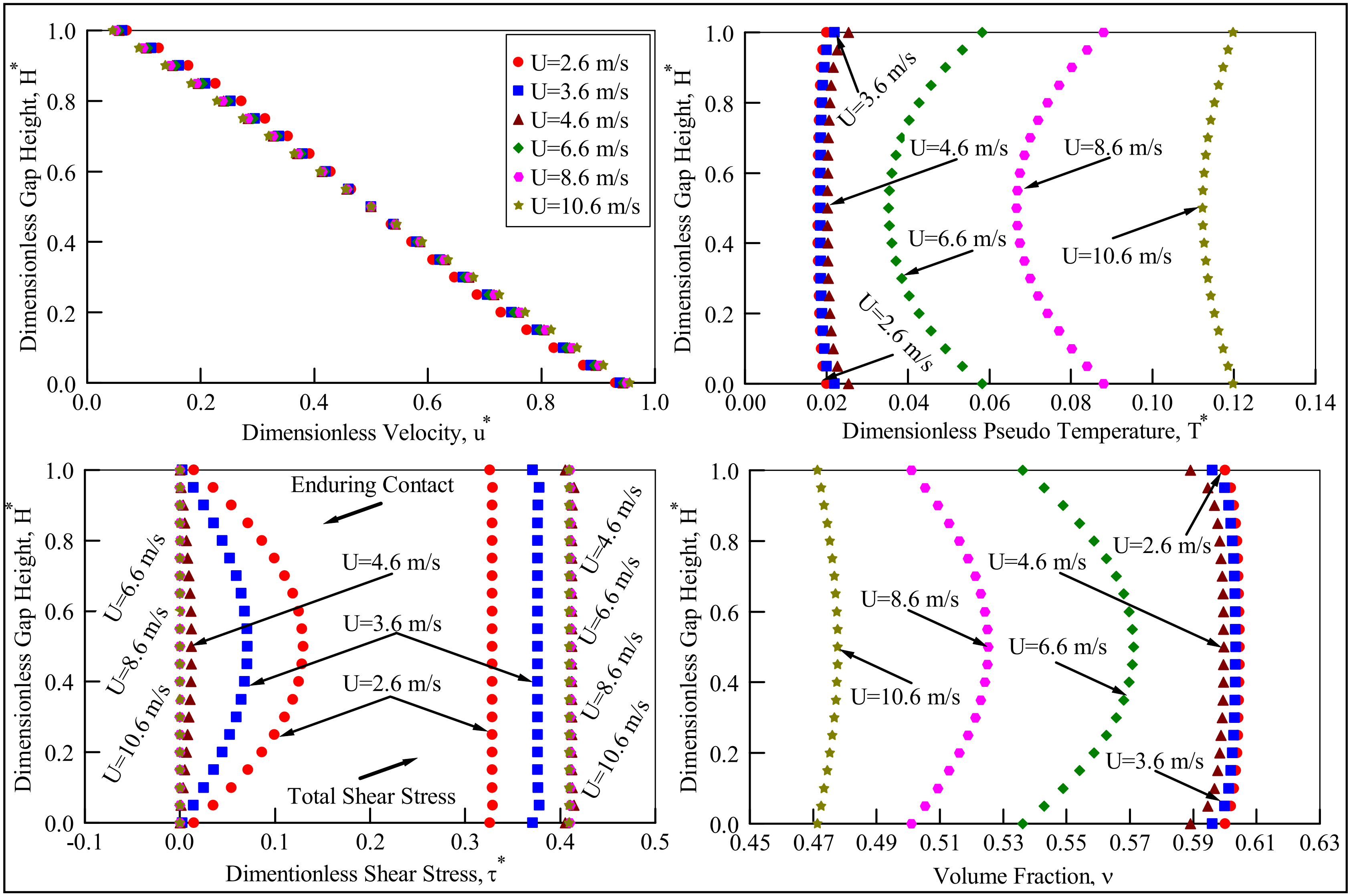

Figure 12.4 : Effect of the Sliding Velocity, U

stress increases. Beyond a certain sliding speed, the effect of enduring contact becomes negligibly small and the total shear stress and the shear stress due to enduring contact becomes constant across the gap.

12.10.3 Variation of the Friction Coefficient with the Sliding Speed

Figure 12.5 demonstrates the variation of the friction coefficient with the sliding speed from 2 m/s to 30 m/s. Above a certain speed (approximately 4.6 m/s), the predicted friction coefficient for both cases is identical since the effect of the enduring contact is nil as explained in Fig. 5. Below this speed, the friction coefficient tends to drop when considering the enduring contact effect. On the other hand, when the enduring contact is neglected, the friction coefficient is predicted to be high even at these very low speeds.

This behavior of friction can be explained as follows. At very low sliding speed, due to the enduring contact effect, the total shear stress is small and since the normal stress is fixed in these simulations, a reduction in the total shear stress causes a decrease in the friction coefficient. At a relatively high speed, the effect of the enduring contact is nil. Therefore, the friction coefficient is identical to the case without the effect of the enduring contact. In addition, as the speed increases beyond 8.6 m/s, a small reduction in the friction coefficient is observed. The reason for this drop is due to the fact that by increasing the speed, the collision rate between the granules increases causing an increase in the displacement between the top and bottom discs and in turn a slight reduction in the friction coefficient. At approximately 26 m/s, no more reduction in the friction coefficient is obtained and the trend starts to stabilize indicating that a complete lift between the two discs occurs.

12.10.4 Effect of the Sliding Speed on the Total Shear Stress

Figure 12.6 further explores the behavior of the friction coefficient through a comparison of the solid volume fraction and the dimensionless shear stresses at different speeds for the cases with and without the effect of enduring contact. At a relatively high speed (6.6 m/s), there is an increase in the collision rate between the granules where the grains become loosely packed. Hence, there is no possibility for the granules to slide against each other which causes the frictional stress to be zero across the gap. Therefore, at this relatively high speed, the collisional-kinetic stress for the case with enduring contact is equal to the total stress and is identical to the

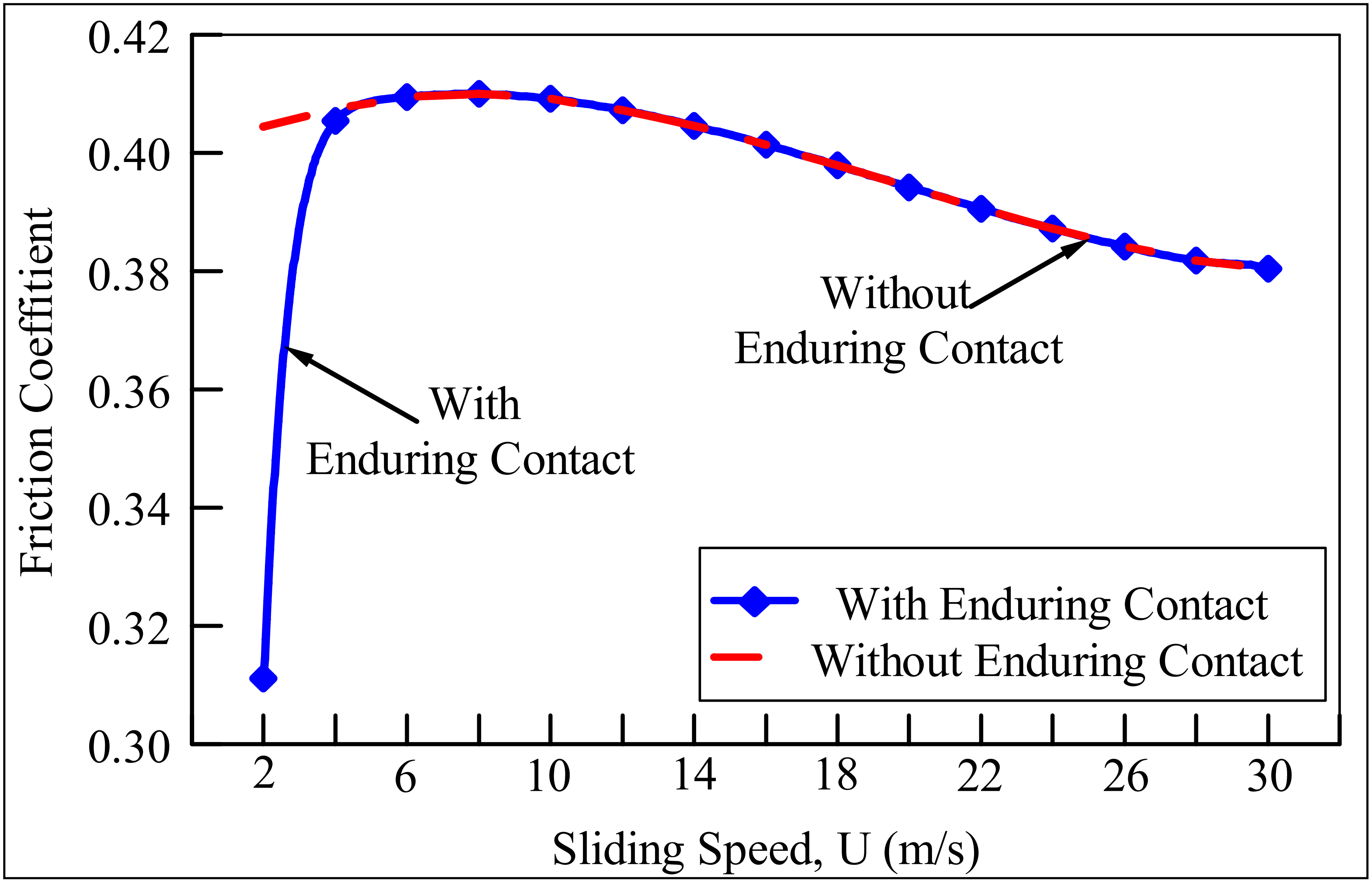

Figure 12.5 : Variation of the Friction Coefficient with the Sliding Speed

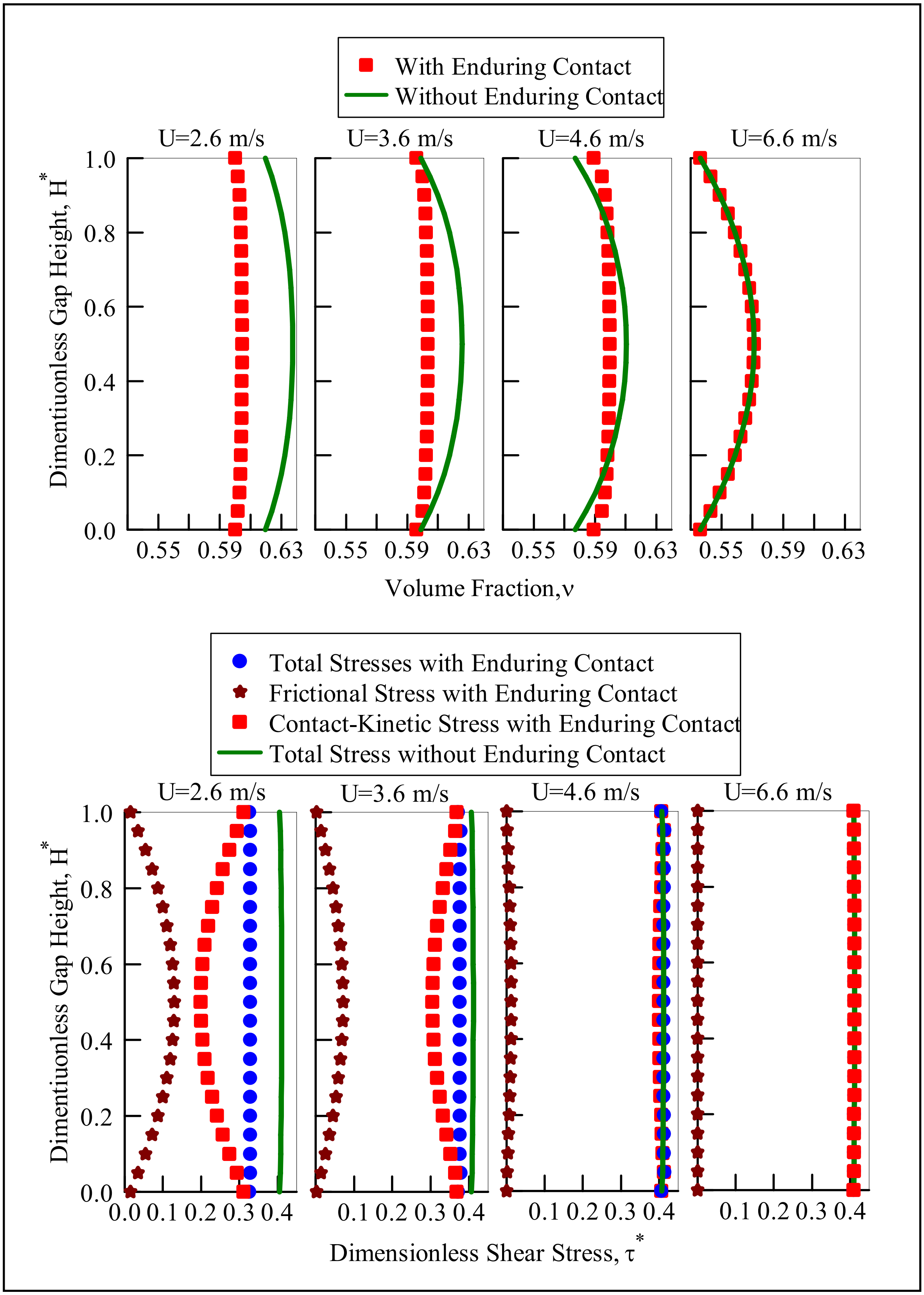

Figure 12.6 : Effect of the Sliding Speed on the Volume Fraction and Shear Stress

case without the consideration of enduring contact. Hence, the volume fraction profiles for both cases are also identical.

As the speed decreases, the effect of the frictional stress starts to become visible causing a reduction in the total stress compared to the total stress without enduring contact. Therefore, the friction coefficient starts to decrease. By lowering the speed to 2.6 m/s, the frictional stress is more pronounced and the total stress becomes smaller than its corresponding stress without enduring contact and hence, a reduction in the friction coefficient is observed. Also, as the speed decreases, the distribution of the solid volume fraction is nearly flat and the load is exclusively carried by the stationary granules.

12.10.5 Granular Flow Time Scales

There are essentially two time scales that describe the granular shear flows, the time between granule-granule collisions (t_c) and the contact time between collisions (t_f). The kinetic theory is valid if the contact time is much shorter than the time between collisions (Jang & Khonsari [40]). The time between granule-granule collisions depends on the volume fraction, granule size, and the fluctuation velocity. Gidaspow [91] derived the time between collisions for monosized granules as follow:

$$t_c = \frac{d}{24 g_o \upsilon}\sqrt{\frac{\pi}{T}} \tag{12-43}$$

where d represents the granule diameter, T is the pseudo temperature, υ represents the solid volume fraction, and g_o is the radial distribution function defined by equation (4-4).

The contact time between collisions is defined as:

$$t_f = \pi\sqrt{\frac{m}{2K\left(1-\zeta^2\right)}} \tag{12-44}$$

where K represents the stiffness constant, m is the granule mass, and ζ is the damping coefficient defined by: $\zeta = -\ln e_p / \sqrt{\pi^2 + \ln^2 e_p}$.

According to the Hertzian model, the stiffness constant (Johnson [92]) is equal to: $K = \left[3E^2 dF / 8\left(1-\nu^2\right)^2\right]^{1/3}$, where E represents the Young's modulus, ν is the Poisson's ratio and F represents the load acting on the granule. For TiO_2, $E = 270\ \text{GPa}$, $\zeta = 0.07085$ and $\nu = 0.27$. The load acting on the granule F can be determined from the conservation of momentum as follow: $Ft_c/2 = mV$, where *m* is the granule mass as given in equation (4-7), and *V* is the mean fluctuation velocity.

Appropriate calculations for the time between collisions and the contact time for different sliding speeds are summarized in Table 12.3. The parameter *n*, which controls the influence of the enduring contact, is 23 in this analysis. It is clear that the volume fraction plays an important role on t_c and t_f at different speeds. As shown in Table 12.3, an increase in the solid volume fraction causes a decrease in the pseudo temperature, which results in a decrease in the time between collisions (t_c). In addition, increasing the solid volume fraction results in a decrease in the stiffness constant, which causes an increase in the contact time between collisions (t_f). This explanation concurs with equations (12-43) and (12-44). On the other hand, as the sliding speed increases, t_c increases and t_f decreases. Therefore, the results agree with the previous discussion that the larger the sliding speed becomes, the smaller the effect of the enduring contact until it becomes nil. Furthermore, Table 12.3 demonstrates that the ratio t_f/t_c is less than 1; hence the kinetic theory is valid for all the presented cases.

Table 12.3 : Effect of the Sliding Speed on the Time between Collisions

Sliding Speed U (m/s)	Volume Fraction, υ	Radial Distribution, g_o	Pseudo Temperature, T (m^2/s^2)	Time between Collisions, t_c(s)	Stiffness Constant, K (N/m)	Contact Time, t_f(s)	t_f/t_c
2.6	0.601	38.039	0.034	$8.763\text{x}10^{-8}$	$0.687\text{x}10^{4}$	$1.003\text{x}10^{-8}$	$1.145\text{x}10^{-1}$
3.6	0.596	35.133	0.037	$9.123\text{x}10^{-8}$	$0.688\text{x}10^{4}$	$1.002\text{x}10^{-8}$	$1.098\text{x}10^{-1}$
4.6	0.589	31.029	0.043	$9.717\text{x}10^{-8}$	$0.690\text{x}10^{4}$	$1.001\text{x}10^{-8}$	$1.029\text{x}10^{-1}$
5.6	0.556	19.773	0.075	$1.223\text{x}10^{-7}$	$0.701\text{x}10^{4}$	$9.928\text{x}10^{-9}$	$8.116\text{x}10^{-2}$
6.6	0.536	16.092	0.099	$1.361\text{x}10^{-7}$	$0.708\text{x}10^{4}$	$9.879\text{x}10^{-9}$	$7.261\text{x}10^{-2}$
7.6	0.518	13.705	0.124	$1.479\text{x}10^{-7}$	$0.715\text{x}10^{4}$	$9.833\text{x}10^{-9}$	$6.647\text{x}10^{-2}$
8.6	0.501	12.029	0.149	$1.584\text{x}10^{-7}$	$0.721\text{x}10^{4}$	$9.789\text{x}10^{-9}$	$6.179\text{x}10^{-2}$

12.10.6 Effect of the Granular Coefficient of Restitution, e_p

Figure 12.7 shows the predictions of the flow characteristics with the variation of the granular coefficient of restitution e_p. All the other input data are the same as listed in Table 12.1.

As the coefficient of restitution increases, the collision between the granules becomes more elastic and there is less energy loss by inelastic collision between the granules. Therefore, the fluctuation of the granules in the middle of the gap becomes larger, resulting in an increase in the pseudo temperature. The behavior of the volume fraction and the pseudo temperature are inversely related: As the volume fraction decreases, the pseudo temperature increases. The slip velocity decreases at the boundaries and the velocity gradient increases in the middle of the gap which causes the viscous dissipation to increase. The granular coefficient of restitution is directly related to the viscous dissipation: The parameter η that appears in the viscous dissipation equation (4-10) is a constant characterizing the inelastic collision between granules (4-3) and defined as $\eta = 0.5(1+e_p)$. The coefficient of restitution parameter e_p =1 for perfectly elastic granules, and e_p =0 for perfectly inelastic granules. On the boundaries, since increasing the coefficient of restitution causes a reduction in the slip velocity, the pseudo temperature becomes smaller.

Figure 12.7 also demonstrates the effect of the granular coefficient of restitution on the dimensionless total shear stress and the stress due to the enduring contact. The shear stress due to the enduring contact is slightly larger when e_p is small. As e_p increases, the fluctuation of the granules in the middle of the gap becomes larger and the effect of the enduring contact diminishes. The total shear stress is mostly influenced by the change in volume fraction. As e_p increases, the volume fraction decreases and causes the total shear stress to decrease but remains constant across the gap. When e_p is 0.98, the friction coefficient is 0.16 at the bottom plate and the normalized mass flow rate is 0.2. Thus, the mass flow rate is reduced compared to the benchmark case where the friction coefficient is 0.4 and the normalized mass flow rate is 0.3. Note that the normal load is specified and the gap height is fixed in the simulations.

It is noted that the trend of the pseudo temperature and the solid volume fraction changes considerably at the higher values of e_p (0.9 and 0.98) compared to the benchmark case where e_p = 0.8. This interesting phenomenon can be explained by examining to the two energy sources that supply energy to the granules. One comes from the slip velocity at the boundary and the other is the viscous dissipation in the interior of the flow. When e_p is large, the slip velocity at the boundary decreases and the viscous dissipation in the gap increases. Therefore, there is more energy generated in the gap than at the boundaries by the slip velocity mechanism. Hence, the boundaries receive more heat from the interior flow. The solid fraction trend is directly related to

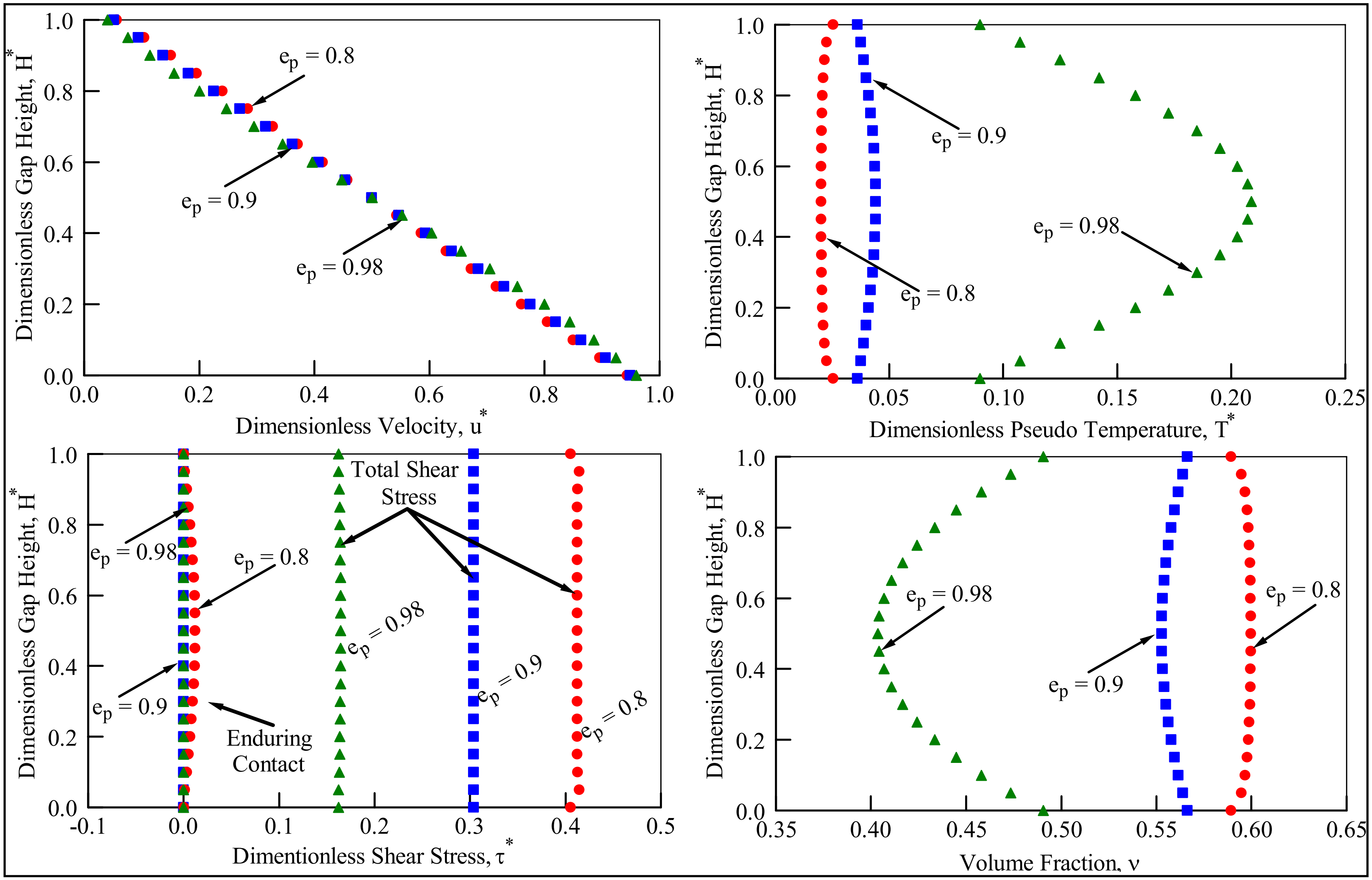

Figure 12.7 : Effect of the Granular Coefficient of Restitution, e_p

the granular temperature. When there is more pseudo energy generated within the gap thickness, the surrounding granules within the gap have much larger fluctuation velocity than the ones near the boundaries. Hence, the granular distribution becomes less dense within the gap and much more granules accumulate at the boundaries.

12.10.7 Effect of the Wall Coefficient of Restitution, e_w

Figure 12.8 shows the variation of the flow velocity, granular temperature, solid volume fraction, and the normalized shear stress to the coefficient of restitution of both, top and bottom plates. In these simulations, the granular coefficient of restitution e_p is kept at 0.8 and the wall restitution e_w is varied from 0.8 to 1. The slip velocity increases as e_w increases. An increase in e_w means that the wall is more elastic. Thus, near the boundaries the granules are loosely packed and there is less energy loss during collision between the wall and the granules which implies that there will be a rise in the pseudo temperature as a result of greater fluctuation. Therefore, more energy is supplied from the boundaries to the flow. Since the granular temperature increases near the wall, the solid volume fraction decreases at the boundaries. Away from the top and bottom boundaries and towards the middle of the gap, the volume fraction increases implying a greater concentration of granular solids, associated with a reduction in the fluctuation velocity. Hence, in the middle of the gap where the granules are more densely packed, there will be less fluctuation and the amount of energy dissipation is lower, and the pseudo temperature is reduced. As e_w increases, the curvature profile of the granular temperature and the solid volume fraction becomes greater because of the change in the mass flow rate to match the specified normal load.

As e_w increases, the mass flow rate decreases but there is no change in the trends of the granular temperature and the solid volume fraction. The parameter e_w affects only the slip velocity, not the interior of the flow. When e_w is large, no significant effect is noticed on the mass flow rate. When e_w = 1.0, the mass flow rate is $\overset{\bullet}{m}^* = 0.298$ and the friction coefficient is $f = 0.37$ and at benchmark simulations when e_w is 0.8, the mass flow rate is $\overset{\bullet}{m}^* = 0.3$ and the friction coefficient is $f = 0.4$. Hence, the effect on the mass flow rate caused by changing e_w is much less than that of e_p which implies that the coefficient of restitution between the granules play a much more substantial role than the coefficient of restitution between the granules and the

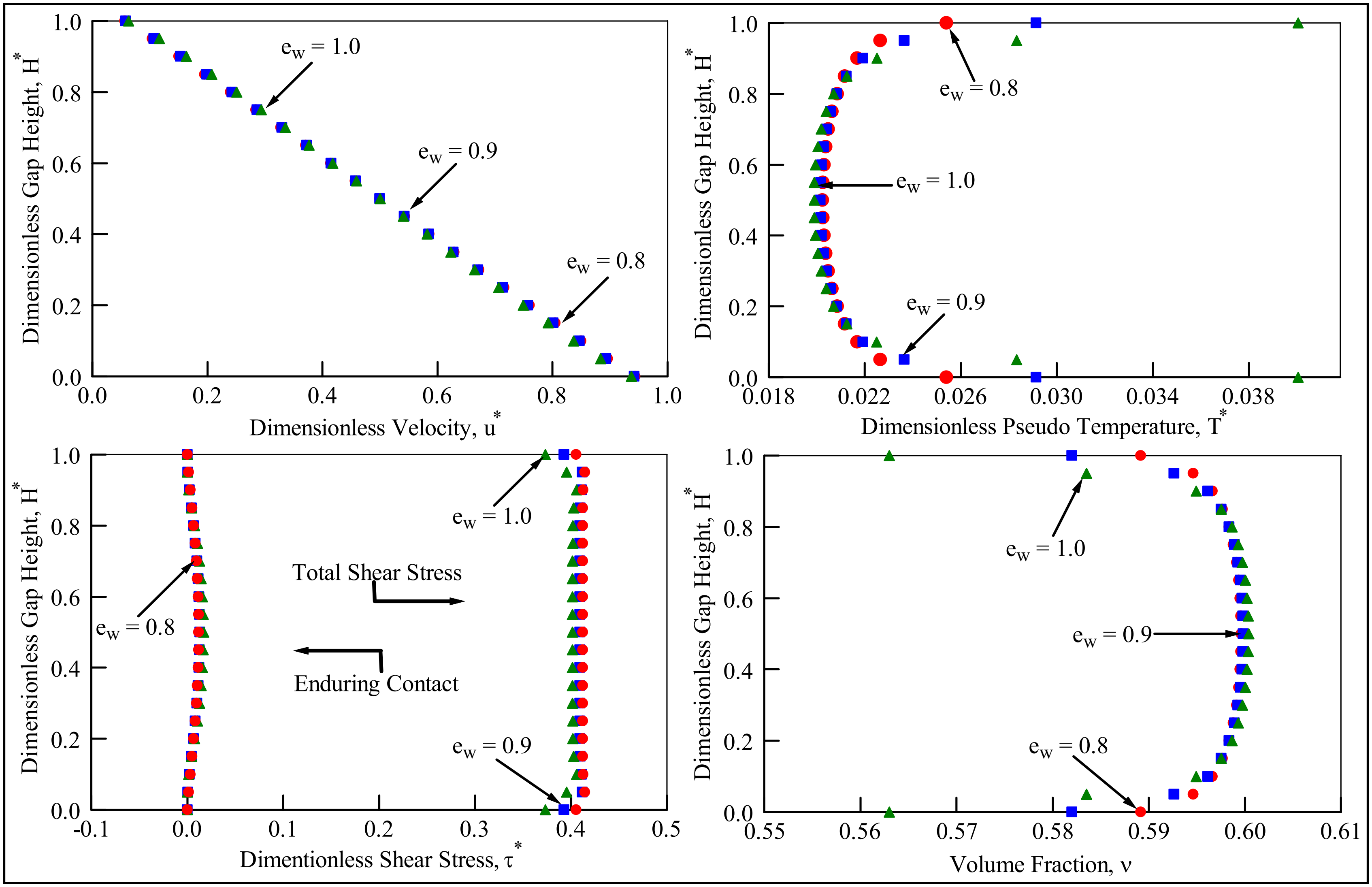

Figure 12.8 : Effect of the Wall Coefficient of Restitution, e_w

wall. Similarly the effect on the shear stress and the stress due to enduring contact is almost negligible. As e_w increases, the total shear stresses and the shear stresses due to enduring contact does not show any changes and remain constant across the gap.

12.10.8 Effect of the Enduring Contact on the True Temperature, T_R

The results presented in this section focus on applying the theory to determine the true temperature of the granular flow sheared between two parallel plates and also predict how hot the interfaces of the top and bottom plates can become. These predictions are based on the solution of the flow velocity, pseudo temperature, and solid volume fraction presented earlier. Both the top and the bottom plates are made of Stainless Steel. They both have a length of 26 mm and thickness of 13 mm. The top plate is stationary, while the velocity of the bottom plate is $U = 4.6\,\text{m/sec}$. From the properties of the Stainless Steel [85], the thermal conductivity, the specific heat, and the density are selected as $k_{Top} = k_{Bott} = 16.3\,\text{W/mK}$, $c_{Top} = c_{Bott} = 500\ \text{J/kgK}$, $\rho_{Top} = \rho_{Bott} = 8000\,\text{kg/m}^3$ respectively. The properties of the Titanium Dioxide [88] are assumed to be $\rho_p = 4260\,\text{kg/m}^3$, $k_p = 8.79\ \text{W/mK}$, and $c_p = 711\ \text{J/kgK}$. The effective thermal conductivity is computed based on the prediction of the solid volume fraction. The value of the convection heat transfer coefficient (*h)* for the moving plate is unknown. Based on Holman [86] and Incropera & DeWitt [87], the convection heat transfer coefficient for the moving plate is assumed to be $h_{Bott} = 50\ \text{W/m}^2\text{K}$, while for the stationary plate the convection heat transfer coefficient is much smaller and is assumed to be $h_{Top} = 15\ \text{W/m}^2\text{K}$.

Figure 12.9 represents the predicted distribution of the true temperature including the enduring contact effect at the bottom interface, mid-plane and top interface along the moving x-direction. The results are compared to the benchmark simulations without the consideration of the enduring contact. The true temperature increases from inlet to outlet and the rise predicted over the stationary disc is greater than the one predicted over the moving disc. This phenomenon can be explained by examining the energy equation of the granular flow. Three terms governed this equation: the convection, the conduction, and the dissipation. The convection term represents the rate of temperature transported through the movement of the flow from inlet to outlet by convection relative to the interfaces. The dissipation term supplies the energy to the flow as a result of inelastic collision between the granules. As a result of the convection and dissipation terms, heat is produced due to the inelastic collision between the granules and thus the true temperature is predicted to increase from the inlet to the outlet. Since the effective thermal conductivity for the granular flow used is very small, it results in a prediction of small rise in the temperatures at the interfaces and heat is retained within the granular flow.

It is clear that the magnitude of true temperature with consideration of enduring contact is greater than the case without enduring contact at the interfaces, as well as in the middle of the gap. This increase is a result of the role of enduring contact between the granules. When the enduring contact exists, it causes an increase in the friction between the granules and therefore a higher temperature within the flow. The increase in the friction between the granules means that the frictional stress due to the enduring contact starts to become noticeable. An increase in the frictional stress results in a reduction in the total shear stress as explained in Figure 12.6, which causes reduction in the friction coefficient. In addition, as shown in Figure 12.3, the solid volume fraction decreases and the pseudo temperature tends to increase due to the existence of enduring force. The larger the pseudo temperature, the greater the dissipation causing the true temperature to increase compared to the case without enduring effect. This phenomenon indicates that the enduring contact plays a significant role in predicting the true temperature.

Figure 12.10 demonstrates how the true temperature is distributed within the granular flow and in the fields of both bottom and top plates. The energy is transferred to the top and bottom plates via the thin layer of the plates' thickness that is in contact with the temperature produced within the flow of the granular material. It is noted that the temperature at the top plate interface is slightly larger than the bottom plate interface due to the high heat convection coefficient of the moving plate. The true temperature distribution within the granular flow demonstrates the effect of the viscous dissipation term. The true temperature builds up from the inlet to the outlet due to the heat source.

12.11 Conclusions

This chapter deals with the granular flow sheared between two parallel plates with consideration of the enduring contact. The formulation of the governing equations and boundary conditions are presented. The characteristics of the flow are investigated in a "transient regime" where both kinetic-collision effect and enduring contact exists concurrently.

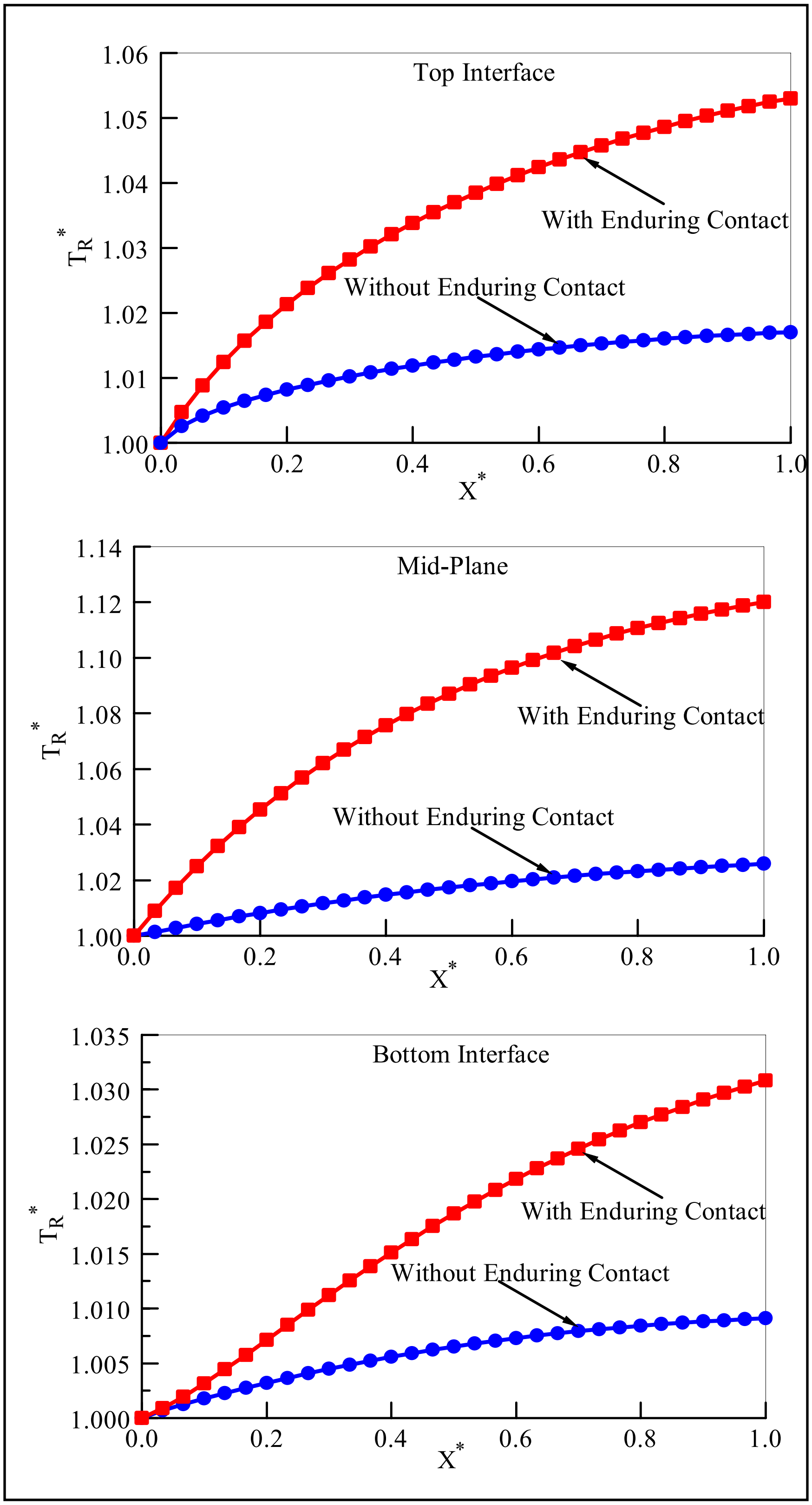

Figure 12.9 : The True Temperature at the Top Interface, Middle of the Gap, and Bottom Interface (Benchmark Simulations – *U*=4.6 m/s)

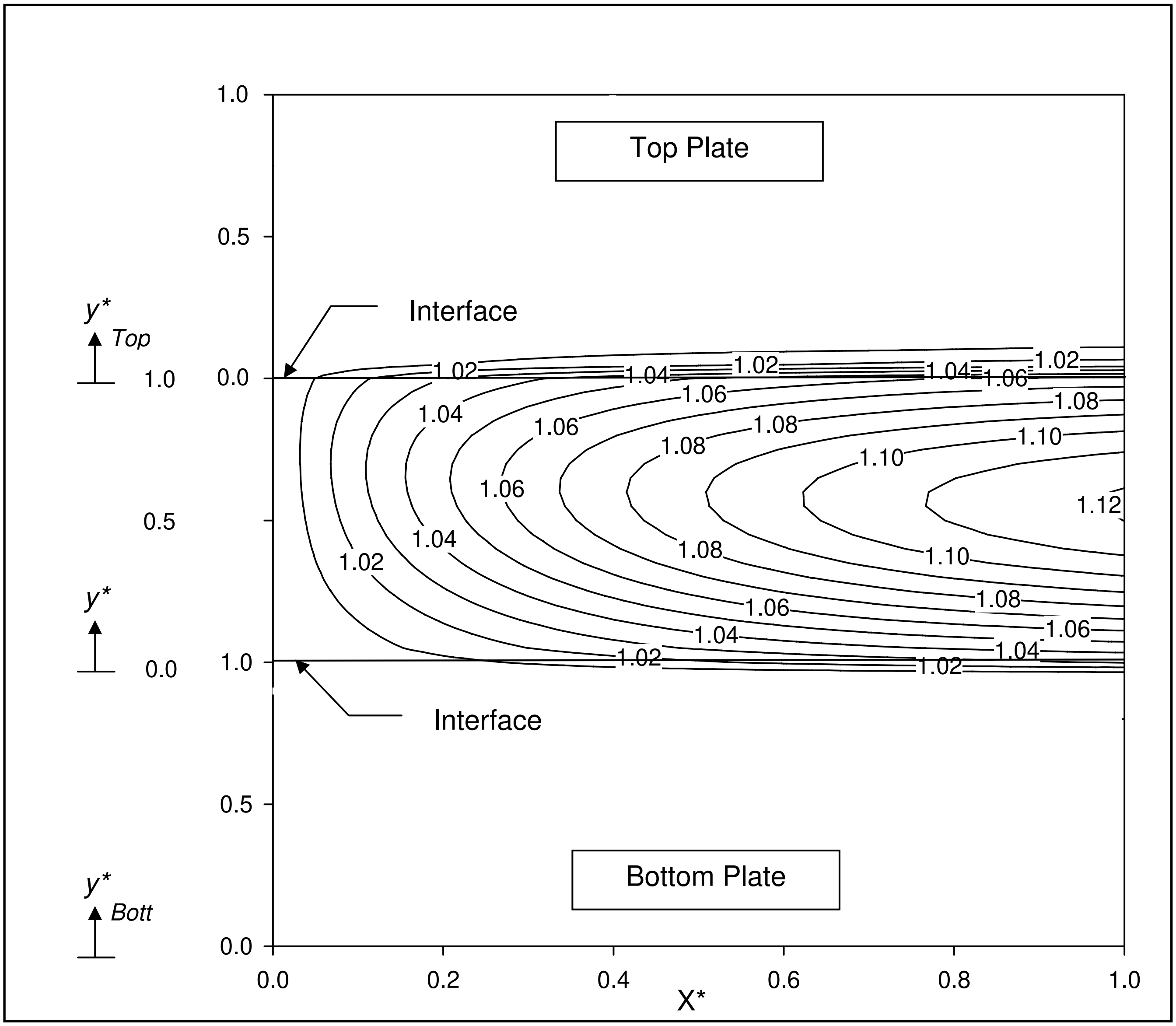

Figure 12.10 : The distribution of the true temperature in the granular flow and the fields of the top and bottom plates (Benchmark Simulations – *U*=4.6 m/s)

The results of this chapter reveal that the effect of enduring contact between granules is very important and must be considered especially at low operating speeds and when dealing with high solid volume fractions, which is typically the case when dealing with granular lubrication, and it also show a definite effect on the true temperature. At a moderately high speed, the effect of enduring contact is very small and the trends are analogous to the case without the consideration of the enduring contact. As the sliding speed decreases, the enduring contact force between the granules begins to play a role in supporting the applied load. In this case, the profiles of the volume fraction and the pseudo temperature across the gap become more flattened and the load is solely carried by the stationary granules. The lower the speed, the larger the effect of the enduring contact and the less is the collision between the granules. As a result, the total shear stress becomes smaller. As the speed increases, the enduring contact effect becomes less and more collision occurs in the flow. Thus, the total shear stress increases. Furthermore, at very low speed the granules are almost stationary and a lower friction coefficient is predicted. However, at relatively high speed where the effect of enduring contact is nil, the friction coefficient is identical to the case without the effect of the enduring contact.

The true temperature is also studied. The distribution of the true temperature at both top and bottom interfaces along the x-direction is predicted. The true temperature increases from the inlet to the outlet for both top and bottom interfaces, as well as the mid-plane. When comparing with the case without the enduring contact effect, it is found that the enduring contact has noticeable influence on increasing the true temperature due to the friction between the granules. The viscous dissipation term is found to play a role on predicting the true temperature. It supplies energy to the flow as a result of inelastic collision between the granules. The viscous dissipation appears in the pseudo energy equation and is a function of the fluctuation velocity (pseudo temperature) and the solid volume fraction. The larger the fluctuation velocity, the greater becomes the chance of collision between granules. Therefore, the energy dissipation caused by the inelastic collision increases which cause the true temperature to increase.

It is concluded that for a flow between two parallel plates, a very small rise of the true temperature is experienced in the direction of motion from inlet to outlet, whereas Heshmat and Brewe [89] experienced a higher temperature rise but with a larger speed as previously explained in Chapter 11.

CHAPTER 13. CONCLUDING REMARKS

It is well known that conventional lubricating oils are completely ineffective beyond a certain operating temperature. They tend to break down at operating temperature exceeding 200 ^{o}C, thereby degrading their ability to support load. Unlike conventional lubricants, a suitable granular material can effectively lubricate a bearing under extreme temperatures and can resist breaking down as a result of large shear forces. Thus, it has been identified as a promising lubricant for this purpose.

The motivation for this dissertation arises from the need for bearing technology that can accommodate the future generation of engines aiming for higher thermodynamic efficiency, less fuel consumption and increased thrust-to-weight ratio in turbine engines. Other applications using granular materials can vary from auxiliary bearings particularly during start-up periods, to the use in micro-nano-scale systems such as MEMS devices. Despite the fact that there is a general agreement on the needs for such a new oil-free granular lubrication mechanisms, modeling and prediction of granular flows still remains distant from being well understood. While the archival literature contains a great deal of research on granular lubrication, a number of important issues remain largely unexplored.

In this dissertation, a detailed study of the granular collision lubrication, both theoretically and experimentally is presented based on the kinetic theory of the granular material where the granules interact with each other and with the boundary surfaces through instantaneous, binary collisions, characterized by a constant coefficient of restitution. The granular lubrication in Couette flows is of particular interest. The governing equations and the proper boundary conditions are derived based on the Lun's constitutive relations and Johnson and Jackson's general model for the frictional-collisional mechanism of the granular material sheared between two infinitely parallel plates. A series of simulations are reported where the effect of the viscous dissipation in the energy equation is considered. It was found that the energy supply to the granular flow arises from the slip velocity at the boundaries, and from the viscous dissipation in the middle of the gap.

Granular slippage is one of the important characteristics of granular lubrication. During shearing, the slip velocity provides energy from the boundaries into the granules contained within the gap. The slip at the boundaries increases the pseudo temperature and hence more energy is being supplied to the interior flow. The viscous dissipation term that appears in the pseudo energy equation is ruled mainly by the coefficient of restitution. The coefficient of restitution is a constant parameter that describes the inelastic collision between the granules where it plays a major role in predicting the pseudo temperature and the solid volume fraction. When the granules become nearly elastic (large e_p), there is less energy loss by inelastic collision and the viscous dissipation in the interior flow increases. The results show good agreement with several published papers.

Also, a theory that ties the true temperature to the grain mobility is developed by predicting the true temperature of granular lubricants sheared between two infinitely wide parallel plates. The true temperature of a granular material depends on the balance between the source of energy, and the dissipation of energy due to inelastic collisions. The distribution of the true temperature at both top and bottom interfaces along the x-direction is predicted and the effect of a number of important parameters investigated. The results show that the temperature increases from the inlet to the outlet for both top and bottom interfaces. The viscous dissipation term appears in the pseudo energy equation and is a function of the fluctuation velocity (pseudo temperature) and the solid volume fraction. As the fluctuation velocity increases, the chance of collision between granules becomes larger. Therefore, the energy dissipation caused by the inelastic collision increase results in an increase in the true temperature.

Increasing the coefficient of restitution of the granular material reduces the energy loss by inelastic collision between the granules (less heat dissipation). Therefore, a reduction in the true temperature at the interfaces is predicted. Additionally, it is found that the pseudo temperature tends to increase by increasing the sliding velocity of the bottom plate for both interfaces.

While most of the previous published researches on granular lubrication have dealt with rapid shearing regime where collisions are considered instantaneous, the effect of so-called enduring contact between granules has been largely ignored. However, in a dense regime and at relatively small sliding speeds, the contact time between the granules is larger than the time between collisions and thus the friction between the granules starts to play an important role. Therefore, the enduring contact becomes dominant over the kinetic and collisional stresses. To characterize the effect of enduring contact, the Coulomb friction model is utilized to take enduring contact into consideration. The characteristics of the granular flow are investigated in a transient regime, where both kinetic-collision effect and enduring contact exist concurrently. The results reveal that the enduring contact is a strong function of the solid volume fraction and its effect tends to dominate the solution at relatively small sliding speeds.

The results reveal that at a moderately high speed, the effect of enduring contact is very small and the trends are analogous to the case without the consideration of the enduring contact. As the sliding speed decreases, the enduring contact force between the granules begins to play a role in supporting the applied load. In this case, the profiles of the volume fraction and the pseudo temperature across the gap become more flattened and the load is solely carried by the stationary granules. Furthermore, at very low speed the granules are almost stationary and a lower friction coefficient is predicted. However, at relatively high speed where the effect of enduring contact is nil, the friction coefficient is identical to the case without the effect of the enduring contact. In addition, it is found that the enduring contact has a noticeable effect on increasing the true temperature at the interfaces due to the friction between the granules.

In addition, it is established that granular material plays a major role in determining the axial load (lift) transmitted between the surfaces, the sliding friction and the slip velocity, but uncertainties still remain on several issues which require more investigation. Experimental investigations are presented to demonstrate the lift phenomenon observed in an annular shear cell apparatus using 3-mm stainless steel balls. The effects of the friction coefficient and the surface roughness are expressed as a function of the rotational speed and the applied load. Simulations of the kinetic theory for the granular material are performed and compared with the experimental results. The agreement between the theory and the experiment is illustrated. Furthermore, no adjustments for the friction coefficients or displacements were made to obtain a better fit.

It is found that the frictional force that can be generated within a sheared granular material is critical to understanding its strength but has significant applications in geophysics and technology. When shear stress is applied, sliding starts gradually at a frictional force smaller than the frictional force generated during steady sliding, but by increasing the shear, the frictional strength increases and sliding stabilizes. At low speed spherical granules accommodate strain preferentially by rolling, then by increasing the speed, the proportion of rolling to sliding decreases leading to higher friction. Consequently, by increasing the speed of the rotating disk, the collision rate of the granules is enhanced and more momentum is passed on to the lower disk to ensure complete lift between the top and bottom surfaces and then reach a steady state. The larger the applied load, the lesser the lift produced due to the increase of compactness of the granules within the gap. As such, these above presented set of experiments provide a unique quantitative evidence for the measure of the phenomenon of the lift.

Granular flows exhibit a variety of phenomena that have both fluid and solid aspects. Stick-slip is a complex phenomenon that depends on many parameters. Given the recent interest in the tribology of granules, it is surprising that there have been limited studies relevant to investigation of the stick-slip phenomenon in granular lubrication. Therefore, a series of experimental investigation on the nature of stick-slip associated with granular materials sheared at low speeds is demonstrated using 1.4-mm ceramic balls. Specifically, the effect of stick-slip on the friction and the change in the spatial arrangement of granules in a granular shear cell are demonstrated. Microscopic events for the non-periodic stick-slip motion at high stiffness are also demonstrated. The results revealed the occurrence of stick-slip phenomenon at low speed and its behavior is found to be similar to the results presented by several researchers.

BIBLIOGRAPHY

[1] Reynolds, O., 1886, "On the Theory of Lubrication and its Application to Mr. Beauchamp Tower's Experiments, Including an Experimental Determination of the Viscosity of Olive Oil," Proceedings of the Royal Society of London, **40**, pp. 191-203.

[2] Bagnold, R., 1954, "Experiments on a Gravity-Free Dispersion of Large Solid Spheres in a Newtonian Fluid under Shear," Proceedings of the Royal Society of London. Series A, Mathematical and Physical Sciences, **225**(1160), pp. 49–63.

[3] Heshmat, H., 1992, "The Quasi-Hydrodynamic Mechanism of Powder Lubrication – Part II. Lubricant Film Pressure Profile," Journal of STLE, Lubrication Engineering, **48**(5), pp. 373–383.

[4] Heshmat, H., 1991, "The Rheology and Hydrodynamics of Dry Powder Lubrication," Society of Tribologists and Lubrication Engineers (STLE), Tribology Transactions **34**(3), pp. 433-439.

[5] Savage, S.B. and Jeffrey, D.J., 1981, "The Stress Tensor in a Granular Flow at High Shear Rates," Journal of Fluid Mechanics, **110**, pp. 255-272.

[6] Carnahan, F.N. and Starling, E.K., 1969, "Equation of State for Nonattracting Rigid Spheres," The Journal of Chemical Physics, **51**(2), pp. 635-636.

[7] Jenkins, J.T. and Savage, S.B., 1983, "A Theory for the Rapid Flow of Identical, Smooth, Nearly Elastic, Spherical Particles," Journal of Fluid Mechanics, **130**, pp. 187-202.

[8] Lun, C.K.K., Savage, S.B., Jeffrey, D.J., and Chepurniy, N., 1984, "Kinetic Theories for Granular Flows: Inelastic Particles in Couette Flow and Slightly Inelastic Particles in a General Flow Field," Journal of Fluid Mechanics, **140**, pp. 223–256.

[9] Jenkins, J.T. and Richman, M.W., 1986, "Boundary Conditions for Plane Flows of Smooth, Nearly Elastic, Circular Disks," Journal of Fluid Mechanics, **171**, pp. 53–69.

[10] Jenkins, J.T. and Richman, M.W., 1985, "Kinetic Theory for Plane Flows of a Dense Gas of Identical Rough, Inelastic, Circular Disks," Physics of Fluids, **28**(12), pp. 3485-3494.

[11] Jenkins, J.T. and Mancini, F., 1987, "Balance Laws and Constitutive Relations for Plane Flows of a Dense, Binary Mixture of Smooth, Nearly Elastic, Circular Disks," ASME Journal of Applied Mechanics, **54**, pp. 27-34.

[12] Lun, C.K.K. and Savage, S.B., 1986, "The Effects of an Impact Velocity Dependent Coefficient of Restitution on Stresses Developed by Sheared Granular Materials," Acta Mechanica, **63**(1-4), pp. 15-44.

[13] Walton, O.R., 1993, "Numerical Simulations of Inclined Chute Flows of Monodisperse, Inelastic, Frictional Spheres," Mechanics of Materials, **16**(1-2), pp. 239-247.

[14] Haff, P.K., 1983, "Grain Flow as a Fluid-Mechanical Phenomenon," Journal of Fluid Mechanics, **134**, pp. 401–430.

[15] Johnson, P.C. and Jackson, R., 1987, "Frictional-Collisional Constitutive Relations for Granular Materials with Applications to Plane Shearing," Journal of Fluid Mechanics, **176**, pp. 67–93.

[16] Elrod, H.G., 1988, "Granular Flow as a Tribological Mechanism – A First Look," Interface Dynamics, Leeds-Lyon Symposium, BHRA, pp. 75–102.

[17] Khonsari, M.M., 1997, "On the Modeling of Multi-Body Interaction Problems in Tribology," Wear, **207**(1-2), pp. 55–62.

[18] Kaur, R.G. and Heshmat, H., 2002, "100mm Diameter Self-Contained Solid/Powder Lubricated Auxiliary Bearing Operated at 30,000 rpm," Society of Tribologists and Lubrication Engineers (STLE), Tribology Transactions **45**, pp. 76–84.

[19] Craig, K., Buckholz, R., and Domoto, G., 1986, "An Experimental Study of the Rapid Flow of Dry Cohesionless Metal Powders," ASME Journal of Applied Mechanics, **53**, pp. 935–942.

[20] Heshmat, H., 1991, "High-Temperature Solid-Lubricated Bearing Development – Dry Powder-Lubricated Traction Testing," American Institute of Aeronautics and Astronautics (AIAA), Journal of Propulsion and Power, **75**, pp. 814–820.

[21] Savage, S. and Sayed, M., 1984, "Stresses Developed by Dry Cohesionless Granular Materials Sheared in an Annular Shear Cell," Journal of Fluid Mechanics, **142**, pp. 391–430.

[22] Hanes, D.M. and Inman, D.L., 1985, "Observations of Rapidly Flowing Granular Fluid Materials," Journal of Fluid Mechanics, **150**, pp. 357–380.

[23] Yu, C.M., Craig, K., and Tichy, J., 1994, "Granular Collision Lubrication," Journal of Rheology, **38**(4), pp. 921–936.

[24] Yu, C.M. and Tichy, J., 1996, "Granular Collisional Lubrication: Effect of Surface Roughness, Particle Size and Solid Fraction," Society of Tribologists and Lubrication Engineers (STLE), Tribology Transactions **39**(3), pp. 537–546.

[25] Dai, F., Khonsari, M.M., and Lu, Y.Z., 1994, "On the Lubrication Mechanism of Grain Flows," Society of Tribologists and Lubrication Engineers (STLE), Tribology Transactions **37**, pp. 516–524.

[26] McKeague, K.T. and Khonsari, M.M., 1996, "Generalized Boundary Interactions for Powder Lubricated Couette Flow," ASME Journal of Tribology, **118**(3), pp. 580–588.

[27] Hui, K., Haff, P.K., Ungar, J.E., and Jackson, R., 1984, "Boundary Conditions for High-Shear Grain Flows," Journal of Fluid Mechanics, **145**, pp. 223–233.

[28] Campbell, C.S., 1993, "Boundary Interactions for Two-Dimensional Granular Flow–Part I. Flat Boundaries, Asymmetric Stress and Couple Stress," Journal of Fluid Mechanics, **247**, pp. 137–156.

[29] Elrod, H.G. and Brewe, D.E., 1991, "Numerical Experiments With Flows of Elongated Granules," 18th Leeds Lyon Symposium on Tribology, Elsevier Tribology Series, **No.21**, pp. 219–226.

[30] Zhou, L. and Khonsari, M.M., 2000, "Flow Characteristics of a Powder Lubricant Sheared Between Parallel Plates," ASME Journal of Tribology, **122**(1), pp. 147–155.

[31] Sawyer, G.W. and Tichy, J.A., 2001, "Lubrication With Granular Flow: Continuum Theory, Particle Simulation, Comparison With Experiment," ASME Journal of Tribology, **123**(4), pp. 777–784.

[32] Wornyoh, E., Jasti, V., and Higgs, C.F.I., 2007, "A Review of Dry Particulate Lubrication: Powder and Granular Materials," ASME Journal of Tribology, **129**(2), pp. 438-449

[33] Pappur, M. and Khonsari, M.M., 2002, "Flow Characterization and Performance of a Powder Lubricated Slider Bearing," ASME J. Tribol., **124**, pp. 1–10.

[34] Iordanoff, I., Seve, B., and Berthier, Y., 2002, "Solid Third Body Analysis Using a Discrete Approach: Influence of Adhesion and Particle Size on the Macroscopic Behavior of the Contact," ASME Journal of Tribology, **124**(3), pp. 530–538.

[35] Iordanoff, I. and Khonsari, M.M., 2004, "Granular Lubrication: Towards an Understanding of the Transition Between Kinetic and Quasi-Fluid Regime," ASME Journal of Tribology, **126**(1), pp. 137–145.

[36] Hassanpour, A., Ding, Y., and Ghadiri, M., 2004, "Shear Deformation of Binary Mixtures of Dry Particulate Solids," Advanced Powder Technology, **15**(6), pp. 687–697.

[37] Higgs, C.F., III and Tichy, J., 2004, "Granular Flow Lubrication: Continuum Modeling of Shear Behavior," ASME Journal of Tribology, **126**(3), pp. 499–510.

[38] Fillot, N., Iordanoff, I., and Berthier, Y., 2004, "A Granular Dynamic Model for the Degradation of Material," ASME, Journal of Tribology, **126**(3), pp. 606–614.

[39] Wang, D.F. and Kato, K., 2003, "Humidity Effect on the Critical Number of Friction Cycles for Wear Particle Generation in Carbon Nitride Coatings," Wear, **254**(1-2), pp. 10–22.

[40] Jang, J.Y. and Khonsari, M.M., 2005, "On the Granular Lubrication Theory," Proceedings of the Royal Society of London. Series A, Mathematical and Physical Sciences, **461**(2062), pp. 3255–3278.

[41] Tsai, H. and Jeng, Y., 2006, "Characteristics of Powder Lubricated Finite-Width Journal Bearings: A Hydrodynamic Analysis," ASME Journal of Tribology, **128**(2), pp. 351–357.

[42] Kaur, R., 2001, "The Power of Powder," Lubs-n-Greases, **7**(5), pp. 50-54.

[43] McKeague, K.T. and Khonsari, M.M., 1996, "An Analysis of Powder Lubricated Slider Bearings," ASME Journal of Tribology, **118**(1), pp. 206-214.

[44] Aranson, I.S., Tsimring, L.S., and Vinokur, V.M., 2002, "Stick-Slip Friction and Nucleation Dynamics of Ultra-thin Liquid Films," Physical Review B, **65**(125402), pp. 1 – 7.

[45] Hayakawa, H., 1999, "Simple Model for Granular Friction," Physical Review E, **60**(4), pp. 4500–4504.

[46] Frye, K.M. and Marone, C., 2002, "Influence of Particle Dimensionality on Granular Friction in Laboratory Shear Zones," Geophysical Research Letters, **29**(19), pp. 22-1 – 22-4.

[47] Mair, K., Frye, K.M., and C., M., 2002, "Influence of Grain Characteristics on the Friction of Granular Shear Zones," Journal of Geophysical Research, **107**(B10), pp. ECV 1–9.

[48] Kudrolli, A., Wolpert, M., and Gollub, J.P., 1997, "Cluster Formation Due to Collisions in Granular Material," Physical Review Letters, **78**(7), pp. 1383–1386.

[49] Craig, K., Buckholz, R., and Domoto, G., 1987, "The Effect of Shear Surface Boundaries on Stress for Shearing Flow of Dry Metal Powders-An Experimental Study," ASME Journal of Tribology, **109**, pp. 232–237.

[50] Johansen, A., Dimon, P., Ellegaard, C., Larsen, J.S., and Rugh, H.H., 1993, "Dynamic Phases in a Spring-Block System," Physical Review E, **48**(6), pp. 4779 – 4790.

[51] Pöschel, T. and Buchholtz, V., 1993, "Static Friction Phenomena in Granular Materials: Coulomb Law Versus Particle Geometry," Physical Review Letters, **71**(24), pp. 3963 – 3966.

[52] Morales, E., Peralta-Fabi, R., and Romero-Rochín, V., 1996, "Testing Predictability Criteria in Avalanches," Physical Review E, **54**(4), pp. 3488 – 3494.

[53] Cartwright, J.H.E., Hernández-García, E., and Piro, O., 1997, "Burridge-Knopoff Models as Elastic Excitable Media," Physical Review Letters, **79**(3), pp. 527 – 530.

[54] Albert, I., Tegzes, P., Albert, R., Sample, J.G., Barabási, A.-L., Vicsek, T., Kahng, B., and Schiffer, P., 2001, "Stick-Slip Fluctuations in Granular Drag," Physical Review E., **64**(031307), pp. 1– 9.

[55] Campbell, C.S., 1990, "Rapid Granular Flows," Annual Review of Fluid Mechanics, **22**(1), pp. 57-90.

[56] Jaeger, H.M., Nagel, S.R., and Behringer, R.P., 1996, "Granular Solids, Liquids, and Gases," Reviews of Modern Physics, **68**(4), pp. 1259 – 1273.

[57] Rabinowicz, E., 1951, "The Nature of the Static and Kinetic Coefficients of Friction," Journal of Applied Physics, **22**(11), pp. 1373 – 1379.

[58] Burridge, R. and Knopoff, L., 1967, "Model and Theoretical Seismicity," Bulletin of the Seismological Society of America **57**(3), pp. 341-371.

[59] Brace, W. and Byerlee, J., 1966, "Stick-Slip as a Mechanism for Earthquakes," Science, **153**(3739), pp. 990 – 992.

[60] Byerlee, J., 1967, "Frictional Characteristics of Granite Under High Confining Pressure," Journal of Geophysical Research, **72**(14), pp. 3639 – 3648.

[61] Dieterich, J.H., 1978, "Time-Dependent Friction and the Mechanics of Stick-Slip," Pure and Applied Geophysics, **116**(4-5), pp. 790 – 806.

[62] Ruina, A., 1983, "Slip Instability and State Variable Friction Laws," Journal of Geophysical Research, **88** (B13), pp. 10359-10370

[63] Persson, B.N.J., 1997, "Sliding Friction: Physical Principles and Applications," Springer, Nanoscience and Technology. 462.

[64] Scholz, C.H., 2002, "The Mechanics of Earthquakes and Faulting." 2nd ed., Cambridge University Press. 496

[65] Meyer, E., Overney, R.M., Dransfeld, K., and Gyalog, T., 1998, "Nanoscience: Friction and Rheology on the Nanometer Scale," World Scientific. 392.

[66] Yoshizawa, H. and Israelachvili, J., 1993, "Fundamental Mechanisms of Interfacial Friction II: Stick-Slip Friction of Spherical and Chain Molecules," Journal of Physical Chemistry **97**(43), pp. 11300 – 11313.

[67] Israelachvili, J.N., McGuiggan, P.M., and Homola, A.M., 1988, "Dynamic Properties of Molecularly Thin Liquid Films," Science, **240**(4849), pp. 189-191.

[68] Gee, M.L., McGuiggan, P.M., Israelachvili, J.N., and Homola, A., 1990, "Liquid to Solid-Like Transitions of Molecularly Thin Films Under Shear," Journal of Chemical Physics, **93**(3), pp. 1895 – 1906.

[69] Heslot, F., Baumberger, T., Perrin, B., Caroli, B., and Caroli, C., 1994, "Creep, Stick-Slip, and Dry-Friction Dynamics: Experiments and a Heuristic Model," Physical Review E, **49**(6), pp. 4973 – 4988.

[70] Nasuno, S., Kudrolli, A., and Gollub, J.P., 1997, "Friction in Granular Layers: Hysteresis and Precursors," Physical Review Letters, **79**(5), pp. 949 – 952.

[71] Batista, A.A. and Carlson, J.M., 1998, "Bifurcations from Steady Sliding to Stick Slip in Boundary Lubrication," Physical Review E **57**(5), pp. 4986-4996.

[72] Baumberger, T., Caroli, C., Perrin, B., and Ronsin, O., 1995, "Nonlinear Analysis of the Stick-Slip Bifurcation in the Creep-Controlled Regime of Dry Friction," Physical Review E, **51**(5), pp. 4005 – 4010.

[73] Gayvallet, H. and Géminard, J.-C., 2002, "Ageing of the Avalanche Angle in Immersed Granular Matter," The European Physical Journal B - Condensed Matter and Complex Systems, **30**(3), pp. 369 – 375.

[74] Radjai, F., Evesque, P., Bideau, D., and Roux, S., 1995, "Stick-Slip Dynamics of a One-Dimensional Array of Particles," Physical Review E, **52**(5), pp. 5555 – 5564.

[75] Nasuno, S., Kudrolli, A., Bak, A., and Gollub, J.P., 1998, "Time-Resolved Studies of Stick-Slip Friction in Sheared Granular Layers," Physical Review E, **58**(2), pp. 2161–2171.

[76] Howell, D., Behringer, R.P., and Veje, C., 1999, "Stress Fluctuations in a 2D Granular Couette Experiment: A Continuous Transition," Physical Review Letters, **82**(26), pp. 5241-5244.

[77] Adjemian, F. and Evesque, P., 2004, "Experimental Study of Stick-Slip Behavior," International Journal for Numerical and Analytical Methods in Geomechanics, **28**(6), pp. 501– 530.

[78] Alshibli, K. and Roussel, L., 2006, "Experimental Investigation of Stick-Slip Behavior in Granular Materials," International Journal for Numerical and Analytical Methods in Geomechanics, **30** (14), pp. 1391 – 1407.

[79] Elkholy, K. and Khonsari, M.M., 2007, "Granular Collision Lubrication: Experimental Investigation and Comparison with Theory," to appear in ASME Journal of Tribology.

[80] Sammis, C.G., King G., and R., B., 1987, "The Kinematics of Gouge Deformation," Pure and Applied Geophysics, **125**(5), pp. 777– 812.

[81] Cain, R.G., Page, N.W., and Biggs, S., 2001, "Microscopic and Macroscopic Aspects of Stick-Slip Motion in Granular Shear," Physical Review E, **64**(1), pp. 1–8.

[82] Gonzo, E.E., 2002, "Estimating Correlations for the Effective Thermal Conductivity of Granular Materials," Chemical Engineering Journal, **90**(3), pp. 299–302.

[83] Maxwell, J.C., 1873, "A Treatise on Electricity and Magnetism," Oxford, Claredon Press. 365.

[84] Chiew, Y.C. and Glandt, E., 1983, "The Effect of Structure on the Conductivity of a Dispersion," Journal of Colloid and Interface Science, **94**, pp. 90-104.

[85] Shackelford, J.F. and Alexander, W., 1994, "Materials Science and Engineering Handbook." 2nd ed., C. 4250, CRC Press. 261-263.

[86] Holman, J.P., 1986, "Heat Transfer," New York, McGraw Hill. 675.

[87] Incropera, F.P. and DeWitt, D.P., 1996, "Fundamentals of Heat and Mass Transfer," New York Wiley. 886.

[88] Karnutsch, C., "Rutile Crystals (TiO2)," [cited July 18, 2007; Available from: **http://www.sciner.com/Crystals/TiO2.htm**.

[89] Jang, J.Y. and Khonsari, M.M., 2006, "On the Role of Enduring Contact in Powder Lubrication," ASME Journal of Tribology, **128**(1), pp. 168-175

[90] Zhou, L., 1998, "Application of Continuum Mechanics to Powder Lubrication," University of Pittsburgh, **Ph.D**.

[91] Gidaspow, D., 1994, "Multiphase Flow and Fluidization: Continuum and Kinetic Theory Descriptions," Boston, Academic Press. 467.

[92] Johnson, K.L., 1985, "Contact Mechanics," Cambridge, University of Cambridge Press. 464.

VITA

Karim N. El Kholy was born and grew up in Alexandria, Egypt. He received his bachelor degree in marine engineering from the Arab Academy for Science and Technology and Maritime Transport (AASTMT) in 1994. After graduation, he worked with Santa Fe International Drilling Company as an assistant barge engineer. He later joined the AASTMT in 1996 as a teaching assistant while completing his master's degree in marine engineering. Upon his graduation in late 1999, he continued working at AASTMT until he moved to the United States and joined Louisiana State University in August 2000 to pursue a doctoral degree in the department of mechanical engineering. He was hired since then in the Center of Rotating Machinery (CeRoM) as a research assistant under the supervision of Dr. Michael Khonsari, as well as the mechanical engineering department as a teaching assistant for the machine design under the supervision of Dr. Su-Seng Pang. In 2005, he received an NSF graduate fellowship in the GK-12 program under the supervision of Dr. Frank Neubrander. He expects to receive the degree of Doctor of Philosophy in mechanical engineering in August 2007.